Alexander Wilk

Particle Identification Using Artificial Neural Networks with the ALICE Transition Radiation Detector

— 2010 —

Experimentelle Physik

Particle Identification Using Artificial Neural Networks with the ALICE Transition Radiation Detector

Inauguraldissertation
zur Erlangung des Doktorgrades
der Naturwissenschaften im Fachbereich Physik
der Mathematisch-Naturwissenschaftlichen Fakultät
der Westfälischen Wilhelms-Universität Münster

vorgelegt von
Alexander Wilk
aus Schäßburg

— 2010 —

Für Swannet, Kolja, Frederik und Moritz!

Contents

1. Introduction

ALICE is the acronym for "A Large Ion Collider Experiment" [Aam08] which is the dedicated heavy-ion experiment at the Large Hadron Collider (LHC) [Eva08] at the European Organization for Nuclear Research (CERN). The LHC is currently the most powerful accelerator for protons as well as for ions. On November 23rd 2009 the first proton-proton collisions were detected in ALICE [Aam10] (see Figure 1.1). While the first proton-proton collisions occurred with a center-of-mass energy $\sqrt{s} = 900\,\text{GeV}$ the maximum energy is $\sqrt{s} = 14\,\text{TeV}$ for proton collisions and $\sqrt{s_{NN}} = 5.5\,\text{TeV}$ for lead ion collisions. Such high energies will provide a deeper insight into the structure of matter than ever before. It is expected to complete the experimental verification of the standard model of particle physics (observation of the *Higgs boson*), but also to discover new phenomena which can only be explained by theoretical models beyond the standard model (e.g. *supersymmetry*).
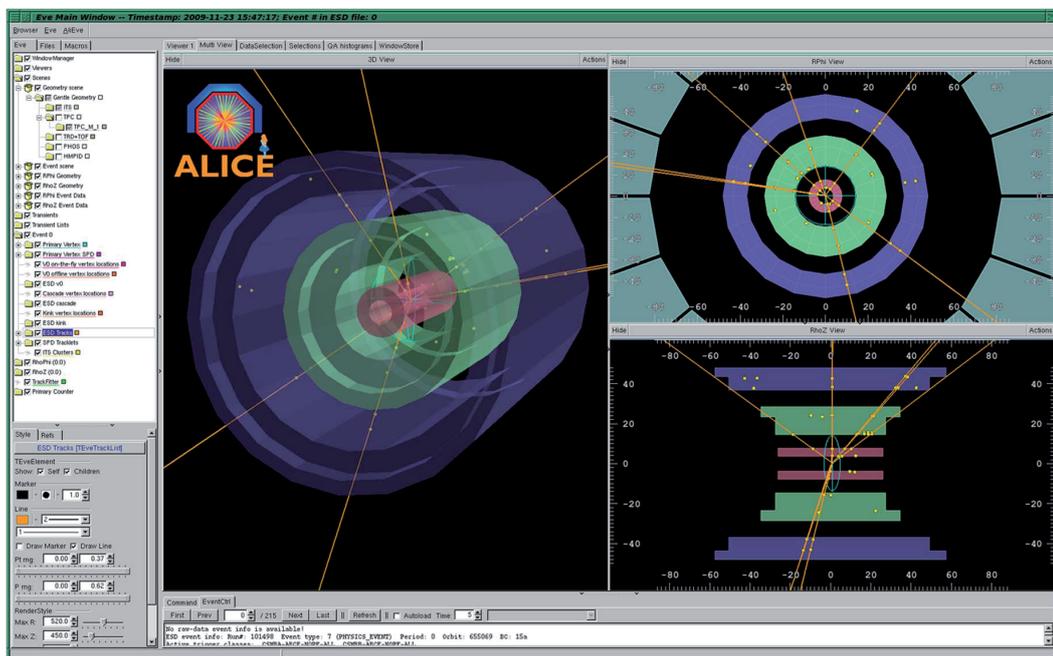
Figure 1.1: First *pp* collision candidate at an energy of $\sqrt{s} = 900\,\text{GeV}$ as seen on the online event display in the ALICE counting room [Aam10].

While most of the LHC experiments are concentrating on open questions in elementary particle physics, ALICE is designed to investigate the formation of the *quark-gluon plasma* (QGP). The quark-gluon plasma is an exotic state of matter that existed presumably until about 10^{-5} s after the big bang. It can be created under laboratory conditions in heavy-ion collisions. The large collision energy that will be reached for lead nuclei at LHC allows to study the QGP with a larger volume, higher energy density, and longer lifetime than in experiments at previous accelerators like the Super Proton Synchrotron (SPS) at CERN or the Relativistic Heavy Ion Collider (RHIC) at Brookhaven National Laboratory (BNL).

The central topic of this work is the particle identification capability of the ALICE Transition Radiation Detector (TRD). The TRD was designed to improve the momentum resolution of ALICE to 5% at a momentum of 5 GeV/*c*, to provide electron identification, and to serve as a trigger for electrons with momenta above 1 GeV/*c*. The design goal for electron identification was to reach a pion suppression of 100 at a given electron efficiency of 90% [TRD01]. These requirements are crucial for the background reduction in analyses like the reconstruction of the J/ψ or Υ via their decay into an electron positron pair in an environment that is dominated by pions. The expected ratio between electrons and pions coming from the primary vertex is at about 1:1000.

The signal that is produced by electrons in the Transition Radiation Detector is different from the signal generated by other particles. For a given momentum ($p \gtrsim 1.0$ GeV/*c*) the pure amount of charge deposition caused by ionization (*Bethe-Bloch* energy loss) exceeds that of hadrons and muons due to lower mass of the electron. In addition, electrons produce transition radiation photons by traversing the TRD radiator. These photons are absorbed in the gaseous volume of the TRD and contribute to the total charge deposition, too. Hadrons and muons with momenta below about 100 GeV/*c* do not produce transition radiation. The total charge deposition is the basis for all particle identification methods that can be used with the Transition Radiation Detector. Besides the total amount of charge the temporal structure of the signal is different for electrons compared to other particles. Transition radiation photons are preferably absorbed within the first few millimeters of the gaseous drift volume. This time information can be used to further improve the discrimination of electrons from other particles. However, it is not easy to disentangle the two signal components. An approach to exploit this additional information is based on artificial neural networks. In this thesis, the potential for particle identification (PID) using artificial neural networks with the ALICE Transition Radiation Detector was analyzed and a framework for its application was developed.

The theoretical and experimental background is discussed in Chapters $2 - 6$. The performance of the TRD particle identification is analyzed in Chapter 7 for test beam

data and in Chapter 8 for simulations. Chapter 9 presents three studies which are related to the application of the TRD's particle identification in the final setup of ALICE. The appendix contains a short overview of kinematic variables, an overview of the ALICE coordinate system, and tables with the analyzed test beam runs.

2. The Quark-Gluon Plasma and its Signatures

In 1964 *Gell-Mann* and *Zweig* proposed independently that nuclear matter would consist of quarks [GM64, Zwe64]. The interpretation of deep inelastic scattering experiments at the *Stanford Linear Accelerator Center* (SLAC) verified this model [Blo69, Bre69]. The interaction between these constituents is mediated by gluons and is described by *quantum chromodynamics* (QCD). As a consequence of QCD single quarks and gluons cannot be observed directly as free particles – they are confined to hadrons[1].

---

[1]Hadrons are strongly interacting particles. They are split into two groups: the mesons and the baryons. Mesons consist of a quark and an antiquark, while baryons are formed of three quarks. More about quarks, gluons and QCD can be found in several works, e.g. in References [Mes06, Dem05, Per00].
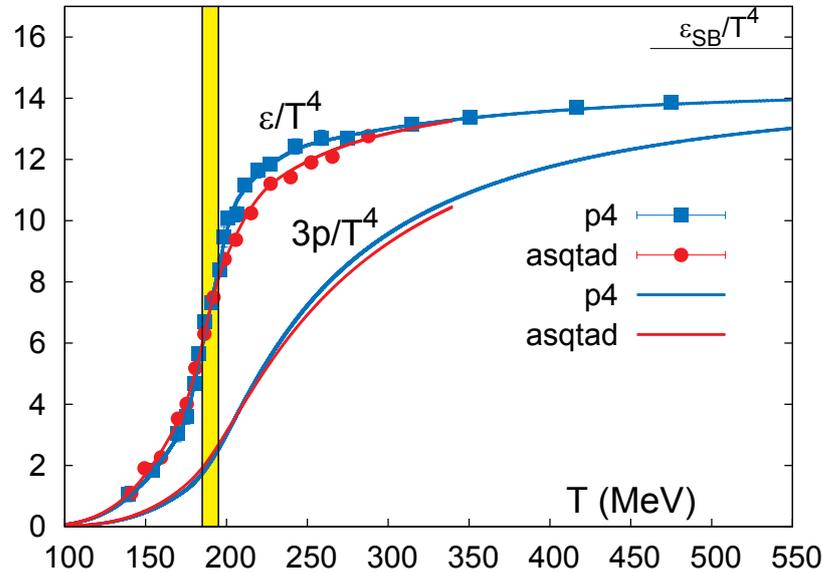
Figure 2.1: Results of lattice QCD calculations for energy density ε/T^4 and pressure $3p/T^4$ [Baz09]. The energy density and the pressure are calculated for three quark flavors (two degenerated light quarks and one heavy quark) for two different theoretical models. The Stefan-Boltzmann limit for an ideal gas is also shown. The yellow band indicates a phase transition at a temperature region of $185 < T < 195\,\text{MeV}$.
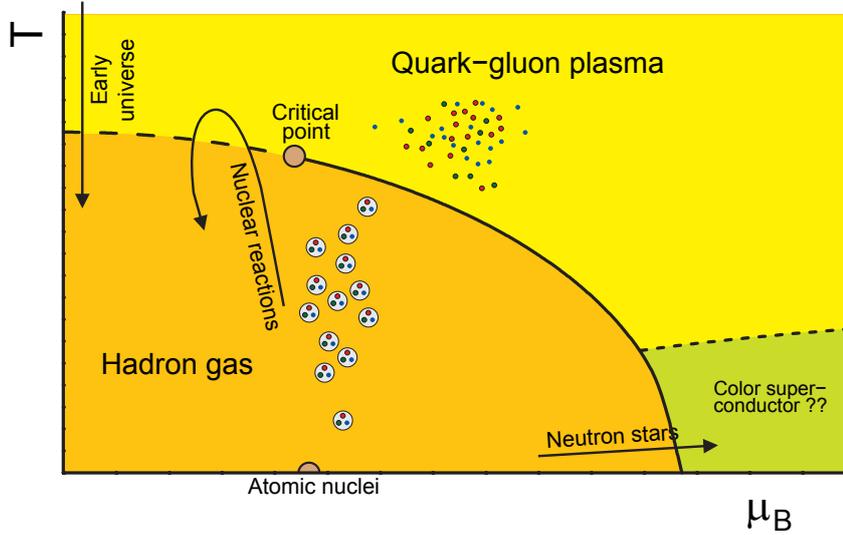
Figure 2.2: A schematic illustration of the phase diagram of strongly interacting matter. Shown are the states of matter as a function of temperature T and baryochemical potential μ_B. In the orange area quarks and gluons are confined to hadrons, the brown dot at zero temperature represents matter in atomic nuclei. In case the temperature and the baryochemical potential is high enough an other state of matter is formed, the quark-gluon plasma. The solid line represents a first order phase transition, while the dashed line between hadron gas and QGP indicates a crossover transition. The brown dot between the solid and the dashed line stands for the critical endpoint. The green area is a color superconducting phase that is predicted at low temperature but high μ_B. This plot is adapted from Reference [KB04b].

QCD calculations show, that under certain conditions the quarks and gluons are not confined anymore [Cab75]. For very high temperatures (larger than $150 - 190\,\text{MeV}$ [Che06, Aok06]) or high net baryon densities the confinement is repealed. This state is called *quark-gluon plasma* (QGP). In Figure 2.1 recent results from lattice calculations for energy density ε/T^4 and pressure $3p/T^4$ versus temperature T are shown. The sudden rise at a temperature $185 < T < 195\,\text{MeV}$ is interpreted as a crossover transition from the hadron gas phase to the quark-gluon plasma phase [Baz09].

2.1   The Phase Diagram of Strongly Interacting Matter

In Figure 2.2 a schematic illustration of the phase diagram of strongly interacting matter is presented. Shown are different states of matter as a function of temperature T and baryochemical potential μ_B, which is a measure for the net baryon density. The orange area represents a state where quarks and gluons are confined into hadrons; the brown dot

at zero temperature represents the ground state of nuclear matter. In case the temperature or μ_B increases the yellow area will be reached: the quark-gluon plasma. The type of transition from the hadron gas phase to the plasma phase depends on the net baryon density. For higher μ_B this is a first order phase transition, for smaller densities it is a smooth crossover. However, the precise location of the critical endpoint is not yet known and of high current interest.

Today, this concept, including a critical point and a first order phase transition, is the most favored model of the phase diagram, but it is not the only possibility. Theorists have shown that a first order phase transition is not needed at all and that a pure crossover transition from hadron gas to the QGP is also consistent with QCD calculations [dF07]. There are predictions about other exotic states of nuclear matter, like *quarkyonic matter* [McL07], *color superconducting* phases, or the *restoration of chiral symmetry*. A review of the phase diagram of strongly interacting matter was presented by e.g. *Braun-Munzinger* and *Wambach* [BM09b].

Experimental results indicate that the nature of the quark-gluon plasma at high temperatures is not as simple as presented here. It seems that in contrast to the picture of quasi-free quarks and gluons (the classical model of a quark-gluon plasma), the matter is strongly coupled and behaves more like a liquid [Gyu05] instead of a gas. This state of nuclear matter is called *strongly coupled quark-gluon plasma* (sQGP).

It is assumed that a quark-gluon plasma is naturally occuring in two scenarios. First, the early universe, until approximately 10^{-5} s after the big bang, the energy density (and therefore the temperature) was too high to form confined matter [BM07]. The second natural appearance of a QGP might be found in interior of neutron stars. In comparison to the early universe, the temperatures here are low, but, due to the strong gravitational forces, the baryon densities are very high.

2.2   Ultrarelativistic Heavy-Ion Collisions

The only means to create hot and dense nuclear matter under laboratory conditions are *ultrarelativistic heavy-ion collisions*. In such processes nuclei of heavy elements such as gold or lead are collided with velocities close to the speed of light, at center of mass energies per nucleon ($\sqrt{s_{NN}}$) between 17.3 GeV at the *Super Proton Synchrotron* (SPS) up to 5.5 TeV at the LHC. The energy density ε_0 in central collisions as estimated by the
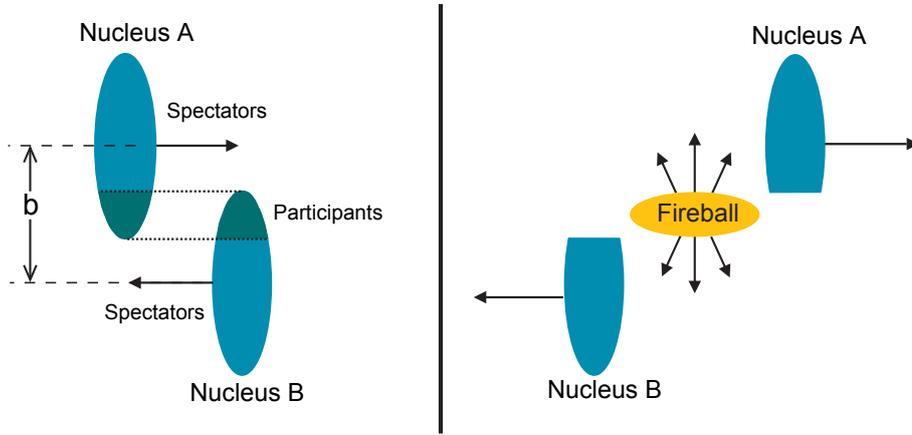
Figure 2.3: Schematic view of the participant-spectator model. The centrality of a collision is described by the impact parameter *b*. The nucleons in the overlapping regions of the two nuclei are the participants and form the fireball. The particles outside of the overlap are the spectators, they are affected only with comprehensively small excitation energies by the collision. This plot is adapted from Reference [KB04b].

────────

measured transverse energy E_T exceeds the theoretical limit for confinement. The energy density can be evaluated using the *Bjørken formula* [Yag05]:

$$\varepsilon_0 = \frac{1}{\pi R^2 \tau_0} \frac{dE_T}{dy}\bigg|_{y \simeq 0}, \qquad (2.1)$$

where R is the nuclear radius, τ_0 the initial time for the creation of a medium in thermal equilibrium ($\approx 1\,\mathrm{fm}/c$), and y is the rapidity. Results from the SPS heavy-ion program actually indicate the creation of a new state of matter [CER00], while some publications on results from the RHIC experiments go even further and suggest the creation of an sQGP [Gyu05].

Due to Lorentz contraction the nuclei in ultrarelativistic heavy-ion collisions can be envisaged as thin discs. The protons and neutrons have a small *de Broglie* wavelength compared to the dimension of the nucleus. Therefore the nucleus can be treated as an accumulation of independent nucleons. Consequently, several collision characteristics follow from pure geometrical considerations. The centrality of a collision is described by the impact parameter *b*; the smaller the impact parameter, the more central the collision. Only protons and neutrons in the overlap region participate in the collision. These *participants* form a zone of hot and dense nuclear matter, the so called *fireball*. The other nucleons, *spectators*, are affected only with comprehensively small excitation energies by the reaction and follow their initial paths. A schematic view of the participant-spectator model is shown in Figure 2.3.
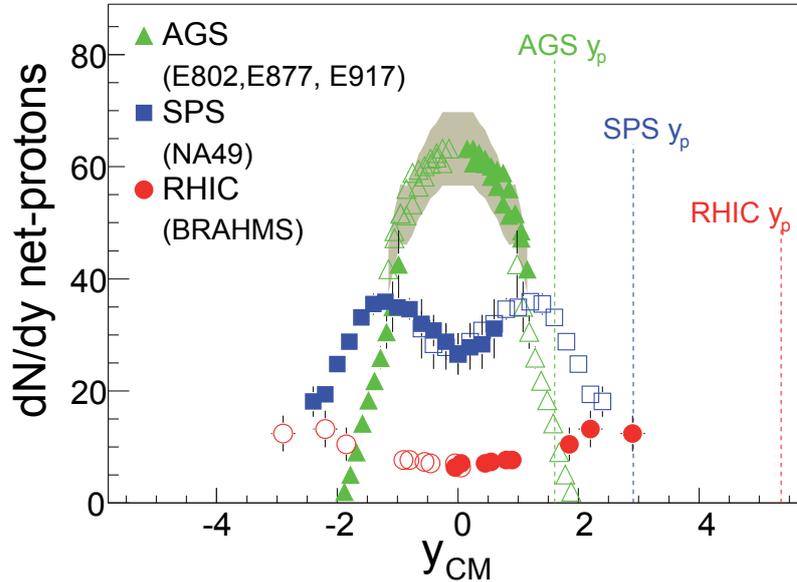
Figure 2.4: Comparison of net proton rapidity distributions for different center of mass energies [Bea04]. For AGS energies the distribution corresponds to the Landau model of nuclear collisions. For higher energies the distribution is better explained by the Bjørken-McLerran picture.

———————

Depending on the center of mass energy the nuclei will become more transparent to each other as was shown for AGS[2], SPS and RHIC[3] energies [Bea04]. In Figure 2.4 the net-proton rapidity measured at these accelerators can be found. This is consistent with a transition from the *Landau* picture of nuclear collisions, where the nucleons lose most of their kinetic energy due to *nuclear stopping* and form a baryon rich fireball, to the *Bjørken-McLerran* model [Bea04]. Here, the nuclei will penetrate each other. Consequently, the nuclear stopping is reduced. This results in the observed transparency. The created fireball will have a small net-baryon density and high temperature. At the LHC very low baryon densities but very high temperatures will be reached. Eventually also a transition from an sQGP to a 'classical' quark gluon plasma, where only a weak coupling between the quarks and gluons exists might be observed.

In Figure 2.5 the space time evolution of a high-energy heavy-ion collision is plotted. Following the Bjørken-McLerran model [Bjo83], at the beginning of the reaction – after the initial hard processes – a zone of highly excited matter is formed. At this stage

---

[2]The **A**lternating **G**radient **S**ynchrotron is a hadron accelerator at BNL with an energy range in *Au-Au* collisions up to $\sqrt{s_{NN}} = 4.9$ GeV.

[3]The **R**elativistic **H**eavy **I**on **C**ollider is a hadron collider at BNL. The center-of-mass energy reaches values of 200 GeV per nucleon-nucleon pair in *Au-Au* collisions.
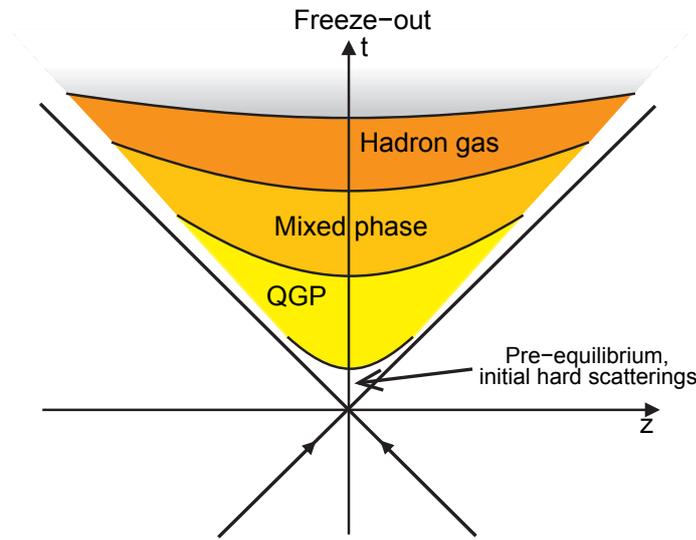
Figure 2.5: Space-time evolution of a central ultrarelativistic heavy-ion collision. After a non-equilibrated phase with initial hard collisions, the system thermalizes and a quark-gluon plasma is formed. With increasing time the system expands and therefore cools. The fireball is transformed to a phase where regions of quark-gluon plasma and hadron gas exist in parallel. Finally the hadronization takes place and the system freezes out. This plot is adapted from Reference [KB04a].

the fireball is in a pre-equilibrated state. The fireball expands and reaches thermal equilibrium. In case the energy density is high enough, a quark-gluon plasma is formed. The energy density decreases with further expansion and finally the quarks and gluons condensate to hadrons. At this point (the *chemical freeze-out*) the hadron abundances are fixed. Eventually there is also a *mixed phase* where regions of quark-gluon plasma and hadron gas exist simultaneously. After the *thermal freeze-out*, the momenta of the particles are fixed too, and the reaction comes to an end. The particles stream freely towards the detectors.

2.3   Signatures of the QGP

Several signatures are considered fingerprints for the formation of a quark-gluon plasma in ultrarelativistic heavy-ion collisions. However, each of the signatures could come from alternative non-QGP scenarios. Only the combination of several of them is currently regarded as evidence for the existence of a deconfined state of matter. The various signals can be classified in the following categories:
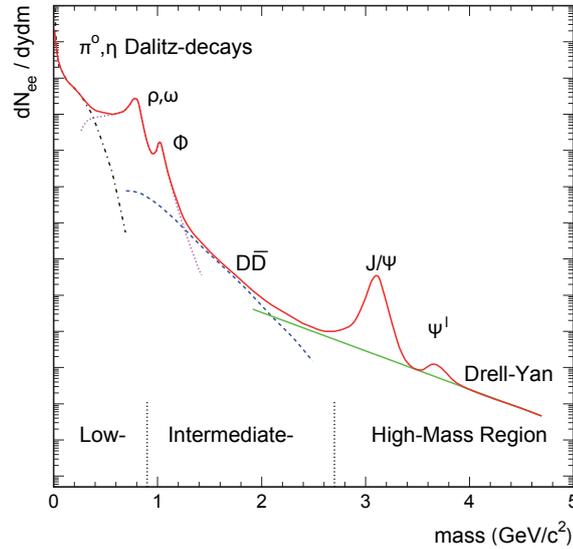
Figure 2.6: Schematic view of the expected invariant mass spectrum of dileptons and its sources in heavy ion collisions [Rap00].

- changes of thermodynamical observables, such as temperature and spatial dimension, indicating a phase transition,

- signals that point to medium effects from a deconfined phase,

- signals coming from the *restoration of chiral symmetry*.

Chiral symmetry breaking is the main source for the masses of the light quarks. QCD predicts the restoration of chiral symmetry for high temperatures and densities. As long as the matter is confined, chiral symmetry should not be restored. Hence, signals that point to this phase transition are signals for a QGP, but the transition point is not necessarily the same as for the deconfinement [Pei97]. An observable effect for the restoration of chiral symmetry would be e.g. the shifting and broadening of light vector meson masses. For more details please refer to Reference [Koc97].

In this section some of these signals are presented. The main emphasis is placed on signatures that can be observed by or with help of the TRD. More complete overviews of the different QGP signatures can be found in several works, e.g. References [Won94, Yag05, Ale06].
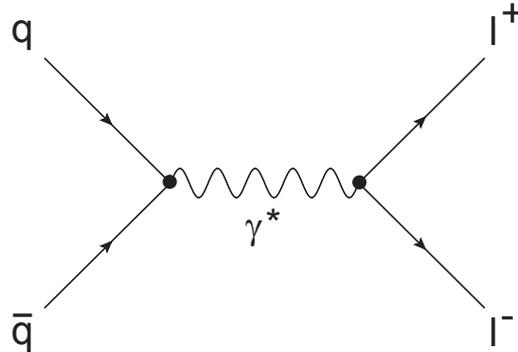
Figure 2.7: The Drell-Yan process.

2.3.1   Dileptons

Leptons are appropriate probes for the exploration of hot hadronic matter or quark-gluon plasma since they do not interact strongly. Once formed in the hot and dense phase of the collision, their mean-free path is large compared to the dimensions of the fireball. The probability for a further collision, which consequently leads to a loss of information, is comprehensively small. This means that leptons trace the history of space-time evolution of the stages of the collision in which they were produced.

Important sources of leptons are the various production mechanisms of dileptons, such as their production in the initial hard parton collisions, the decay of hadrons into dileptons and their thermal production in the hot medium. The relative contributions from the different sources vary at different mass intervals in the invariant mass spectrum of dileptons (see Figure 2.6). In the low-mass region signals from photon conversions, *Dalitz*-decays of the π^0 and the η, as well as dileptonic decays of light vector mesons such as the ρ, ω and ϕ can be found. Decays of D mesons dominate the medium-mass region. In the high-mass region the *Drell-Yan* mechanism is the most prominent source. Here, also the invariant mass peaks from J/ψ and Υ decays can be found. The J/ψ signal will be discussed in more detail in Section 2.3.2.

The Drell-Yan Mechanism   Lepton pairs (or $l\bar{l}$ pairs) can directly be produced in the very early state of the collision via virtual photons. These are created by the annihilation of one nucleon's quark with a sea antiquark of the other nucleon (see Figure 2.7). This mechanism is called Drell-Yan process and carries information from the first hard nucleon scatterings of the impact. The cross section of this process can be well evaluated by using perturbative methods which opens the possibility to use the Drell-Yan dileptons as reference for the other processes. For the Drell-Yan process in heavy-ion collisions the

nucleons can be treated as independent within the nuclei [Won94]. Thus, the number of produced $l\bar{l}$ pairs by the Drell-Yan mechanism in heavy-ion collisions depends on the number of nucleon-nucleon collisions (N_{coll}). The number of collisions can be estimated by *Glauber model* [Gla70] calculations and roughly scales with $A^{4/3}$ for central collisions of two equal nuclei [Mil07]. Here, A is the atomic number of the nuclei participating the collision. The signal from this process contributes to spectrum in a continuum, noticeably at high invariant masses ($m_{ll} > 3\,\text{GeV}/c$).

Open Charm and Open Beauty Another important process contributing to the invariant mass spectrum is the semi-leptonic decay of charm or beauty mesons. In the initial hard scatterings of a nucleon-nucleon collision the creation of heavy quark pairs, like charm or beauty, takes place. These heavy quark pairs can form charmonia or separate and form, together with light quarks, pairs of charmed (e.g. $D^+ = \bar{d}c$ and $D^- = d\bar{c}$) or beauty (e.g. $B^+ = u\bar{b}$ and $B^- = \bar{u}b$) mesons, so called open charm or open beauty. These mesons can decay weakly via semileptonic channels with a branching ratio of about 10%. A typical decay is e.g. $D^+ \rightarrow \overline{K}^0 l^+ \nu_l$. This leads to correlated electron positron pairs which populate a continuum in the intermediate mass region between the ϕ and the J/ψ.

Thermal Dilepton Production In the plasma phase the annihilation of a quark-antiquark pair can lead to the production of dileptons via virtual photons ($q\bar{q} \rightarrow \gamma^* \rightarrow e^+e^-$). Virtual photons carry a mass and therefore contribute to the invariant mass spectrum of dileptons. Since the quarks are thermalized in the plasma phase, the virtual photons are a tool to access directly the thermodynamic information of the QGP. Thermal photons are also expected from the hadron gas phase. However, these photons should have smaller energies than those from the QGP phase.

Medium Modifications of Vector Mesons In the late phase of the collision, the matter forms a hadron gas, but has not reached the thermal freeze-out point. Here, the main sources of dileptons are pion annihilation or scattering via the channel $\pi\pi \rightleftharpoons \rho \rightarrow \gamma^* \rightarrow e^+e^-$. Since the lifetime of the ρ meson ($\tau \approx 1.3\,\text{fm}/c$) is shorter than the expected time between chemical and thermal freeze-out ($\tau \approx 10\,\text{fm}/c$), most of the ρs will decay inside the hadron gas. Any medium attribute affecting the lifetime of the meson or the thermal distribution of the decay meson will be preserved by the dilepton pair.

In order to extract information from the dilepton spectrum it is crucial to understand the different contributions and their yields. SPS experiments (CERES [Aga05]
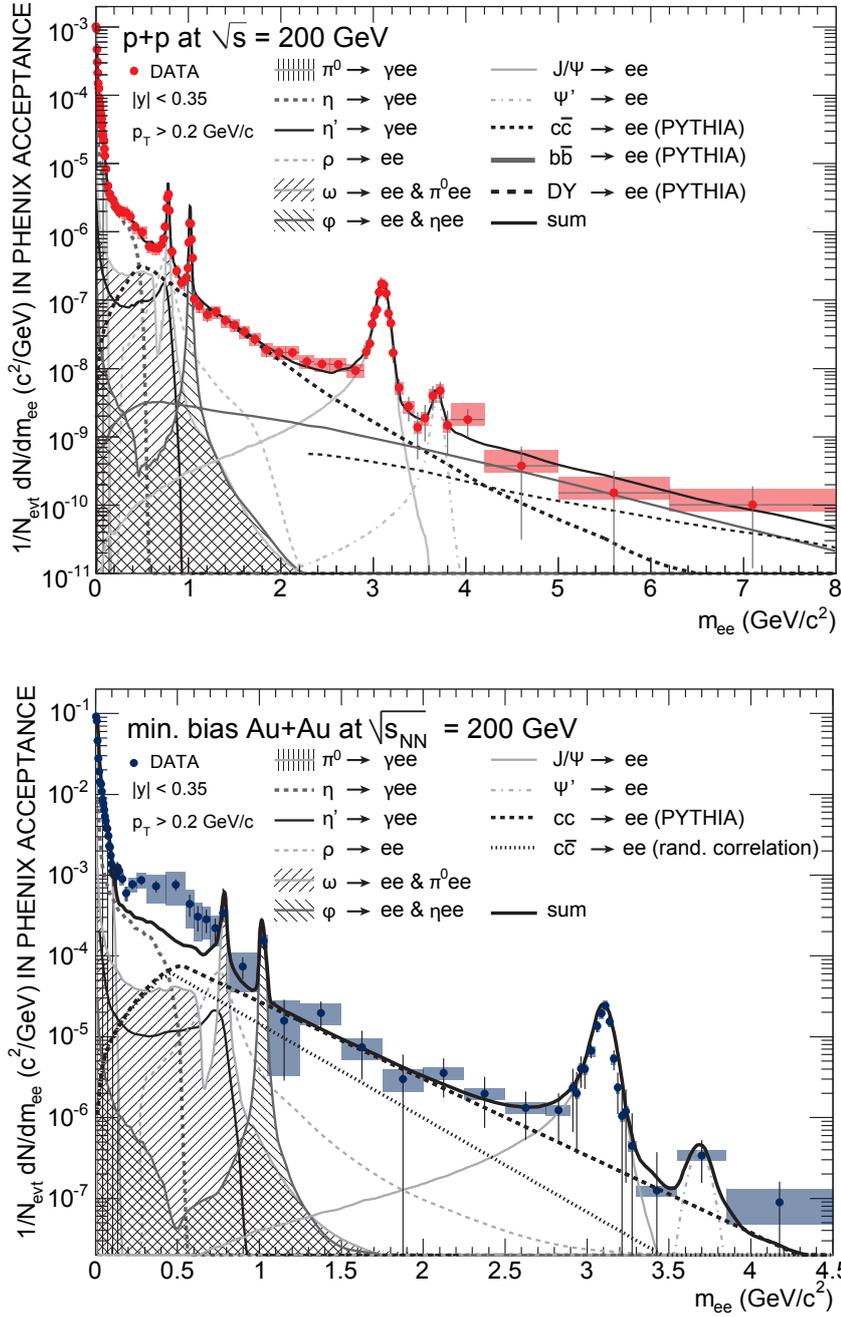
Figure 2.8: Dileptonic signal from Phenix for *pp* (upper plot) [Ada09b] and *AuAu* (lower plot) [Afa07]. The spectra are compared to the yield expected from the different contributions. While the data from proton collisions fit well to the model, the extracted signal from heavy ion events shows a significant excess at low dielectron masses over the expectations.
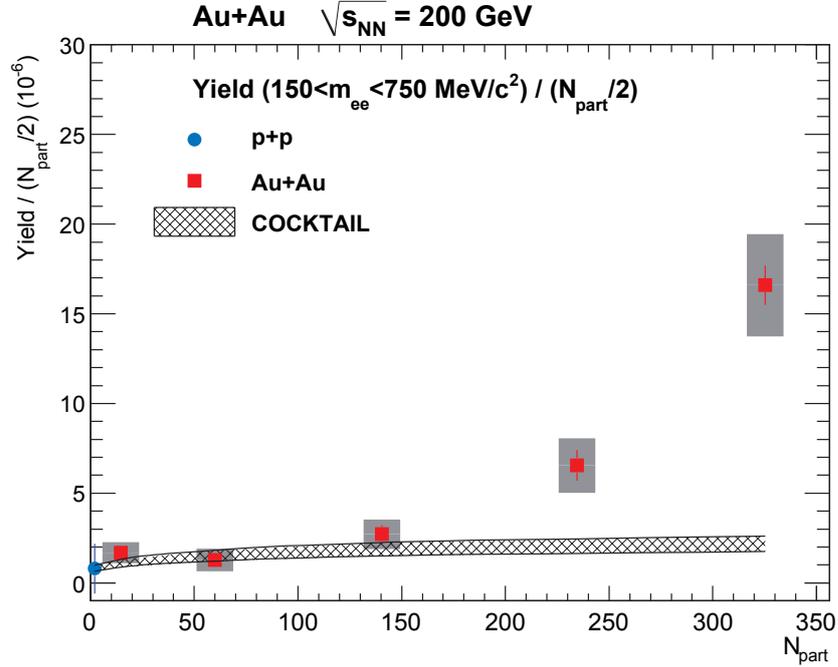
Figure 2.9: Dielectron yield per participating nucleon pair ($N_{part}/2$) as a function of N_{part} for the invariant mass range $0.15 < m_{inv} < 0.75 \, \text{GeV}/c^2$ measured by PHENIX [Ada09a]. The yield is compared to the expected dielectron yield from hadron decays (patterned region). It can be seen that the measured yield shows a large excess over the expectations in central collisions.

————————

and NA60 [Arn06]) as well as RHIC experiments (PHENIX [Afa07]) observed an enhancement over the expected dilepton yield from hadron decays in the low-mass region. In Figure 2.8 the results from *pp* and *AuAu* collisions in PHENIX are compared to a cocktail of various sources. In the *AuAu* spectrum a clear enhancement above the expectations is visible for the mass region between 200-750 MeV/c^2 [Afa07]. The dilepton yield in *pp* data does not show this behavior [Ada09b] which leads to the suggestion that this contribution originates from medium effects and not from unconsidered hadron decays. In Figure 2.9 the dielectron yield measured by PHENIX is compared to the expectations from hadron decays for different centrality classes. It can be seen that the measured yield shows a large excess over the expectations in central collisions. Figure 2.10 shows the transverse momentum (p_T) dependence of the observed excess of dielectrons. The excess over the expectations is mainly seen at low p_T. These observations are qualitatively consistent with the interpretation that the enhancement is caused by annihilation processes like $q\bar{q} \to \gamma^* \to e^+e^-$ or $\pi^+\pi^- \to \gamma^* \to e^+e^-$.
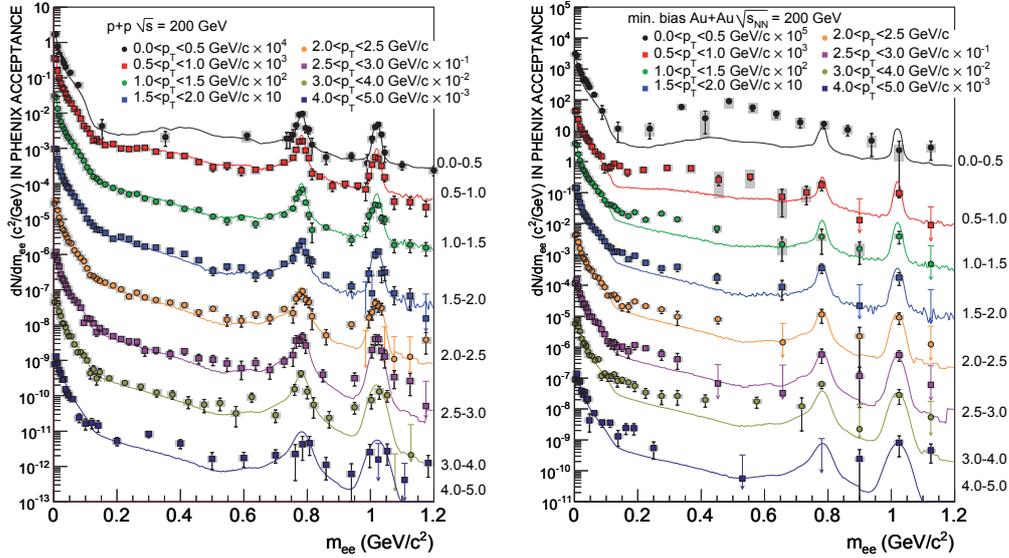
Figure 2.10: Dielectron invariant mass distributions for *pp* (left) and *AuAu* collisions (right) [Ada09a]. The distributions are plotted for different intervals of transverse momentum p_T and are compared to the expected spectra from hadron decays.

The most favored scenario for the excess of dileptons in the low-mass region is at the moment a medium modification in the hadron gas phase [vH06], but it seems that there are some differences between the SPS and the RHIC scenario [Dah08]. While the enhancement at SPS energies can be well described by some theoretical approaches, the enhancement seen by PHENIX can not be reproduced using the same models [Bra08].

2.3.2   Quarkonium Production

The signatures, that are the most interesting ones for this thesis, are dileptonic signals from the decay of quarkonia. This means mainly the detection of bound states of heavy quark-antiquark pairs, like a charm-anticharm ($c\bar{c}$), called charmonium, or a bottom-antibottom ($b\bar{b}$) quark pair, called bottomium, via their dielectron or dimuon decay channel. The 1^3S_1 ground state of the charmonium[4] is the J/ψ and of the bottomium is the Υ meson. It is expected that clear signals from these mesons as well as from more massive states like the Υ' can be found in *pp* and in *PbPb* collisions at the LHC.

---

[4]For a short review on the different charmonium states and on the nomenclature please refer to Reference [Vol08].
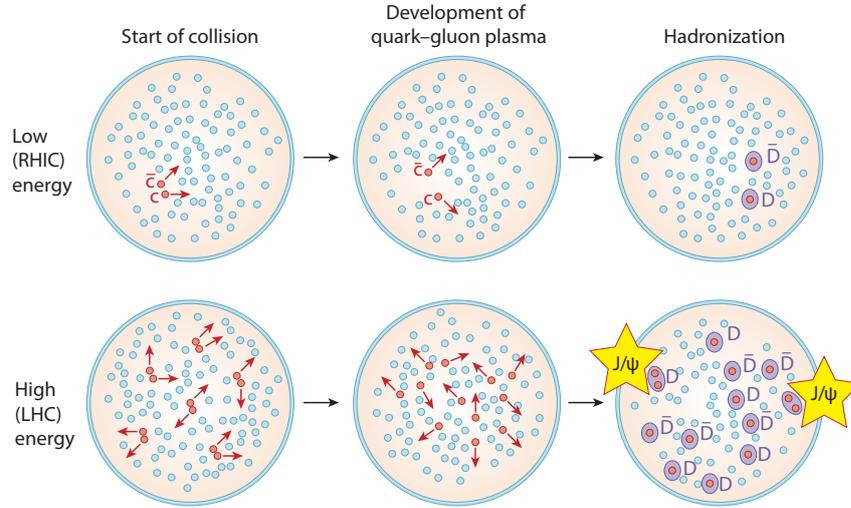
Figure 2.11: The mechanisms of charmonium suppression and enhancement in a quark-gluon plasma. In the upper case (low energy) only small numbers of charm-anticharm pairs (red dots) are produced. The interaction of these two quarks is screened by the other quarks and the gluons of the QGP. In the hadronization phase the charm and the anticharm quark will each form a D meson together with another (light) quark (gray dot) of the medium and the number of observed J/ψs will be smaller than expected. With increasing collision energy (lower scenario) many more charm-anticharm pairs will be produced. As in the low energy case the medium screens the quark antiquark-pairs from each other, but here, charm and anticharm quarks from different original pairs could form J/ψs and lead to a higher number of produced charmonia [BM07].

———————

Heavy quark-antiquark pairs are mostly produced in hard processes in the early stage of the collision. Therefore they are subject to the entire history of the reaction and are excellent probes for exploring the created medium in its early states. In 1986 a suppression of J/ψ production compared to a scenario without forming a QGP was predicted by Matsui and Satz [Mat86]. The underlying mechanism was explained in terms of a QCD equivalent to the *Debye screening* in electromagnetic plasmas. A parameter for the screening is the *Debye radius* r_D which is dependent on the temperature T of the plasma. In case the temperature reaches a critical value T_C, r_D is smaller than the J/ψ's binding radius $r_{J/\psi}$, the quarks are not confined any more and the meson dissolves. The constituents of the charmonium now move independently through the plasma. During the hadronization phase they find new partners, light quarks, and will form charmed mesons. The number of J/ψs is smaller than expected. An illustration of the suppression mechanism is given in the upper example of Figure 2.11.
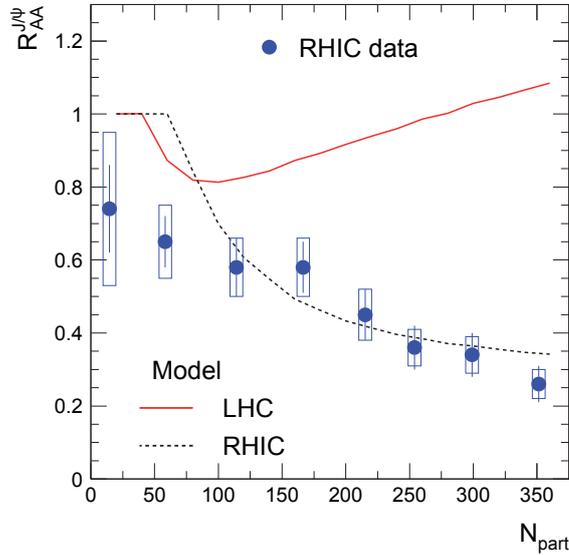
Figure 2.12: Comparison of the measured J/ψ yield $R_{AA}^{J/\psi}$ in PHENIX compared to theoretical predictions for RHIC and LHC energies for different centralities at mid rapidity. While the measured charmonium suppression is in good agreement with the model prediction at LHC an enhancement of the J/ψ yield is expected [And07a].

The scenario, described above, takes place when the average number of $c\bar{c}$ pairs created per nucleus-nucleus collision is about one or smaller. At the LHC the creation of about 200 charm quarks is expected per *PbPb* collision [BM07]. Calculations show that for RHIC and LHC energies the formation time of the J/ψ is much longer than the plasma formation time [And08b]. Therefore the charmonium will not be formed at all. As in the case where only a few $c\bar{c}$ pairs are produced, there are deconfined charm and anticharm quarks moving independently through the quark-gluon plasma. But in contrast, there is a chance that during the hadronization phase charm and anticharm quarks from different initial pairs can recombine to form quarkonia (Fig. 2.11, lower example). This statistical effect would lead to an enhancement instead of a suppression of the J/ψ [And07a]. While a pure suppression could be explained by scenarios without the formation of a quark-gluon plasma, the described enhancement can only happen in a scenario, where charm quarks are deconfined [BM07]. This would be a clear signature of a QGP formation.

Experimental data from the NA50 experiment at SPS show a clear suppression as expected in this energy range [Ale05]. Results from PHENIX at RHIC show also a suppression but not as large as expected if a suppression mechanism is the only effect that is responsible for the J/ψ yield [Ada07b]. In a comparison between the experimental results from RHIC and theoretical calculations it is shown that this effect can be well

described by statistical recombination of charm quarks to charmonia which would lead to a smaller suppression or even an enhancement at higher energies [And07a].

A possible observable to decide if a J/ψ suppression or enhancement takes place is the *nuclear modification factor* $R_{AA}^{J/\psi}$. It compares the number of J/ψ particles produced in nucleus-nucleus collisions $dN_{J/\psi}^{AA}$, to the expected number in a scenario where no medium effect affects the total yield:

$$R_{AA}^{J/\psi} = \frac{dN_{J/\psi}^{AA}/dp_T}{N_{coll} \cdot dN_{J/\psi}^{pp}/dp_T}, \tag{2.2}$$

with $dN_{J/\psi}^{pp}$ being the number of produced J/ψs in a *p-p* collision and N_{coll} being the number of inelastic nucleon collisions that occurs during the *AA* collision. In Figure 2.12 the J/ψ yield is plotted for different centralities and is compared to model calculations for RHIC and LHC energies. While the model describes the RHIC data very well, the prediction for the LHC shows an enhancement for $R_{AA}^{J/\psi}$ above one for central collisions. At LHC a significant number of J/ψs will originate from beauty particle decays. Therefore, B decays need to be measured first in order to estimate the number of primary charmonia.

2.3.3 Direct Photons

Like leptons, photons do not interact strongly. Therefore, they can carry information from all phases of the collision. *Direct photons* are all photons which are not produced by hadron decays after the chemical freeze-out. They can be subdivided into *prompt* photons and *thermal* photons. Prompt photons are produced directly in the initial hard collisions via quark-antiquark annihilations resulting in the production of a gluon and a photon ($q\bar{q} \rightarrow g\gamma$, Figure 2.13 **a)**). The energy range where they are expected to be measurable at ALICE starts at about 10 GeV [Ale06]. Below this energy the background from other processes will be much too large compared to the prompt photon yield. Quark-antiquark annihilation is also partly responsible for the thermal photon production in a quark-gluon plasma. The difference to the prompt photon production is, that the quarks are in thermal equilibrium and therefore the photons do not reach the same energy range; the spectrum is softer. The other process contributing to the thermal photons from QGP is quark-gluon Compton scattering ($qg \rightarrow q\gamma$, Figure 2.13 **b)**). Thermal photons can also be produced in the hadron gas phase. Typical creation processes are pion annihilations ($\pi^+\pi^- \rightarrow \rho^0\gamma$, Figure 2.14 **a)**)), Compton scattering ($\pi^\pm\rho^0 \rightarrow \pi^\pm\gamma$, Figure 2.14 **b)**)) and decays of ρ^0s ($\rho^0 \rightarrow \pi^+\pi^-\gamma$ Figure 2.14 **c)**)) [Pei02]. Thermal
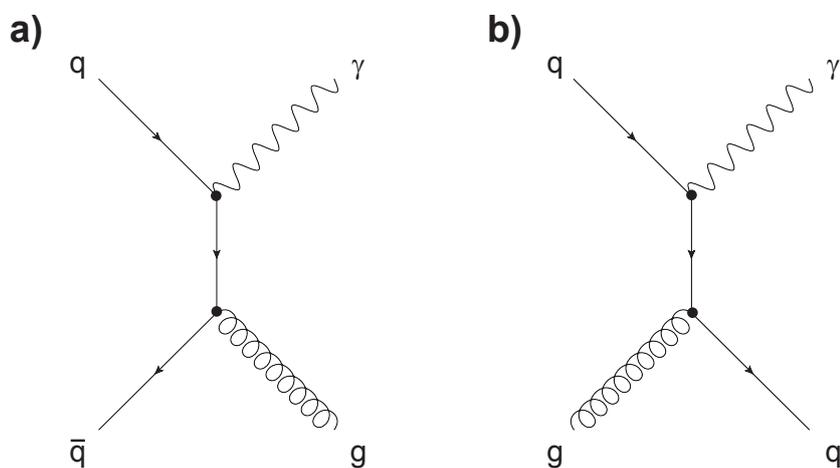
Figure 2.13: Feynman graphs of the main contributions to direct photons: **a)** quark-antiquark annihilation and **b)** quark-gluon Compton scattering.

———————
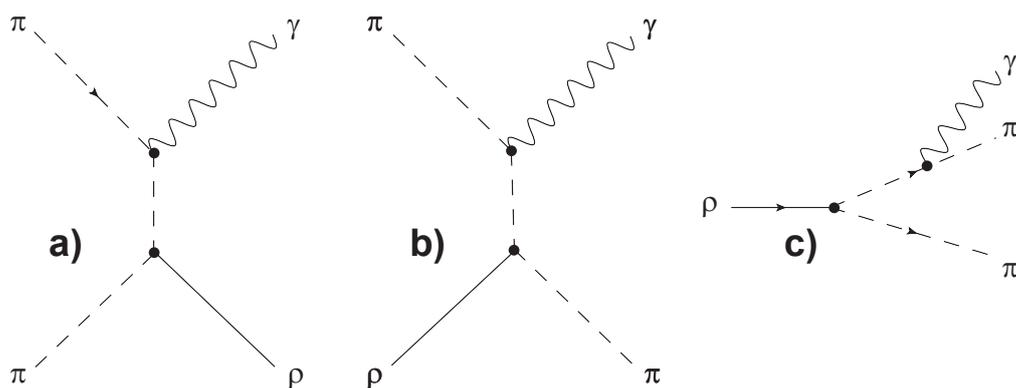
Figure 2.14: Examples of photon production in the hadron gas phase: **a)** pion annihilation, **b)** Compton scattering, and **c)** decays of ρ^0 mesons.

———————

photons from a quark-gluon plasma phase should reach energies up to several GeV. Simulations show thermal photons from the hadron gas phase can be found in energy ranges between a few hundred MeV and a few GeV [Car04].

Photon production in heavy-ion collisions show many parallels to the generation of dileptons. Many production mechanisms are identical, the only difference is that in dileptonic signals the photon is not real but virtual. Similar to dilepton analyses, the photon signal has to be extracted from a large background. Measurements of direct photons in heavy ion collisions succeeded e.g. at WA98 [Agg00, Buc99] and PHENIX [Adl05c, KB04b].

2.3.4 Jet Physics in Heavy-Ion Collisions

In 1975 cascades of particles with well defined opposite emission directions were observed in e^+e^- collisions at the Stanford Linear Accelerator Center [Han75]. These *dijets* are produced due to the creation of quark-antiquark pairs with large opposite (back-to-back) momenta. Due to the confinement the quarks undergo fragmentation and create the observed collimated spray of hadrons. In hadron collisions hard parton scatterings are responsible for the jet production. In *pp* collisions the scattered partons produce dijets exactly as in the e^+e^- case. In an environment where the partons traverse hot and dense hadronic matter the particles interact with the medium. The predictions of the jet's energy loss is different for cold nuclear matter and for a scenario where a quark-gluon plasma is formed [Wan92, Bai95]. Depending on the spatial position of the hard scattering, the parton has to traverse a larger or shorter distance through the fireball. This leads to a larger energy loss by soft gluon radiation for one of the two jets and therefore to a deviation from the back-to-back geometry of the jets. This *jet quenching* can also be observed as an overall suppression of hadrons, such as π^0 or η, at larger transverse momenta compared to non-QGP-forming cases. Particles that do not interact strongly should not be suppressed since they are not affected by the hot hadronic matter.

Measurements at RHIC experiments at $\sqrt{s} = 200$ GeV *AuAu* collisions agree well with the theoretical models for QGP formation. In PHENIX a clear suppression of neutral pions [Adl06, Adl07a, Ada08] and η mesons [Adl07b] at high transverse momenta was observed, while STAR confirmed that observation for charged pions and protons [Abe06]. To exclude other (unknown) effects caused by cold nuclear matter, collisions of deuterons with gold nuclei were measured, where it is not expected that large volumes of quark-gluon plasma will be formed. As expected no jet quenching was observed in this case [Adl03, KB04b, Sah04, Ada03]. This confirms that the observed suppression in *AuAu* collisions is not caused by initial state effects.
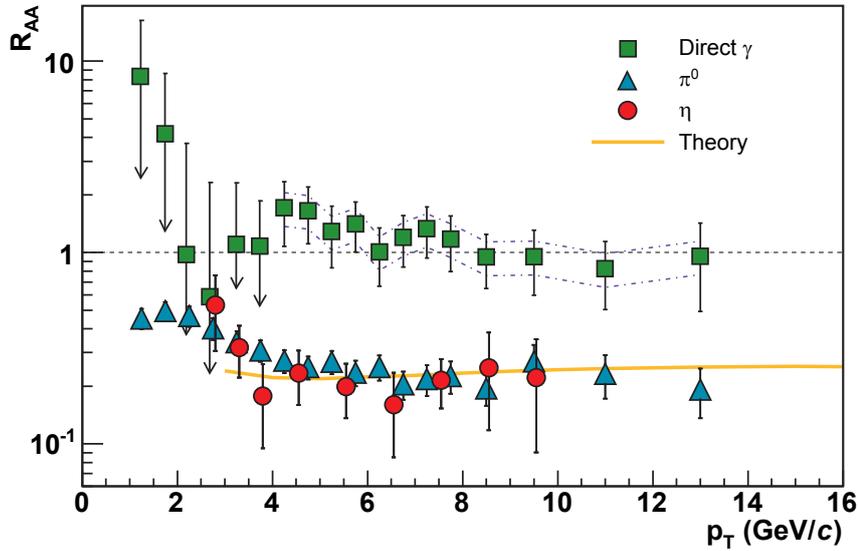
Figure 2.15: Jet quenching at PHENIX for $\sqrt{s_{NN}} = 200$ GeV [Adl06]. Shown is the suppression of high p_T π^0s and ηs in *AuAu* collisions compared to *pp* events. As predicted for a QGP formation the number of hadrons is smaller than for the non-QGP case. Particles which do not interact strongly as directly produced photons should not be suppressed. The results agree well with the predictions for a quark-gluon plasma formation.

A jet quenching study was also performed by PHENIX on heavy quarks measured via single electron measurements [Ada07a]. It was expected that heavy quark jets should show less suppression than the light quark jets [Awe08]. The energy loss of heavy quarks via gluon bremsstrahlung should be suppressed for small forward emission angles ($\theta = M/E$), where M is the heavy quark mass and E is its energy [Dok01]. This effect is known as the so called *dead cone* phenomenon. Actually at low p_T the observed suppression of electrons from heavy flavors is smaller than that of π^0. However, in contradiction to the expectations, at $p_T > 4$ GeV/c the suppression factor reaches the same value as for neutral pions. The results indicate a strong coupling of the heavy quarks to the medium [Ada07a].

3. ALICE and the LHC

3.1 The Large Hadron Collider

The Large Hadron Collider (LHC) at CERN has a circumference of about 27 km and is with a nominal beam energy of 7 TeV for protons and 2.76 TeV per nucleon for heavy ions the most powerful accelerator in the world [Eva08, LHC08]. For lead ions this corresponds to an energy of 1.15 PeV per nucleus. It has been built in the old Large Electron-Positron Collider (LEP) tunnel, between 50 and 175 m below the surface (see Fig. 3.1). The collider consists of two beam pipes where the particles are accelerated in opposite directions. The design luminosity for *proton-proton* collisions is $L = 10^{34}$ cm^{-2}s^{-1} and for *PbPb* collisions $L = 10^{27}$ cm^{-2}s^{-1} [Brü04]. At maximum luminosity there will be 20 *pp* collisions per bunch crossing. With 2808 bunches at a time in each beam pipe and a frequency of about 11 kHz this leads to around 600 million collisions per second [LHC08].

Preexisting infrastructure is used as far as possible for the generation of particles which are injected into the LHC. A schematic view of the CERN accelerator facility is given in Figure 3.2. Lead is vaporized and ionized with a charge maximum around Pb^{29+}
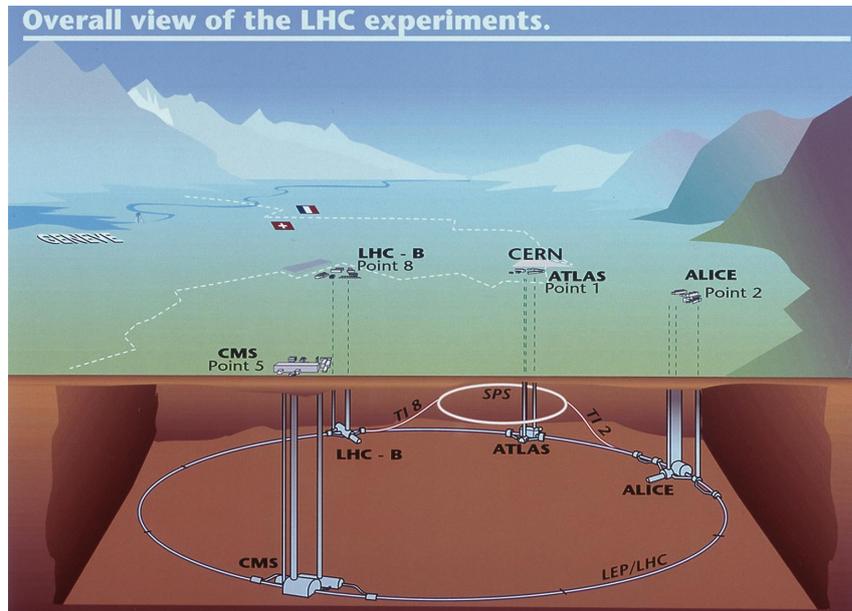
Figure 3.1: The four large experiments ATLAS, CMS, LHCb and ALICE at the Large Hadron Collider.
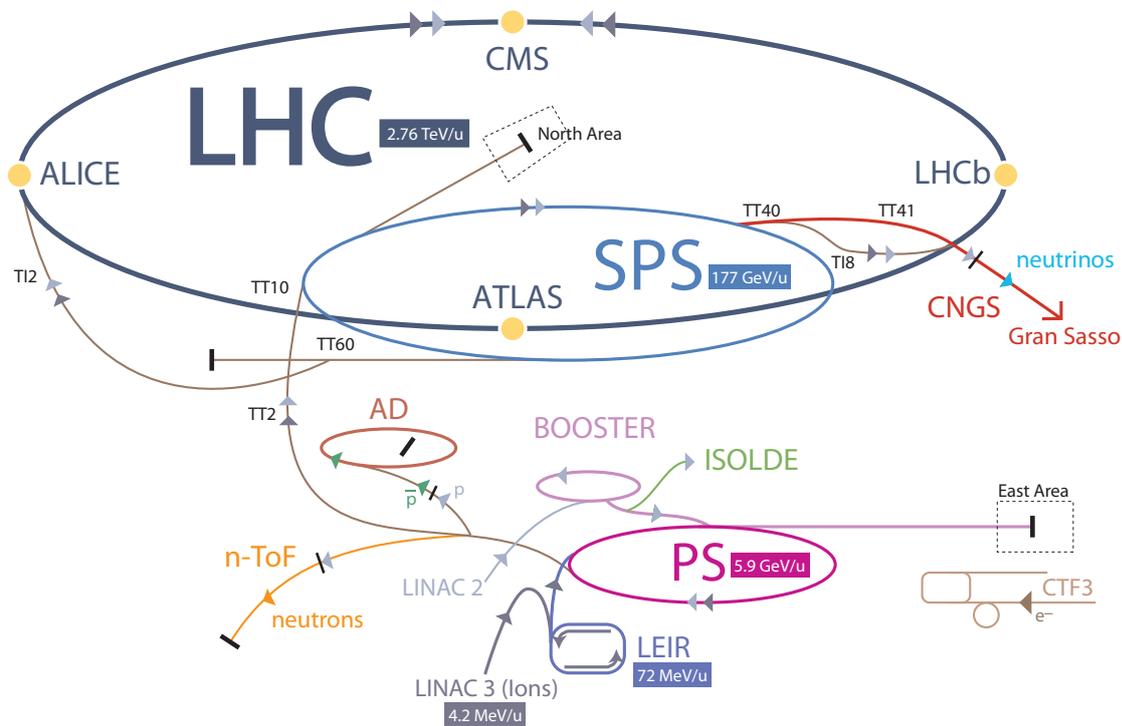
Figure 3.2: The CERN accelerator complex [LHC08]. Shown are the different beam lines and accelerators as well as the corresponding energies for lead ions. Dark grey arrows indicate the beam line for heavy ions, light grey arrows that for protons.

in the GTS-LHC ion source [Hil05]. These ions are accelerated in LINAC3 up to an energy of 4.2 MeV/u. The ions are stripped further to Pb^{54+} and accelerated at the Low Energy Ion Ring (LEIR) to 72 MeV/u. In the Proton Synchrotron (PS) the ions get another boost to 5.9 GeV/u before the lead is fully stripped to Pb^{82+}. These nuclei are transferred subsequently to the Super Proton Synchrotron (SPS) where the energy per nucleon is increased further to 177 GeV/u. The last step is the transfer to the LHC where the ions reach their maximum energy of 2.76 TeV [LHC08].

The Experiments

There are six experiments installed at four collision points. The largest experiments ATLAS[1] and CMS[2] were built to clarify open questions of particle physics, such as the existence and mass of the Higgs bosons or the search for supersymmetric

---

[1] A Toroidal LHC Aparatus
[2] Compact Muon Solenoid

particles [ATL99, dR06]. LHCb[3] studies the asymmetry between matter and antimatter via CP-violation in decays of B-mesons. There are also two small experiments at LHC, TOTEM[4] [Ane08] and LHCf[5] [Adr08]. TOTEM is located close to the CMS experiment and will measure the total cross section of the *proton-proton* collisions; with LHCf (close to ATLAS) models for the very high energy region of cosmic rays will be tested. The focus of this thesis lies on ALICE, which is the only dedicated heavy ion experiment at LHC. ALICE will be discussed in more detail in Section 3.2.

ATLAS is 46 m long with a diameter of 25 m and a weight of about 7,000 t [Aad08]. It is built in a barrel design including end caps to cover all the possible emission directions particles can have. ATLAS consists of three major detector components: the *Inner Detector*, the *Calorimeter* and the *Muon Spectrometer*. The Inner Detector provides tracking and particle identification. As in ALICE, a detector exploiting transition radiation is used for the identification of electrons, the Transition Radiation Tracker (TRT). The TRT design is different from the ALICE TRD's one and is based on a drift-tube system[6]. The Inner Detector is surrounded by a solenoid magnet which provides a magnetic field of 2 T in the inner barrel. The Calorimeter is divided in the *Electromagnetic Calorimeter* and the *Hadron Calorimeter*. This section is located between the central magnet and the outermost component, the Muon Spectrometer.

CMS with a weight of 12,000 t is the heaviest of the LHC experiments [Ado08]. It has a length of 21 m and a diameter of 15 m and is more compact than ATLAS. As ATLAS, CMS is constructed in a barrel design including end caps. The central component of CMS is the superconducting magnet. It is 11 m long, has a radius of 3 m and provides a 4 T magnetic field. The innermost detector system is the *Inner Tracking System*, consisting of a pixel detector and a silicon strip detector. Also inside of the magnet are an electromagnetic and a hadronic calorimeter. Outside of the solenoid the muon system provides muon identification and momentum measurement. It also works as a trigger.

ATLAS and CMS are built to measure *pp* events at high luminosity. I.e. they are optimized for high event rates and low multiplicities. However, both experiments have a heavy-ion program [ATL04, d'E07] and will complement the ALICE measurements. A short overview of the CMS dilepton capabilities will be given in Section 9.3.1.

LHCb, in contrast to ATLAS and CMS, is not barrel-designed but specialized to detect particles in forward direction [Alv08] with an angular coverage between 10 mrad and 300 mrad. LHCb is 21 m long, 10 m high and 13 m wide. The total weight is 5,600 t. The

---

[3]Large Hadron Collider beauty Experiment
[4]Total Cross Section, Elastic Scattering and Diffractive Dissociation at the LHC
[5]Large Hadron Collider forward Experiment
[6]For more information about the ATLAS TRT please refer to Reference [ATL97, Mit03].

Vertex Locator (VELO) is the detector closest to the collision point. VELO is followed by tracking detectors and RICHs[7]. An electromagnetic and a hadronic calorimeter as well as a muon detection system complete the design of LHCb.

3.2   The ALICE Experiment

ALICE (see Figure 3.3) is the only LHC experiment designed to study heavy-ion collisions. It is optimized to measure a broad set of observables which could indicate the generation of a QGP. Contrary to ATLAS and CMS, ALICE is built for smaller event rates, but is able to handle high multiplicity events (up to 8,000 charged particles per rapidity unit). In addition, due to its lower magnetic field ($B = 0.5\,\mathrm{T}$) ALICE can measure and identify charged particles down to lower p_T than CMS and ATLAS. The experiment's dimensions are $16\,\mathrm{m} \times 16\,\mathrm{m} \times 26\,\mathrm{m}$ and its weight is about $10,000\,\mathrm{t}$ [ALI95, Aam08]. ALICE is composed of two large detector arrays, the central barrel and the muon arm. The first covers the mid-rapidity region ($-0.9 < \eta < 0.9$), while the latter detects muons with rapidities between -2.5 and -4. In the following section the detectors of ALICE will be shortly presented. An overview of the pseudo-rapidity ranges of all ALICE detector subsystems is given in Figure 3.4, a summary of their particle identification capabilities in Figure 3.5, and the ALICE coordinate system can found in Apendix B.

3.2.1   The Central Barrel

The detectors of the central barrel are embedded in the *L3 solenoid*. This magnet works at room temperature and provides a magnetic field of $0.5\,\mathrm{T}$. The detector components surround the collision point in several layers. Each of the detectors has its special tasks. The Inner Tracking System (ITS) is specialized for vertex finding, the Time Projection Chamber (TPC) is the main tracking and particle identification (PID) device and the Transition Radiation Detector's (TRD) main task is to identify and to serve as trigger for electrons with momenta $> 1\,\mathrm{GeV}/c$. Together these three detectors provide a momentum resolution of about 5% at a transverse momentum of about $100\,\mathrm{GeV}/c$ [Aam08]. The Time Of Flight Detector improves the hadron identification capability, HMPID is a RICH detector, and PHOS as well as EMCal are electromagnetic calorimeters. A detailed overview about the TRD is given in Chapter 4, the other detectors are described here.

---

[7]**R**ing **I**maging **CH**erenkov Counters for electron identification.
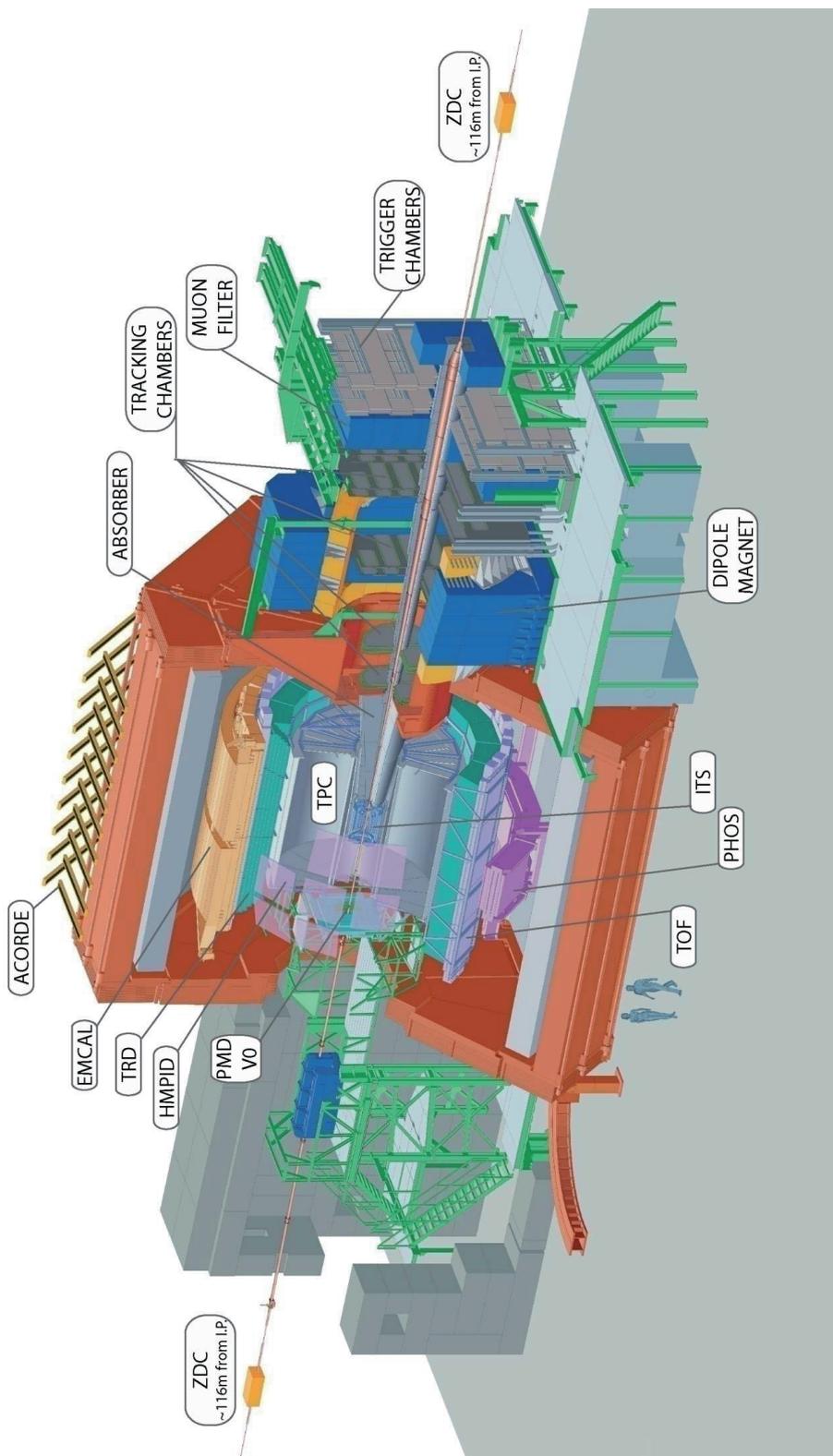
Figure 3.3: A Large Ion Collider Experiment.
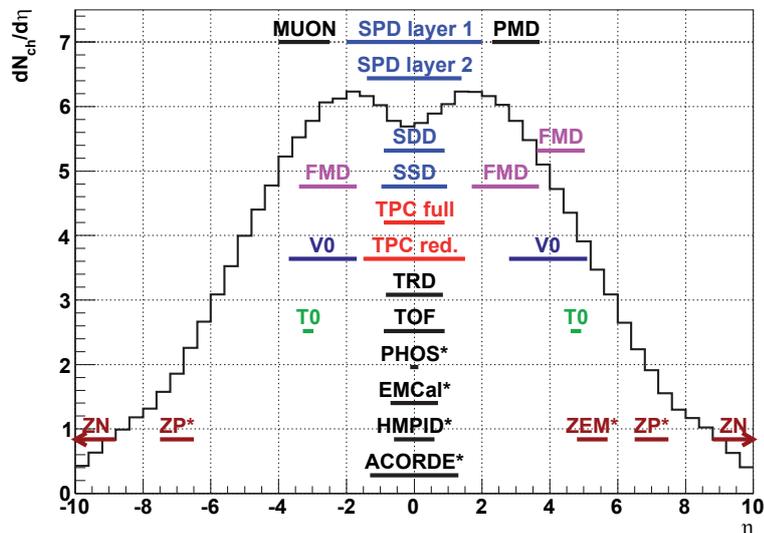
Figure 3.4: Pseudo-rapidity ranges of the ALICE detector systems with a prediction for the charged multiplicity obtained from PYTHIA simulations of *pp* collisions. The detectors have full azimuthal coverage, unless marked with an asterisk. SPD, SDD, and SSD are subsystems of the ITS, ZN, ZP, and ZEM are parts of the ZDC. For the TPC two η ranges are given. "Full" stands for tracks which traverse the TPC over the full radial length, "reduced" means that the track leaves the TPC before reaching the outer radius. The limit is given for tracks which traverse 1/3 of the TPC's radial length. The plot was adapted from Reference [GO09].
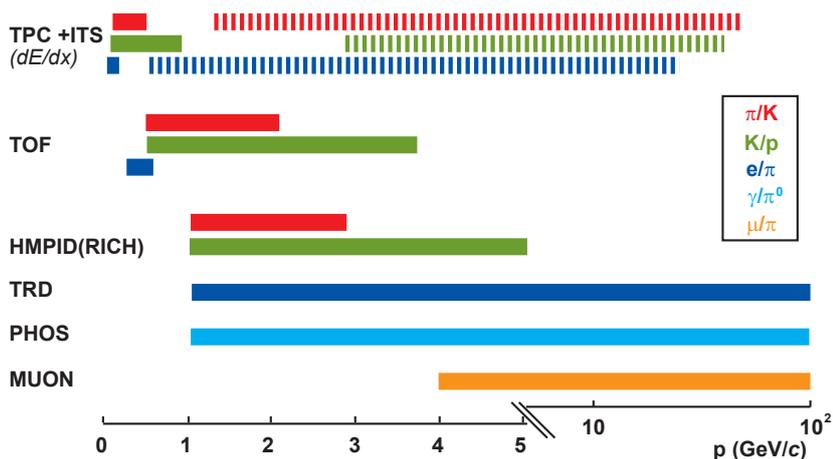
Figure 3.5: Particle identification performance of the ALICE detectors. This plot is based on values presented in Reference [Car04] and is adapted from Reference [Sch04].

The Inner Tracking System

The Inner Tracking System is composed of six layers high resolution silicon detectors with about 12.5 million of readout channels in total. It is described in detail in the *ITS Design Report* [ITS99]. The two innermost layers are Silicon Pixel Detectors (SPD), followed by two layers of Silicon Drift Detectors (SDD) and the two outermost layers are Silicon Strip Detectors (SSD). With this detector array a vertex reconstruction with an accuracy better than $100\,\mu$m is possible. The ITS enables a reconstruction of secondary vertices from the decay of hyperons, D mesons and B mesons in ALICE and completes the PID capabilities to charged particles with momenta smaller than $100\,$MeV/c. It also improves the momentum resolution of particles reconstructed in the TPC.

The Time Projection Chamber

ALICE's largest detector, with an inner radius of about 85 cm and an outer radius of 250 cm, is the Time Projection Chamber [TPC00]. It has a cylindrical shape with a length of 5 m along the beam axis and is filled with a mixture of Ne/CO_2/N_2 (90:10:5) [Gar04]. The TPC is the main tracking device in ALICE. Another important feature of the TPC is its particle identification capability. For momenta between $100\,$MeV/c and $1\,$GeV/c, the TPC is the main tool for hadron, as well as for electron, identification. For momenta above a few GeV/c the hadron identification is good enough to separate different species at a statistical basis [Car04]. Even at larger momenta the TPC's dE/dx measurement improves the electron PID capability of ALICE.

The Time Projection Chamber is designed to handle up to 20,000 charged tracks simultaneously, which is the maximum expected multiplicity of charged particles in the TPC acceptance for central *PbPb* collisions. A readout rate of $200\,$Hz for central heavy ion collisions will be reached. The limiting factor in *pp* collisions is not the charged particle multiplicity, but the high event rate. Although ALICE will operate at a reduced luminosity of $10^{30}\,$cm^{-2}s^{-1} [Sch09], the rate of $350\,$kHz leads to tracks from about 10 - 20 events at a time (from past and future events) in the TPC. For a triggered event, the tracks which do not point to the vertex of that event have to be eliminated [Aam08].

The Time of Flight Detector

The outermost detector that has the full azimuthal coverage is the Time-Of-Flight system [TOF00, Cor02]. The TOF is a PID detector for the separation of kaons (for momenta up to $2.5\,$GeV/c) and protons (up to $4\,$GeV/c) from pions. This is possible since the intrinsic time resolution is at about $40\,$ps. The 90 TOF modules are arranged

in 18 supermodules; the modules are gaseous detectors designed as Multi-gap Resistive-Plate Chambers (MRPC). The basic unit is a MRPC strip with a width of 130 mm and a length of 1220 mm. Depending on the position in z direction, 15 or 19 of these strips are combined in a module. For an effective operation of the TOF a maximum occupancy of 10-15% is acceptable. This requirement results in a design with more than 10^5 independent readout channels [Car04]. TOF will also provide a pretrigger signal for the Transition Radiation Detector.

HMPID, PHOS, and EMCal

The *High Momentum Particle Identification Detector* (HMPID) is a RICH detector which is specialized in separation of pions from kaons and kaons from protons for momenta up to 3 GeV/c and 5 GeV/c respectively [HMP98]. In addition, light nuclei such as d, t, ^3He and α can be identified [Aam08]. The HMPID covers only about 5% of the acceptance of the inner detectors ITS, TPC, TRD and TOF.

The *Photon Spectrometer* (PHOS) has an azimuthal acceptance of $\Delta\phi = 100°$ and covers a pseudo-rapidity $-0.12 \leq \eta \leq 0.12$ [PHO99]. The five modules are composed of an electromagnetic calorimeter (made of lead-tungstate crystal) and a multi-wire proportional chamber which identifies charged particles, *Charged Particle Veto* (CPV). It is positioned at the bottom of ALICE at a distance of 4.6 m from the collision point. The main task of PHOS is the measurement of low-p_T photons as well as the measurement of high-p_t π^0 and γ-jet correlations [Aam08].

The *Electromagnetic Calorimeter* (EMCAL) is the second electromagnetic calorimeter in ALICE [ALI06]. It is designed as a *Pb*-scintillator sampling calorimeter, has a smaller energy resolution than PHOS but exceeds its spatial coverage by a factor of more than six ($\Delta\phi = 107°$ and $|\eta| = 0.7$). EMCAL improves ALICE's capability of jet-quenching measurement, the jet energy resolution, and measurement of high-p_T photons and electrons.

3.2.2   The Other Detectors

The Forward Detectors

Two *Zero Degree Calorimeters* (ZDC) are positioned 116 m on either side from the interaction point [ZDC99]. They measure the energy in beam direction which is correlated to the number of spectator nucleons. This allows to estimate the centrality of a collision.

The *Photon Multiplicity Detector* (PMD) measures the distribution of photons close to the beam direction [PMD99, PMD03]. It is designed as a sandwiched-preshower detector

and uses gas proportional counters for the read out. The gas volumes are positioned in front of, as well as behind of the converter. Therefore the volumes closer to the collision point can be used as veto detectors for charged particles. The PMD is installed 3.6 m from the interaction point, opposite to the muon spectrometer, covering the region of $2.3 \leq \eta \leq 3.5$.

FMD, *T0* and *V0* are described in detail in their combined technical design report [FWD04]. The *Forward Multiplicity Detector* (FMD) is a silicon strip detector and extends the acceptance for charged particles together with the ITS to $-3.4 \leq \eta \leq 5.0$. T0 is a Cherenkov counter and has a time resolution of about 50 ps. It can be operated as a trigger and also provides the signal to start the time measurement in the TOF. V0 is a plastic scintillator. Its main task is to work as an on-line centrality trigger. The TRD derives its main pretrigger signal from T0 and V0.

The Muon Spectrometer

The second large subsystem of ALICE besides the central barrel is the muon spectrometer [ALI96, Muo99, Muo00]. It is designed to detect muons in the pseudo-rapidity region $-4.0 < \eta < -2.5$. The muon spectrometer will focus on dilepton physics, i.e. the reconstruction of quarkonia via their dimuon decay and the measurement of the dimuon continuum up to masses of about 10 GeV/c^2. The dimuon continuum in ALICE is dominated by the semileptonic decay of D mesons and B mesons, which allows to analyse the production of open charm and open beauty [Car04]. Heavy flavor is also measurable in the range of $-2.5 < \eta < -1.0$. Here a muon, measured in the muon spectrometer, is combined with an electron, identified by the TRD [Aam08].

The muon spectrometer is subdivided into four components: a dipole magnet, absorbers, tracking chambers and trigger chambers. The magnet is positioned 7 m from the vertex point and provides a nominal magnetic field of B$_{nom}$ = 0.67 T. Absorbers are placed inside of the L3 magnet (*front absorber*), in front of the trigger chambers (*muon filter*) and around the beam pipe (*beam shield*). The front absorber is 4.13 m thick and made of carbon and concrete which corresponds to 10 times of the interaction length λ_{int} for hadrons. The muon filter (1.2 m of iron, $\approx 7.2 \lambda_{int}$) suppresses muons with momenta smaller than 4 GeV/c and is installed directly in front of the trigger modules. The tracking system is arranged in five tracking stations with two cathode pad chambers at each station. With increasing distance to the interaction point the pad size increases. The spectrometer reaches resolutions around 100 μm, which allows a mass resolution for the Υ of about 100 MeV/c^2. The expected dimuon spectra in the mass region of the J/ψ and the Υ for 10^6 *PbPb* events are presented in Figure 3.6. A trigger on high-p_T (di-)muons is provided
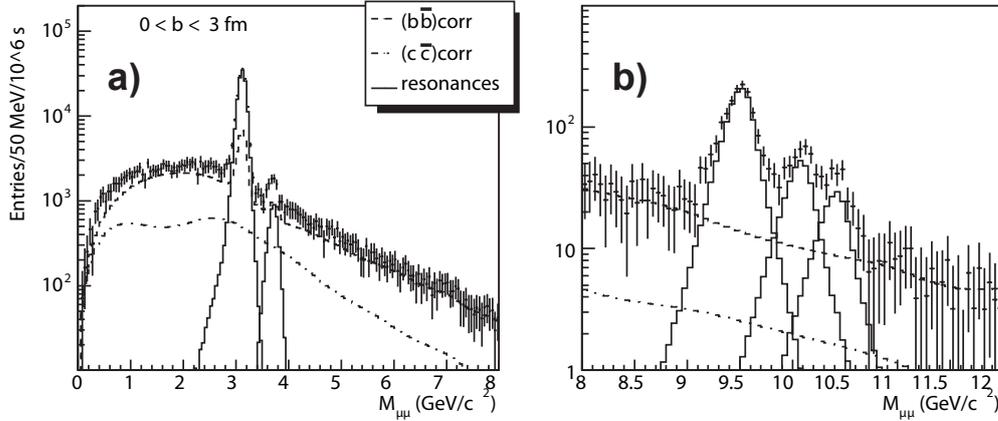
Figure 3.6: The expected invariant mass spectra for one heavy-ion running year of ALICE (about $2 \cdot 10^8$ collisions at $\sqrt{s_{NN}} = 5.5 \, \text{TeV}$) obtained with the muon spectrometer **a)** in the $J\psi$ and **b)** the Υ mass region [Ale06].

by two tracking stations, equipped with two RPCs each. In order to achieve the necessary transverse momentum resolution, the trigger chambers have a position resolution better than 1 cm.

ACORDE

The *ALICE Cosmic Ray Detector* (ACORDE) is an array of plastic scintillators placed on top of the L3 magnet [Aam08]. ACORDE is arranged in 60 modules with an effective detector area of $190 \, \text{cm} \times 20 \, \text{cm}$ each. It was originally built to provide a fast cosmic ray trigger signal for the alignment and calibration of the tracking detectors. Feasibility studies show that ACORDE (together with the TPC, the TRD and TOF) allows to study cosmic rays with primary energies around $10^{15} - 10^{17} \, \text{eV}$ [Ale06].

3.3   The AliRoot Framework

AliRoot [Alia] is the official software framework that is used within ALICE. The ALICE computing framework is used for data simulation, event reconstruction, detector calibration, detector alignment, visualization, and data analysis. The amount of data is about 4 PB for reconstructed *PbPb* events per year [Aam08]. Therefore, the needed computing resources in ALICE will be so large, that a single computing center will not be able to process the data solely. Instead ALICE uses the Grid technology [Fos99]
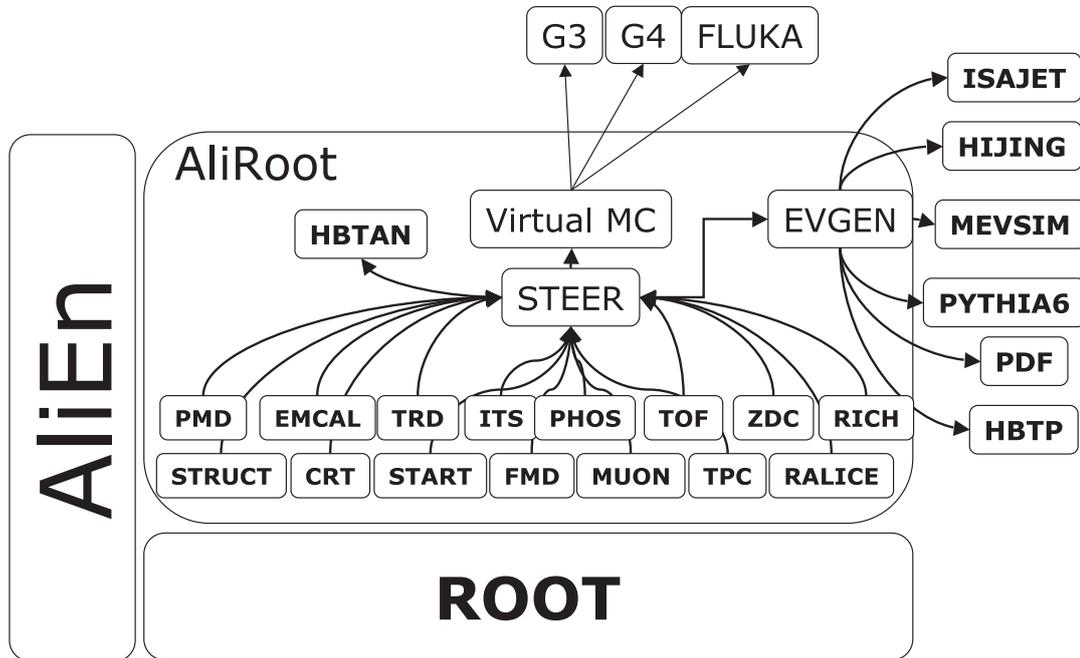
Figure 3.7: Schematic overview of AliRoot [Aam08]. AliRoot is based on the Root framework, the interface to the Grid is AliEn. The central module is STEER, which connects the detector and analysis modules to external event generators, such as HIJING or PYTHIA and to transport packages, like GEANT3.

for decentralization and distribution of computing tasks to computer centers all over the world. The ALICE computing framework is presented in References [COM05, Aam08].

3.3.1 Overview of AliRoot

AliRoot is an Object-Oriented framework written in C++ and is based on *Root* [Roo]. A schematic overview is presented in Figure 3.7. AliRoot consists of independent modules and can also access external programs such as event generators or particle transport packages. The central module in AliRoot is STEER. It provides steering, run management, interface classes and base classes. The code needed for simulation and reconstruction of the different detectors is available in the corresponding detector modules. Furthermore, AliRoot contains data analysis modules and modules that allow access to external programs. AliEn [Sai03] complements the offline framework and provides access to the computing Grid.

The concept of AliRoot's data simulation and processing is shown in Figure 3.8. On the left different steps of the simulation are shown. The first step is the generation of particles by event generators. At this step, the *Monte Carlo* level, the full information
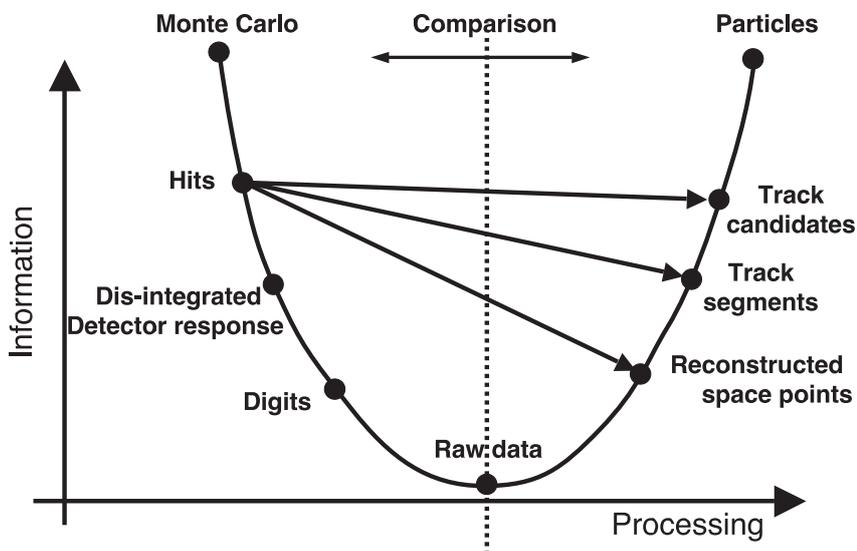
Figure 3.8: Comparison of the simulation (left side) and the reconstruction (right side) in AliRoot [Aam08].
The simulation starts at full event information (Monte Carlo) and is processed to minimum information
(Raw data). Minimum information means that no global information of the event is available, just the local
detector responses. The reconstruction starts at minimum information and accumulates more information
with ongoing processing time, until the properties of the event are reconstructed.

___

of the produced particles, such as species, momentum, charge, and mother-daughter
relationship, is available. In the next step the interaction of the particles with the detectors
is calculated and stored as *Hits* using a transport package, e.g. GEANT3. The responses
of the detectors to the traversing particles are saved as *Digits* and, in a further step, the
Digits can be transformed to *Raw data* as produced by the ALICE data acquisition (DAQ).
At this stage the reconstruction chain starts and can be applied to simulated raw data
produced by AliRoot as well as to real raw data produced by the experiment. The first
reconstruction steps are typically the reconstruction of clusters and, in case of a tracking
detector, a first local track reconstruction. The reconstruction processes the data from a
very simple level (raw data) to a level where as much as possible of the information is
available [Car04, COM05, Aam08, Alib].

3.3.2   Simulations with AliRoot

A simulation in AliRoot can be subdivided into two parts. The first is the simulation of the
event itself, the second is the simulation of the detector response. The simulation of the

event is done by event generators. The event generator base class `AliGenerator` gives access to a large variety of generators [Aam08]:

- External generators, such as PYTHIA [Ben87] or HIJING [Wan91].

- Generators with parameterized p_T and η distributions.

- Box generators of various particle types with flat momentum distributions.

- Generators which combine different generator types to a cocktail of generated particles.

- Afterburners which allow the simulation of particle correlations [COM05].

This flexibility is needed since existing event generators differ in their predictions for observables such as particle multiplicity, p_T or rapidity distributions. In addition, they do not reproduce open charm and open beauty, quarkonia, and high-p_T observables correctly [Car04]. The possibility of combining different generators allows the simulation and tuning of several kinds of events. Here, especially the combination of "background" events of external event generators and "signal" events are interesting e.g. for the simulation of heavy flavor quarks or jet events. These events can be tuned in order to match theoretical predictions and to compare different scenarios. Another example of the various applications is the analysis and tuning of detector reconstruction capabilities. For example, for the optimization of the particle identification performance of the Transition Radiation Detector a cocktail of charged particles with fixed momenta was used. This is presented in more detail in Section 8.1.

Following the event generation the resulting particles are further processed by transport programs. In this step, the interactions of the particles with the detector material and the resulting signals are simulated. In addition, the detector response is digitized taking into account parameterized response functions of the front-end electronics. Optionally the simulated data can be transformed into raw data, which is the data format generated by the readout electronics. AliRoot supports three different transport codes: GEANT3 [Bru93], GEANT4 [Ago03] and FLUKA [Fas03]. Although the user interfaces of the transport programs are very different, AliRoot allows to simulate the detectors with the same code, regardless of the transport program that was chosen.

Due to the fact that the transport calculation in high-multiplicity events is very time consuming, it is also possible to use so called "fast simulations". Here, the event generators are used in the same way as in a simulation described before. The difference to the full simulation and reconstruction is that the particles are not transported through
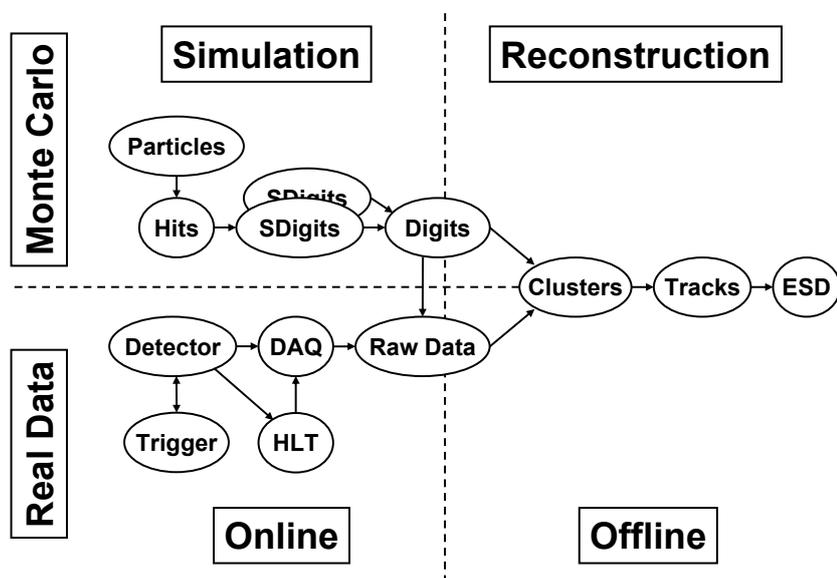
Figure 3.9: Interaction of the reconstruction code with other parts of AliRoot [Aam08]. The reconstruction processes raw data into Event Summary Data. In case of simulations it is also possible to directly use Digits for the reconstruction in order to save computing time.

the experiment by transport packages and reconstructed afterwards. Instead, the detector response is taken from parameterizations stored in look-up tables. A fast simulation of the Time Projection Chamber and the Transition Radiation Detector is used in Section 9.3.2.

3.3.3   Reconstruction and Particle Identification

The reconstruction is another large part of AliRoot. The interaction of the reconstruction with other modules of AliRoot is shown in Figure 3.9. The reconstruction can work on both simulated and real data. Its input is usually data in raw format. In case simulated data is used, the reconstruction can also work on Digits in order to save computing time. The output of the reconstruction is called *Event Summary Data* (ESD). An ESD file contains the information about the the event's primary vertex, secondary vertices, and reconstructed charged particle tracks. The particle track includes the reconstructed track positions, reconstructed momenta, and particle identification information from each detector as well as a combined PID [Aam08].

The steering class for the reconstruction is `AliReconstruction`. This class enables the user to include or exclude detectors and to switch between different reconstruction options. These options can be of general type for the global reconstruction or detector specific options. In the case of the TRD the user can switch for example between

different methods of particle identification. The reconstruction follows a given sequence. The first step is a local reconstruction in each detector, e.g. the transformation of the digital detector signal into clusters. The local information is then combined including the reconstruction of the primary vertex, track reconstruction, and particle identification. Finally also secondary vertices such as V^0 (e.g. $K_s^0 \rightarrow \pi^+\pi^-$), γ conversions, kinks in tracks (e.g. $K \rightarrow \mu\nu$), and cascades (e.g $\Xi \rightarrow \Lambda\pi \rightarrow p\pi\pi$) are reconstructed [Aam08, COM05].

ESDs are not the only data storage container in AliRoot. For a limited number of events additional data will be saved, the ESDfriends. ESDfriends contain information of the detector subsystems that is not needed for the global event characterization but is used in the local reconstruction. ESDfriends contain for instance the reconstructed local tracks and clusters of a subdetector. The ESDfriends are used for the calibration of the detectors. Another data storage format is the *Analysis Object Data* (AOD) format. Such a data object contains only information that is needed for a physics analysis. For different analyses, different AODs can be created for an event.

The particle identification in the Central Barrel of ALICE has to combine very different detector responses. In case of the Time Projection Chamber the information about the particle comes from the measurement of the deposited charge, in case of the Time-of-Flight Detector it is the measured flight time. An approach to combine various detector signals was presented in References [AB91, Ale06]. The probability $w(i|s)$ to observe a signal s of a particle of type i in a single detector is given by:

$$w(i|s) = \frac{r(s|i)\,C_i}{\sum_k r(s|k)\,C_k}. \tag{3.1}$$

In this equation k represents the loop over particles that are taken into account. For the ALICE Central Barrel these are electrons, muons, pions, kaons and protons. $r(s|i)$ is the intrinsic probability response of the detector. The total probability differs from this one, since the a priori probability C_i for a particle of type i also has to be taken into account. The total probability to be a particle of type i compared to the other types is higher if the relative concentration type i particles is larger. While the intrinsic probability from the detector remains the same for a given signal, the a priori probability can differ depending on the type of analysis and the used cuts.

Equation 3.1 can be easily transformed for the combined particle identification. It is [Ale06]:

$$W(i|\bar{s}) = \frac{R(\bar{s}|i)\,C_i}{\sum_k R(\bar{s}|k)\,C_k}. \tag{3.2}$$

Here, $\bar{s}$ is a vector of signals from the different contributing detectors and $R(\bar{s}|i)$ is the combined response function. In ALICE the particle identification signals are

approximately uncorrelated. Thus $R(\bar{s}|k)$ for a number of N detectors can be written as:

$$R(\bar{s}|k) = \prod_{j=1}^{N} r(s_j|k).$$ (3.3)

The resulting equation is then [Ale06]:

$$W(i|s_1, s_2, ..., s_N) = \frac{C_i \prod_{j=1}^{N} r(s_j|i)}{\sum_k C_k \prod_{j=1}^{N} r(s_j|k)}.$$ (3.4)

In case a detector does not contribute to the particle identification $r(s|i)$ is identical for all particle types. The resulting combined response function $R(\bar{s}|k)$, not the total probability, is saved in the ESD files. Since the relative particle concentration depends on the selection by analysis cuts and event samples, W is calculated during the physics analyses [Ale06].

3.3.4 Analysis

The analysis in ALICE is performed by so called `AliAnalysisTasks`. The concept of analysis tasks provides the functionality to run locally on a desktop computer, to use a Parallel Root Facility (PROOF) [Bal03] for parallel computing on a computer cluster, or to run the analysis task on the Grid. The analysis tasks can be added to an analysis train. The train collects the tasks and carries them through the data [Ale06].

The input and the output of an analysis task are defined by the class `AliAnalysisDataContainer`. This container object can contain data of arbitrary type deriving from the Root class `TObject` [Alia]. Usually it is of type `TTree` or `TList`. It is possible that one task generates output in a container that is subsequently used as input by another analysis task. The connection or chaining between tasks is performed by an `AliAnalysisManager` object.

The analysis performed by an `AliAnalysisTask` can be subdivided into a local part and a global part. The local part is implemented in the function `Exec()`. In case of parallel computing using PROOF or the Grid, each computer node runs this part of the analysis locally and independent from any other results. When the local part has ran over all data, the output can be merged and a final function (`Terminate()`) can be called, e.g to draw histograms or to extract fit results [Alib].

4. The Transition Radiation Detector

Transition radiation detectors (TRDs) are particularly suitable for discriminating relativistic particles with different *Lorentz factor* γ. They exploit the radiation which is emitted when a charged particle with $\gamma \gtrsim 10^3$ [Ams08] crosses a boundary of two media with different refractive indices. Several accelerator experiments, such as the *Neutrino Oscillation Magnetic Detector* (NOMAD) at the SPS [Bas98] and ATLAS [Ake98], use or used TRDs for the separation of electrons from pions. For the *Compressed Baryonic Matter* (CBM) experiment which is planned to be installed at the future *Facility for Antiproton and Ion Research* (FAIR) in Darmstadt a TRD is also discussed [And06a, KB09]. Transition radiation detectors are not only used in accelerator experiments, but also in space experiments, e.g. in the *Alpha Magnetic Spectrometer* (AMS02) which is planned to be installed at the *International Space Station* (ISS) [Kir07].

In 1999 the Transition Radiation Detector for ALICE was presented in an addendum to the ALICE proposal [ALI99]. The main goal of the TRD is the identification of electrons with momenta larger than $1\,\text{GeV}/c$ in the central barrel. At such large momenta the measurement of the deposited charge in the Time Projection Chamber is not sufficient to provide an adequate electron/pion separation. In the following section the role of the TRD within ALICE is discussed. A short review of the theoretical background of transition radiation and the energy loss of charged particles is given in Section 4.2. In Section 4.3 the design and working principle is presented, and finally, in Section 4.4, the TRD track reconstruction code is described shortly.

4.1   The TRD within ALICE

4.1.1   TRD Design Requirements

In the *Technical Design Report of the ALICE Transition Radiation Detector* [TRD01] the following design goals for the TRD were defined:

Pion Rejection   One of the main tasks of the TRD is the discrimination of electrons from a large background of pions. The design goal is a *pion efficiency* below 1% at momenta above $3\,\text{GeV}/c$ at an *electron efficiency* of 90%. The pion efficiency is the fraction of pions that is misidentified as electrons at a given electron efficiency. Sometimes, the *pion*
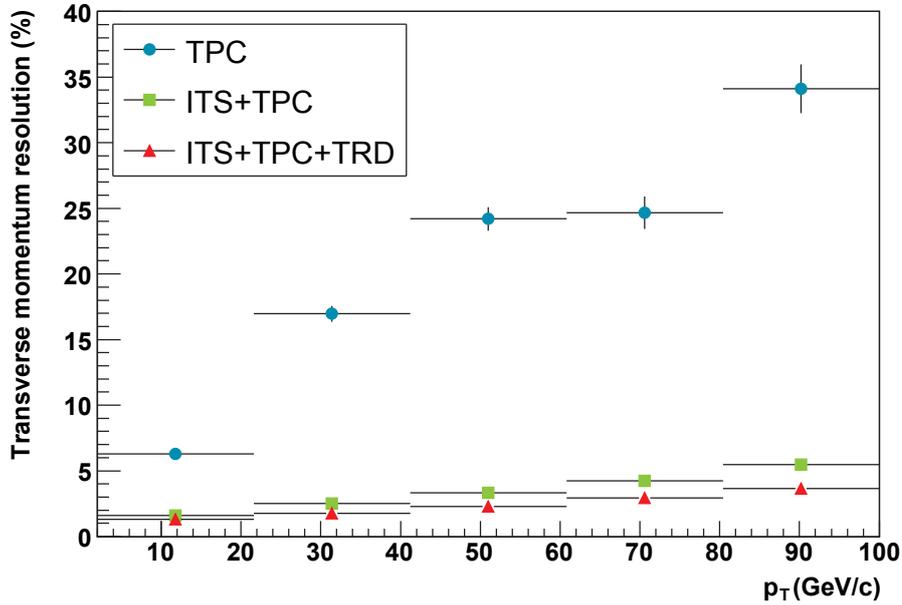
Figure 4.1: Momentum Resolution using the three tracking detectors of the ALICE central barrel for central *PbPb* collisions [Aam08]. Especially for tracks with high transverse momentum the momentum resolution is improved significantly by adding the Transition Radiation Detector to the combined tracking of the Time Projection Chamber and the Inner Tracking System.

———————

rejection factor is used instead. It is the reciprocal value of the pion efficiency. The electron efficiency is the fraction of electrons which are correctly identified as electrons. Particle identification, and therefore pion rejection, is the main topic of this thesis. A detailed overview of the working principle of the particle identification in the TRD is presented in Chapter 6.

Momentum Resolution The required momentum resolution for the central barrel is determined by the desired invariant mass resolution of dielectrons. In the Υ mass region the resolution is at about $100\,\text{MeV}/c^2$ at a magnetic field of $0.4\,\text{T}$. The measured momenta of the electron positron pair are used for the reconstruction of the invariant mass (see Equation 9.1). Thus, such a good momentum resolution is needed in order to be able to separate the three Υ states from each other. In Figure 4.1 the momentum resolution for the central barrel tracking detectors is presented. Including the TRD, the anticipated momentum resolution is below 5% at a momentum of $90\,\text{GeV}/c$ for central *PbPb* collisions [Aam08].

Radiation Length   The thickness of the TRD in radiation lengths is required to be as small as possible. Additional material causes a higher probability for photon conversions and leads therefore to a larger background of secondary electrons. In addition, it enhances the energy loss of electrons due to emission of bremsstrahlung. This leads to a smearing towards lower invariant masses for dielectrons. For the TRD a radiation length in radial direction of $X/X_0 = 23.4\%$ will be achieved [Aam08].

Granularity   The required granularity in the bending direction of the magnetic field is determined by the desired momentum resolution. This results in a typical pad width of 0.7 cm. In z-direction, which is parallel to the beam axis, the expected multiplicity is the decisive factor for the granularity. The Transition Radiation Detector was designed to cope with multiplicities up to 8,000 charged particles per pseudo-rapidity unit. Using a typical pad length of 8.8 cm this corresponds to an occupancy of 34% for all readout pixels [TRD01].

4.1.2   Physics Performance of ALICE with the TRD

Fulfilling the design goals presented above, the TRD enables ALICE to detect and identify electrons with momenta larger than 1 GeV/c at pseudo-rapidities between $-0.9 < \eta < 0.9$ in a high multiplicity environment with a good efficiency. Consequently, the Transition Radiation Detector contributes to the measurement of all the signatures presented in Section 2.3: dielectrons in general, quarkonia, direct photons and single electrons from heavy flavor decays.

Dielectron Measurements in the Central Barrel

Detailed simulations on quarkonia measurements using the ALICE inner barrel were made for *pp* [Kra06, Kru08] and *PbPb* collisions [Som08]. In Figure 4.2 the expected dielectron mass spectrum for 10^7 central *PbPb* collisions extracted with the inner barrel detectors normalized to one event is shown. In the invariant mass spectrum without the TRD no signal for any quarkonium is visible. Including the TRD, the background is reduced significantly. The J/ψ, Υ and Υ' particles can be identified. The main contribution to the background are pions which can be well discriminated from electrons by the TRD. In this analysis a parameterization for fast simulations [GO05] was used. The pion efficiency of the TRD was assumed to be 1% at 90% electron efficiency for all momenta. Results from test beams (see Chapter 7) and simulations (see Chapter 8) suggest that the pion efficiency (at least at low momenta) is better by up to a factor of 5. This reduces the
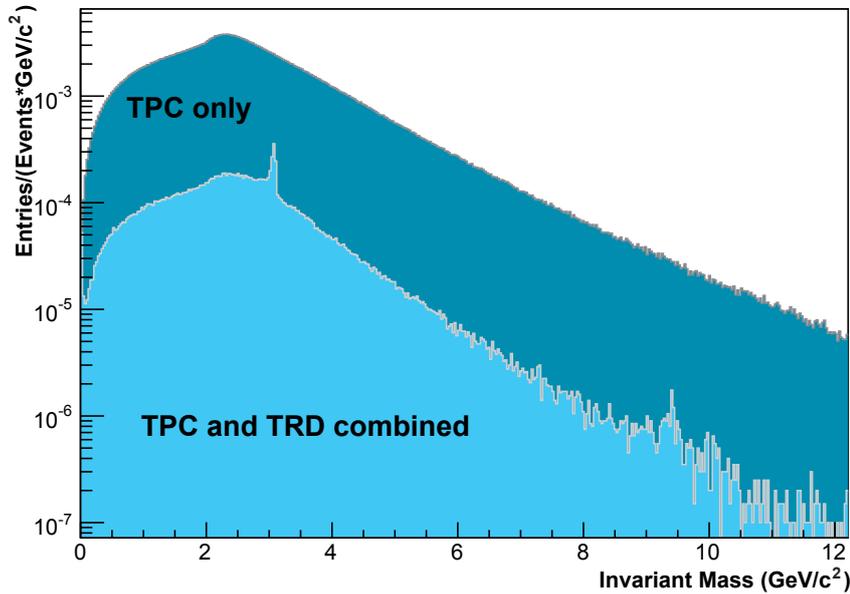
Figure 4.2: Dielectron mass spectrum with the ALICE central detectors [Som08]. Shown is the expected yield for 10^7 central *PbPb* collisions. The darker area represents the yield of dielectron pairs if the PID information is extracted by the TPC only. With the TRD (lighter area) peaks at the masses of the J/ψ, Υ and Υ' are visible. This study was done using a parameterization for fast simulations [GO05]. Here, a constant pion efficiency of 1% for the TRD is assumed for all momenta.

---

pion background further and improves the signal to noise ratio slightly. A closer look at this effect is presented in Section 9.3.2.

Direct Photons and Neutral Mesons

The dedicated detectors for photon measurements in ALICE are the Photon Spectrometer (PHOS) and the Electromagnetic Calorimeter (EMCAL). Results from STAR show that it is also possible to measure photons using charged particle tracking devices such as a time projection chamber [Joh03, Ada04, Wet06]. Since photons are neutral particles, they cannot be measured directly. They are accessible via their conversion to electron positron pairs ($\gamma Z \rightarrow e^+e^-Z$).

electron positron pairs from γ conversions are identified through the reconstruction of their invariant mass (which is $M_{e^+e^-} = 0\,\text{GeV}/c^2$) and their vertex position (which is displaced compared to the position of the primary vertex). In ALICE, the photon conversion probability between the interaction point and the first half of the Time Projection Chamber is about 6.3% [Ale06]. Conversions that happen in the second half of
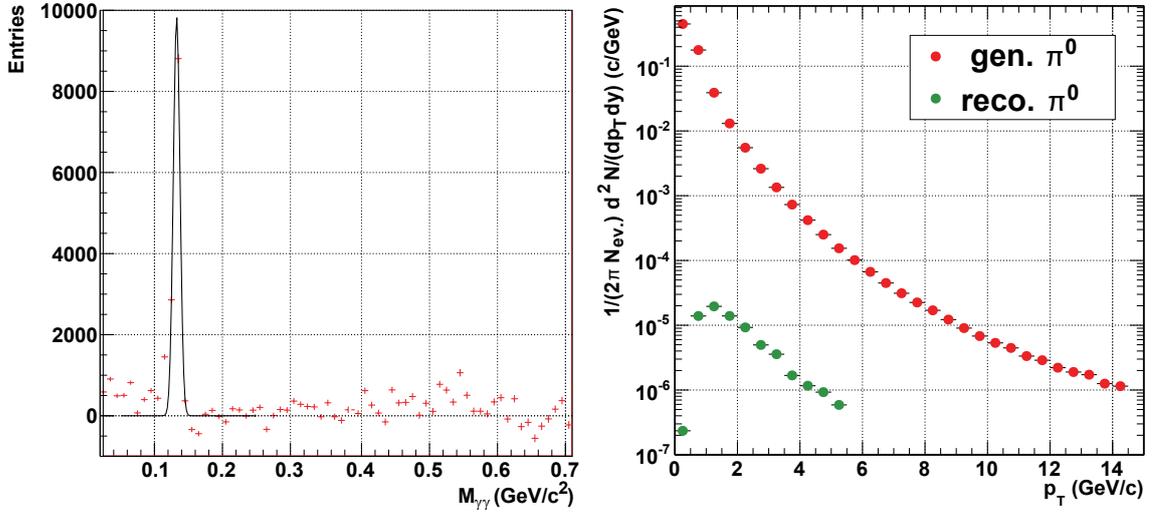
Figure 4.3: Left: Invariant mass spectrum of diphotons after background subtraction extracted with the inner barrel detectors [Mar08]. A clear peak can be seen at the invariant mass of the π^0 ($m \approx 135\,\text{MeV}/c^2$). **Right:** Comparison of the π^0 yield of the inner barrel to the expected total yield. Plotted is the yield per *pp* event versus the transverse momentum of the neutral pion [Mar08].

————

the TPC can hardly be reconstructed due to the limited track length of the electron positron pair. Nevertheless, the photon conversion probability facilitates a photon measurement in ALICE also with the tracking detectors of the inner barrel (ITS, TPC and TRD) [Mar07]. Although the conversion probability is small, the photon measurements with the inner barrel can compete with the measurements using electromagnetic calorimeters in ALICE. The inner barrel detectors have a more than three times larger acceptance than the EMCAL and a more than 20 times larger acceptance than PHOS. In addition, neutrons contribute to the background in the EMCAL and PHOS measurements at low transverse momenta [Ale06]. The inner barrel detectors do not suffer from this background source. In Section 9.1.2 the photon measurement using the inner barrel will be presented as a method to extract reference electrons for the calibration of the TRD particle identification. Even without the TRD this method provides high-purity electron samples in *pp* collisions. However, with inclusion of the TRD possible background from non-electrons will be further reduced.

Large contributions to the photon spectrum originate from the decay of neutral mesons, such as $\pi^0 \to \gamma\gamma$ or $\eta \to \gamma\gamma$. In order to measure direct photons the photon yields from these contributions have to be determined precisely and need to be subtracted properly from an inclusive measurement. Simulations of *pp* collisions show that a
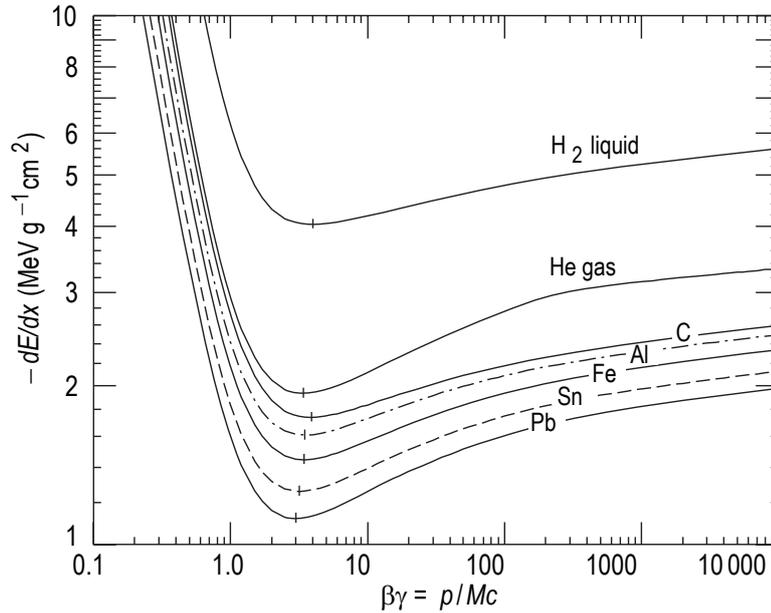
Figure 4.4: Calculated mean energy loss of pions in different materials. Taken into account is only the energy loss by ionization. The curve follows the *Bethe-Bloch Formula* [Ams08].

———————

measurement of neutral pions and η mesons is possible using the inner barrel detectors down to transverse momenta of $0.4\,\text{GeV}/c$ [Mar08] (see Figure 4.3).

4.2   Interactions of Charged Particles with Matter

In the transition radiation detector two processes contribute to the signal that is used for particle identification. Charged particles deposit energy in the gaseous volume of the TRD. This process is described by the *Bethe-Bloch* formula. In addition, charged particles produce under certain conditions *transition radiation* in the radiator material. The generated photons are absorbed in the detector gas and contribute to the signal. In this section the theoretical description of these processes is presented.

4.2.1 Energy Loss of Charged Particles

The Bethe-Bloch Formula

Charged particles deposit energy in a material caused by collisions with the atoms in the traversed material. This energy loss per unit of path length is described by the *Bethe-Bloch* formula [Blu08]:

$$-\frac{dE}{dx} = \frac{4\pi N e^4}{m_e c^2 \beta^2} z^2 \left(\ln \frac{2 m_e c^2 \beta^2 \gamma^2}{I} - \beta^2 - \frac{\delta(\beta)}{2} \right). \tag{4.1}$$

Here, N is the number density of electrons in the matter, e is the elementary charge, m_e represents the rest mass of the electron, and c is the speed of light in the vacuum. The velocity of the traversing particle is given by $\beta (= v/c)$, and $\gamma (= 1/\sqrt{(1 - \beta^2)})$ is the *Lorentz factor*. z represents the electric charge of the particle, the mean excitation energy of the atoms of the traversed matter is described by I. δ is a correction factor for density effects.

This equation describes the mean value for the energy loss of charged particles caused by ionization. The calculated energy loss of pions in different materials is shown in Figure 4.4. For $\beta\gamma \lesssim 3$ the deposited energy decreases with rising velocity. This can be described by a classical approach, since the traversing particle has less time to interact with the atoms of the traversed material. A particle that is at the minimum of the curve is called a *minimum ionizing particle*. With velocities larger than $\beta\gamma = 3$ relativistic effects become important. The transverse electric field flattens and extends [Ams08] due to *Lorentz contraction* and affects atoms with a larger distance to the track than at lower velocities. The strength of the *relativistic rise* is given by the mean ionization energy I. This energy rises with the atomic number Z:

$$I \approx AZ. \tag{4.2}$$

For xenon the mean ionization energy is $482\pm30\,\text{eV}$ [Sel82]. The deposited energy does not increase infinitely. Instead, the medium becomes polarized and screens the electric field of the traversing particle and the energy loss is reduced [Gru93]. The curve in Figure 4.4 reaches the so called *Fermi-Plateau*. This screening is described by the density correction factor δ and depends on the traversed material and its density. A parametrization to describe the effect of the density correction as well as summary tables for different materials can be found in Reference [Ste84].

It has to be noted that the Bethe-Bloch formula describes only the energy loss by ionization for muons and heavier particles correctly. Since the mass of electrons
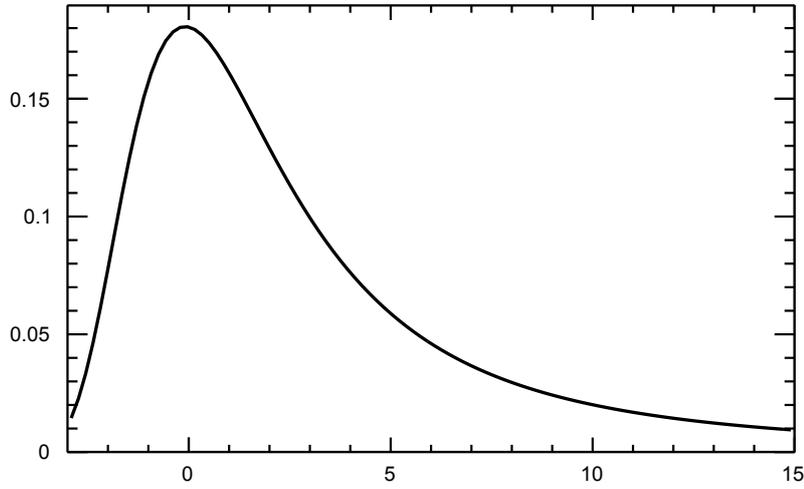
Figure 4.5: Schematic illustration of the Landau distribution.

and positrons is the same as the mass of the collision partner a correction has to be implemented. It can be shown that with this correction the mean of the deposited energy for electrons and heavier particles is the same for large values of γ [Blu08].

Energy Fluctuations

The energy loss caused by ionization is a statistical process. It can happen that the energy transfer to a single electron is that large that this electron also ionizes the medium along its path. Such electrons are called δ *electrons*, or *knock-on electrons*.

Especially for thin layers of material the fluctuations of the deposited energy may be very large. The energy fluctuations follow a *Landau* distribution. An approximation for the Landau distribution (see Figure 4.5) is given by Reference [Gru93]:

$$L(\lambda) = \frac{1}{\sqrt{2\pi}} \exp\left\{ -\frac{1}{2}(\lambda + e^{-\lambda}) \right\},$$ (4.3)

where λ is the deviation of the actual energy loss ΔE in a layer with thickness x from the most probable energy loss ΔE^{MPV}:

$$\lambda = \frac{\Delta E - \Delta E^{\mathrm{MPV}}}{\xi},$$ (4.4)

Here, ξ is defined as:

$$\xi = \frac{2\pi N e^4}{m_e c^2 \beta^2} z^2 x,$$ (4.5)

with x as the thickness of the traversed medium.

Bremsstrahlung

Relativistic particles lose energy not only due to ionization but also through the emission of *bremsstrahlung*. The traversing particle is affected by the Coulomb field of the traversed matter's nuclei, and hence, decelerated. The energy loss results in the emission of photons. Following Reference [Gru93], the energy loss due to bremsstrahlung for high energies is given by:

$$-\frac{dE}{dx} = 4\alpha N_A \cdot \frac{Z^2}{A} \cdot z^2 \left(\frac{1}{4\pi\varepsilon_0}\frac{e^2}{mc^2}\right)^2 \cdot E \ln\frac{183}{Z^{1/3}}. \tag{4.6}$$

α_e the fine-structure constant of the electromagnetic interaction, N_A is the Avogadro number, Z is the atomic number of the traversed material, and A is its mass number. ε_0 is the electric constant, while z, m, and E are the charge, the mass, and the energy of the decelerated particle. The energy loss caused by bremsstrahlung is proportional to E/m^2. Hence, it plays an important role for light particles, such as electrons. This radiative energy loss exceeds the loss due to ionization at the critical energy E_c. For electrons and $Z \geq 13$ it is [Gru93]:

$$E_c = \frac{550\,\text{MeV}}{Z}. \tag{4.7}$$

4.2.2   Transition Radiation

The measurement of the deposited energy caused by ionization effects allows to identify particles with different masses. In Figure 4.6 the measurement of the deposited charge is plotted versus the momentum [Ams08]. This measurement was done with a time projection chamber and illustrates the possibility of identifying various particle types via their deposited charge. Different bands can be easily identified at least at small momenta. With larger momenta the bands of the hadrons (and muons) overlap more and the particles become indistinguishable. At momenta $\lesssim 2\,\text{GeV}/c$ the electron band is clearly separated from the others, only at the crossing points no clear separation is possible. Is the momentum above $3\,\text{GeV}/c$ the pions and the muons start to overlap with the electron band. The identification via ionization energy loss is not efficient anymore. Instead, another effect has to be exploited to provide a separation at these high momenta: the *transition radiation* (TR).

Ginzburg and *Frank* predicted in 1945 the emission of electromagnetic radiation in the optical region when a charged particle crosses the boundary between two media with different dielectric constants [Gin45]. Since the intensity of the radiation is very small in the optical region, it seemed that TR could not be exploited for the identification
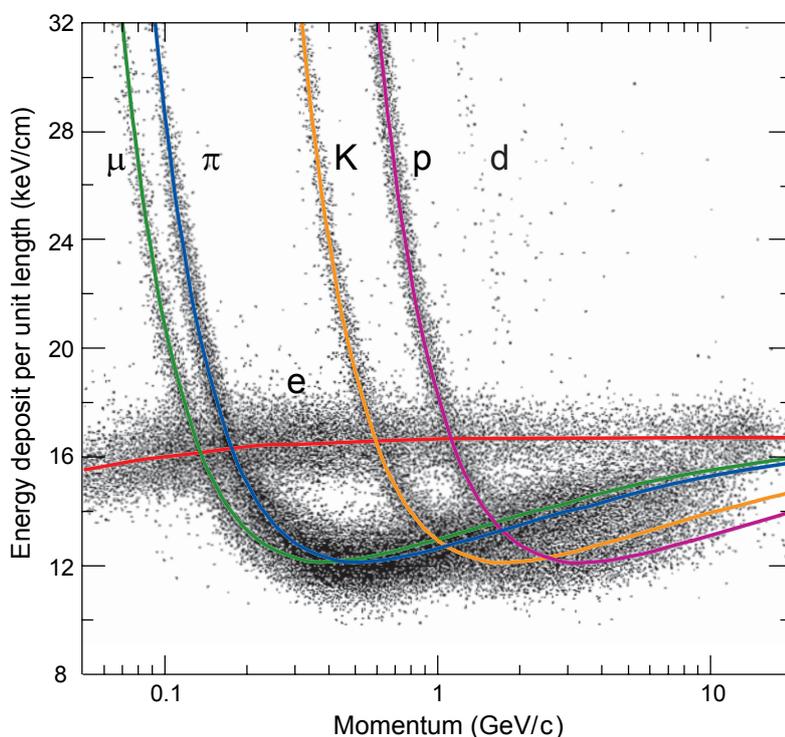
Figure 4.6: The most probable values of the ionization of electrons (red), muons (green), pions (blue), kaons (yellow), and protons (pink) are compared to energy deposit measurements in the PEP4/9-TPC [Ams08].

of individual particles [Dol93]. In 1957 *Garibian* showed that ultrarelativistic particles ($\gamma \gg 1$) emit transition radiation in the X-ray region [Gar57]. In addition, it was predicted that the energy loss caused by transition radiation depends on the Lorentz factor γ. This is very interesting for particle identification since other methods, such as the detection of *Cherenkov radiation*[1], depend on the velocity and fail for ultrarelativistic particles.

Based on Reference [Jac98], the emission of transition radiation can be understood phenomenologically in the following way: Deep inside of the first medium the electromagnetic fields of the traversing particle are characterized by its velocity and the surrounding medium. Deep in the second medium the fields are again determined by the particle's velocity and the surrounding medium. The velocity stays constant, but now the characteristics of this second medium have to be taken into account. Since the dielectric constants of the media differ, the electromagnetic fields are different. In case a particle

---

[1]Cherenkov radiation is emitted when a charged particle traverses a medium with a velocity that is higher than the velocity of light in the medium.

passes a boundary between these media, the electromagnetic fields must reorganize, i.e. work needs to be done. As a consequence of this reorganization, transition radiation is emitted.

Transition Radiation at a Single Boundary

For ultrarelativistic particles crossing a boundary, the emitted radiation intensity W depends on the frequency and the emission angle of the photon. It is given by [Che74b]:

$$\frac{d^2W}{d\omega d\theta} = \frac{2\alpha_e \hbar \theta^3}{\pi} \left(\frac{1}{1/\gamma^2 + \theta^2 + \omega_1^2/\omega^2} - \frac{1}{1/\gamma^2 + \theta^2 + \omega_2^2/\omega^2} \right)^2, \tag{4.8}$$

with θ as the emission angle of the TR photon with respect to the particle trajectory. ω is the TR photon frequency and ω_1 and ω_2 are the *plasma frequencies*[2] of the traversed media. Solving Equation (4.8) shows that most of the photons are emitted within an angle of $\theta = 1/\gamma$ [Ego00].

Following Reference [Che74b], the energy spectrum of the emitted photons is given by:

$$\frac{dW}{d\omega} = \frac{\alpha \hbar}{\pi} \left[\left(\frac{\omega_1^2 + \omega_2^2 + 2\omega^2/\gamma^2}{\omega_1^2 - \omega_2^2} \right) \cdot \left(\ln \frac{1/\gamma^2 + \omega_1^2/\omega^2}{1/\gamma^2 + \omega_2^2/\omega^2} \right) - 2 \right]. \tag{4.9}$$

With $\omega_1 > \omega_2$, this leads to a constant production yield at small energies ($\omega < \gamma\omega_2 \approx 1\,\text{keV}$), to a logarithmic decrease at medium energies ($\gamma\omega_2 < \omega < \gamma\omega_1$), and to a large intensity drop for high energies ($\omega > \gamma\omega_1$). The resulting curve is shown in Figure 4.7.

The total energy emitted at a single boundary is [Che74b]:

$$W = \int \int \left(\frac{d^2W}{d\theta d\omega} \right) d\theta d\omega \tag{4.10a}$$

$$= \frac{\alpha \hbar}{3} \frac{(\omega_1 - \omega_2)^2}{\omega_1 + \omega_2} \gamma. \tag{4.10b}$$

This equation is the key formula for particle identification with transition radiation since it shows the linear dependence of the total emitted energy on the Lorentz factor γ.

Radiators with Periodic Layers

The probability for the creation of a photon is only of the order of α ($\approx 1/137$) [Ego00]. A possibility to enhance the number of transition radiation photons on a particle trajectory

---

[2]The plasma frequency is the self-oscillation of an electrically neutral medium, where the opposite electric charges are displaced. The charges perform a spatial oscillation. The frequency of this oscillation is the plasma frequency of the medium [Dem00].
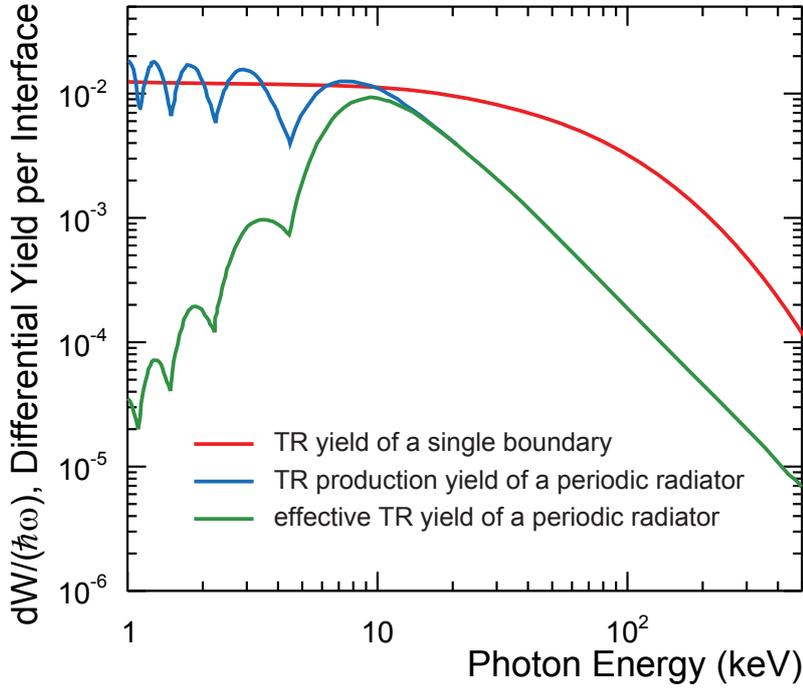
Figure 4.7: The differential yield per interface as a function of TR photon energy [Ego00]. In the case of a single boundary (plotted in red) at low photon energies the yield is constant and then decreases rapidly at higher energies. The photon production in a regular radiator (blue) fluctuates around the value of a single boundary at low energies due to interference effects. Caused by the finite thickness of the foils formation zone effects suppress the yield at higher energies. For a real radiator (green) the absorption of TR photons also plays a role at lower energies.

---

is to increase the number of crossed boundaries. In this case the equations get more complicated since interference effects and absorption have to be taken into account. These effects lead to a modulation of the spectrum for one interface and to a saturation of the yield for high values of γ.

A typical periodic radiator consists of thin foils with constant spacing. In this case usually air is the second material. For a radiator with N foils, foil thickness l_1 and spacing l_2 the differential spectrum is [Che74b]:

$$\frac{d^2 W_N}{d\theta d\omega} = \frac{d^2 W}{d\theta d\omega} 4 \sin^2\left(\frac{l_1}{Z_1}\right) \frac{\sin^2\left[N\left(l_1/Z_1 + l_2/Z_2\right)\right]}{\sin^2\left(l_1/Z_1 + l_2/Z_2\right)}, \tag{4.11}$$

with

$$Z_{1,2} = \frac{4c}{\omega}\left(\frac{1}{\gamma^2} + \theta^2 + \frac{\omega_{1,2}^2}{\omega^2}\right)^{-1}. \tag{4.12}$$
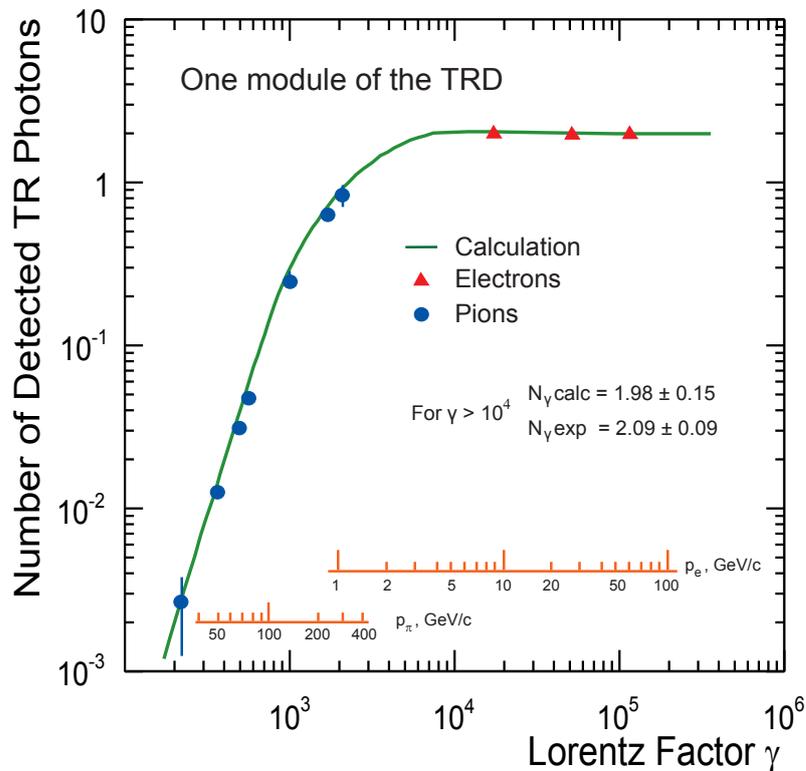
Figure 4.8: Number of detected TR photons versus Lorentz factor γ measured with the E715 TRD at Fermilab and compared to calculations [Den84]. With rising γ the number of produced TR photons increases. At $\gamma \gtrsim 6000$ the yield reaches a plateau. Also shown are the momenta of electrons and pions for different values of γ. It can be seen that transition radiation is well suited to separate electrons and pions with high momenta.

Z_1 and Z_2 are the formation zones for the two media, which can be understood as the minimum distance that is required for the electromagnetic field of the particle to reach its new equilibrium configuration [Art75]. In case the foil thickness is smaller than the formation zone of the foil material, or the spacing between the foils is smaller than the formation zone of air, the production of transition radiation is suppressed.

In Figure 4.7 the resulting differential production yield is plotted against the photon energy (blue curve). At low energies the yield oscillates around the expectations for a single interface (red curve), at higher photon energies the yield is suppressed. This suppression originates from the formation zone's dependence on the frequency of the emitted photon. The higher the photon energy, the larger is the formation zone, and the thicker the foils have to be in order to exploit the full TR yield at high photon energies. Thick radiator foils are not practical, since the material will absorb the photons. Figure 4.7

also shows the effective yield of an "optimized" radiator (green curve): photons with small energies are suppressed due to absorption, photons with large energies are suppressed because of the "formation zone effect". The maximum yield is adjusted by variation of the foil thickness and the spacing. Since the absorption cross section σ is a function of the atomic number ($\sigma \sim Z^5$), the radiator material should have a small Z. Typical radiator materials for periodic radiators are lithium foils or polypropylene foils [Ego00].

Figure 4.8 shows the number of transition radiation photons as a function of γ. The data was taken with the E715 TRD at Fermilab[3] and is compared to theoretical predictions of the transition radiation yield [Den84]. The periodic radiator consisted of 210 layers of $17\,\mu$m of polypropylene separated by 1 mm air. It can be seen, that the expectation from a single boundary, a linearly increasing total yield with rising γ, is not fulfilled for particles with high Lorentz factors. However, this measurement confirms the theoretical predictions for the transition radiation yield with periodic layers and shows that electrons and pions can be clearly separated using transition radiation.

Irregular Radiators

The usage of periodic radiators consisting of a stack of foils is often not practicable. A constant spacing of the foils would need, at least for a barrel design TRD, a lot of heavy support structures. This causes additional material which increases the probability for particle scatterings or photon conversions. Instead of foil radiators other substances with many boundaries and low Z can be used. Typical materials are e.g. carbon fibers, different types of foams, or a combination of both [TRD01], but there are also more exotic materials used, such as e.g. an aluminum honeycomb structure [Che03] for measurements at very high momenta.

The theoretical description of irregular radiators is not easy and a successful description depends on the complexity of the radiator type. A general approach of describing irregular radiators including absorption effects was made by *Garibian et. al.* [Gar75]. The basic idea is to transform the formulas for radiators with strict periodicity to formulas using average values for the thicknesses of the "foils"[4] and gaps. In addition the number of crossed interfaces has to be substituted with the number of effectively crossed boundaries.

The simplest irregular radiator is one that consists of a stack of foils but with various thicknesses or gaps. An example of such a radiator type is the aluminum honeycomb

---

[3]Fermi National Accelerator Laboratory in Batavia, Illinois

[4]In this context and in the following paragraphs "foil" means a layer of a given material.

radiator of the planned ACCESS STRD[5] [Che03]. Its theoretical description is discussed in Reference [Cas03]. An example for more complex conditions is the ATLAS Transition Radiation Tracker [ATL97]. Here, the read-out chambers (straw tubes) are embedded in the radiator, which is in the barrel part made of carbon fibers. For a correct description of transition radiation not only the radiator has to be taken into account, but also surfaces of the straw tube itself. Consequently, the transition radiation production happens also inside of the active detector volume and more than two media must be considered for the calculations. A detailed derivation can be found in References [Gri02a, Gri02b].

For the simulation of ALICE and its detectors the software framework AliRoot [Alia] (see also Section 3.3.1) was developed. The standard toolkit for the simulation of particles traversing the detectors in AliRoot is GEANT3 [Bru93]. Here, the simulation of transition radiation is not implemented. Instead of simulating the irregular ALICE TRD radiator an approximation is used in AliRoot, by taking into account the transition radiation yield of a regular radiator including absorption effects. The parameters for this "equivalent" regular radiator, such as foil thickness and gap thickness, were set to reasonable values. The total number of foils that is needed to reproduce the TR spectrum is momentum dependent [And04a, And09a] and was tuned to reproduce measurements taken at two test beam times in 2002 and 2004 for momenta between 1 and 10 GeV/c [Bus04, And06b]. It was shown that this parametrization reproduces the measured TR production (see Figure 4.9).

4.3   The ALICE TRD Layout

The ALICE Transition Radiation Detector is part of the central barrel. It is composed of 18 supermodules, which consist of 30 TRD chambers each, which corresponds to 540 chambers in total. The TRD layout is schematically presented in Figure 4.10. The 30 TRD chambers of one supermodule are arranged in 5 stacks with 6 layers. The TRD with an inner radius of 2.9 m and an outer radius of 3.68 m is located between the TPC and TOF. The TRD covers the full azimuthal angle and a pseudo-rapidity region of $|\eta| <$ 0.84 [Aam08]. This leads to a total active detector area of 694 m^2 and a total gas volume of 25.8 m^3. Each TRD chamber consists of a radiator, a drift chamber with pad readout and an electronic part. A single TRD chamber is depicted schematically in Figure 4.11.

---

[5]The Advanced Cosmic ray Composition Experiment for Space Science is a cosmic ray space experiment that was planned to be installed at the ISS. The Scintillator Transition Radiation Detector is an example of a non-gaseous TRD.
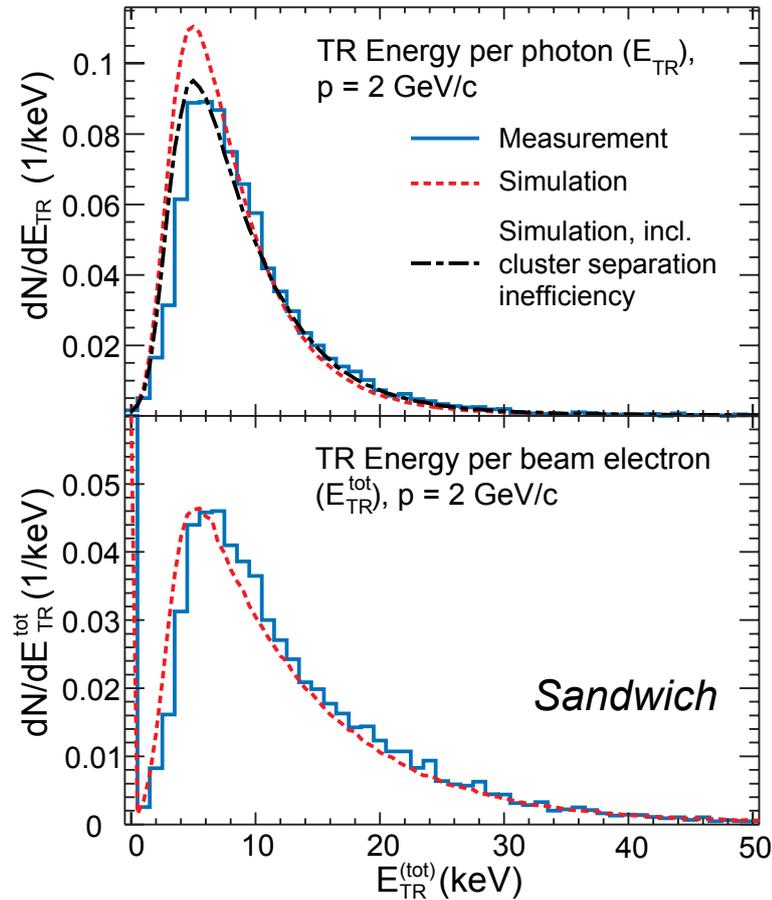
Figure 4.9: Measured and simulated transition radiation spectra [And06b]. The measurement (blue line) was performed with 2 GeV/c electrons during the test beam 2004. The red line represents a simulation using a parameterization for generating transition radiation, the black curve shows the same simulation but with a correction for cluster reconstruction inefficiency. In **a)** the transition radiation energy per photon is shown, in **b)** the total energy deposit is plotted [And06b].

4.3.1 The Radiator

In 2000 different radiators, made of foils, fibers, and foams, were tested at GSI[6] [And01]. The conclusions from this test led to the final design of the radiator. It has a thickness of 4.8 cm and is built in a sandwich design, composed of polypropylene fiber mats which are surrounded by 8 mm thick carbon fiber laminated Rohacell® HF 71. It is optimized in order to provide a good transition radiation yield, and, in addition, a good mechanical

---

[6]Gesellschaft für Schwerionenforschung
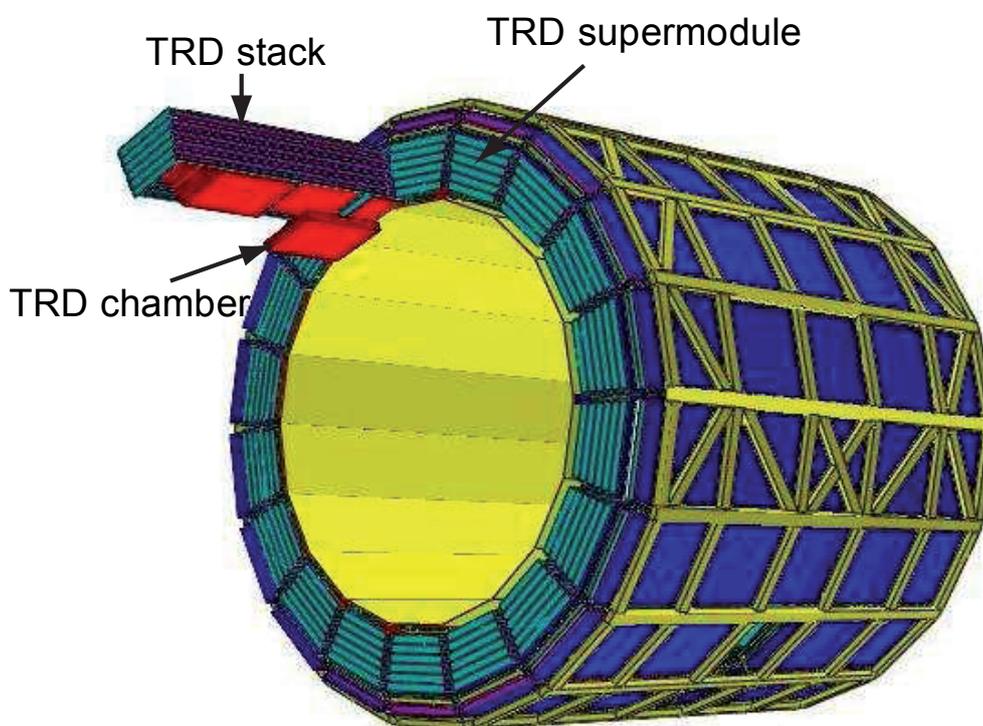
Figure 4.10: The ALICE Transition Radiation Detector [Aam08]. The barrel designed TRD consists of 18 supermodules, which are positioned around the collision point, parallel to the beam axis. Each supermodule is made of 30 single chambers which are arranged in 5 stacks with 6 layers each.

---

stability. Polypropylene mats provide a TR yield comparable to that of foils. Rohacell$^{®}$ is a stable material and contributes also to the transition radiation production. Together with the carbon fiber laminate it provides mechanical rigidity, which is needed, since the radiator is also the inner boundary of the drift chamber and the drift cathode is glued directly on the surface of the radiator. The drift chambers are operated with an overpressure of at most 1 mbar. In case the radiator would not be solid enough, as a consequence, the drift electrode would be deformed which would lead to unacceptably deformed electrical drift fields. This is discussed in detail in Reference [Zau03].

4.3.2   The Readout Chambers

The drift chamber is split into the 3 cm thick drift region and the multi-wire proportional chamber section (or amplification region) which has a thickness of 0.7 cm. The two regions are separated by cathode wires, with a diameter of 75 μm and a pitch of 2.5 mm. The cathode wires have the same electrical potential as the readout pads and allow an
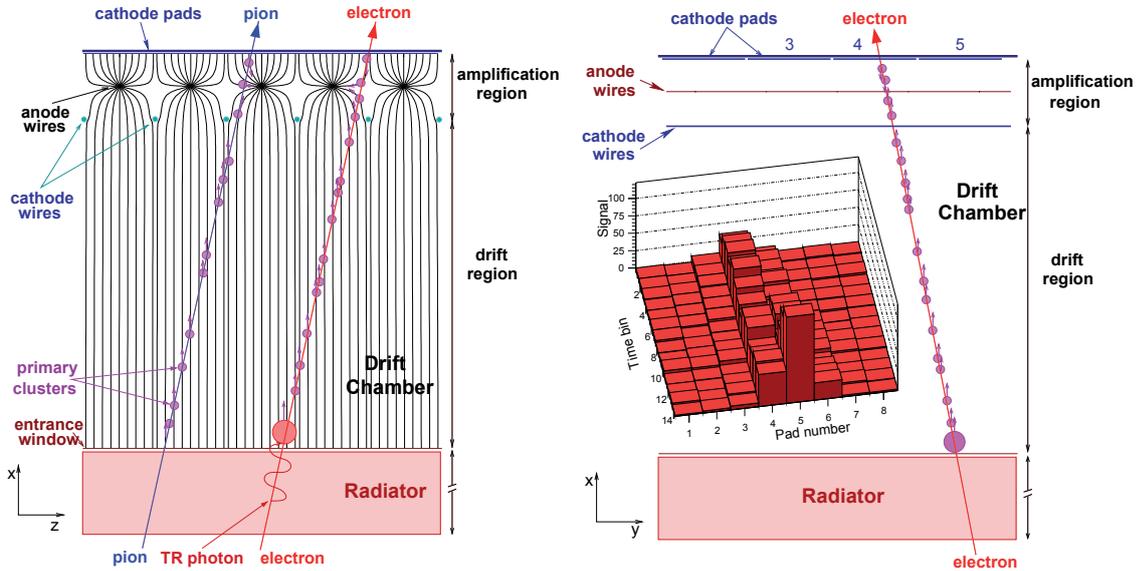
Figure 4.11: The working principle of the ALICE Transition Radiation Detector [Aam08]. A particle that traverses the TRD ionizes the chamber gas. The resulting electron clusters drift to the amplification region. In the amplification region the clusters are accelerated to the anode wires and avalanches are formed out. The avalanches induce charges on the pads which are read out. In case the Lorentz factor of a particle is large enough a transition radiation photon is generated inside of the radiator. This photon is absorbed early in the chamber gas and contributes to the signal.

––––––––––

independent adjustment of the drift velocity and gas gain. The anode wires are positioned in the center of the amplification region and are staggered with respect to the cathode wires. The positions of the anode and the cathode wires in the amplification region are shown in Figure 4.12. The anode wires have diameters of $20\,\mu$m and the pitch between them is $5\,$mm. The nominal value for the voltage of the anode wires is $U_a = 1.4\,$kV and for the voltage of the drift plane is $U_d = -2.1\,$kV [TRD01]. Each readout chamber has 144×16 (12 for the central stack) readout pads, which results in a total number of
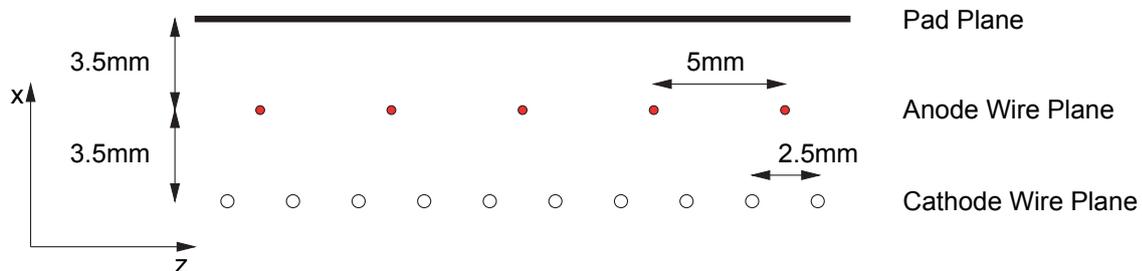
Figure 4.12: Wire geometry of a readout chamber of the Transition Radiation Detector [TRD01].
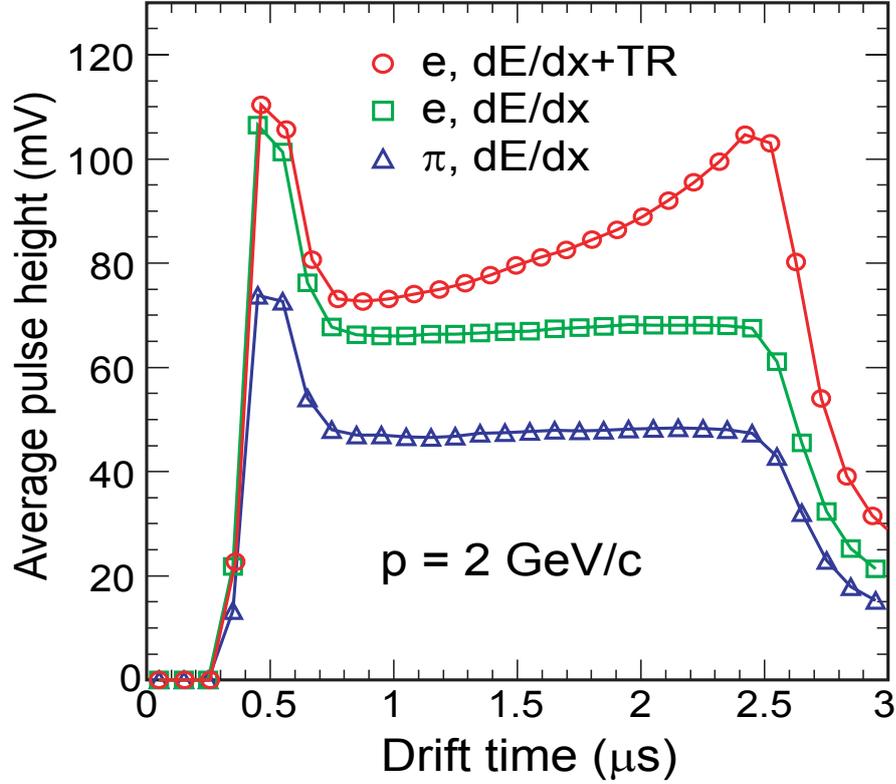
Figure 4.13: The average pulse height in the Transition Radiation Detector for electrons (with and without TR) and pions [Aam08]. The peak at small drift time origins from the amplification region. At larger drift time a plateau can be seen for pions and electrons without TR. The electron signal is about 1.4 times larger than that of pions. In case transition radiation is produced instead of the plateau a second peak can be identified at large drift times. Transition radiation photons are dominantly absorbed within the first few millimeters in the chamber gas and result in the TR peak.

————————

1.18×10^6 pads for the complete detector. The size of the pads depends on the chamber position in a supermodule, typical values are $0.7 \times 8.8 \, cm^2$ [Aam08]. The pads are tilted by $2°$ alternating from layer to layer, in order to improve the position resolution along the z coordinate [TRD01]. In this coordinate system, x is perpendicular to the pad plane, y is in direction of the pad width, and z the direction of the pad length.

The gas is a mixture of 85% xenon and 15% CO_2. The gas has to be protected from oxygen contamination. Otherwise, electrons would attach to oxygen which results in a lower electron yield [And03]. The process of track generation is illustrated in Figure 4.11.

A particle that traverses the chamber ionizes the gas on its track. The resulting ionization clusters drift along the field lines of the electric field to the amplification region. Here, the clusters are accelerated towards the anode wires and avalanches of electrons are formed. The avalanches induce an electrical charge on the readout pads which generates the signal. This is read out with a sampling rate of 10 MHz [Aam08] and corresponding to a time bin width of 100 ns.

Particles with very high $\gamma(\approx 1000)$ produce one or more transition radiation photons in the radiator, which are absorbed early in the drift chamber. The absorption length for a photon in the used gas mixture (with a pressure of 1000 mbar) with an energy of 8 keV is about 1.07 cm [Ber09b]. The charge deposited by transition radiation photons is large compared to that originating from ionization processes. The number of electrons that are liberated by a minimum-ionizing particle is 275 e^-/cm [TRD01], while the transition radiation photon liberates about 460 electrons[7]. In Figure 4.13 the average pulse height is plotted versus drift time for particles with momenta of 2 GeV/c. At small drift times a peak can be seen for both particle types. This peak originates from the amplification region and is followed by a plateau in case transition radiation does not contribute to the signal. It can be seen that the average pulse height of electrons is about 1.4 times higher than that of the pions. An additional peak occurs at larger drift times for the electrons if transition radiation is produced. The position of the absorption and the amount of deposited charge allows to identify clusters originating from transition radiation photons, and therefore, to identify electrons. This will be discussed in more detail in Chapter 6.1.

4.3.3   Readout Electronics

An overview of the TRD readout electronics is given in Figure 4.14. It consists of local components which are located on a readout board directly on the backside of the chambers and a central unit which combines the information of the single chambers. Local components are the PreAmplifier and Shaping Amplifier (PASA) and the TRAcklet Processor (TRAP) which are combined on a Multi Chip Module (MCM) as well as the Optical Readout Interface (ORI). Each chamber has two ORIs and 16 (12 in the central stack) readout boards. Each readout board has 17 or 18 MCMs. The central component is the Global Tracking Unit (GTU) [Aam08].

---

[7]From test beam measurements [And04b] the average deposited energy in keV for minimum ionizing particles can be extrapolated to about 4.8 keV/cm. Transition radiation photons are expected to be completely absorbed in the gas. Using the number of electrons per centimeter for a minimum-ionizing particle, the number of liberated electrons for a transition radiation photon with an energy of 8 keV can be estimated.
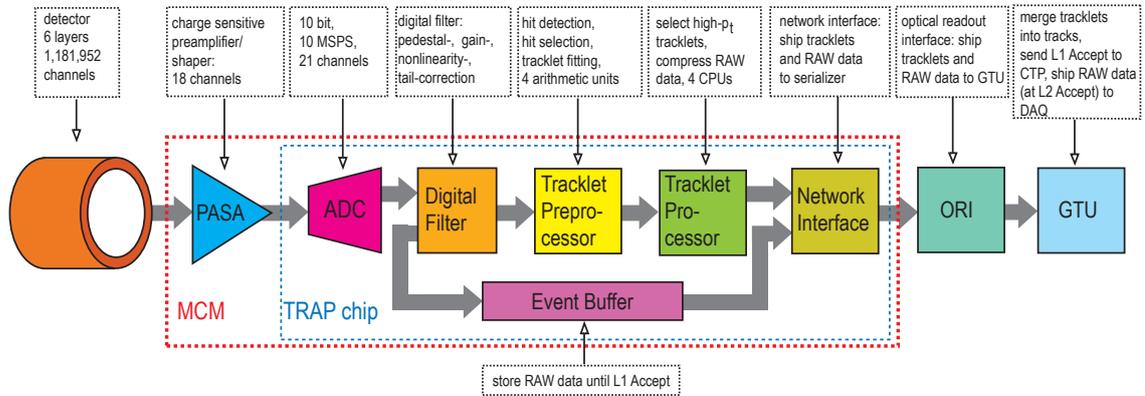
Figure 4.14: Schematic overview of the readout electronics [Aam08].

The PASA chip [Ang06] amplifies and shapes the analog signals of 18 readout pads. It has 18 input channels, corresponding to the 18 pads, and 21 output channels. The channels on the boundaries (one on one side and two on the other) are not connected to the actual TRAP but with the neighboring ones. This allows continuous charge sharing across the boundaries of one MCM [Aam08].

The TRAP chip [Ang05] performs analog-to-digital conversion, digital filtering and preprocessing, online tracking, data formatting and data shipping. Its ADCs converts the charge signal from the PASAs to 10 bits at a rate of 10 MHz. The digital signal processing is performed in two steps. During the drift time the signal is digitally filtered and corrected. This process includes non-linearity correction, gain correction, pedestal subtraction, tail cancellation and cross-talk correction. After the filtering process, the data is stored in the event buffer and is shipped via the Network Interface to the ORIs following a positive trigger decision. In parallel, the data is further processed. The hit detection units of the Tracklet Preprocessor select clusters if they satisfy certain adjustable conditions [Ang06]. The position of the clusters, the slope of a tracklet candidate and the deposited charge in two time slices are calculated. A straight line fit is performed and the fit parameters are shipped to the Tracklet Processor (see Figure 4.14). When all data of one event is accumulated and preprocessed, the CPUs of the Tracklet Processor check whether the tracklets fulfill some programmable constraints, such as slope, fit quality, and electron probability [MP08]. Finally the tracklet information is stored in a 32-bit word and is subsequently shipped via the Network Interface to the ORIs.

Each ORI collects the data (online tracklets and raw data) of a half chamber and sends it with 2.5 Gb/s to the GTU. The GTU consists of 90 Track Matching Units (TMU). Each TMU collects the data of one TRD stack and matches the tracklets of different layers to form one track. Subsequently, the transverse momentum of the track can be determined.

In case given conditions are fulfilled a positive trigger signal is sent to the Central Trigger Processor (CTP) about $6.5\,\mu$s after the event has occured [dC03]. The trigger signal is sent in case a given number of tracks exceeding a certain transverse momentum or a particle with a large probability to be an electron is measured.

The readout electronics of the Transition Radiation Detector is usually in a standby state. It needs a pre-trigger signal to wake up and be ready for the read out. This signal is provided by V0, T0 and the Time-of-Flight Detector [Aam08].

4.4   The TRD Reconstruction Code

In the TRD part of the software, classes are implemented for the simulation of the detector, for the reconstruction, its calibration, and alignment. In this section only those parts of the code are discussed which affect the particle identification in the TRD.

The particle identification capability of the Transition Radiation Detector is strongly correlated with the track reconstruction (tracking). The first step during the reconstruction is the cluster reconstruction (clusterization) based on the digital signal coming from the Transition Radiation Detector. This signal is not the pure signal as generated in the detector, but the signal after the digital filtering which is performed by the readout electronics online during the data taking (see Section 4.3.3).

4.4.1   Pad Response and Position Reconstruction

As described in Section 4.3.2 electron avalanches are accelerated in direction of the anode wires and induce an electric charge on the readout pads. The best position resolution is reached when the charge is distributed over two or three adjacent pads [TRD01]. The *pad response function* describes the fraction of the total signal on a pad for different distances between a point-like avalanche and the pad center. The pad response function $P(y)$ can be calculated by the integration of the *cathode charge distribution* $\rho(y)$ [Blu08]:

$$P(y) = \int_{y-W/2}^{y+W/2} \rho\left(y'\right) dy', \tag{4.13}$$

where y is the distance between the pad center and the actual position of the track in units of pad size. An empirical formula for the cathode charge distribution was presented by *Gatti et al.* [Gat79]. It was shown by *Mathieson* that the distribution depends solely on one parameter given by the chamber geometry [Mat84]. It is possible to determine the position of a cluster due to charge sharing using the pad response function very precisely. For the ALICE TRD the measured position resolution is better than $300\,\mu$m [Adl05b].
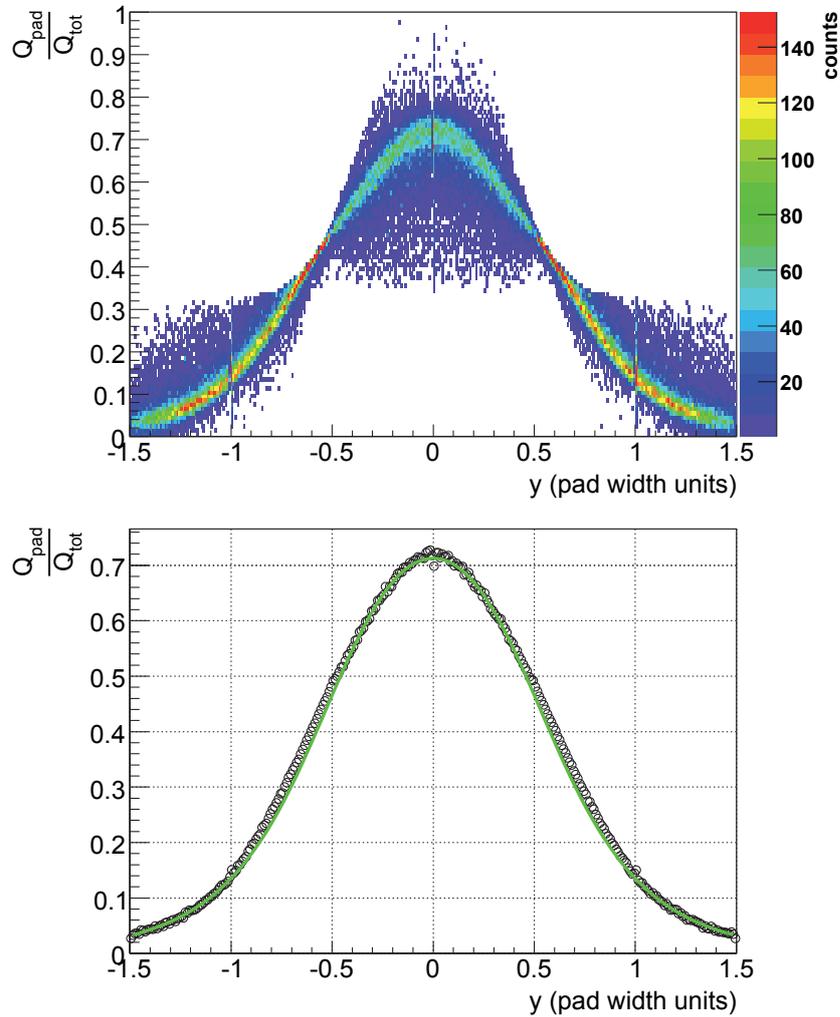
Figure 4.15: Pad Response Function measured with cosmic rays in Münster. The upper plot shows the ratio of pad charge to the total amount of charge versus the distance of the cluster to the pad center. The lower plot shows the measured pad response function (dark dots) and a fit using the Mathieson parametrization [Wul09].

In Figure 4.15 the measured pad response function of a TRD chamber with a pad width of 6.95 mm is shown. Data from a run with cosmic rays taken in Münster were used. The upper plot shows the ratio of pad charge to the total amount of charge versus the distance of the cluster to the pad center for 10^6 events. The distance between cluster and pad center is calculated assuming three pad clusters and a Gaussian shape for the pad response function. The lower plot shows the calculated pad response function (dark dots)
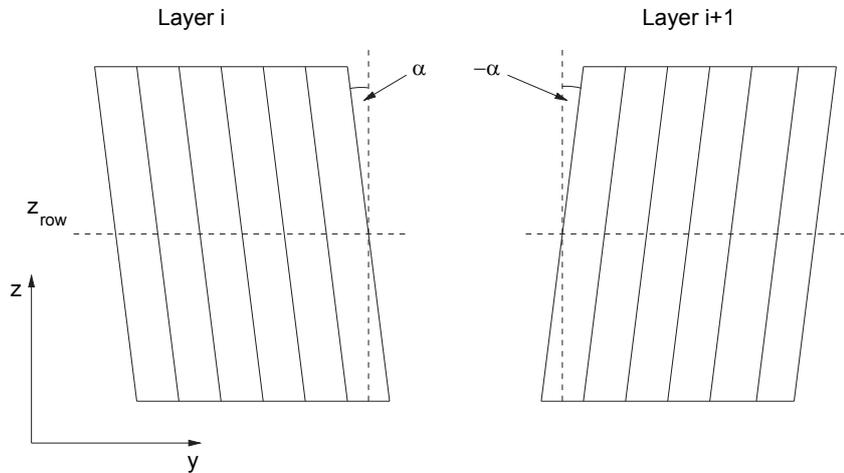
Figure 4.16: In order to improve the position resolution in direction of the long side of the pads (z direction) the readout pads are tilted by an angle α. The direction of the tilt angle is changed in consecutive layers [TRD01].

together with a fit of Formula (4.13) (green line) using the parametrization by Mathieson. Usually the Mathieson parameter is fixed and given by the chamber geometry. For this measurement a variation of the parameter reproduces the measured pad response function with a better accuracy than its calculation with the parameter that is given by the chamber geometry [Wul09].

The longer side of the pads in the TRD chambers is parallel to the beam axis and perpendicular to the bending plane of the magnetic field. The pad width ($y \approx 7\,\text{mm}$) is small compared to its length ($z \approx 85\,\text{mm}$). While most of the clusters induce charge on two, three, or more pads in the y direction, most of the clusters in the z direction lead to an induced signal on only one pad. Since the position resolution depends on charge sharing on adjacent pads, one pad clusters result in a position resolution of:

$$\sigma = \frac{w}{\sqrt{12}}, \tag{4.14}$$

where w is the pad width (or length). In order to improve the resolution in the z direction the readout pads are tilted by an angle α with respect to the z axis. The direction of the tilt angle is changed in consecutive layers [TRD01]. In Figure 4.16 the geometry of the tilted pads is shown. Apart from the improved resolution in z direction, the tilted pads also affect the position reconstruction in y direction. The reconstructed y coordinate depends directly on the z coordinate. This has to be taken into account in the reconstruction of the cluster position.
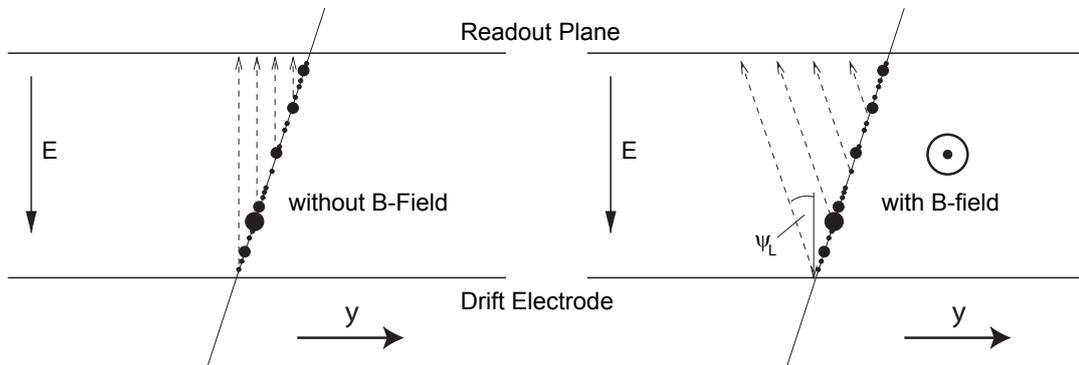
Figure 4.17: The electron clusters in an environment without magnetic field drift directly to the readout plane. In a magnetic field they are deflected in y direction. The deflection angle ψ_L is called Lorentz angle [TRD01].

———————

A further correction of the cluster position has to be made if the magnetic field in ALICE is turned on. The generated electron clusters drift towards of the amplification region, but are deflected by the magnetic field. The deflection is illustrated in Figure 4.17. The deflection angle ψ_L is called *Lorentz angle*.

4.4.2 Time Response and Tail Cancellation

Although the *time response function* (TRF) and the *tail cancellation* are not part of the reconstruction code, they will be discussed here, since they have a significant influence on the position resolution. The time response function characterizes the time dependent detector response. An ideal time response would be a δ-peak. Since the signal on the readout pads is induced by ions with a mobility much smaller than the mobility of electrons, the signal has a long tail towards longer drift times [TRD01]. In the upper part of Figure 4.18 a simulation of the induced current is shown. The *ion tail* leads to a time-dependent asymmetry in the induced charge. The resulting time response function is a convolution of the induced charge and the response of the preamplifier/shaper (PASA, see Section 4.3.3). It is shown in the lower part of Figure 4.18.

The long tail of the time response function leads to a significant correlation of the signal in subsequent time bins. In addition, for inclined tracks, the reconstructed clusters are broadened and their reconstructed position is shifted to smaller angles. The tail of
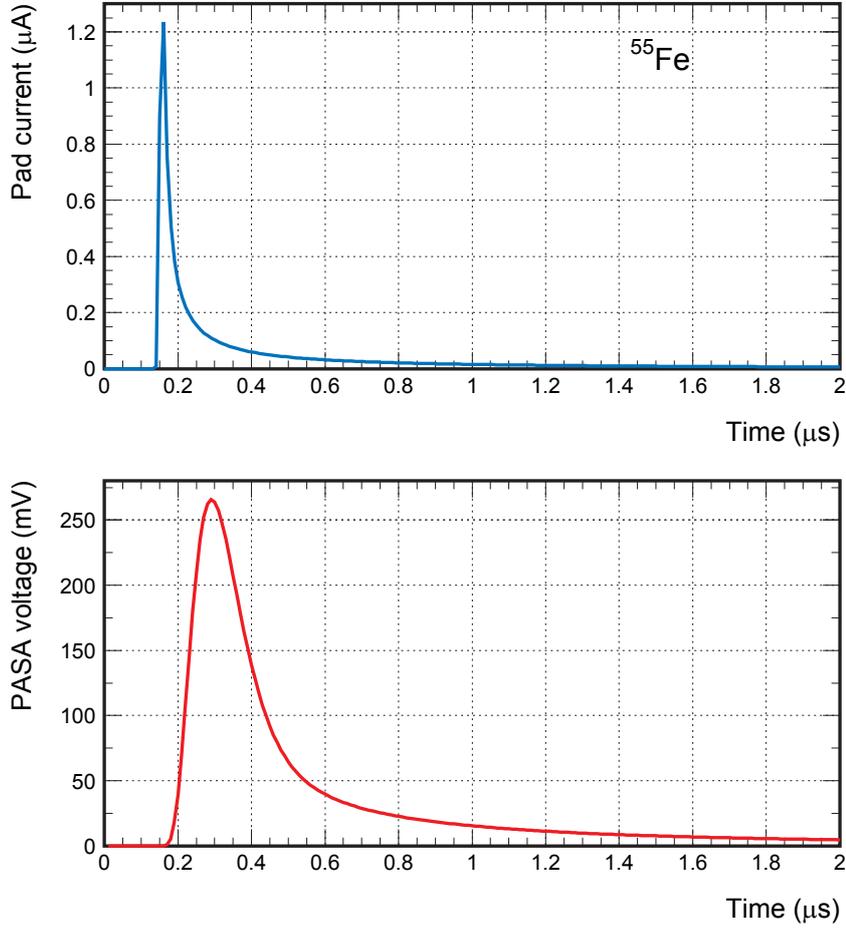
Figure 4.18: The current induced on the readout pads (upper plot) and the electronic response (lower plot), which is the Time Response Function [TRD01].

the time response function can be approximated by a sum of exponential functions. The signal $S(t)$ for $t > 0$ is then given by [Ang05]:

$$S(t) = \sum_{n=1}^{N} \alpha_n e^{-t/\tau_n} + R_N(t).$$ (4.15)

$R_N(t)$ is a residual term which is not described by the exponential functions. Usually this term is small and can be ignored. τ_n are the time constants and the α_n are the amplitudes of the exponential functions. The recursive tail cancellation filter for a time bin t_i is given by [Gut06]:

$$O_{Tail}(t_i) = I_{Tail}(t_i) - \sum_{n=1}^{N} r_n(t_i),$$ (4.16)
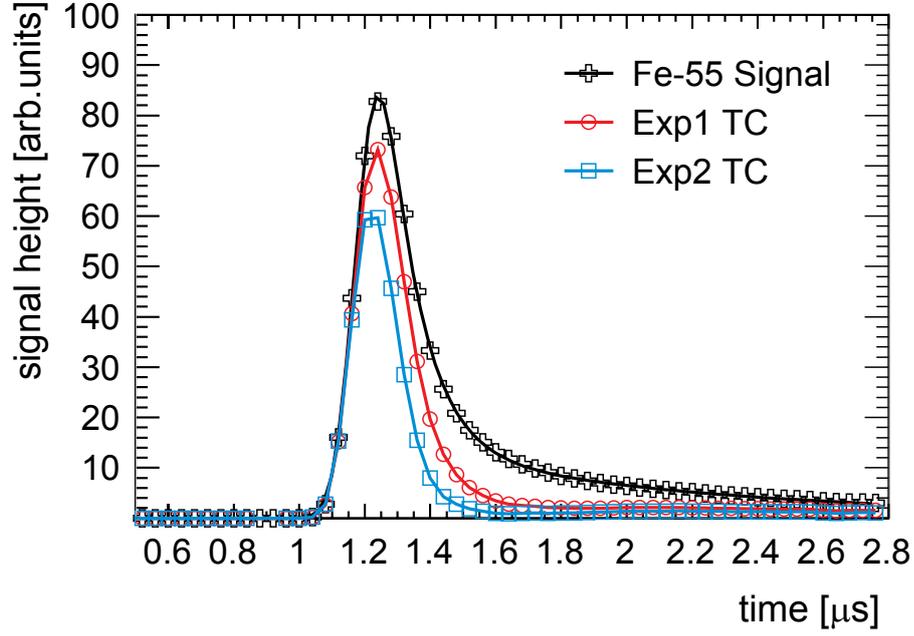
Figure 4.19: Time Response Function measured with an ^{55}Fe source in black. The effect of tail cancellation can be seen in red and blue. The blue curve shows the resulting time response for a tail cancellation with two exponential functions. The red curve shows the time response if only the long time component is suppressed [Adl05b].

––––––––––

with

$$r_n(t_i) = \lambda_n \left(r_n(t_{i-1}) + \alpha_n O_{Tail}(t_{i-1}) \right), \tag{4.17}$$

and

$$\lambda_n = e^{-\frac{1}{T_n}t}. \tag{4.18}$$

I_{Tail} is the input signal for the filter and O_{Tail} is the output signal.

The time response function of the Transition Radiation Detector can be described with two characteristic decay times T_{short} and T_{long} [Gut02]. In Figure 4.19 the effect of the tail cancellation can be seen. The measurement was made with x-ray photons of an ^{55}Fe source, small prototype chambers (see Section 7.1.1) and a prototype of the PASA [Adl05b][8]. The black curve corresponds to the signal from the PASA without tail cancellation, the red one suppresses only the exponential function with the larger time constant (EXP1 TC), and the blue one shows the signal after tail cancellation with two exponentials (EXP2 TC). The filter using one exponential shows a significant reduction of

––––––––––––––––––––––––––

[8]It has to be noted that in this measurement the number of time bins was 60 instead of 30, which is the number that is used in the electronic readout.
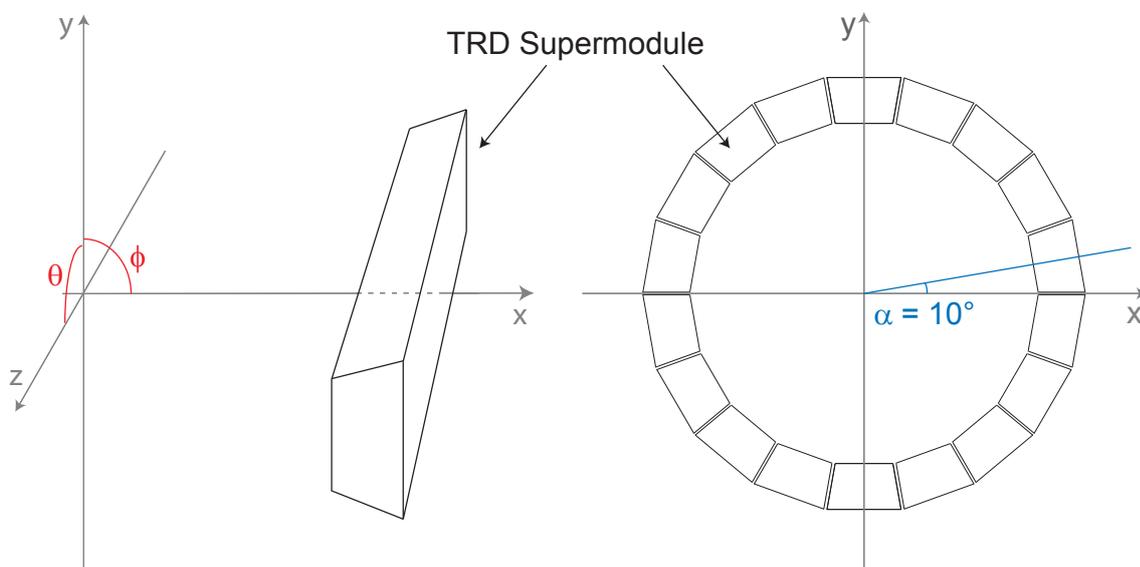
Figure 4.20: Local coordinates of a TRD supermodule. The *z* axis and the origin are identical to the global coordinate system in ALICE. Local *x* and local *y* can be transformed to the global variables by rotation using the angle α.

the ion tail. At the same time it leads to a reduction of the maximum amplitude by about 10%. An almost full tail cancellation is achieved if two exponential functions are taken into account. However, the reduction around the maximum amplitude is about 30%. This leads to a reduced signal-to-noise ratio.

The tail cancellation can be applied online using the digital filters implemented in the readout electronics or offline in the reconstruction. In the current AliRoot version (v4-17-Rev-10) the tail cancellation is done in the reconstruction using one exponential function [Alia].

4.4.3   Track Finding in the Transition Radiation Detector

In the reconstruction code of the Transition Radiation Detector it is possible to switch between two different track finding approaches. The first is part of the global track reconstruction. Here, the tracks coming from the Time Projection Chamber are propagated through the TRD in the direction of the Time-Of-Flight detector. This is called *barrel tracking*, since the detectors of the barrel part of ALICE are involved. The second one is a stand-alone tracking, which works solely on the reconstructed clusters in the TRD and does not take into account the other detectors [Fas08].

The barrel tracking is based on the *Kalman filter* method [Bil84]. It is applicable when a "system" (in this context a particle track) is determined by a state vector x_k at each step k [Ale06]. Each state vector needs an associated covariance matrix which describes the uncertainties of the vector elements. Given the case that x_k can be described with a deterministic transfer function $f(x_{k-1})$, it is possible to make a prediction for the value of the state vector at each step, if a "seed" as a starting point is available. If an estimate of the state vector is available, it is combined with the prediction and the prediction is subsequently updated. These steps are repeated for each measured state vector. With each step the accuracy of the prediction for the state vector increases [Ale06].

In ALICE the state vector of a track is given by five parameters: y, z, $\sin\phi(p)$, $\tan\lambda$, and $1/p_T$. y and z are the position, and $\phi(p)$ the azimuthal angle of the momentum in local coordinates of a sub-detector, e.g. of a TRD supermodule. $\lambda (= 90° - \theta)$ is the local dip angle and p_T is the transverse momentum. The local coordinate system of a supermodule is plotted in Figure 4.20. The origin of the local coordinate system and the z axis correspond to that of the global coordinate system. The position in the global coordinate system can be determined easily by a rotation using the rotation angle α. The local coordinate system allows to treat all tracks with the same tracking procedure in the Transition Radiation Detector, independent of which supermodule is hit. For the Kalman filter based tracking in the TRD the outermost track references of the Time Projection Chamber are used as seeds. The measured track points are in case of the Transition Radiation Detector so called tracklets [Fas08]. Tracklets are linear fits to the cluster positions attached to one track in one TRD module [Ber08c].

Tracklets are also the entities which are used for particle identification. At the moment two different methods for particle identification exist in the TRD module of AliRoot. Depending on the chosen PID method the tracklets contain three or eight measurements of the deposited charge divided by the tracklet length. The particle identification using the Transition Radiation Detector will be discussed in detail in the following chapter, Chapter 6.

The local tracking method (also called *stand-alone* tracking) fits a track model to the clusters [Fas08]. In the *x-z* plane this is a linear parametrization, while in the *x-y* plane (the bending plane of the magnetic field) a *Riemann* parametrization for a circle is used. The Riemann parametrization is given by [Ber08c]:

$$(x - x_0)^2 + (y - y_0)^2 = R. \tag{4.19}$$

A detailed description of the stand-alone tracking can be found in Reference [Sic09].

Both tracking methods have different advantages. The Kalman filtering allows to take energy loss or multiple scattering into account by adjusting the track parameters. A stand-

alone track model has to deal with constant track parameters. The barrel tracking with variable tracking parameters lead to higher accuracy of the offline track reconstruction compared to the stand-alone tracking [Fas08]. However, the stand-alone tracking is able to reconstruct tracks even if no seed (or track) in the Time Projection Chamber is available. This can be the case if a photon conversion happens in the material between the TPC and the Transition Radiation Detector, or if the TRD is the only detector that is considered. E.g. the reconstruction of the test beam data in 2007 was performed using the stand-alone tracking (see also Section 7.5).

5. Artificial Neural Networks

Charged particles produce characteristic patterns when they traverse the Transition Radiation Detector. These patterns differ for different particle types in several ways (see Section 6.1). It is possible to distinguish these patterns with conventional methods (Section 6.2), but the most effective procedure is the discrimination using artificial neural networks (Section 6.3). After a short introduction, the theoretical background of artificial neural networks, their application in high-energy physics, and the specific implementation in Root will be presented in this chapter.

5.1   Introduction to Artificial Neural Networks

Nowadays, computers are able to process large amounts of data and perform complicated calculations in a small amount of time. No human being is able to compete in these tasks against a machine. However, there are some tasks which are better performed by humans. This is the case when no strict algorithm is able to execute the given challenge perfectly. Examples for this are the recognition of human faces, reading hand writings, or driving a car. The essential qualification to perform these tasks successfully is the ability of adaption. Artificial neural networks try to combine the capability of adaption and the ability of learning with the performance of computers. This is done by simulating a system of biological neurons.

The first concept of an artificial neuron was presented in 1943 by *McCulloch* and *Pitts* [McC43]. It was shown that even simple types of artificial neural networks could in principle compute any arithmetic or logical function. Their model, the *McCulloch-Pitts Neuron*, is the origin of neuron models which are used today. An important invention concerning the artificial synapses was made in 1949. *Hebb* proposed a specific learning law for the synapses of a neuron [Heb49]: In case two connected neurons are active the weight of the connection should be increased. Hebb's learning law is the basis for today's learning algorithms. In 1957 *Rosenblatt* invented the *perceptron* (or feedforward network) [Ros58] and proved that a perceptron can distinguish linearly separable classes in a finite number of training loops, independently of the starting point. The perceptron will be presented in more detail in Section 5.3. The last important invention that is used in this thesis is the *backpropagation* algorithm. Originally it was invented by *Werbos* in

1974 [Wer74], but it became popular through its reinvention by *Rummehart*, *Hinton*, and *Williams* in 1986 [Rum86]. Backpropagation will be discussed in detail in Section 5.4.

Artificial neural networks are used in many different areas. Typical applications are function approximation, classification, optimization, and robotics. The working scheme of a neural network follows the same principle for all cases and all network types: an input vector is transformed by the neural network into an output vector. The input vector and the output vector can have different dimensionality.

Neural networks are composed of a number of small entities called neurons. These neurons are small processors whose abilities are limited to simple calculations, e.g. the summation of weighted input data. The connection between the neurons are the synapses. Each synapse has its own weight. The output of the network using a given input vector can be adjusted by changing the weights of the synapses. In order to use an artificial neural network properly the following components are needed:

- a suitable network with a suitable topology,

- a suitable learning algorithm,

- training data,

- validation data for testing the network with unknown patterns.

The most important features of artificial neural networks are [Sch97]:

- Learning aptitude: Artificial neural networks are able to "learn" which output vector is associated with which input vector. They are able to reproduce the correct output vectors.

- Fault tolerance: Neural networks are fault-tolerant to the blackout of parts of the network.

- Speed: The transformation of an input vector into an output vector can be processed quickly. However, the training of the network may take some time.

- Robustness: Artificial neural networks are able to process noisy data.

- Generalization aptitude: They are able to assign unknown patterns to the correct output vector.
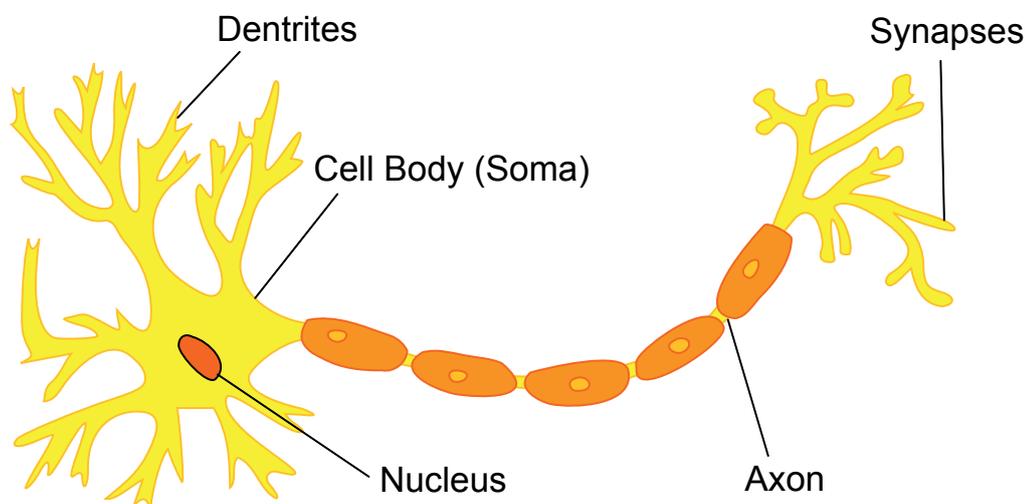
Figure 5.1: Schematical view of a biological neuron. A neuron consists of a cell body including a nucleus (soma), dentrites, an axon, and synapses. The plot is adapted from Reference [Wik10]

Although artificial neural networks have been successfully applied to several tasks, not every problem is optimal to be solved by them. Neural networks have the big disadvantage, that they behave like black boxes. Due to their highly non-linear character it is not possible to analyze which factor leads to a successful or non-successful performance. Consequently, neural networks can be used as a tool but are not well suited for an analytical approach. More about artificial neural networks can be found in References [HN90, Sch97, Lip06].

5.2 Biological and Artificial Neurons

The human brain consists of $10^{10} - 10^{12}$ neurons [Wil88]. Each neuron is made of a cell body (soma) including a nucleus, dendrites, an axon, and synapses (see Figure 5.1). The dendrites transmit the input from the synapses of other cells to the soma. The soma collects the input and, if a threshold is exceeded, generates an output signal. The output signal is sent to the axon. The axon branches and conducts the signal to other neurons. This happens at the end caps of the axon branches, called synapses. They transform the electric signal in an electrochemical one. It is propagated to other neurons via neurotransmitters. Signal transfer is not the only task of the synapses. They are also responsible for the signal's amplitude. The synapses can either amplify or dampen the signal.
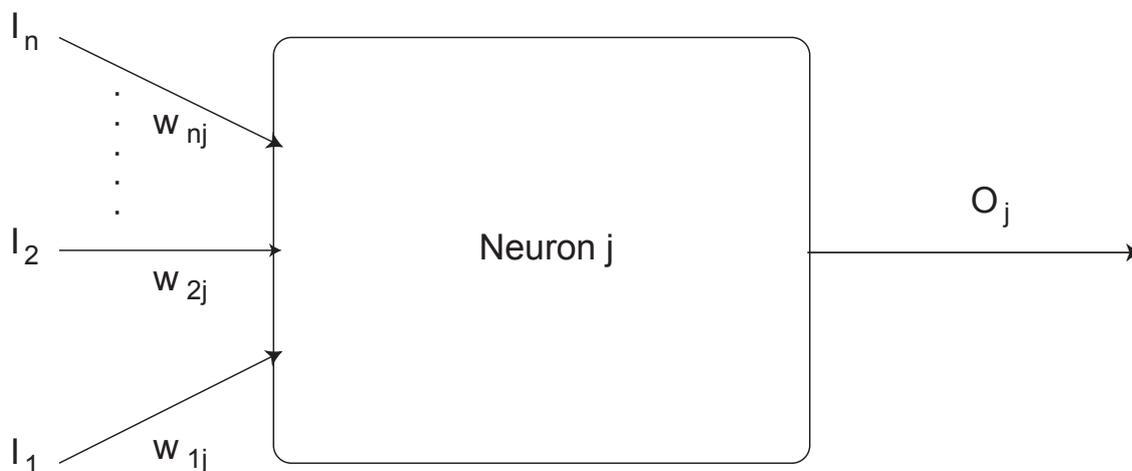
Figure 5.2: Schematical view of an artificial neuron. Input signals I_n are multiplied with associated weights w_{ij} and are transformed by an artificial neuron j into an output O_j.

Artificial neurons are constructed alike the biological model (see Figure 5.2). Input signals I_n are propagated to the neuron j. The signals are amplified or damped by multiplication with an associated weight w_{ij}. They are further processed by the neuron j using a propagation function. A typical propagation function is the addition of weighted signals. Other examples of propagation functions are the usage of the maximum, the minimum, or a multiplication of the weighted signals. The activation function determines the output that is transferred to the following neurons. Commonly used activation functions are the identity function, threshold functions, sigmoid functions, or the softmax function. Sometimes an additional threshold (called *bias*) is used, which can be adjusted for each neuron. This bias results in a shift of the function with respect to the *input* axis. In this work a sigmoid function including a bias is used as activation function for the hidden layer neurons [Roo]. The output of a hidden neuron is:

$$O_j(t+1) = \frac{1}{1 + e^{-\left(\sum_i w_{ij} O_i(t) - \theta_j\right)}}. \tag{5.1}$$

$O_j(t+1)$ is the output of neuron j at time $t+1$. "Time" is equivalent to a certain step in the calculation of a network. w_{ij} are the weights of the connections between neurons i and j, $O_i(t)$ is the output of neuron i at time t and θ_j is the bias of neuron j. The function is plotted in Figure 5.3.

The activation function for the output layer is the softmax function:

$$O_k(t+1) = \frac{e^{\left(\sum_j w_{jk} O_j(t)\right)}}{\sum_k e^{\left(\sum_j w_{jk} O_j(t)\right)}}. \tag{5.2}$$
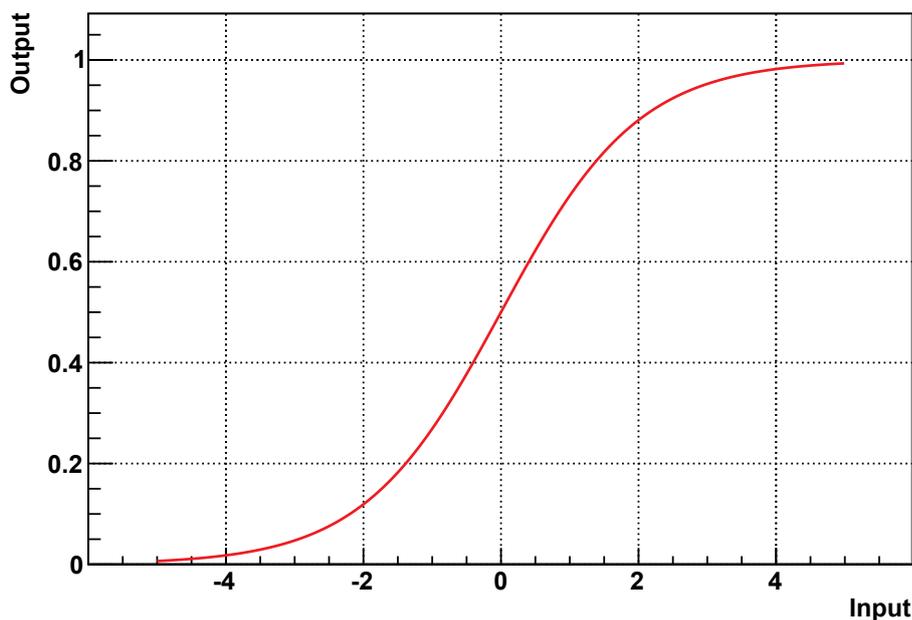
Figure 5.3: The sigmoid function.

Using the softmax function as activation function for the output layer ensures that the sum of all output neurons is unity and allows to interpret the output of a neuron as *a-posteriori* Bayesian probability [Bri90, Roo].

5.3 The Perceptron

The different network types can be subdivided into *feedforward* and *feedback* networks. Feedforward networks have a hierarchical layer structure, consisting of an input layer, an output layer, and any number of hidden layers. These types of networks are called "perceptrons". The number of hidden layers depends on the complexity of the problem and can also be zero (*single layer perceptron*).

The different layers of the perceptron are strictly separated. Connections between neurons of one layer always go from the bottom to the top, from neurons of one layer to neurons of one of the following layers. A pattern is hierarchically processed step by step from the input layer to the output layer. In case the neurons are only connected to the directly following layer, the network is a feedforward network of first order. In case some of the synapses connect neurons to layers of higher hierarchical order, the network is a feedforward network of second order.
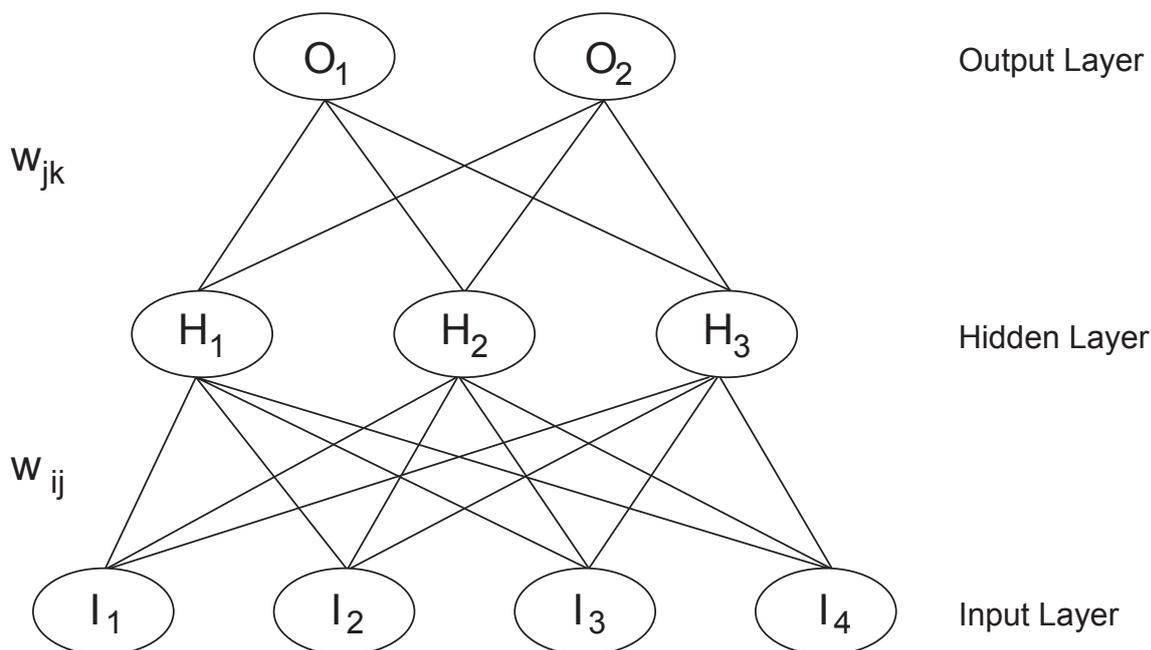
Figure 5.4: A multilayer perceptron with one hidden layer. The network consists of four input neurons I_i which are connected to three hidden neurons H_j. The network has two output neurons O_k. The weights w_{ij} belong to the connections between input neurons and hidden neurons. w_{jk} are the weights of the synapses between hidden layer and output layer.

———————

A perceptron of first order with one hidden layer is plotted in Figure 5.4. An input vector $\mathbf{I} = (I_1, I_2, I_3, I_4)$ is presented to the network via its input neurons and is multiplied by the associated weights $\mathbf{w}_{ij}$

$$\mathbf{w}_{ij} = \begin{pmatrix} w_{11} & w_{12} & w_{13} \\ w_{21} & w_{22} & w_{23} \\ w_{31} & w_{32} & w_{33} \\ w_{41} & w_{42} & w_{43} \end{pmatrix}.$$

The output of the input layer is summed in the neurons of the hidden layers h_j:

$$h_j = \sum_{i=1}^{4} w_{ij} I_i. \tag{5.3}$$

h_j is further processed by the activation function a_j. Then the output of the hidden layer neuron $H_j(I)$ is:

$$H_j(I) = a_j \left(\sum_{i=1}^{4} w_{ij} I_i \right). \tag{5.4}$$

These outputs H_j are now multiplied with weights $\mathbf{w}_{jk}$

$$\mathbf{w}_{jk} = \begin{pmatrix} w_{11} & w_{12} \\ w_{21} & w_{22} \\ w_{31} & w_{32} \end{pmatrix}$$

associated to the connections between the hidden layer and the output layer. This is summed up by the output neurons:

$$o_k = \sum_{j=1}^{3} w_{jk} H_j. \tag{5.5}$$

The output of the output layer O_k is given by:

$$O_k = a_k(o_k), \tag{5.6}$$

where a_k is the activation function of the output layer. This is not necessarily the same as for the hidden layers. For the output of a network O_k depending on the input vector $\mathbf{I}$ it is:

$$O_k(\mathbf{I}) = a_k \left(\sum_{j=1}^{3} w_{jk} a_j \left(\sum_{i=1}^{4} w_{ij} I_i \right) \right). \tag{5.7}$$

Contrary to feedforward networks, feedback networks also have synapses which connect neurons of the same layer, lead back to the same neuron, or connect neurons of a higher layer to neurons of a lower layer. A clear separation of different layers is often not possible anymore. An example of feedback networks are *Hopfield* networks [Hop82]. Feedback networks will not be discussed here, since they do not play a role in this thesis.

In order to find an optimal network it is necessary to have some experience with networks or to make some tests. Following the theorem of *Kolmogorov* [HN90], there exists an optimal network with one hidden layer and $2n + 1$ hidden neurons if the input vector is given by n values. However, there is no general rule for the determination of the weights that are associated to this network. It can happen that it takes many training cycles or it is not even possible to find the optimum weights. Therefore it is often a better strategy to use a different network topology which provides a well trained network after fewer training steps. In this thesis a neural network with two hidden layers was used. The used network topology is presented in Section 6.3.2.

5.4   Backpropagation

Backpropagation is an algorithm which allows to train multi-layer perceptrons of first order which use a continuous (e.g. a sigmoidal) activation function. Backpropagation is a gradient descent method taking into account the gradient of the error function. The network is propagated from back to front.

5.4.1   Derivation

The following derivation is adapted from References [HN90, Ott96, Sch97]. There are two variants of backpropagation, the *offline* and the *online* method. The offline method adjusts the network after all patterns were presented to the network. The method described here is the so called *online* backpropagation. This means that the weights in the network are adjusted after each pattern.

In order to estimate the success of the learning an error function is needed. Each pattern p has a target vector T_p. The target vector is the vector that should be the output of a network. The error ε_p for a given pattern is the quadratic difference between the target value of an output neuron $T_{p,k}$ and the real output of the neuron $O_{p,k}$:

$$\varepsilon_p = \frac{1}{2} \sum_k \left(T_{p,k} - O_{p,k} \right)^2.$$ (5.8)

The weights at training step s are given by w_{jk}^s. They are adjusted at the next step $s+1$:

$$w_{jk}^{s+1} = w_{jk}^s + \Delta w_{jk}.$$ (5.9)

The size of the adjustment depends on the weight's w_{ij} contribution to the error ε_p:

$$\Delta w_{jk} = -\eta \frac{\partial \varepsilon_p}{\partial w_{jk}}.$$ (5.10)

η is the learning parameter. It determines the speed of the training. The change of the error depends on the variation of the output which is calculated using the activation function a. With Equations 5.3 and 5.7 and applying the chain rule, the right side of Equation 5.10 can be written as:

$$\frac{\partial \varepsilon_p}{\partial w_{jk}} = \frac{\partial \varepsilon_p}{\partial a \left(\sum_{j'} w_{j'k} H_{p,j'} \right)} \frac{\partial a \left(\sum_{j'} w_{j'k} H_{p,j'} \right)}{\partial w_{jk}}.$$ (5.11)

$H_{p,j'}$ are the outputs of the hidden neurons n'_j for pattern p.

First we take a look at the second part of the equation. The activation function depends on all weights $w_{j'k}$ between the neurons j' and neuron k. Using again the chain rule the second part of the equation is:

$$\frac{\partial a \left(\sum_{j'} w_{j'k} H_{p,j'} \right)}{\partial w_{jk}} = \frac{\partial a \left(\sum_{j'} w_{j'k} H_{p,j'} \right)}{\partial w_{jk} H_{p,j}} \frac{\partial w_{jk} H_{p,j}}{\partial w_{jk}} \tag{5.12}$$

$$= a' \left(\sum_{j'} w_{j'k} H_{p,j'} \right) H_{p,j}. \tag{5.13}$$

a' is the derivative of the activation function.

The first part of Equation 5.11 can be written as:

$$\frac{\partial \varepsilon_p}{\partial a \left(\sum_{j'} w_{j'k} H_{p,j'} \right)} = \frac{\partial}{\partial O_{p,k}} \frac{1}{2} \left(T_{p,k} - O_{p,k} \right)^2 \tag{5.14}$$

$$= - \left(T_{p,k} - O_{p,k} \right), \tag{5.15}$$

since the error of an output neuron k is:

$$\varepsilon_p = \frac{1}{2} \left(T_{p,k} - O_{p,k} \right)^2 \tag{5.16}$$

and the activation function gives the output of neuron k $O_{p,k}$:

$$a \left(\sum_{j'} w_{j'k} H_{p,j'} \right) = O_{p,k}. \tag{5.17}$$

For a connection between a hidden neuron and an output neuron we define:

$$\delta_{p,k} = \left(T_{p,k} - O_{p,k} \right) a' \left(\sum_{j'} w_{j'k} H_{p,j'} \right). \tag{5.18}$$

The adjustment of the weight is then:

$$\Delta w_{jk} = \eta \delta_{p,k} H_{p,j}. \tag{5.19}$$

For a connection that leads to a hidden neuron j, $\delta_{p,j}$ has to be modified. Such a weight contributes not only to the error of one output neuron, but to the error of all output neurons:

$$\delta_{p,j} = \sum_k \delta_{p,k} w_{jk} \cdot a' \left(\sum_i w_{ij} H_{p,i}^{h-1} \right). \tag{5.20}$$

$H_{p,i}^{h-1}$ is the output of neuron i of the underlying layer, w_{ij} is the weight of the connection to neuron j, and w_{jk} are the weights of all connections to the neurons k of the following layer.

5.4.2 Principle of Operation

Backpropagation is an iterative procedure. The input pattern is propagated from the input neurons step-by-step towards the output layer (feed forward). In this procedure, the activations of all neurons in the network are determined. The network output is compared to the target vector. Based on the difference between target vector and output vector the contribution of each neuron to the total error is calculated. The weights are adjusted following the formulas in Section 5.4.1. The adjustment follows the steepest slope of the error function. Starting with the output layer, the δs of each weight are determined. When all of them are recalculated the δs of the previous layer are computed. The information about the output is propagated from back to front (backpropagation). A complete loop over all training patterns is called an *epoch*.

In this thesis backpropagation is used only with the *online* method, which was also described in Section 5.4.1. Here, a randomized presentation of the patterns leads to a noisy error function. This is often appreciated, since local minima can be avoided (see also Section 5.4.3). In the *offline* method all patterns are presented to the network and a global error is calculated. The network is adjusted only taking into account the mean error of all patterns after each epoch.

5.4.3 Problematic Aspects of Backpropagation

Backpropagation is a very successful strategy for the training of feedforward networks. Nevertheless, using backpropagation some aspects have to be considered (see also References [Sch97, Lip06]):

Initialization of the Weights

Before starting the training with backpropagation, the weights of the connections between the neurons have to be set to different values. Generally, this is done with a randomized initialization. In case all connections would have equal weights, the outgoing connections of one neuron to the next would stay constant, regardless of how many epochs the training is performed. The reason for this is that all the connections contribute in the same way to the error and therefore are adjusted with identical values.

Learning Parameter η

The error function can be regarded as a surface with maxima and minima. The dimensionality of the surface is that of the number of weighted connections between the neurons of the artificial neural network. The goal of backpropagation is to find the lowest point (minimum) of this surface. This is illustrated in Figure 5.5**d)**. The learning parameter η is the central variable of the backpropagation algorithm. It is crucial to choose its size such, that it is not too small and not too large. If η is too large, the learning is faster, but it is possible that the global minimum is not reached. If η is too small, it could take very long to reach the minimum. It may even be possible that the minimum is not reached at all.

Local and Global Minima   It is possible that backpropagation does not reach the global minimum but only a local one. The randomized initialization determines the starting point. It could happen that the starting point is separated from the global minimum by a "wall" (see Figure 5.5**a)**). In this case the global minimum will not be reached. In order to prevent this, the network can be trained several times using different starting points. Another possibility of reducing the probability of being trapped in a local minimum, is the application of online backpropagation (as used in this thesis). Here, the error surface is different for each pattern. This leads to a noisy error surface and potential "walls" can be overcome.

Plateaus   The size of the weight adjustment Δw_{ij} depends on the absolute value of the error surface's gradient. In case a plateau with a small slope is reached the learning gets very slow or could even stop completely, given the gradient approaches zero. This is illustrated in Figure 5.5b.
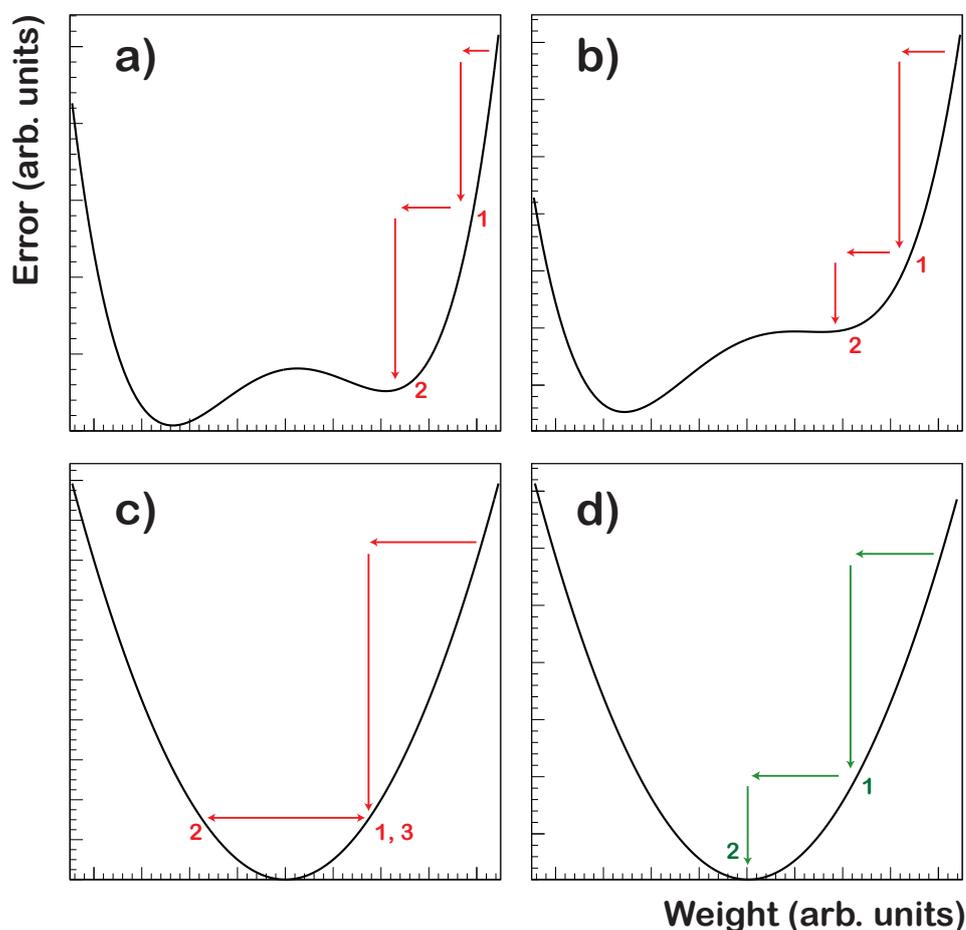
Figure 5.5: Examples of error development of the backpropagation algorithm. In each diagram the error is plotted versus the weight of one synapse. **a)**: After two steps only a local minimum is found. The learning parameter is too small to reach the global minimum. **b)**: The procedure stops at a plateau after two steps. The step size of the backpropagation algorithm depends on the gradient. In case of being zero the procedure stops. **c)**: The learning parameter is too large to reach the minimum. The algorithm oscillates between steps 1,3 and 2. **d)**: The learning parameter is optimal. The global minimum is reached after two steps.

Oscillations   In case the learning parameter η is too large another problem can occur. The walls of a valley could be so close to each other that the procedure jumps from one wall to the other and is not able to reach the minimum (see Figure 5.5c). In the worst case the steps are so large that the valley will be left and a region is reached where only local minima exist.

Backpropagation with a Momentum Term

In order to circumvent some of the mentioned problems the backpropagation algorithm can be extended. One possibility is the addition of a *momentum term*. The idea behind this is that the learning parameter η can be adjusted depending on the structure of the error surface. A relatively flat surface with a constant slope should be crossed quickly with a large η. Close to a minimum the learning parameter should be small in order to find the minimum. A momentum term takes into account the direction of a slope. At a plateau, the sign of the gradient stays constant, while it would change in a valley. In case the sign stays constant, the step width is increased by the momentum term. Given a change of the gradient's sign, the step width decreases [Lip06].

Backpropagation with a momentum term, also called *conjugate gradient descent*, can increase the learning rate a lot. However, there are cases where the procedure fails to increase the training speed or even does not converge at all. The momentum given by the procedure could be so large, that the weights are adjusted into the direction of the gradient where the error increases.

In this thesis a momentum term was not used for the training. It was found that no improvement neither for the training speed nor for the electron/pion discrimination could be achieved.

General Considerations on Backpropagation

As described before, backpropagation in the online mode (update of the weights after each pattern) leads to a smeared error surface. This is welcome since it allows to circumvent some of the problems that may occur using this algorithm in the offline mode (update of the weights after each epoch). In order to exploit this advantage it is necessary to present the patterns to the network in a randomized order. In case the patterns would be presented in the same order each time, the smearing of the error is lost and the probability for the algorithm to get stuck in a local minimum is increased. It was shown that online backpropagation converges faster than offline [LeC98].

Besides improvements concerning the training method, before starting the training a number of issues concerning the input could be taken into account which helps the network to find the optimum weights faster. In order to achieve a fast convergence of the network it is recommended to normalize the input such, that its values are between zero and one. This allows a faster learning since the derivation of the activation function is much steeper than for values larger than one. Further improvement can be achieved if the mean of the input is centered around a value of 0.5. In this thesis the input was

normalized for the training, but no improvement of the electron identification was found by centering the input. For a fast convergence of the network it is suggested to decorrelate the input variables. A decorrelation of the signal is not possible for the ALICE TRD signal (see Section 6.1). Neural networks are used in this thesis, since they are able to extract information even from correlated data. There exist several additional suggestions for improved training speed which are discussed in Reference [LeC98]. However, they do not play a role for the application of artificial neural networks for electron identification.

5.5   Training and Validation

In order to train an artificial neural network and to decide whether it is well suited to solve a given problem two data sets are needed. The first one, the *training data*, is needed to train the network, e.g. using the backpropagation algorithm. The number of training patterns should be large, ideally the number should go to infinity. The network is adjusted with the input patterns using a training algorithm. The other one, the *test data*, is needed to determine the generalization ability of a trained network. Generalization ability is the aptitude of the network to identify unknown patterns correctly.

A continuous supervision of the training is needed in order to stop it, in case the maximum generalization capability is achieved. Generally, this is done with the test patterns, but the result is slightly biased in positive direction, since a minimum error for the test patterns is then used as termination condition. It is not guaranteed that the minimum error for the test patterns indicates the best network for all possible patterns. A better test for the generalization capacity can be performed with a third data set, which is presented to the network after the training has finished. This allows a completely independent (and unbiased) generalization test. In contrast to that, no conclusion on the general performance can be obtained from a test with the patterns used for training before. The result of the generalization test would be strongly shifted towards small errors and it is only possible to determine the network's identification capability for known patterns.

Another aspect which influences the performance of an artificial neural network is the termination condition for the training. A commonly used termination condition using the online supervision is the termination of the training in case no further improvement (minimization of the error) can be achieved for training and test data, or in case *overfitting* occurs. Overfitting means that the network is adjusted too much to the training data and its generalization capability decreases with further training. Artificial neural networks with many hidden neurons tend to show overfitting. Their high dimensionality allows them to fit their weights to the smearing of the training data. Another possibility for terminating
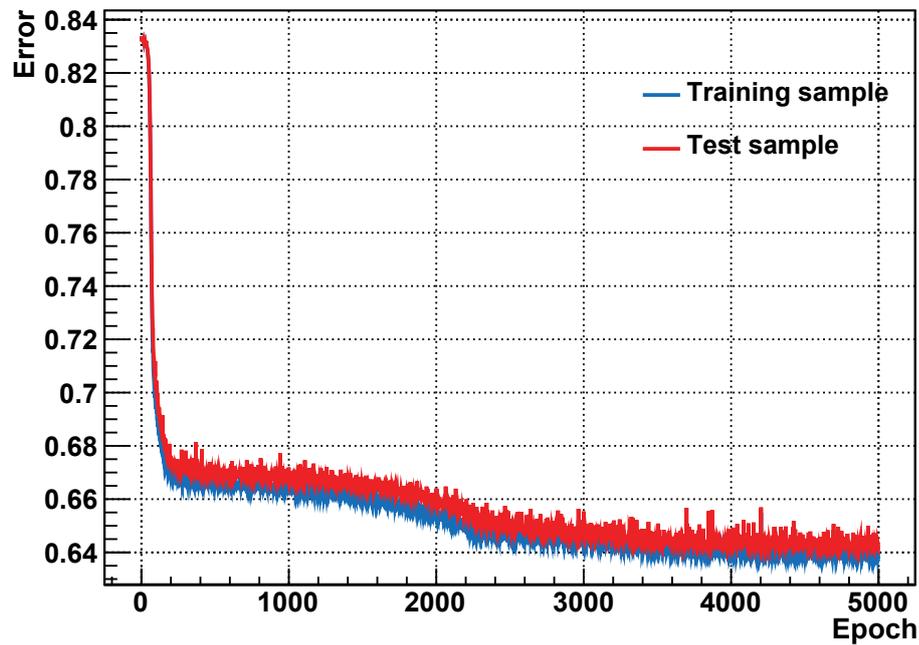
Figure 5.6: Error development of training data (blue) and validation data (red) versus number of epochs. Shown are the curves for the training of one ALICE Transition Radiation Detector prototype chamber from the test beam 2002. It can be seen that after a first fast drop the error reaches a plateau. With increasing number of training epochs the error decreases further and converges. The error curves of training data as well as that of test data fluctuates, which can be understood as noisiness of the error surface.

———————

the training is to stop it after a fixed number of epochs. This allows to compare the performance of different networks. A generalization test with the test data set here would not lead to a biased result, since it is not used for the termination condition. Instead of the conditions described above, the training could also be stopped if the error ε or the *mean square error* reaches a certain value.

In Figure 5.6 a typical training progress is shown. The error decreases fast at the beginning for both, training data (blue) and test data (red). After the first learning a plateau is reached. With rising number of epochs the error decreases again until it converges at a lower level. In case of overfitting the training curve would further decrease with increasing number of epochs, but the test curve would stay at a certain value and then rise again to larger values of ε.

5.6 Artificial Neural Networks in High Energy Physics

Artificial neural networks have been and are presently used in high energy physics. Following Reference [Den99] the applications can be subdivided into two different fields. The first field is *low level pattern recognition*. This includes particle identification tasks as well as other "simple" reconstruction tasks. The second one is *physics process determination*. This is the application of artificial neural networks to the identification of physics events. An overview (until 1999) on artificial neural networks in high energy physics can be found in Reference [Den99]. Newer applications will be discussed here shortly, excluding their application to particle identification in transition radiation detectors. This will be discussed in Section 6.3.

5.6.1 Neural Networks for Reconstruction Tasks

The main background for the identification of electrons in electromagnetic calorimeters are hadrons (mainly charged pions) with high momenta. The largest background for single photons are photon pairs originating from neutral pion decays. An important attribute that can be used for their discrimination is the shape of the shower. A shower induced by a hadron spreads wider in transverse and longitudinal direction than that induced by electrons or photons. The geometric shape, transformed into different variables, was successfully applied for particle identification using artificial neural networks. In test beam experiments for NA48 [Lit03] and ATLAS [Col05] as well as in simulations for the WA80 and WA93 electromagnetic calorimeter [Ott96] the performance of particle separation was improved compared to conventional methods.

Ring Imaging Cherenkov (RICH) detectors discriminate electrons from pions and other hadrons based on the production of Cherenkov radiation. Particles that have a velocity larger than the speed of light in a medium produce Cherenkov radiation. This radiation is emitted under a characteristic angle determined by the particle's velocity. A Ring Imaging Cherenkov detector makes use of mirrors which reflect the radiation. The reflected photons hit the active detector plane in a circle around a projection of the according track. The radius of the circle depends on the particle's velocity. For most electrons, their velocity is very close to the speed of light in vacuum. Therefore, the ring radius electrons is well known. The task is to match a reconstructed track to potential photon rings and check if the ring is formed by an electron. Artificial neural networks can be used to suppress rings which are falsely reconstructed. Examples of true and fake rings are plotted in Figure 5.7. In simulations for the Compressed Baryonic Matter (CBM)
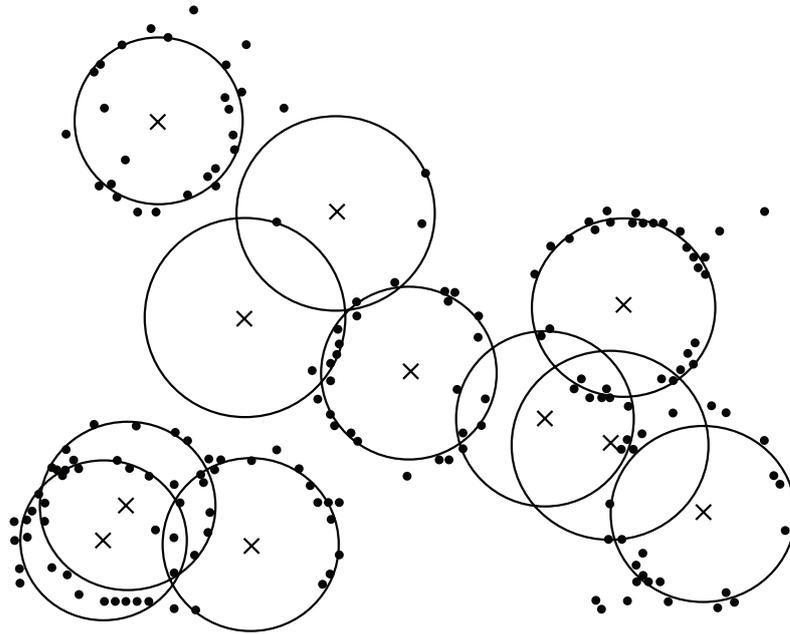
Figure 5.7: Example of true and fake Cherenkov rings. This plot is taken from [Leb09].

experiment artificial neural networks were successfully applied to fake ring suppression. They are also planned to be used in the real experiment [Hoe08, Leb09].

5.6.2 Applications in Analyses

The D0 collaboration used artificial neural networks for the direct measurement of the top quark mass [Aba97] and the search for the hypothetical leptoquarks [Abb97] at the Fermilab Tevatron accelerator. For the measurement of the top quark mass the decay of $t\bar{t}$ quark pairs into a final state of four jets, one lepton, and one neutrino ($t\bar{t} \rightarrow W^+b + W^-\bar{b} \rightarrow q\bar{q} + b + l\nu_l + \bar{b}$) was analyzed. The leptoquark pair decay channel with two jets and two electrons was investigated. For both procedures a set of (correlated) variables was defined and fed to a multilayer perceptron. The top quark mass was measured with an uncertainty of only a few percent and a lower limit for the mass of leptoquarks of $225\,\text{GeV}/c^2$ was found.

The BABAR collaboration used an artificial neural network for the measurement of CP-violation in B^0 decays [Aub01]. The networks were trained in order to tag B^0s or $\overline{B}^0$s in events where no simple tagging criterion could be applied. The input was a combination of the momentum and charge of the track with the largest center-of-mass momentum and the outputs of primary networks for particle identification. The combination of

conventional tagging criteria and neural network tagging confirmed previous *CP*-violation measurements. It improved its accuracy compared to previous results.

5.7   Neural Networks in Root

Many different software packages for the application of artificial neural networks exist. These packages allow to construct many different network types. For pattern recognition a multilayer perceptron is well suited. The software framework Root, which is the basis of the software used in ALICE, provides classes for the construction of multilayer perceptrons since version v3-10. The multilayer perceptron (TMLP) module was written by *Delaere* [Roo] and is based on the MLPfit package [Sch]. The classes used in the package are `TMultiLayerPerceptron`, `TNeuron`, and `TSynapse`.

The main class of the TMLP module is `TMultiLayerPerceptron`. Using this class all the attributes of the multilayer perceptron, such as network topology, training method, or training parameters, can be defined and adjusted. The multilayer perceptron is connected to a `TTree`. `TBranches` of this `TTree` are used as input vector and as target output vector. The network topology is set in the constructor by a single string. The only network structure that is supported are multilayer perceptrons of first order, i.e. all neurons of a lower layer are (only) connected to all neurons of an upper layer. No shortcuts are allowed and no recursive connections are available. In the string which describes the topology, the different layers are separated by a colon. The `TBranches` which are connected to the input and the output neurons are separated by commas. The hidden layers are defined by the number of neurons only. An example for the initialization of a `TMultiLayerPerceptron` with two input neurons, five neurons in one hidden layer, and one output neuron is given here:

`TMultiLayerPerceptron("in[0],in[1]:5:out",tIn)`.

`in[0]` and `in[1]` are two `TBranches` of the `TTree` `tIn` connected to the network. `out` is another `TBranch` of the same `TTree`.

The default `TNeuron` types for the different layers are inactive[1] neurons for the input layer, sigmoid neurons for the hidden layer, and linear neurons for the output layer. In order to get the Bayesian probabilities it is possible to change the neuron type of the output layer by adding an exclamation mark at the end of the network topology string. This converts the output neuron into a sigmoid `TNeuron` in case only one output neuron is used. In case more output neurons are in the output layer they are converted into softmax

---

[1]"Inactive" means that the neuron just returns the input.

neurons. In this thesis softmax neurons are used in the output layer. All `TNeurons` of a lower layer are connected with the `TNeurons` of the next higher layer via `TSynapses`.

It is possible to define the training data and test data with `TEventLists`. The two `TEventLists` contain the entries of the `TTree` which are used for training and testing. They can either be connected to the network directly in the constructor or added afterwards using a dedicated setter. In the following analyses 2/3 of the data was used as training data and 1/3 for validation.

The TMLP module provides different training methods. In this thesis online backpropagation is used which corresponds to the `TMultiLayerPerceptron::kStochastic` training method. Using this method, the weights of the synapses are initialized with random values. The patterns are presented to the network in randomized order. The only variable for this method is the learning parameter η. It can be adjusted using the function `TMultiLayerPerceptron::SetEta(Double_t eta)`. The training is started with

`TMultiLayerPerceptron::Train(Int_t nEpoch, Option_t).`

`nEpoch` is the number of epochs that should be trained. In addition, several options can be added. It is possible to monitor the error development graphically and/or in a text. In addition, it is possible to skip the random initialization of the weights at the start of the training by adding a plus sign. This allows to save trained networks and to continue the training later on.

6. Particle Identification with the Transition Radiation Detector

One of the main tasks of the Transition Radiation Detector is the identification of electrons in a very pion-rich environment. In this Chapter the principles and methods which can be used for the electron/pion separation are discussed. The last section describes the implementation of TRD's particle identification in AliRoot.

6.1 Principles of PID using the TRD

The key to access the particle identification (PID) capabilities of the ALICE Transition Radiation Detector is the information on the average pulse height and its dependence on the drift time (shown in Figure 6.1). There are two obvious differences between the data points for pions and for electrons. The first one is the total amount of deposited charge. At a momentum of $2\,\text{GeV}/c$ the amplitude of the electron signal is about 1.5 times larger than that of pions in the amplification region and about twice as large in the region where transition radiation photons are absorbed preferably. The total amount of deposited
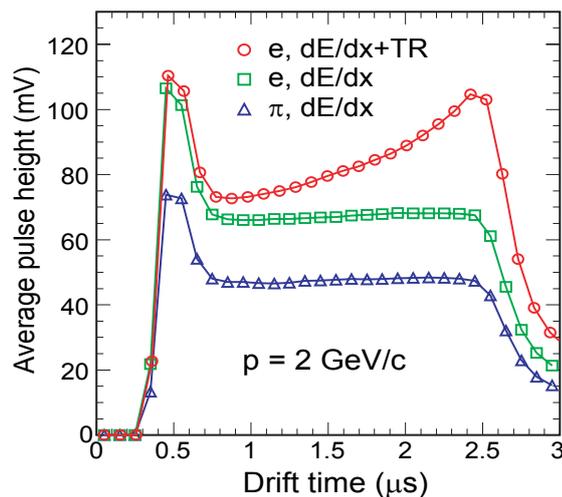
Figure 6.1: The average pulse height in the Transition Radiation Detector for electrons (with and without transition radiation) and pions [Aam08].
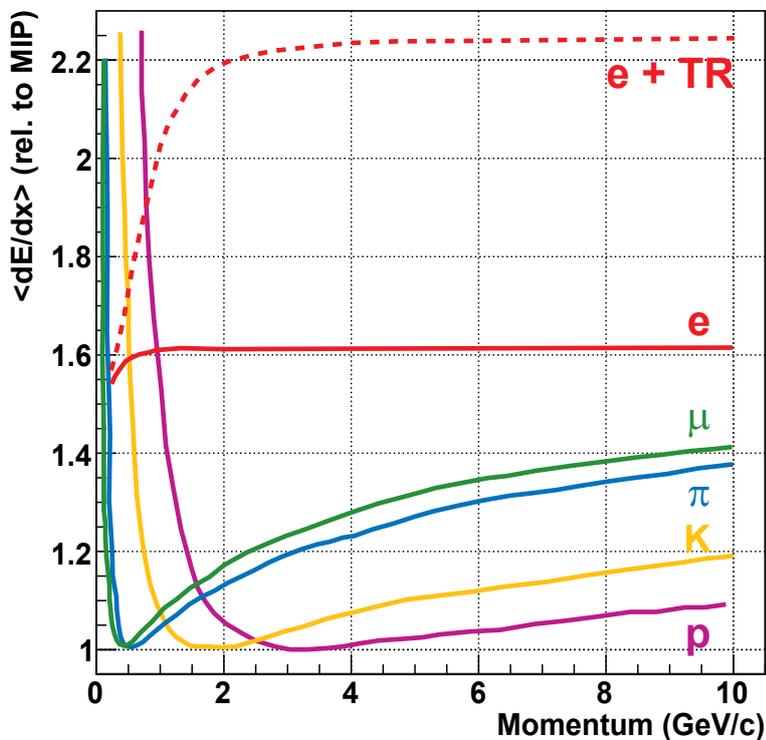
Figure 6.2: The average deposited charge of electrons (with (red dashed line) and without transition radiation (red solid line)), muons (green), pions (blue), kaons (orange), and protons (purple) [And09b]. The deposited charge is plotted relative to the charge deposited by a minimum ionizing particle.

---

charge is used by cluster counting methods [Lud81], by truncation methods [And01], and a likelihood method (*LQ* method) [Che74a]. LQ stands for likelihood on total charge.

The shapes of the average pulse height for particles which do not produce transition radiation (hadrons and muons) are similar to that of pions. They only differ in amplitude, due to their different charge deposit caused by their different masses (see Equation 4.1). This also allows their discrimination from electrons similar to the electron/pion discrimination. Above momenta of 1 GeV/*c* for kaons and about 1.5 GeV/*c* for protons the average deposited charge is lower than that of pions (see Figure 6.2). The difference between a kaon or proton signal compared to an electron signal is larger than that of a pion compared to an electron signal. Consequently, the separation of kaons and protons from electrons is expected to be better than that of pions above these momenta. The separation of muons from electrons will be worse for momenta above about 0.5 GeV/*c*. Figure 6.2 also shows that a discrimination of hadrons from other

hadrons is possible using information of the TRD (see Section 8.3.3). However, the separation of different hadrons is only possible with low accuracy since the expected deposited charges differ much less from each other.

The second difference between the electron and the pion signal in their average pulse height distributions is the transition radiation peak. At longer drift times the electron signal does not stay flat like the signal of the pions, but increases since the transition radiation photons are predominantly absorbed within the first few millimeters of the drift region. Consequently, the exploitation of the signal's time information increases the identification capacity of the Transition Radiation Detector. Two likelihood methods make use of the time information, the *LQX* method [And01] and *2-dim LQ* method [Ber08a]. LQX stands for likelihood on total charge and the local *x* position (which is approximately identical with a time information) of the largest cluster. The 2-dim LQ method is based on the deposited charge in two chamber regions – the region where transition radiation is expected, and the amplification region including a part of the drift region. The time information has no influence on the discrimination of hadrons from each other since they do not produce transition radiation in the momentum region below about 100 GeV/*c*. All particle identification methods described above will be discussed in the following Section 6.2.

It is not trivial to access the full information with likelihood methods, since the signal is correlated in time within one Transition Radiation Detector module. These correlations have to be taken into account. A successful approach to exploit the full information is the application of artificial neural networks as was shown in References [Wil04, Adl05a]. This method will be described in detail in Section 6.3.

The signals in the detector modules which contribute to the particle identification are assumed to be uncorrelated. Therefore, most of the particle identification methods combine the signals using the Bayesian probability of each TRD module, analogous to the approach in AliRoot for the combination of the PID signals of different subdetectors (Formula 3.4). The intrinsic detector response of the Transition Radiation Detector $R_{TRD}\left(\bar{s}|i\right)$ for a signal vector $\bar{s}$ to be generated by a particle of type i is given by:

$$R_{TRD}\left(\bar{s}|i\right) = \frac{\prod\limits_{j=1}^{N} r\left(s_j|i\right)}{\sum\limits_{k} \prod\limits_{j=1}^{N} r\left(s_j|k\right)}. \tag{6.1}$$

N is the total number of TRD modules and $r\left(s_j|i\right)$ is the response function of a single detector module j. $\bar{s}$ represents a vector of all the signals and k is the total number of
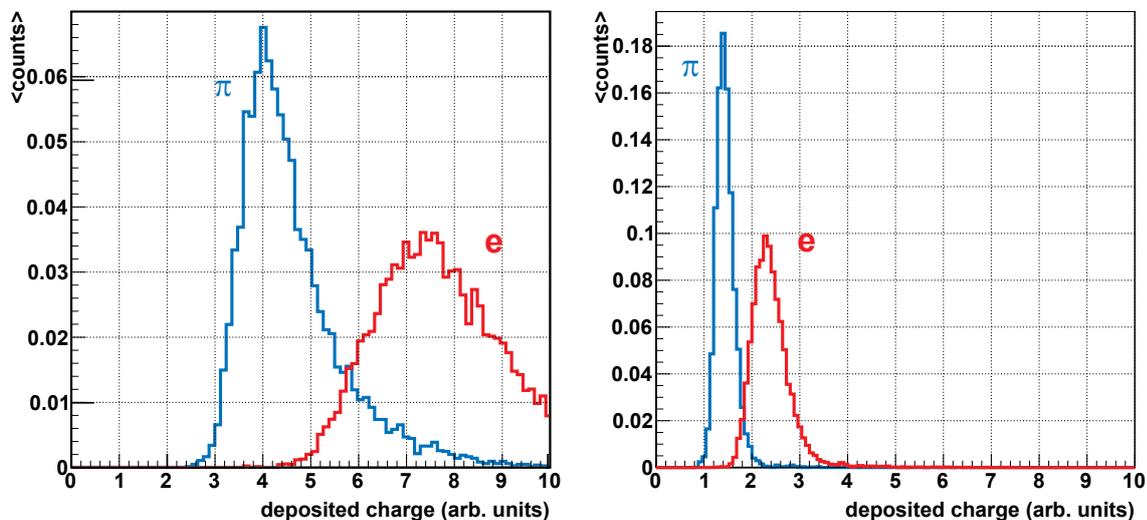
Figure 6.3: Truncated Mean for $4\,\mathrm{GeV}/c$ test beam data from 2004. On the left side the deposited charge integrated over all 6 Transition Radiation Detector layers for electrons (red) and pions (blue) are plotted. The pion signal has a long tail towards larger deposited charges. This leads to high contamination of identified electrons. If only the largest 60% of clusters with the smallest deposited charges are taken into account, the contamination decreases significantly.

particle types which are taken into account. In ALICE these are five particle species: electrons, muons, pions, kaons and protons as well as their anti-particles. In the analyses of test beam data (Chapter 7) only electrons and pions were taken into account.

A measure for the electron/pion discrimination performance of a detector is the *pion efficiency* ε_π (see Section 6.4). It is the fraction of pions that is misidentified at a fixed *electron efficiency* ε_e. The electron efficiency is the fraction of electrons that is identified correctly. In the following analyses the electron efficiency is required to be 90%. Sometimes, instead of the pion efficiency the *pion suppression* is used. This is the reciprocal of the pion efficiency. The design goal of the ALICE Transition Radiation Detector is a pion efficiency of 1%, i.e. a pion suppression of 100.

6.2 Classical Methods of Particle Identification

6.2.1 Truncated Mean

The simplest approach for particle discrimination using the ALICE Transition Radiation Detector is the integration of deposited charge along the particle track in all traversed modules. The resulting distributions of integrated charge are plotted on the left side in

Figure 6.3. The distribution for pions is shown in blue, that of electrons in red. It can be seen that the two particle types are clearly separable by this method. However, both distributions have a long tail towards large charge deposits. The main problem is the tail of the pion distribution. The tail is caused by δ electrons which produce electron clusters with high charge deposition. The idea behind the *truncated mean* method is to suppress clusters from δ electrons and thus suppress the tails of the charge deposit distributions.

For detectors of the ALICE TRD type truncation methods can be performed in two different ways. The first one uses the integrated deposited charge in all chambers. The largest value is cut and only the values of the five other deposited charges are taken into account. This method was used in References [App88, And01].

For the second truncated mean method a limited number of clusters is used. Clusters with smaller deposited charge are considered, while the larger clusters are not taken into account [Wat86, Shu05]. Here, for the Transition Radiation Detector "cluster" means charge deposit in one time bin. On the right side of Figure 6.3 the deposited charge distribution for electrons and pions is shown, where only the 60% smallest clusters are taken into account. Again, the electron distribution is shown in red, the pion distribution in blue. It can be seen that the tail of the pion distribution is not as large as in the plot without truncation. This leads to an improvement of the electron/pion discrimination by about a factor of 5 for the ALICE Transition Radiation Detector (see Section 7.6).

The truncated mean method is the standard method for particle identification in time projection chambers. It is used e.g. in the ALICE TPC [Aam08]. Truncation methods are well suited for detectors with a large homogeneous area where all clusters are of the same size, independently of their spatial position. This is not the case for the ALICE TRD. Due to the larger charge deposit at small drift times caused by the amplification region, preferably clusters from this region are suppressed. Practically, this leads to a smaller considered gas volume used for particle identification and consequently to a worse pion rejection performance. Another effect is that clusters originating from transition radiation are rejected. This cutting of TR shifts the electron distribution of deposited charge to larger values, since more of the ionization clusters pass the cut. Thus, the transition radiation improves the separation compared to a scenario without TR. However, it seems to be paradoxical to improve the particle identification by cutting the signal that is especially generated for it.

Results from previous experiments [Wat86, App88] as well as from test beam data taken with ALICE TRD prototypes show that the truncated mean method has a worse performance in electron/pion separation than likelihood methods [And01]. However, it has to be noted that data from the test beam 2004 show comparable performance for

truncated mean and for the likelihood method on deposited charge [Shu05]. This will be discussed in Section 7.6.

6.2.2   Cluster Counting

The deposited charge of TR clusters is relatively large (about 460 electrons for 8 keV photons in the ALICE TRD, see Section 4.3.2) compared to that coming from ionization (40 electrons per time bin for a minimum-ionizing particle in the ALICE TRD [TRD01]). Thus, the signal produced by a transition radiation photon is expected to be above a threshold which has to be chosen in a way, that the signals from ionization are suppressed. The basic idea of the cluster counting method is to count predominantly clusters produced by transition radiation. The cluster counting method has to deal with two challenges. The first one is that an electron does not necessarily produce transition radiation. The expected number of transition radiation photons is only around one per detector module in case of the ALICE TRD [And06b]. The second one is the tail of the Landau distribution of the deposited charge. This tail leads to a non-zero probability for pions to produce δ electrons, which could deposit as much charge as TR photons or even more. In 1981 *Ludlam et al.* showed that the cluster counting method can discriminate electrons from pions at the same level as a likelihood method on total deposited charge [Lud81]. The used detectors were of the same design as the ALICE TRD modules (a multi-wire proportional chamber with a drift region), but with a shorter drift region (10 mm).

The cluster counting method could be further improved by the implementation of an "intelligent" threshold [O'B93]. The absorption length for photons in xenon depends on the total energy of the photon. The larger the energy, the deeper the photon penetrates the gas before being absorbed. Consequently, the signal of a transition radiation photon absorbed late (i.e. at small drift times) in the chamber is larger than that of TR photons absorbed early (i.e. at large drift times). Using a threshold which is low at large drift times and high at small drift times suppresses clusters coming from δ electrons. The probability for the production of δ electrons as well as the amount of charge deposited by them does not depend on the position inside the chamber. The improvement of pion efficiency compared to the pure cluster counting is about a factor of 1.5 [O'B93].

Another approach to improve the performance of the cluster counting method is to exploit the deposited charge of the clusters, or the time the signal is above the threshold (*time-over-threshold*) [App88]. The usage of the cluster charge allows to convolute the probabilities for cluster production with that of the amount of deposited charge. The time-over-threshold method bases on the fact that high energy deposition produces a
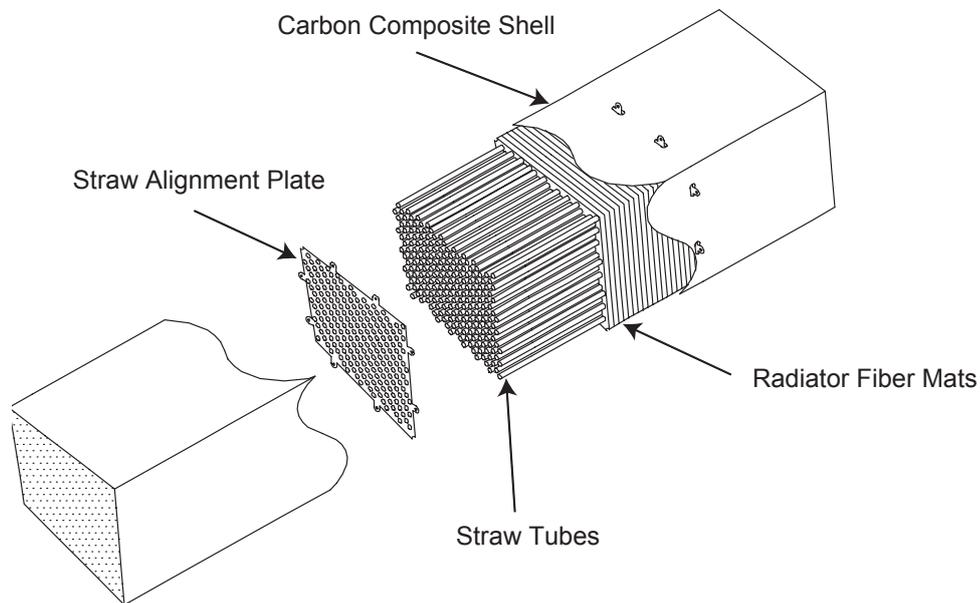
Figure 6.4: A module of the barrel part of the ATLAS Transition Radiation Tracker [Ake98]. The active detector parts is made of small proportional tubes (straw tubes). They are embedded into the radiator material. This detector is optimized for cluster counting methods.

wider electronic signal. While the deposited charge of the clusters shows a performance which is as good as the cluster counting, the time-over-threshold as a stand-alone particle identification method is not very successful. However, time-over-threshold can be used in combination with cluster counting and improves the cluster counting method by a factor of about two [Ake01].

Cluster counting methods are well suited to separate electrons and pions in detectors with many thin layers. The reason for that is the thickness of the gas layers. In thin gas layers the "background" of deposited charge by ionization fluctuates strongly. The distributions of deposited charge have long tails towards large charge deposits, for both, electrons and pions. A measurement of deposited charge would be dominated by these tails. The background of the cluster counting depends on the Poisson statistics for the production of δ electrons, which has a smaller tail than the Landau distribution [Ams08]. The probability for the production of δ electrons is larger for electrons than for pions. The clusters produced by transition radiation further enhance the number of clusters above a threshold for electrons.

An example for a detector with thin gas layers is the ATLAS Transition Radiation Tracker (TRT). It consists of many *straw tubes* which are thin proportional tubes with a diameter of 4 mm [ATL97]. The Transition Radiation Tracker is built in a barrel design
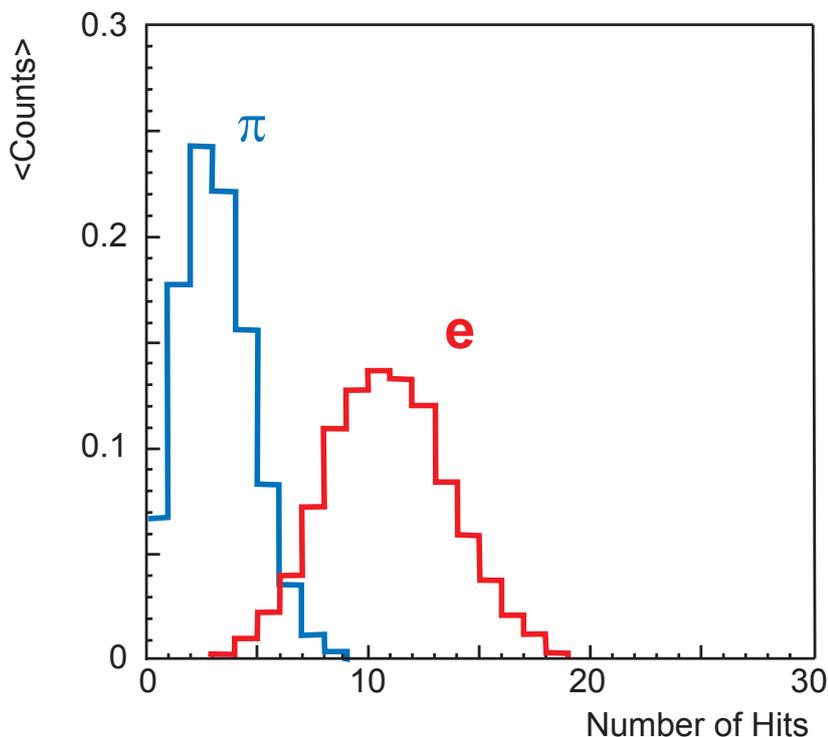
Figure 6.5: Performance of the cluster counting method in the ATLAS Transition Radiation Tracker using an energy threshold of 6 keV [Ake98]. The distribution for electrons is red, that for pions blue. It can be seen that with this method electrons and pions can be well discriminated.

including end-caps. In Figure 6.4 a TRT module of the barrel part is shown. The straw tubes in this part are 144 cm long and are embedded into the radiator material. The barrel part of the Transition Radiation Tracker consists of three rings of modules which are arranged around each other. This guarantees that each particle coming from the vertex has to traverse 36 straw tubes [Aad08].

In Figure 6.5 the number of clusters above a threshold of 6 keV is shown for electrons (red) and pions (blue) for test beam data at a momentum of 20 GeV/c. The diagram shows that the particles can be well discriminated. With the Transition Radiation Tracker a pion suppression of about 80 can be reached at 20 GeV/c using a combination of the number of clusters and the time-over-threshold [Mit03].

For the ALICE Transition Radiation Detector, methods which exploit the deposited charge show a better performance for electron/pion discrimination than cluster counting methods [ALI99]. The thicker the gas layers, the smaller are the fluctuations of charge deposition. The measurement of deposited charge is not dominated by the δ electrons

anymore. Although the probability for a particle to produce a δ electron along its track is larger compared to thin layers, the measurement of the deposited charge on a longer track compensates these fluctuations.

6.2.3 Likelihood on Total Deposited Charge (LQ)

The basic idea of likelihood methods is to interpret measured (or simulated) distributions as probability distributions. Following the Bayesian approach, these distributions can be used to estimate the likelihood for a measured value to be produced by different particle species. Examples for such distributions are e.g. the deposited charge distributions of electrons and pions. In principle the truncated mean or counted clusters can also be used as input distributions, but these methods are often applied using simple threshold cuts. In the following sections likelihoods on deposited charge will be discussed:

- likelihood on total deposited charge (LQ),

- combined likelihood on deposited charge and time bin with the largest charge deposit (LQX),

- and a two dimensional likelihood on charge in two chamber sectors (2-dim LQ).

The likelihood method on total deposited charge was first used by *Cherry et al.* [Che74a]. The input distribution for the likelihood on total charge are normalized charge distributions for electrons and pions in the Transition Radiation Detector modules. They are shown in Figure 6.6, electrons in red and pions in blue. A particle traversing the TRD ideally deposits a charge Q_j in each module j. The probability that an electron deposits this amount charge $P^j\left(Q_j|e\right)$ can be extracted from the deposited charge distribution of module j. The total probability for an electron to deposit exactly the n measured values of charge $\overline{Q}$ is then given by:

$$P\left(\overline{Q}|e\right) = \prod_{j=1}^{n} P^j\left(Q_j|e\right) = \prod_{j=1}^{n} P\left(Q_j|e\right).$$ (6.2)

With the assumption that the distribution is identical for all modules, it is $P_j\left(Q_j|e\right) = P\left(Q_j|e\right)$. This is an approximation, since the deposited charge increases with the number of traversed layers [And04a]. The differences in deposited charge between the layers are small. Hence, the chamber position often is not taken into account. The probability for
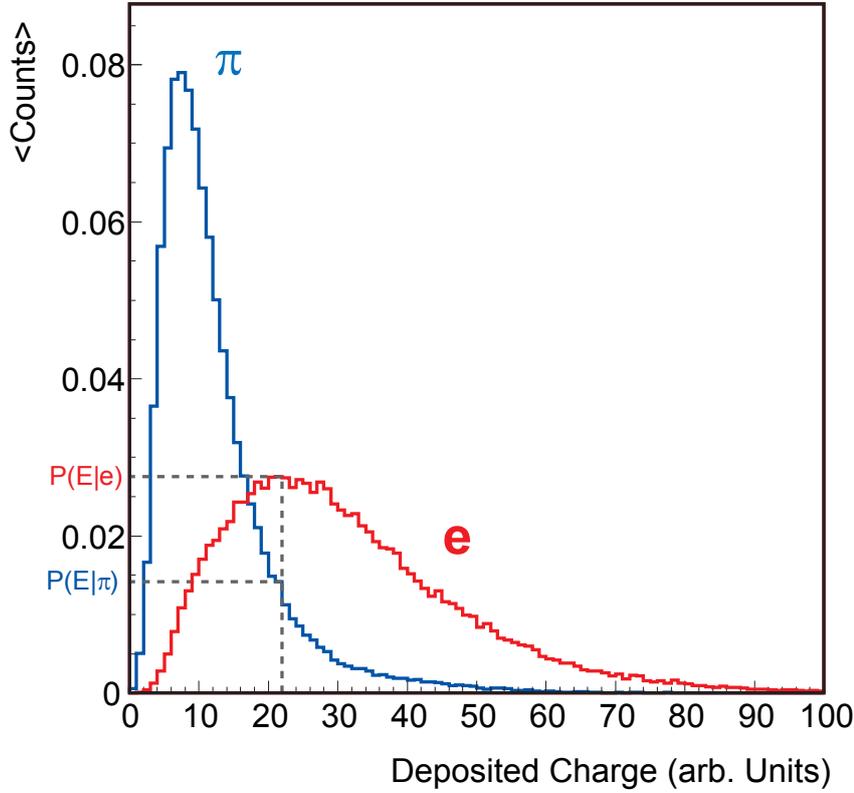
Figure 6.6: Deposited charge for electrons (red) and pions (blue) in one TRD module. This data was taken during the test beam of 2002. The momentum of the particles was $2\,\text{GeV}/c$.

another particle to deposit the charge can be calculated analogously to Equation 6.2. For pions it is:

$$P\left(\overline{Q}|\pi\right) = \prod_{j=1}^{n} P^j\left(Q_j|\pi\right) = \prod_{j=1}^{6} P\left(Q_j|\pi\right). \tag{6.3}$$

Using these probabilities it is possible to estimate the likelihood $L\left(e|\overline{Q}\right)$ that the charges $\overline{Q}$ have been deposited by an electron. In case k particles are taken into account for the likelihood calculation, it is:

$$L\left(e|\overline{Q}\right) = \frac{P\left(\overline{Q}|e\right)}{\sum\limits_{k} P\left(\overline{Q}|k\right)}, \text{ with } 0 \leq L \leq 1. \tag{6.4}$$

In test beam data k stands for electrons or pions, in the real experiment (in AliRoot) for electrons, muons, pions, kaons, or protons. The sum of all likelihoods equals unity:

$$\sum_{k} L\left(k|\overline{Q}\right) = 1. \tag{6.5}$$

The likelihood value to be a particle of type i is equivalent to the intrinsic detector response for this particular hypothesis. It is transfered to the global particle identification of ALICE (see Equations 3.2 and 6.1). Here, the vector of deposited charge $\overline{Q}$ represents the signal vector $\overline{s}$. It is:

$$R_{TRD}\left(\overline{s}|i\right) = L\left(i|\overline{Q}\right). \tag{6.6}$$

The likelihood method on total deposited charge was applied to test beam data from 2000 [And01], 2002 [And04a, Wil04], 2004 [Bai06], and 2007 [Kli09]. It was shown that with this method a pion efficiency around 1% is achievable for particles with momenta of 2 GeV/c and an electron efficiency of 90%. Since this method is well known, easy to implement, and easy to handle, the likelihood on total charge will be used in this thesis as standard method in order to compare different particle identification aproaches.

6.2.4 Likelihood on Total Deposited Charge and Time Bin with Maximum Charge Deposition (LQX)

A closer look at the average pulse height for electrons and pions in Figure 6.1 indicates that the total amount of deposited charge is not the only difference between electrons and pions. For electrons a large peak from conversion of transition radiation at large drift times is visible.

As stated before, transition radiation photons are absorbed in the first few millimeters of gas of the drift chamber. In addition, the amount of charge in transition radiation clusters is large compared to clusters originating from ionization. Consequently, for electrons the largest clusters in the drift region should be preferably found at large drift times while for pions the distribution should be flat. A combined likelihood on the total deposited charge Q and the time bin of the cluster with the largest charge deposit should increase the discrimination power of the Transition Radiation Detector. The time bin is strongly correlated with the x position.

The distributions of the time bin with the largest deposited charge in the drift region for electrons (red) and pions (blue) is shown in Figure 6.7. Similar to the distribution of deposited charge, these distributions are used as probability distributions. The probability that an electron deposits the charges Q_j with the largest amount of deposited charge in time bins x_j is given by:

$$P\left(\overline{Q},\overline{x}|e\right) = \prod_{j=1}^{6} P\left(Q_j|e\right) \cdot \prod_{j=1}^{6} P\left(x_j|e\right). \tag{6.7}$$
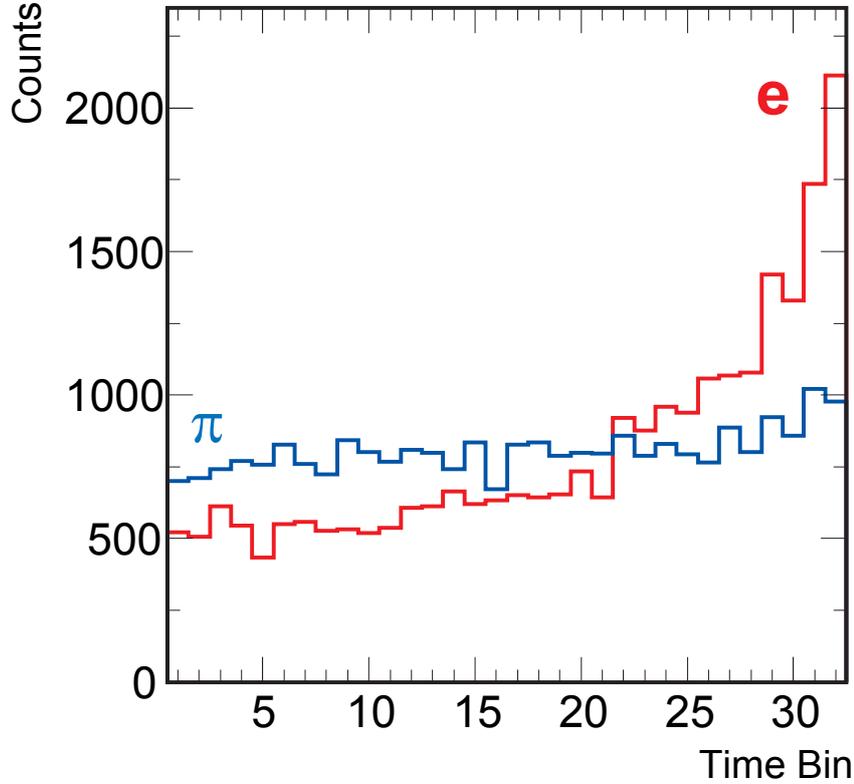
Figure 6.7: Time bin with the largest amount of charge for electrons (red) and pions (blue) in the drift region. The momentum was $1\,\mathrm{GeV}/c$ [And01].

The probability for a pion is:

$$P\left(\overline{Q},\bar{x}|\pi\right) = \prod_{j=1}^{6} P\left(Q_j|\pi\right) \cdot \prod_{j=1}^{6} P\left(x_j|\pi\right). \tag{6.8}$$

The likelihoods are calculated analogously to the procedure outlined in the LQ method (Equation 6.4).

This likelihood method was also performed on test beam data mentioned above. With the LQX method an improvement of the pion efficiency between 15 - 30% can be reached.

The LQX method provides information about the largest cluster in the drift region, which improves the discrimination power of the TRD compared to the likelihood on total deposited charge. However, the absolute charge deposited by the largest cluster is not taken into account and is lost for the particle identification. A small "largest" cluster contributes in the same way as a big one, but especially its deposited charge can be used
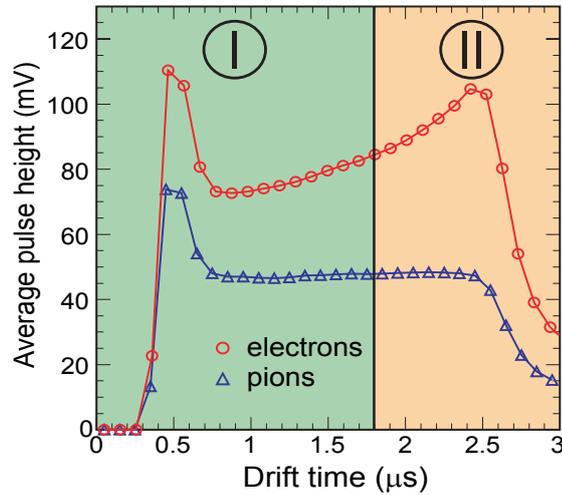
Figure 6.8: Illustration of the two-dimensional likelihood method. The chamber is subdivided into two sectors. In sector II transition radiation is preferably absorbed. The measurement of deposited charge in sector I additionally helps to discriminate electrons from pions.

————————

to distinguish between clusters origination from transition radiation and clusters from ionization.

6.2.5 Two-Dimensional Likelihood on Deposited Charge (2-dim LQ)

An approach to exploit the combined time and charge information is the two-dimensional likelihood method on deposited charge in two chamber regions (2-dim LQ) [Ber08a]. Based on the drift time, the chamber is split into two sectors (or slices). This is illustrated in Figure 6.8. The amplification region including the first part of the drift region is located in sector I (small drift times, green region). The region where transition radiation is absorbed preferably is in sector II (large drift times, red region). Absorption of transition radiation photons results in a large charge amount in this sector. The energy loss due to ionization dominates the charge deposit in sector I.

As in the LQ method the distributions of deposited charges for electrons and pions are taken as probability distributions. In contrast to the likelihood method on total deposited charge with a one-dimensional probability distribution a two-dimensional histogram is used. In Figure 6.9 the AliRoot (v4-17-Rev-12) reference distributions for electrons (upper plot) and pions (lower plot) with a momentum of 2 GeV/c are presented. The deposited charge in sector I is plotted on the x axis, that of sector II on the y axis.
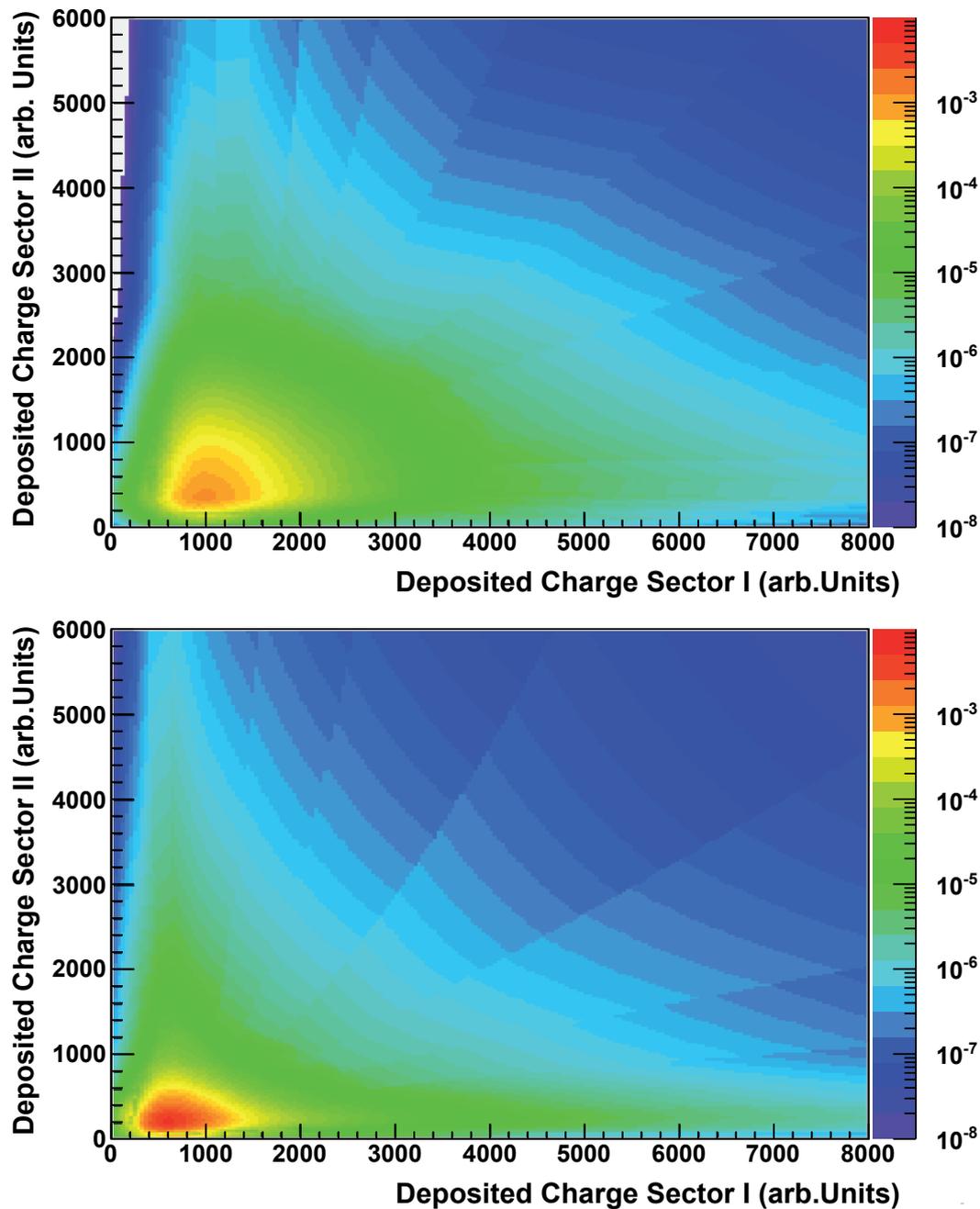
Figure 6.9: Two-dimensional reference histograms for electrons (upper plot) and pions (lower plot) as used in AliRoot (v4-17-Rev-12) for particles with a momentum of $2\,\mathrm{GeV}/c$. On the x axis the deposited charge of sector I is plotted, on the y axis that of sector II. It can be seen that the pion distribution is much narrower than the electron distribution, especially in direction of sector II.

The probability that an electron (or pion) deposits exactly a given amount of charge in sector I and in sector II is encoded by the color. Red indicates a high probability, blue a small probability. It can be seen that the distribution for pions is much narrower towards sector II than the distribution for electrons. The probability that an electron has deposited the charges $Q1_j$ and $Q2_j$ in the two sectors of the six chambers is given by:

$$P\left(\overline{Q1},\overline{Q2}|e\right) = \prod_{j=1}^{6} P\left(Q1_j, Q2_j|e\right).$$

(6.9)

The probability for a pion is:

$$P\left(\overline{Q1},\overline{Q2}|\pi\right) = \prod_{j=1}^{6} P\left(Q1_j, Q2_j|\pi\right).$$

(6.10)

The likelihoods are analogously calculated to the procedure in the LQ method (Equation 6.4):

$$L_e\left(\overline{Q1},\overline{Q2}|e\right) = \frac{P\left(\overline{Q1},\overline{Q2}|e\right)}{\sum_k P\left(\overline{Q1},\overline{Q2}|k\right)}, \text{ with } 0 \leq L_e \leq 1.$$

(6.11)

Compared to the likelihood method based on the total deposited charge the two-dimensional likelihood method shows a performance improvement by a factor of about two (see Section 8.2.2). A factor which improves the particle identification performance is that the measured deposited charge in the two sectors can strengthen or weaken the hypothesis that a particle of a specific type produces the signal. A measurement of a large amount of charge in one sector and a very low amount of charge in the second sector could lead to other particle probabilities than the measurement of two average amounts of charge. The integrated charge would be the same. In case only the integrated deposited charge is taken into account a single large cluster originating from transition radiation or δ electrons could conceal the other part of the signal and lead to a large probability for electrons. Using the measurements of the deposited charge in two chamber regions allows to distinguish more precisely between electrons and other particles. A large cluster originating from transition radiation will be found with larger probability in sector II than in sector I. The probability to find a cluster originating from δ electrons in sector I is 2/3 compared to 1/3 for sector II, since sector I is twice as large as sector II and the probability distribution for the creation of δ electrons is flat over the whole chamber volume. Consequently, the sector in which a large cluster is measured contributes to the discrimination between electrons and non-electrons.

A difficulty in using the 2-dim LQ method is in the generation of the reference histograms due to the number of entries that are needed for adequate filling. The reason for this is the dimensionality of the histogram. In case of a two-dimensional reference histogram the number of entries is squared compared to a one-dimensional histogram if a comparable quality is required. In order to circumvent local fluctuations and to get smooth reference histograms with less entries an interpolation package was implemented into AliRoot [Ber08d].

Up until the writing of this thesis, the two-dimensional likelihood on deposited charge has only been used on simulated data. However, it showed good performance and became one of the standard methods for particle identification used by the Transition Radiation Detector in AliRoot. The 2-dim LQ method as implemented in AliRoot will be compared to other methods of particle identification on simulated data in Chapter 8. It was discussed to expand the two dimensional likelihood method to three dimensions [Ber07], using the charge deposits of three chamber regions instead of two. Although first results showed a performance improvement, this is not yet foreseen in AliRoot as a method for particle identification due to the large number of entries to be stored for the three-dimensional reference histograms.

6.3   Particle Identification with Artificial Neural Networks

As discussed in Section 6.2 several methods have been used for particle identification with a transition radiation detector. In general, the possibility of discriminating between particles requires the production of different signals by the different particle types. This is obviously given for the discrimination of electrons from pions (or other hadrons), since electrons deposit more charge caused by the absorption of transition radiation photons and by ionization of the traversed detector gas. This component of the signal, the integrated deposited charge, is easy to access and to exploit. The one-dimensional likelihood method on integrated deposited charge and the truncation methods use the integrated deposited charge sufficiently. However, there are other signal components, such as the average pulse height in each time bin or the clusters originating from transition radiation photons, which are not that easy to exploit. The performance of likelihood methods which try to combine these information with the measurement of the integrated charge (LQX and 2-dim LQ method) shows that the electron identification can be improved compared to methods which exploit the integrated deposited charge only.

Means to access this additional information are provided by artificial neural networks. The signals in the ALICE Transition Radiation Detector are equivalent to patterns, produced by different particle types. As described in Chapter 5 artificial neural networks are particularly suitable for pattern recognition, especially if it is unknown how to access the pattern differences. This is exactly given in case of particle identification with the TRD.

6.3.1 Particle Identification Using Artificial Neural Networks with other Transition Radiation Detectors

There have been several attempts in order to use artificial neural networks for particle identification in transition radiation detectors. The first successful approach using neural networks was performed by *Bellotti et al.* [Bel93]. In this study a transition radiation detector with ten thin (10 mm) layers was used [Bar92]. The network was a three-layered multilayer perceptron and used as input the deposited charge of the ten layers with a 3-bit resolution. It was shown that the performance using the artificial neural network could be increased by a factor of up to three compared to likelihood methods.

The *Alpha Magnetic Spectrometer* (AMS-02) collaboration also presented a study on particle identification using its transition radiation detector with artificial neural networks [Doe06] for the separation of protons from electrons. The AMS-02 transition radiation detector consists of 20 layers of 6 mm thick straw tubes. For particle identification with artificial neural networks two approaches were tested. In the first approach the deposited charges in the 20 layers were used as input. Here, the performance did not reach the proton rejection that could be achieved with a likelihood method on deposited charge. For the second approach preprocessed variables, namely the output of four different PID methods, were used as input for a neural network. This method combined the output of the neural network from the first approach, a likelihood method on deposited charge, cluster counting, and the Fisher's discriminant. The proton rejection was improved by about 25% compared to the second best method, which was the likelihood on total deposited charge.

Another experiment with a transition radiation detector where a neural network approach was tested is the future *Compressed Baryonic Matter* (CBM) experiment [And06a]. A transition radiation detector with 12 layers, with a thickness of 0.7 mm each, was simulated for this study [Aki07] based on results from previous test beams. The input for the network was the preprocessed deposited charge in each layer. The pion rejection of the artificial neural network was comparable to the performance of other PID methods.

Artificial neural networks have been successfully applied to particle identification using transition radiation detectors. The results described above show that slight improvements can be achieved compared to other methods. The success of the artificial neural network approaches is caused by using additional information compared to the standard methods. The likelihood method in the study presented by *Bellotti et al.* has very limited access to the deposited charge, since the readout resolution was limited to 3 bits. This leads to a rough estimate of the deposited charge in the different layers and consequently to a limited accuracy of the likelihoods. The success of the neural network compared to the likelihood method might be achieved due to the fact that the correlated signal of all ten layers is taken into account. The likelihood method only combines the particle probabilities of the single chambers alone and cannot take into account correlations between the chambers. The successful network of the AMS-02 study combines results achieved with different analysis methods. Each analysis method takes slightly different aspects of the pattern difference into account (deposited charge, number of clusters, etc.). The input of the second network is highly correlated (correlation coefficient $|\bar{r}| \approx 0.7$ [Doe06]) but the network is able to disentangle this information and provide an improved particle discrimination. If no (or only little) additional information is available for a neural network no significant improvement is achieved. This is the case for the network used by the CBM transition radiation detector where only a transformation[1] of the deposited charge in each layer is taken into account.

6.3.2 Working Principles of Artificial Neural Networks with the ALICE Transition Radiation Detector

Compared to the ALICE TRD the transition radiation detectors discussed in the previous section have no drift region, and consequently their signals have no temporal significant structure. The additional information exploited with the neural networks comes from the correlation of several layers or the combination of different PID methods. For the ALICE TRD the correlation between the different layers is assumed to be negligible[2]. Instead, the temporal structure of the signal of one layer contains the additional information that is not accessible with standard PID methods.

In order to access the additional information two approaches can be followed. As described before, electrons and pions create different characteristic patterns in the TRD

---

[1]The transformation is a shift of the deposited charge such that the average value for pions is at zero which results in a faster learning [Aki07].

[2]This is only an approximation. Electrons can produce bremsstrahlung which leads to correlation between the different layers.
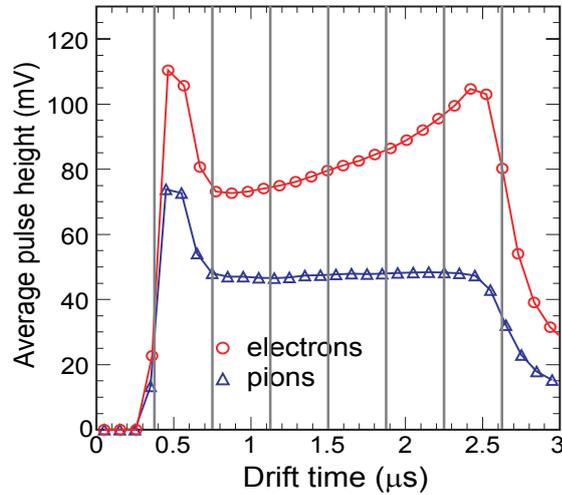
Figure 6.10: Illustration of the input for the artificial neural networks using the deposited charge in eight slices of a TRD module. Analogous to the two-dimensional likelihood method on deposited charge the chamber is divided into several slices.

---

modules. The pure form of these patterns are the time resolved raw ADC signals and are used in the first approach. The second approach uses preprocessed variables. Generally, preprocessed variables allow a faster training since the network does not have to entangle the available information. The disadvantage of this approach is that probably not the complete available information is used. It could be that important variables are not taken into account, in case it is not known that they are important. The presentation of the raw signal to the network lets the network itself "decide" which parts of the patterns are important and which not. The first approach was applied in Reference [Wil04], and will be analyzed in detail in this thesis. The second one was presented in Reference [Kim08].

Neural Networks Using the Deposited Charge Information

The simplest way of providing different patterns to the artificial neural network is the presentation of the deposited charges in several time windows. This is illustrated in Figure 6.10. The average pulse height in each time bin is again plotted for electrons (red) and pions (blue). The grey lines subdivide the chamber into eight time slices, comparable to the division into two slices for the 2-dim LQ method. The number of used slices is not limited to eight. The only limitation in granularity is given by the number of time bins originally read out by the Transition Radiation Detector. In case the number of slices equals the number of time bins, all available information is contained in the pattern and
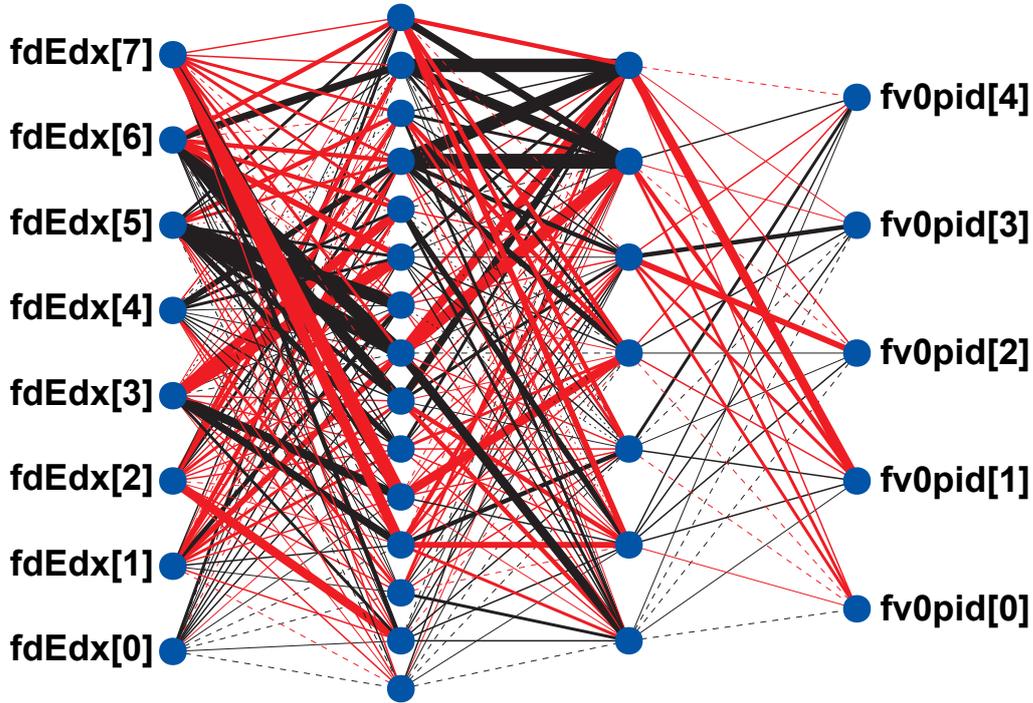
Figure 6.11: Reference network as used in AliRoot v4-17-Rev12 for Layer 1 and particles of 2 GeV/*c*. The input layer has eight input neurons, corresponding to the eight deposited charges which are presented to the neural network. The output layer has five output neurons, one for each particle type that is taken into account. The particle types are from the bottom neuron to the top neuron electron, muon, pion, kaon and proton. The network has two hidden layers with fifteen and seven neurons respectively. The thickness of the connecting synapses represents the absolute value of the weight that is assigned to the connection. Synapses with a positive weight are shown in black, that with a negative weight in red.

---

is therefore (theoretically) available for the particle identification. It will be shown that with increasing number of slices the discrimination power of the network increases but saturates for high granularities.

The approaches of the use of artificial neural networks with other detectors use correlated information across detector layers. In principle, this is also possible for the ALICE TRD. The application of a network using the combined information of six time slices in four ALICE TRD prototype chambers was performed with 2002 test beam data in Reference [Gun03]. The obtained pion suppression was improved compared to likelihood on total deposited charge by a factor of about two. Practically, taking into account all six detector layers and a high granularity leads to a network with a large number of connections. Consequently, the training would be slow and the needed amount of training data would be large. In order to limit the number of input parameters the deposited charges

in one TRD layer is presented to the network. In Figure 6.11 a reference network is plotted as it is used in AliRoot. The network is a feed-forward network and is composed of the input layer (on the left side), two hidden layers, and the output layer (right side). The blue dots represent the neurons, the black lines are the synapses. The thicker the line the larger is the weight used for that synapsis.

The topology of the network is specified by several factors. The number of input neurons is given by the provided number of slices. As a compromise between discrimination power and needed storage space the number of slices is limited to eight in AliRoot. The number of output neurons is determined by the number of particle types taken into account. This is two (electrons and pions) for test beam data and five (electrons, muons, pions, kaons and protons) for data analyzed with AliRoot. The number of hidden layers, as well as the number of hidden neurons is not a priori fixed by any rule (see also Section 5.3). Instead, several tests have been performed and the topology with two hidden layers, with fifteen and seven hidden neurons, was found to give the best performance [Wil04]. However, it is not guaranteed that this topology of the hidden layer(s) is the best possible one. In principle, other solutions might exist which have a better discrimination capability.

The network is constructed in such a way that for the activations of the output neurons O_i it is:

$$0 \leq O_i \leq 1. \tag{6.12}$$

The sum of the k output neuron activations is unity:

$$\sum_i^k O_i = 1. \tag{6.13}$$

The output neurons represent the different particle species which are taken into account. The activation of the different output neurons can be interpreted as likelihood [Ruc90] that the input parameters belong to the represented particle type. Analog to Equation 6.1 the intrinsic detector response R_{TRD} for the neural networks, a stack of N Transition Radiation Detector modules, and the particle type i can be calculated by:

$$R_{TRD}(\bar{s}|i) = L(\bar{s}|i) = \frac{\prod_{j=1}^{N} O_i(s_j)}{\sum_k \prod_{j=1}^{N} O_k(s_j)}. \tag{6.14}$$

s_j is the signal in layer j presented to the artificial neural network and $\bar{s}$ is the vector of signals in all N layers. O_i is the output of the neural network for particle type i and k is the number of particle types taken into account.
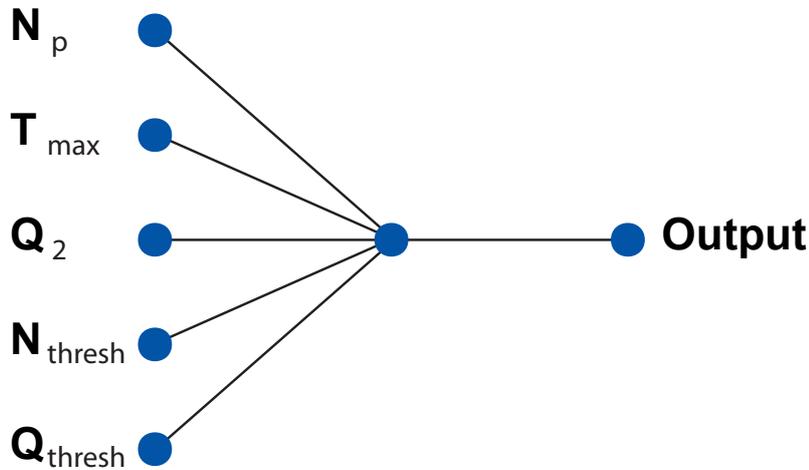
Figure 6.12: The neural network used with preprocessed variables (plot based on Reference [Kim08]). The network uses five input neurons (see text for explanation), one hidden neuron, and one output neuron. This is an untrained net, therefore the connections between the neurons have all the same thickness.

In previous publications [Wil04, Adl05a] it was shown with test beam data from 2002 that this approach is very successful and improves the discrimination power compared to the likelihood method on total deposited charge (LQ) by about a factor of three to four. The performance in simulations is about a factor of two better than the performance of the two-dimensional likelihood (2-dim LQ) approach. The method using artificial neural networks with the deposited charges as input parameters is one of the standard methods for particle identification for the TRD in AliRoot. The performance with test beam data (see Chapter 7) as well as its discrimination power in simulations (see Chapter 8) are the main topic of this thesis and will be discussed and analyzed in detail in this work.

Neural Networks with Preprocessed Variables

As discussed in Section 5.4 "adequate" variables should be presented to an artificial neural network. In this approach variables which are known to be useful in classical methods for particle identification are combined. The variables used for particle identification are:

- the number of clusters above a high threshold N_p,

- the number of time bins above a low threshold N_{thresh},

- the time bin with the largest amount of charge T_{max},

- the deposited charge of the second largest cluster Q_2,

- the integrated charge below the low threshold Q_{sum}.

N_p corresponds to the number of transition radiation photons and δ electrons, N_{thresh} will be higher for electrons than for pions and T_{max} determines the position of a possible TR photon. Q_2 can additionally help to identify electrons since the probability to produce two large clusters (from δ electrons) is very small for pions compared to the production probability of TR photons and δ electrons by electrons. Q_{sum} is very similar to a truncation. The used network consisted of only one hidden neuron and one output neuron (see Figure 6.12). This configuration was used in order to be able to further process and analyze the neural network output.

Even though the network topology is very simple, a network using this set of variables was very successful in separating electrons from pions in simple Monte Carlo simulations [Kwo08]. Adding more hidden neurons might further improve the discrimination power. Additional output neurons could expand the identification capability to other hadrons, as foreseen by AliRoot. Unfortunately, up until the writing of this thesis this approach was not used on test beam data nor on AliRoot simulations which could show its applicability under real conditions.

6.4   Pion Efficiency

6.4.1   Determination of the Pion Efficiency

The determination of the efficiency of a particle identification method in the Transition Radiation Detector is similar for the different PID methods. For its determination two data sets are necessary, signal data and background data. In this section only the discrimination of electrons from pions is discussed, but the procedure is the same for other particle types. Here, the electrons are the signal and the pions are background. The background does not necessarily consist of one particle type only, it can also be a cocktail of several particle types.

In order to determine the pion efficiency ε_π for a given electron efficiency ε_e of e.g. 90%, the calculated likelihoods to be an electron for electrons and pions are filled in a histogram (see Figure 6.13). Electrons are plotted in red and pions in blue. The likelihood
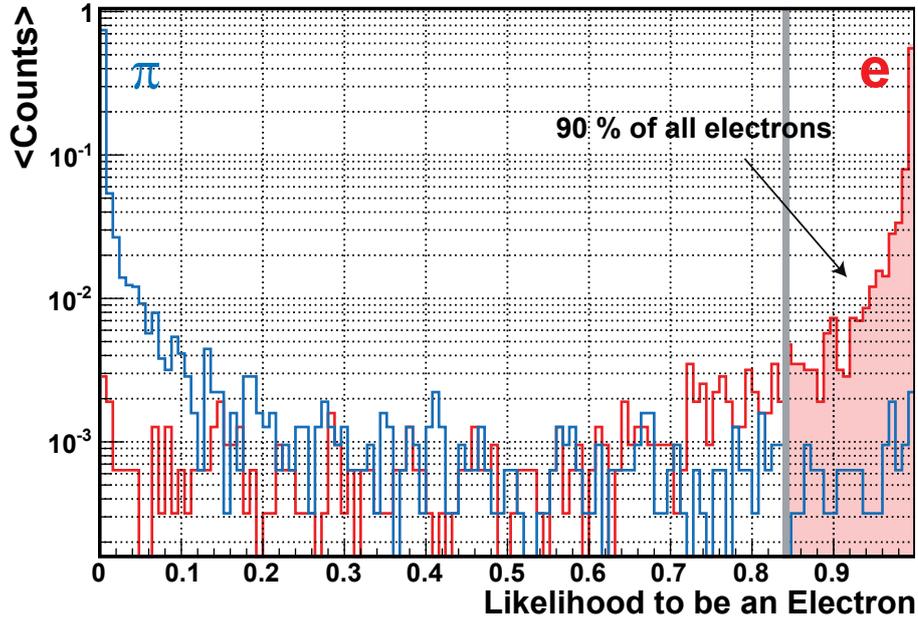
Figure 6.13: Likelihood distribution for electrons (red) and pions (blue) for four TRD layers. This likelihood distribution was extracted from test beam data 2002 using artificial neural networks. In order to determine the pion efficiency at 90% electron efficieny, those 90% of the electrons with the largest electron likelihoods are integrated and a cut is made (grey line). The pion efficiency is the fraction of pions that sits above this integration limit.

distribution for electrons is integrated. The lower limit of the integral is chosen such that 90% of the electrons are taken into account:

$$\varepsilon_e = \frac{\int\limits_{L_e(\varepsilon_e=0.9)}^{1} f^e(L_e)}{\int\limits_{0}^{1} f^e(L_e)} := 0.9, \tag{6.15}$$

where f^e is the likelihood distribution for electrons. The pion efficiency is given by the rate of pions which is inside of the integration limit for electrons:

$$\varepsilon_\pi = \frac{\int\limits_{L_e(\varepsilon_e=0.9)}^{1} f^\pi(L_e)}{\int\limits_{0}^{1} f^\pi(L_e)}. \tag{6.16}$$
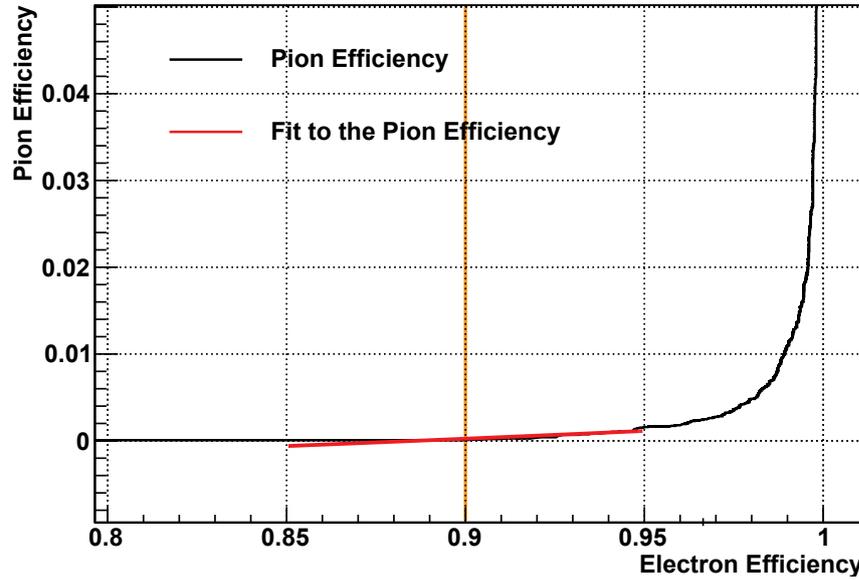
Figure 6.14: Pion efficiency versus electron efficiency for simulated data with a momentum $2\,\mathrm{GeV}/c$. In order to estimate the error of the pion efficiency, the pion efficiency is plotted versus the electron efficiency. The derivative at 90% electron efficiency is estimated using a fit with a second order ploynomial function (red line) and enters the error.

————————

6.4.2 Error Calculation

With the assumption, that the references (the two-dimensional charge distributions or the trained neural networks) are ideal, an infinite number of events which can be used to determine the pion efficiency would lead to a perfectly determined discrimination capacity of the TRD. Unfortunately, the references are not ideal and the number of used events is limited, too. It is not possible to determine the systematic error coming from non-ideal references. Therefore, it is not possible to calculate the error of the detector's discrimination capacity, but only the statistical error of the pion efficiency calculated with the given references. Consequently, the accuracy of the calculated pion efficiency depends on the used number of electrons and pions. In this thesis numbers between 3 thousand and 30 thousand tracks are used for the pion efficiency determination. The following argumentation and the equations follow Reference [Ber08e].

The lower integration limit for the calculation of the pion efficiency can be seen as a threshold t_e. First, the case that this threshold is fixed will be considered. A pion can be on

one side of this threshold or on the other side. The error of the pion efficiency $\sigma_{\varepsilon_\pi(t_e=const)}$ is binomial and it is:

$$\sigma_{\varepsilon_\pi(t_e=const)} = \sqrt{\frac{1}{N_\pi}\varepsilon_\pi(1-\varepsilon_\pi)}, \qquad (6.17)$$

where N_π is the total number of pions.

In reality, the threshold varies with the electron distribution. This variation of the threshold can also be treated as binomial. The size of the variation depends on the influence of the electron efficiency on the pion efficiency. In Figure 6.14 the pion efficiency is plotted versus the electron efficiency. The likelihoods are calculated with artificial neural networks and simulated particles with a momentum of $2\,\mathrm{GeV}/c$. The variation is given by the derivative of the pion efficiency at an electron efficiency $\varepsilon_e = 0.9$. For the error of the pion efficiency the two error components are combined:

$$\sigma_{\varepsilon_\pi} = \sqrt{\sigma^2_{\varepsilon_\pi(t_e=const)} + \sigma^2_{\varepsilon_\pi(\varepsilon_e)}}, \qquad (6.18)$$

with

$$\sigma_{\varepsilon_\pi(\varepsilon_e)} = \left(\frac{d\varepsilon_\pi}{d\varepsilon_e}\right)_{|\varepsilon_e=0.9} \sqrt{\frac{1}{N_e}\varepsilon_e(1-\varepsilon_e)}, \qquad (6.19)$$

and N_e as the total number of electrons. The derivative is extracted from the plot of pion efficiency versus electron efficiency using a polynomial fit function of second order. In Figure 6.14 it is plotted in red. It can be seen that in this case the derivative is small. Consequently, the influence of the threshold on the error of the pion efficiency is small, too.

6.5   AliRoot Implementation of Particle Identification with the TRD

In AliRoot two different methods of particle identification are foreseen for the Transition Radiation Detector. The first one is the two-dimensional likelihood method on deposited charge in two chamber regions (see Section 6.2.5) and the second one is the approach using artificial neural networks which exploit the deposited charge in eight slices (Section 6.3.2). The default PID method is the neural network method. It is possible to switch between the different methods in the macro which steers the reconstruction. The 2-dim LQ method can be activated with `AliTRDReconstructor::SetOption("!nn")`.

The particle identification values are calculated for each tracklet separately. A tracklet is a track segment in one Transition Radiation Detector layer and is represented in AliRoot

by the class `AliTRDseedV1`. For the calculation of the PID, the deposited charges have to be calculated first. Depending on the particle identification method three (for 2-dim LQ) or eight (for neural networks) deposited charges have to be determined per tracklet. This happens in the function `AliTRDseedV1::CookdEdx()`. The deposited charges are calculated on basis of the `AliTRDclusters` which belong to the track. Here, not the total values of the cluster's deposited charge are used. The reason for this is the following: Each cluster belongs to one time bin. Depending on the geometrical position of the cluster its drift time and also the spatial width of a the time bin varies. In addition, the tracklet's total length depends on its angle of incident. In order to take this into account a normalization according to the tracklet's length and the length of its clusters time bins is applied [Ber09b].

In the Offline Conditions Database (OCDB) the references for the particle identification are stored. For the two-dimensional likelihood method two-dimensional histograms (`TH2F`) for eleven momenta and the five particle species are stored, 55 in total. For the neural networks approach `TMultiLayerPerceptrons` for the same eleven momenta and the six TRD layers are stored, 66 in total. Based on the charge deposits the PID probabilities are calculated via `AliTRDCalPID::GetProbability()`. `AliTRDCalPID` is the base class for the OCDB container of the PID references. Using this class the references are called depending on the PID method, the momentum, and the requested particle type (for 2-dim LQ) or the detector layer (for neural networks) respectively. In order to correct the effect of the momentum which is mostly not exactly identical to the ones of the stored references, the PID is calculated for two references. These references are the ones with the next smaller and with the next larger momentum. In case the momentum is smaller than the momentum of the smallest reference, only the reference with the smallest momentum is taken into account. This is also true for momenta larger than the momentum of the largest reference. The resulting particle probability L_i is then:

$$L_i = l_1 + (l_2 - l_1) \frac{p - p_1}{p_2 - p_1}. \tag{6.20}$$

l_1 and l_2 are the calculated probabilities from the two references, p_1 and p_2 are the momenta of the references, and p is the momentum of the track. The PID responses of one TRD track are the combination of the probabilities of the single tracklets following Formula 6.1.

The PID response probabilities of each detector are stored for each reconstructed track in the Event Summary Data tracks (AliESDtrack) in an array. The array has the size of the number of particle species taken into account. In the current AliRoot version (August 2009) five particle types are considered:

electron, muon, pion kaon, and proton.   For the Transition Radiation Detector the information is stored in `AliESDtrack::fTRDr[AliPID::kSPECIES]` and can be accessed via `AliESDtrack::GetTRDpid()`.   In order to be able to recalculate the response probabilities also the deposited charges are stored in the ESD tracks (`AliESDtrack::fTRDslices`). Using this information and the momentum of a track the particle probabilities can be recalculated whenever needed.

7. Particle Identification Performance in Test Beams

An important step during the development of technical apparates like the Transition Radiation Detector is the testing of prototypes. Several TRD prototypes with various radiators and different gas mixtures were tested over the course of the last few years in test beams. In this chapter the particle identification (PID) performances of the chamber prototypes tested in 2002 and 2004 as well as a complete supermodule in its final configuration tested in 2007 are presented. An overview of the different test beams including technical details as well as the corresponding online logbooks can be found in References [And, Ems10].

7.1 Test Beams for the ALICE TRD at CERN PS

The test beam measurements took place in 2002 and 2007 at the T10 and in 2004 at the T9 beam line of the CERN PS (Proton Synchrotron) East Area [Dur97]. The beam was a secondary beam, composed of a mixture of electrons and negative pions and was produced by protons with an energy of $24\,\text{GeV}$ hitting a beryllium target:

$$
\begin{aligned}
p + Be &\rightarrow \pi^+, \pi^-, \pi^0 + X \\
\pi^0 &\rightarrow \gamma + \gamma \\
\gamma &\rightarrow e^+ + e^- \text{ (in Be target)}.
\end{aligned}
$$
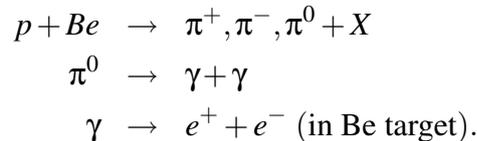
The momentum range that was studied reached from $1\,\text{GeV}/c$ up to $6\,\text{GeV}/c$ for the T10 and from $1\,\text{GeV}/c$ up to $10\,\text{GeV}/c$ for the T9 beam line.

7.1.1 Experimental Setup

One of the main goals of these test beam measurements was to analyze the PID performance of the used TRD chambers. Besides the PID performance, other topics were analyzed with very similar setups. Schematic plots of the test beam setups can be found in Figure 7.1.

The setups for the measurements all followed the same principle. Figure 7.1 **a)** shows the general setup that was used for all the test beam times. It consisted of the following components:

117

a) General Setup

b) 2002

c) 2004

d) 2007
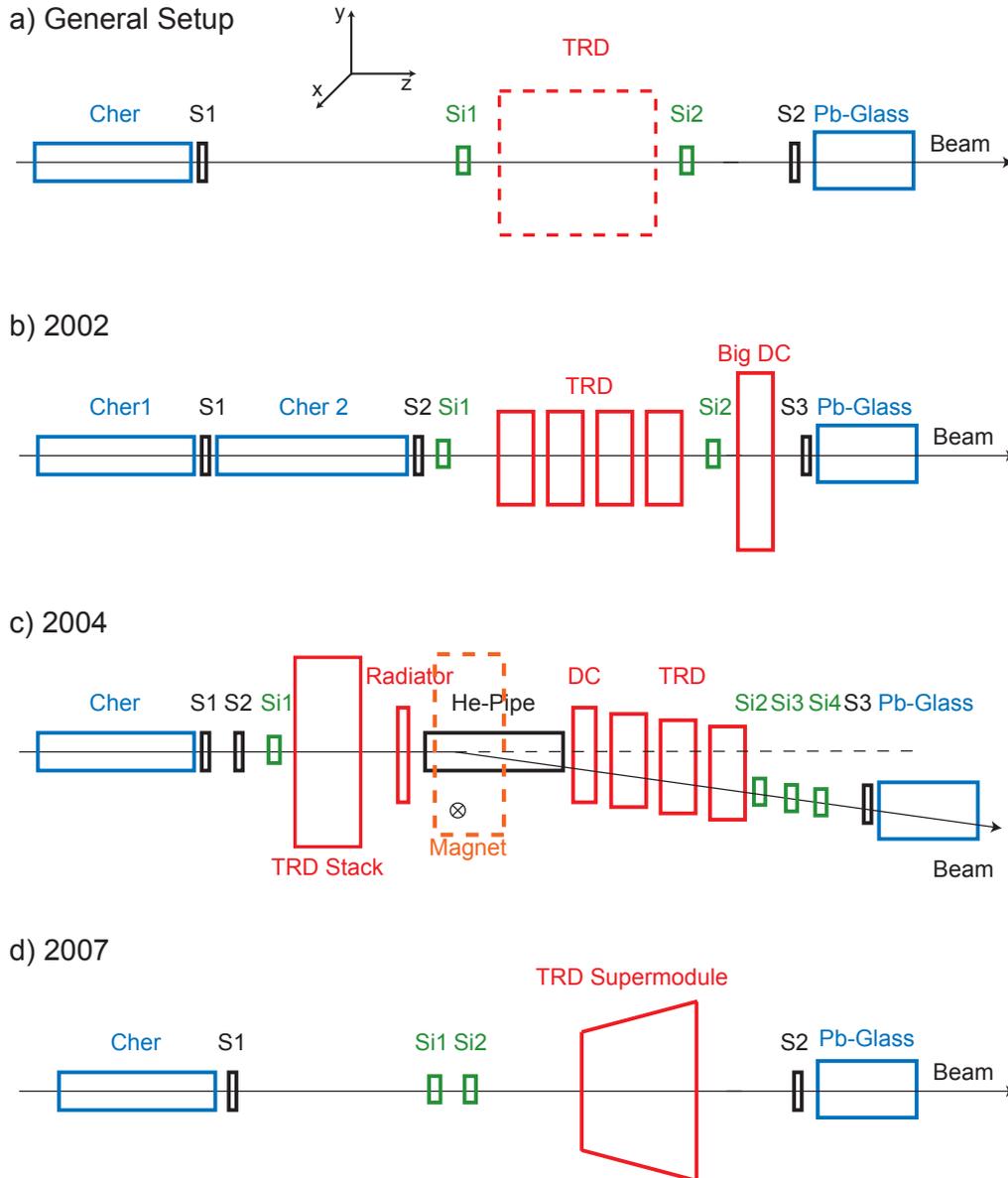
Figure 7.1: Setup of the test beam times [And]. **a)**: The general concept of the setup consisted of two scintillators (S1, S2) working as beam trigger, two silicon strip detectors (Si1, Si2) for beam position monitoring, a Cherenkov threshold counter (Cher) and a lead glass calorimeter (Pb-Glass) for independent particle identification, and finally the Transition Radiation Detector units (TRD). The coordinate system is defined in the following way: x is perpendicular to the beam axis in horizontal direction, y perpendicular to the beam axis and perpendicular to the x axis, and z is parallel to the direction of the particle beam. The setups for the different test beam times (**b**): 2002, **c**): 2004, and **d**): 2007) differed in some aspects from the general concept. The details can be found in the dedicated Sections 7.2.1, 7.3.1, and 7.5.1.

- scintillation detectors (black),

- silicon strip detectors (green),

- a Cherenkov detector (blue),

- a Pb-glass calorimeter (blue),

- and Transition Radiation Detector modules (red).

The scintillation detectors provided a trigger signal. In case both scintillators were hit within a time window, all the detectors were read out. In addition they could be used to scale down the recorded amount of pions. The ratios of pions to electrons at the PS beam lines were a function of the particle momentum. With increasing momentum the ratio of electrons decreased to about 10%. In order to provide a similar number of electrons and pions for the offline analysis, the scintillators were used in coincidence with the Cherenkov counter or the lead-glass calorimeter in order to define an electron trigger. Depending on the beam momentum different scale-down factors were used. The scintillators were also used to monitor the beam intensity.

The silicon strip detectors had an active area of $32 \, \text{mm} \times 32 \, \text{mm}$. They monitored the beam profile with a resolution of $50 \, \mu\text{m}$ in horizontal and vertical direction. Figure 7.2 shows the measured values for Run560 ($2 \, \text{GeV}/c$). The upper plots show the beam profile in the two silicon strip detectors, while the lower plots show the correlation between them. It can be seen on the upper plots that in x direction both were not positioned with respect to the center of the beam. The correlation plots can be used to exclude scattered particles or events with more than one particle.

In order to be able to perform studies on the particle identification capabilities of the TRD, it is necessary to have an independent PID measurement. A part of that identification was provided by a Cherenkov threshold counter. Pions are much heavier ($m_\pi \approx 140 \, \text{MeV}/c^2$) than electrons ($m_e \approx 511 \, \text{keV}/c^2$). In case of equal momenta their velocities differ. In case the velocity of a charged particle exceeds the speed of light in the traversed medium, Cherenkov light is emitted. The radiation can be exploited with the Cherenkov detector. The refractive index n of air at a wavelength of $589 \, \text{nm}$ is 1.000272 [Ger86]. Thus, the required velocity to produce Cherenkov radiation is $\beta > 0.999728$. This is the case for electrons with a momentum $p > 22 \, \text{MeV}/c$ and pions with $p > 6.0 \, \text{GeV}/c$. The velocity of electrons traversing air with a momentum of $1 \, \text{GeV}/c$ is large enough to produce Cherenkov light; that of pions with the same momentum is below the threshold. This is illustrated in Figure 7.3. Measurements of the two Cherenkov counters from the test beam 2002 at particle momenta of $2 \, \text{GeV}/c$ are shown. For both
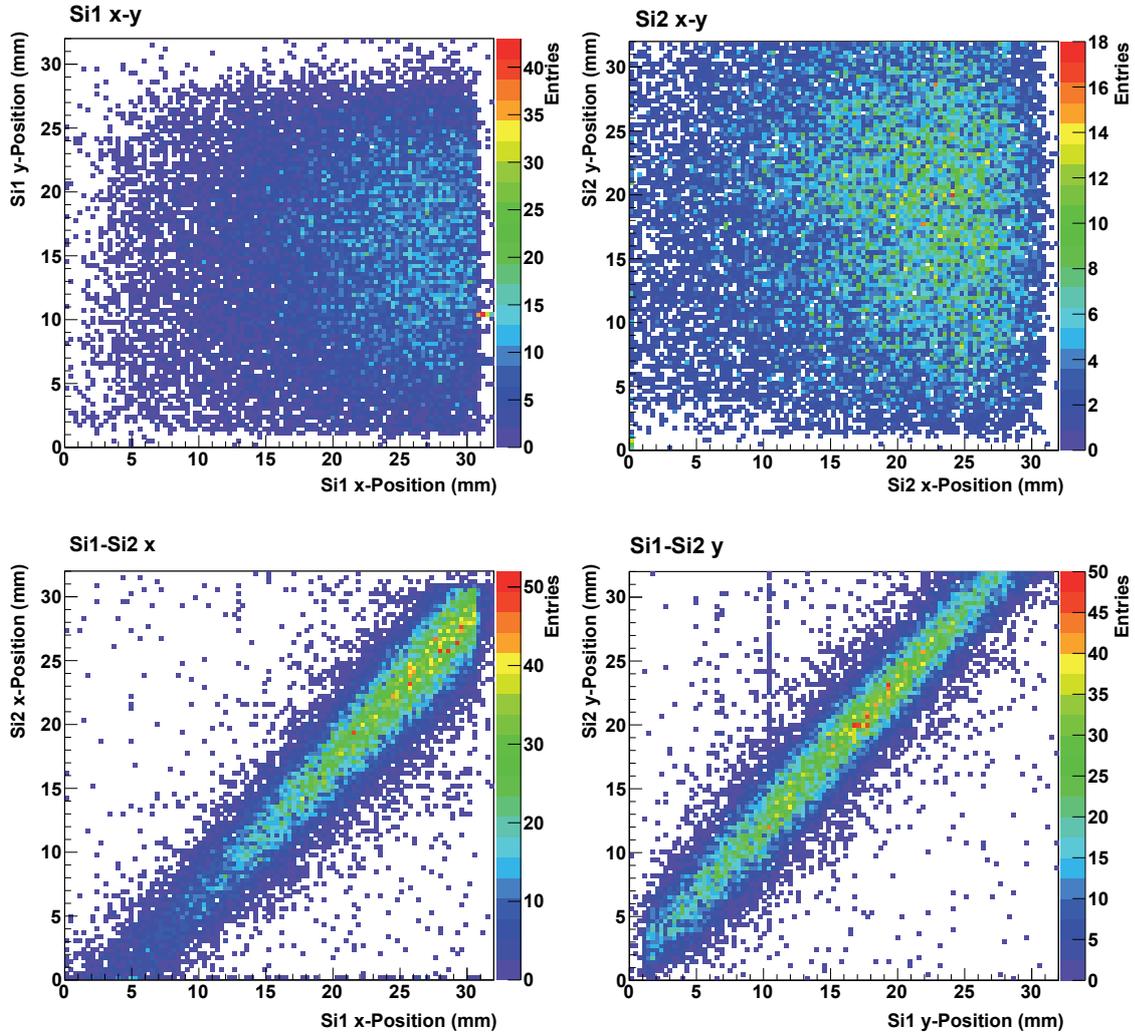
Figure 7.2: The upper plots show the signals of the two silicon strip detectors for $2\,\text{GeV}/c$ beam data from the test beam 2002, Si1 on the left side, Si2 on the right side. The beam profile is visible for both detectors, but they are not centrally hit. The lower plots show the respective correlation between the x position (left) and the y position (right). If both detectors would be perfectly aligned, the entries would lie exactly on a diagonal starting at the origin. It can be seen that the detectors are displaced by about $5\,\text{mm}$ in x and about $2\,\text{mm}$ in y direction with respect to each other.
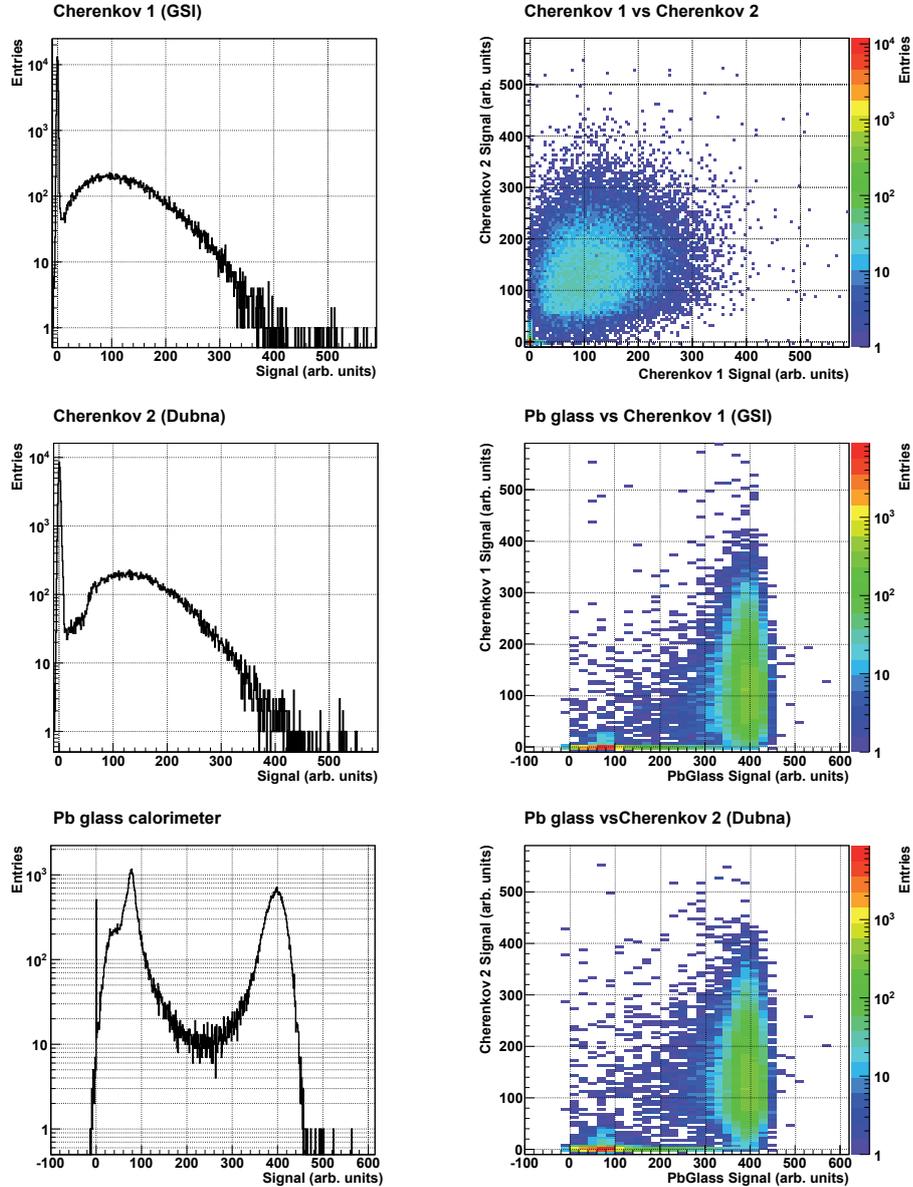
Figure 7.3: The independent particle identification. The detector responses for 2 GeV/*c* test beam data of 2002 are shown. Pions are expected to produce a signal at zero in the Cherenkov detectors and in addition a smaller signal than electrons in the Pb-glass calorimeter. On the left side the responses of the single detectors are shown. On the right side the correlation plots each with two detectors. In order to be tagged as an electron or a pion, a particle has to pass cuts on all three detectors.

Cherenkov detectors a sharp peak caused by pions can be seen at zero. A second peak, but much broader, was produced by electrons.

The second detector that was used for an independent particle identification is a lead-glass calorimeter. Electrons hitting the Pb-glass calorimeter deposit most of their energy in the detector by the production of electromagnetic showers. The mean free path for hadrons is large compared to that of electrons. Consequently, pions deposit only a small fraction of their energy. The measured energy deposit in the Pb-glass detector for $2\,\text{GeV}/c$ particles from the test beam 2002 is shown in Figure 7.3. Two peaks, originating from pions and electrons, can clearly be seen.

Each PID-monitoring detector separately allows the discrimination of pions from electrons to a certain extent. The purity was high enough to suppress pions at the trigger level. Nevertheless, in order to study the particle identification performance very pure samples of electrons and pions were needed. The combination of both, Cherenkov and Pb-glass, provided particle samples with a purity of about 0.1%. Figure 7.3 shows the correlation plots for Cherenkov and Pb-glass. It can be seen that two components (electrons and pions) can be clearly discriminated.

7.1.2   The Extrapolation Method

The ALICE Transition Radiation Detector consists of six layers of modules. For particle identification the responses of the single layers are assumed to be independent of each other and can be combined using Equation 6.1. In case this is valid, and assuming an equal PID performance of each TRD layer, the pion efficiency ε_π of n TRD layers at a constant electron efficiency $\varepsilon_e = 0.9$ follows an exponential function:

$$\varepsilon_\pi(\varepsilon_e = 0.9, n) = ae^{-bn}. \tag{7.1}$$

a and b can be extracted by applying a fit to measured pion efficiencies. With this Equation 7.1 pion efficiencies for any number of layers can be extrapolated.

In the tests of the small prototypes in 2002, four chambers, and in 2004 three chambers were used for particle identification performance measurements. The procedure is illustrated in Figure 7.4 for $2\,\text{GeV}/c$ particles from the test beam in 2002. The pion efficiencies for the first chamber, the first two chambers, the first three chambers, and all four small prototype chambers are calculated (black dots). Equation 7.1 is fitted to the calculated pion efficiencies and the result for six Transition Radiation Detector chambers can be extrapolated (red dot). In addition, the result for the four small prototypes together with the real-size chamber is plotted (blue dot). The deviation of the result from the
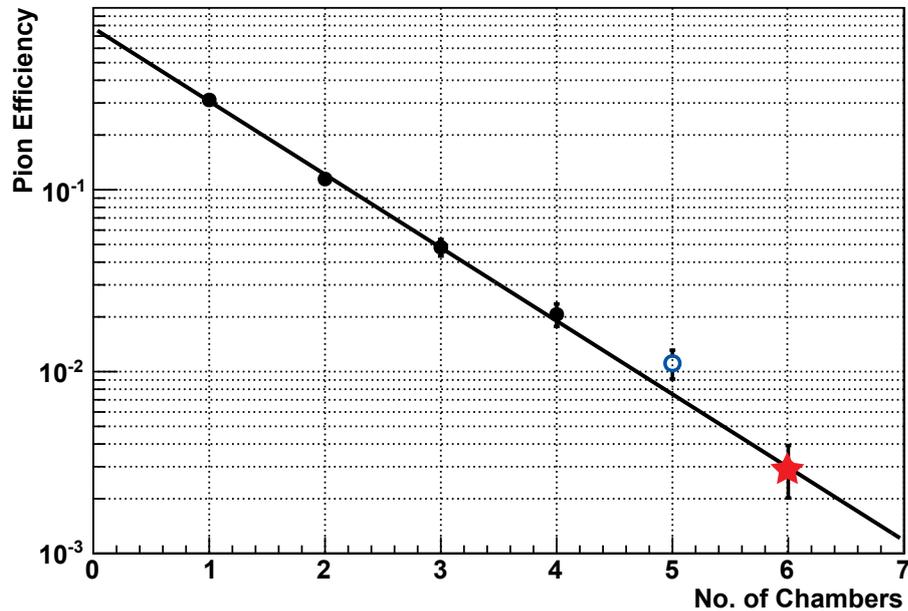
Figure 7.4: Visualization of the extrapolation method. The pion efficiency using artificial neural networks versus the number of TRD layers taken into account for 2 GeV/c particles of 2002 test beam data is shown. Black dots are the calculated pion efficiencies for one, two, three, and four small prototype chambers. The blue circle is the calculated pion efficiency for the small chambers together with a real-size chamber. The red star represents the extrapolated value of pion efficiency using an exponential fit function. The real-size chamber is not taken into account for the extrapolation.

extrapolated value for five chambers might come from different behavior of the large chamber. The real size chamber has a different geometry and also had more noise on the ADC channels. However, it was shown that the particle identification performance of a single chamber is not the same for all layers, but depends on the position in a stack [And04a]. A more detailed discussion about the validity of the extrapolation method will follow in Section 7.4.3. Nevertheless, in the following sections the extrapolation method is applied whenever the number of used chambers deviates from six, which is the numbers of layers used in the final ALICE setup.

7.2   Test Beam 2002 - Prototype Testing

7.2.1   Setup 2002

In 2002 several measurements with different setups were made. One of the goals of this beam time was to test the performance of different radiators. In Figure 7.1 **b)** the setup for the radiator tests which was also used for the particle identification performance measurement is illustrated. Instead of one Cherenkov detector two were used for the particle identification. Instead of two scintillators three (S1, S2, and S3) were in the setup, but only coincidences of S1 and S3 were used as trigger.

One real size Transition Radiation Detector chamber with the final geometry that is used in ALICE and four small prototypes of TRD chambers were tested. The small chambers had an amplification region of 7 mm and a drift region of 30 mm, which is identical to the TRD modules used in ALICE but with a smaller active area ($25 \times 32\,\text{cm}^2$) [And04c]. The readout pads were rectangular with a size of $0.75 \times 8\,\text{cm}$. The signal was read out using an 8-bit non-linear Flash ADC with adjustable baseline and a sampling frequency of 20 MHz. The higher sampling frequency compared to the ALICE TRD readout leads to a larger number of time bins (60 instead of 30) but can be easily reduced to the nominal value. The data of this beam time is analyzed using the recorded ADC values of eight readout pads.

Measurements were taken at the SPS T10 beam line at momenta of 1, 1.5, 2, 3, 4, 5, and 6 GeV/*c*. The ratio between the number of electrons and pions strongly depends on the momentum. Therefore, part of the data was taken with a scale-down factor for pions in order to provide comparable statistics for electrons and pions. The scale-down was achieved by adding a threshold on the signal of one Cherenkov detector (Cherenkov 1) to the trigger. The beam hit the chambers with an incident angle of 15° with respect to the normal to the anode wire. Due to the incident angle space charge effects, which could lead to a worse performance, could be reduced.

7.2.2   Quality Cuts

For the analysis of the pion suppression performance pure samples of electrons and pions are needed. In 2002 three detectors (Cherenkov1, Cherenkov2, and Pb-glass) were available providing an independent particle identification. In the following analysis only particles that have signals above momentum dependent thresholds in all three detectors were used as electrons. Only particles with signals below the thresholds in all detectors were assumed to be pions. The thresholds in the Cherenkov detectors were the same for

electrons and pions, while the threshold in the Pb-glass was different. The different values can be found in Table C.1.1.

Particles that were used in the analysis needed to be well defined. Therefore, only particles that hit both silicon strip detectors were used. An additional cut on the correlated *x* and/or *y* position in both silicon strip detectors could be used to suppress scattered particles. Since the correlation cut had no large influence on the PID performance in the analysis of 2002 test beam data it was not taken into account.

The only cut that affected the chambers directly was a cut on the position of the recorded pad. For each event and each chamber the pad with the largest charge deposit (pad$_{max}$) integrated over the complete drift time was searched. In order to have the complete charge information available, the pad with the largest charge deposit and its two neighbors were used. In case pad$_{max}$ was positioned on the edge and had only one neighbor in any chamber, the complete event was suppressed, since the measured charge was expected to be incomplete.

Data of very good quality were extracted with the described cuts. The analyzed runs, the number of used events, and the influence of the cuts are listed in Table C.1.2.

7.2.3   Pion Efficiency

In this section the results of pion efficiency calculations are presented. All results were obtained using the extrapolation method (see Section 7.1.2) with extrapolating from the pion efficiencies of one, two, three, and four chambers to that of six. The real-size chamber that was also part of the setup was not taken into account for the determination of the pion efficiency. Results for the pion efficiency using artificial neural networks already have been published in References [Wil04, Adl05a]. In the meantime the analysis procedure evolved. The number of used input neurons, the error calculation, and the neural net software were different from the current analysis. In order to be able to compare the analyses of the different test beam times directly and to compare them to results obtained with AliRoot simulations, the test beam data 2002 was here analyzed again. The published results differ slightly from the results presented in this thesis. The differences between the old analysis and the new one are discussed in Section 7.2.4.

The data used for the pion efficiency calculation was extracted from the raw data files using the cuts described in Section 7.2.2. In addition a transformation from 60 time bins to 30 time bins was performed in order to match the final TRD readout electronics. The signal was scaled down by a factor of 4,000 in order to fit into an interval between zero and one and to match the requirements for an optimal neural network input (see Section 5.4.3). The number of events was further limited in order to provide an equal
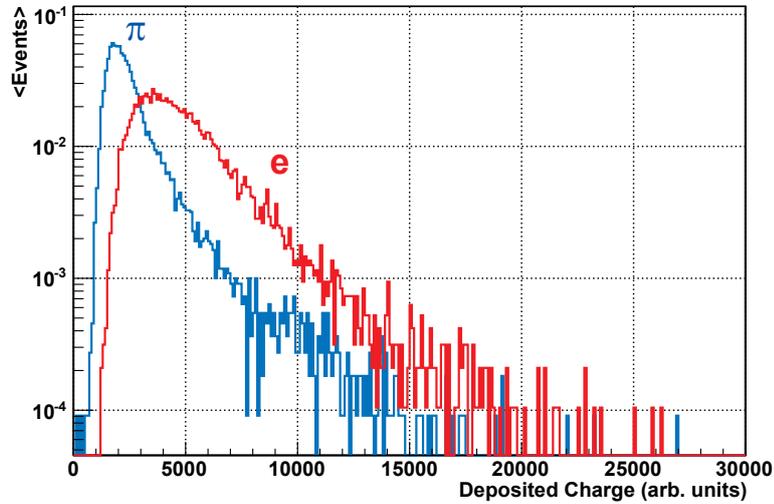
Figure 7.5: Total deposited charge for particles with a momentum of 2 GeV/*c*. Electrons are shown in red, pions in blue.

———————

number of electrons and pions for each run. The data set was split into two subsets again each with equal numbers of electrons and pions. One for training the neural networks and the other one for the determination of the pion efficiency. The training of the neural networks as well as the building of the reference histograms likelihood on total deposited charge was performed for each chamber separately.

Two PID methods were applied to the test beam 2002 data. The first one, the likelihood method on total charge (LQ), is a standard method for particle identification with transition radiation detectors. It is used in this thesis as a "standard candle" in order to compare different PID methods. The results for LQ were compared to results obtained with artificial neural networks for all momenta. For the neural networks ten input neurons were used. The momentum scan of pion efficiency was done with runs cern558 – cern564. The momenta were in a range between 1 and 6 GeV/*c*. The chambers were equipped with the INV6 radiator. In order to reduce the pion/electron ratio a scale-down for pions was implemented.

Likelihood on Total Charge (LQ)

The events that were used for likelihood on total charge were exactly the same ones that were used for the analysis with artificial neural networks. The only difference was, that the reference histograms were built with all the events and not with a dedicated data sample as it was done for the training of neural networks. Using all available data

allowed a fine binning for the reference histograms. The deposited charge distributions for Chamber 2 and a momentum of 2 GeV/c can be found in Figure 7.5. The results of the pion efficiencies are shown in Figure 7.6 **b)**.

Comparison of LQ Results to LQ-like Input for Neural Networks

A nice test for the artificial neural networks is to verify whether they can reproduce the results obtained with the likelihood on total charge. In this case the only information available to the artificial neural network is the information which is available for the likelihood method, i.e. the integrated deposited charge in each chamber. The performance of the neural networks should be of the same order as the performance of LQ.

For the comparison of neural networks to LQ the number of input nodes was reduced to one. The input was the same as for the likelihood on total charge measurement but with the difference that two data samples, a training sample and a validation sample were used. The results are shown in Figure 7.6 **b)**. It can be seen that the neural networks with one input node reproduce the results of pion efficiency with LQ for all momenta very well.

Pion Efficiency versus Input Neurons

The next check was the pion efficiency scan with artificial neural networks for different number of input neurons. It was expected that with a larger number of input neurons the pion suppression power improves, since more information is available for particle identification (see Section 6.3). At some point a further increase in the number of input neurons should not lead to a larger pion rejection, it will saturate. This analysis allows to find the optimum number of input neurons for further analyses.

The run used for this analysis was taken at a momentum of 2 GeV/c. The input vector for the neural network was formed based on the 30 time bins from the first data conversion. The number of time bins that belong to one input neuron was determined by division of the total number of time bins ($t_{tot} = 30$) with the number of designated input neurons n. The assignment of a time bin t_i to the input neuron I_j is given by:

$$I_j = \frac{t_i n}{t_{tot}}. \tag{7.2}$$

This division is an integer division. In case the number of designated input neurons is not a divisor of t_{tot} the remainder was assigned to the last input neuron I_n. The assignment of the time bin to the input neuron is illustrated in Figure 7.7 for seven input neurons.

The networks were trained for 10,000 epochs with a learning parameter of $\eta = 0.001$. The networks were saved after each 100 epochs, which allowed to find the optimal number
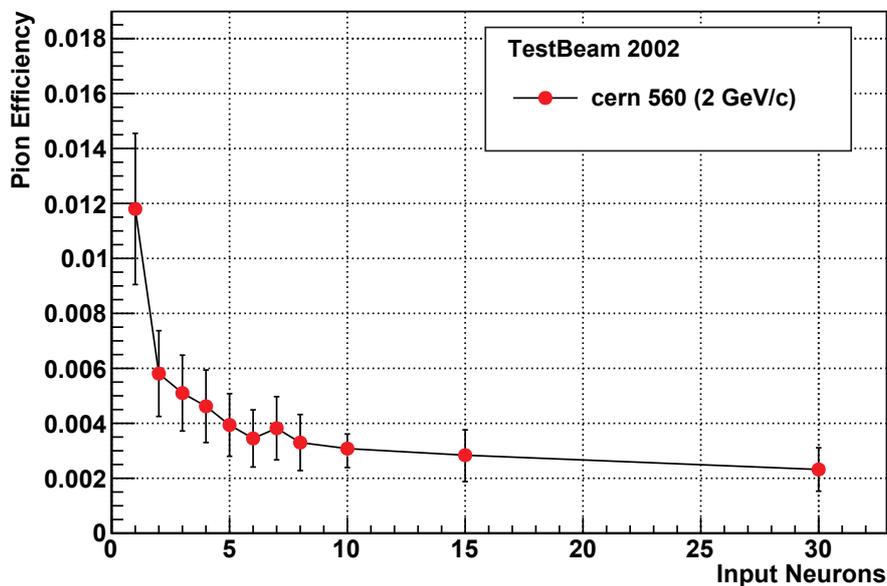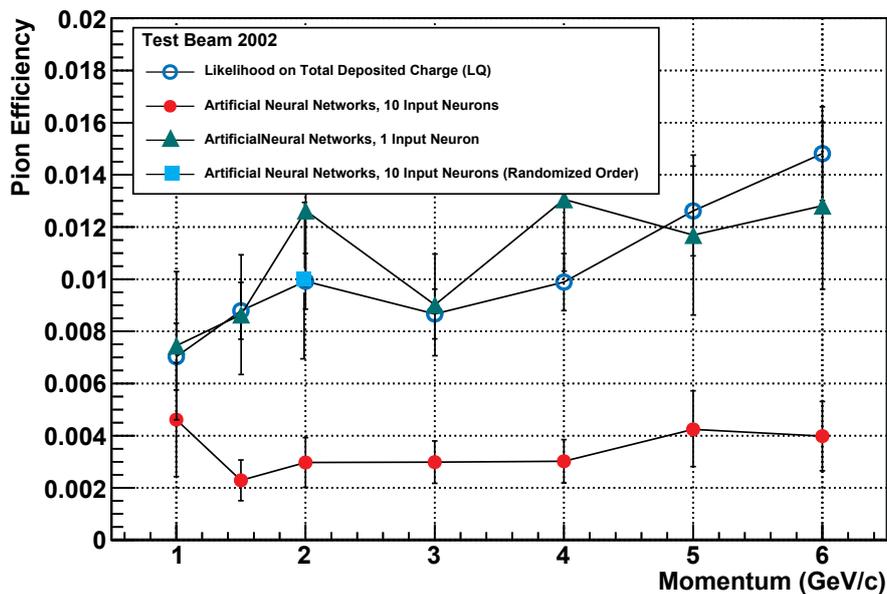
Figure 7.6: a): Pion efficiency (six chambers) at 90% electron efficiency versus number of input neurons for 2 GeV/c data. After a first rapid improvement, the pion efficiency converges. **b)**: Pion efficiency (six chambers) versus momentum. Red dots represent the results of neural networks using 10 input neurons. The neural networks showed an improved pion efficiency by a factor of about three compared to likelihood on total deposited charge.

of training epochs for each number of input neurons. The results for pion efficiency versus the number of input neurons is shown in Figure 7.6 **a)**. The evolution of the pion efficiency was as expected: it decreased very fast for small numbers of input neurons and saturated with higher numbers.

For the further analysis ten input neurons were used. It can be seen that using ten input neurons does not significantly worsen the pion efficiency compared with the maximum possible number of 30. This result also led to the number of eight input neurons used in AliRoot. In AliRoot simulations 24 time bins are available instead of 30 as in the test beam data. The difference comes from additional measurements that were taken during the test beam for each event in order to determine the signal baseline and the noise of a chamber. The significant signal for particle identification is the same for test beams and simulations. The temporal width (number of time bins) of ten input neurons corresponds to that of eight input neurons used in AliRoot simulations.

Artificial Neural Networks with Ten Input Neurons

The momentum scan with neural networks was performed in a similar way as the analysis using different numbers of input neurons. The construction of the input data, the network topology (of the hidden and the output layers), as well as the learning parameter were identical to the previous analysis. However, not the network with the best performance was used for the pion efficiency, but the result was obtained after a fixed number of training epochs. The termination condition for the training was set to a fixed number of training epochs in order to circumvent a possible bias that might be introduced by using the validation data set for determining the best network (see Section 5.5).

The evolution of the pion efficiency versus the number of epochs is plotted in Figure 7.8. The pion efficiencies for the training data set are blue and for the validation data set they are red. Each point represents 100 training epochs. It can be seen that after a first rapid decrease the pion efficiency remained at the level of the LQ method (after about 500 epochs). Further improvement took longer and got very slow after about 4,000 training epochs. The differences in pion efficiency between training and validation data set is within the expected error range.

Figure 7.6 **b)** shows the pion efficiencies for artificial neural networks with ten input neurons and different momenta. It can be seen that with neural networks an improvement of the pion suppression by a factor of about three can be reached using neural networks.
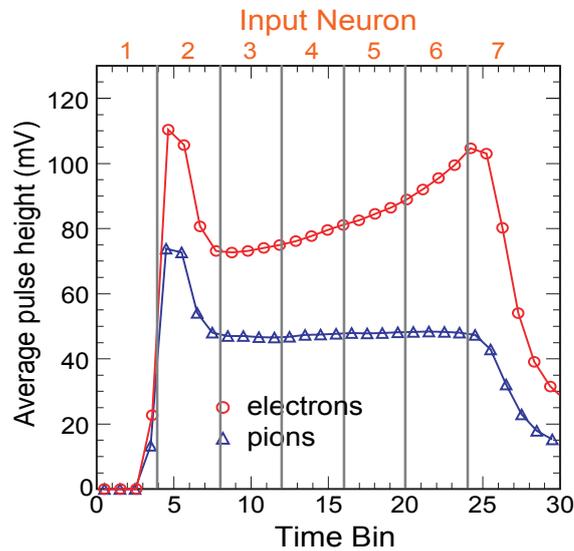
Figure 7.7: Illustration of the input for the artificial neural networks using the deposited charge in seven slices of a TRD module. Analogously to the two-dimensional likelihood method on deposited charge the chamber is divided into several slices.
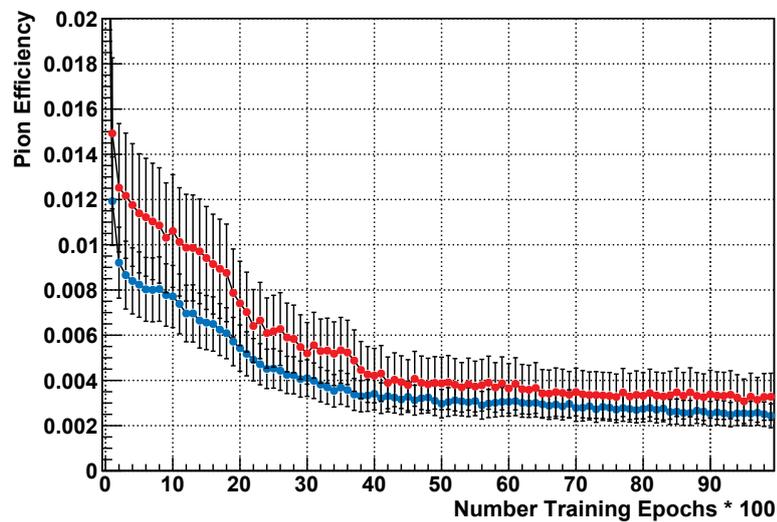
Figure 7.8: Development of pion efficiency versus number of training epochs for $2\,\mathrm{GeV}/c$ data. Results achieved with training data are shown in blue, results of validation data are shown in red.

Artificial Neural Networks with Ten Randomized Input Neurons

As discussed in Section 6.3.2 the improvement of the pion efficiency compared to likelihood on total charge is expected to be caused by the different shape of pion and electron average pulse height distributions. Electrons produce large clusters at large drift times, i.e. early in the drift chamber, due to absorption of transition radiation photons.

In order to test whether the performance improvement of neural networks is really caused by the temporal difference and is not due to a simple multiple measurement of the deposited charge in different drift chamber regions the following check was made. In case the improved pion efficiency does not depend on the temporal structure, but only on multiple charge measurements, the arrangement of the measured charges should not matter. This means, the order of the measured charges should not affect the pion efficiency. As a basis for the check of temporal dependence, the neural networks with ten input neurons and 2 GeV/*c* data were used. The signal vector was presented to the network for training and validation in randomized order. The pion efficiency of the randomized input can also be found in Figure 7.6 **b)**. The result was consistent with the results of likelihood on total charge and neural networks with a single input neuron.

7.2.4 Comparison to Previous Analyses

Analyses of the pion efficiency with artificial neural networks have already been published in References [Wil04, Adl05a]. Since those publications, the analysis procedure evolved. The changes between the two analyses as well as the differences for the pion efficiency results will be discussed in this section.

Changes in the Analysis Procedure

A major change in the analysis procedure was the switch of the neural network software. The older analyses were made using the *Stuttgart Neural Network Simulator* (SNNS) [SNN98]. SNNS is a program with a graphical user interface. It provides various network types, learning algorithms, and analysis tools. AliRoot provides (via Root) artificial neural networks as well. Since their performance is comparable to the Stuttgart Neural Network Simulator, it was decided to use Root's `TMultiLayerPerceptron` instead of SNNS.

Another difference was the used validation data set. During the test beam 2002 also runs without an electron trigger (cern565 - cern569) were taken. Apart from that, these runs were taken under the same conditions as runs cern560 - cern564. The older analyses

used the runs with electron trigger for training and the runs without as validation data. The nominal chamber settings differed a little bit for the runs with the same momenta (see Reference [And]). Although the differences were small, the validation data set was taken from the same run for the current analysis as the training data, in order to minimize systematic effects.

In References [Wil04, Adl05a] the input layer consisted of 45 input nodes. They were organized in a 15×3 matrix, representing three adjacent readout pads and 15 time bins. Later analyses showed that the improvement compared to ten input neurons is not large (see Section 7.2.3). In addition, a need for particle identification methods implemented in AliRoot is the possibility of recalculation at the Event Summary Data (ESD) level. The data size for TRD's particle identification should be as small as possible but sufficiently large to optimize the PID performance.

The last difference of the two analyses concerned the error calculation. The error of the older results was obtained using the pion efficiency variation of two data subsets. This allowed only a rough estimate of the error instead of the calculation presented in Section 6.4.2.

Results and Discussion

The results of pion efficiency versus the number of input neurons for Reference [Adl05a] and the actual analysis procedure are shown in Figure 7.9 **a)**. The pion efficiencies of the older analysis are plotted as blue squares. The training data was run cern560 and the validation data cern565. The results of pion efficiency versus number of input neurons from Section 7.2.3 are represented by red open circles. In addition, results obtained with the same networks but with run cern565 as validation data are shown (green dots). It can be seen that the new results are practically identical, independent of the validation data set that was used. Contrary to this consistence the old results differ for a small number of input neurons. The reason for this is not fully understood. The difference in pion efficiency could be due to a prematurely terminated training or an inappropriate choice of start parameters for the synapses. However, the results of the analysis made in Section 7.2.3 seem to be more reasonable than the old ones.

The momentum scan of pion efficiency in Reference [Adl05a] was more consistent with the new results. The old results are plotted as blue squares. The pion efficiencies with the Root networks using 45 input neurons and runs without electron trigger as validation data are represented by the green dots. The performance for the Root networks using the same runs for training and validation and 45 input neurons are shown as red open circles. Although there were some differences, the results agreed within the error bars. However,
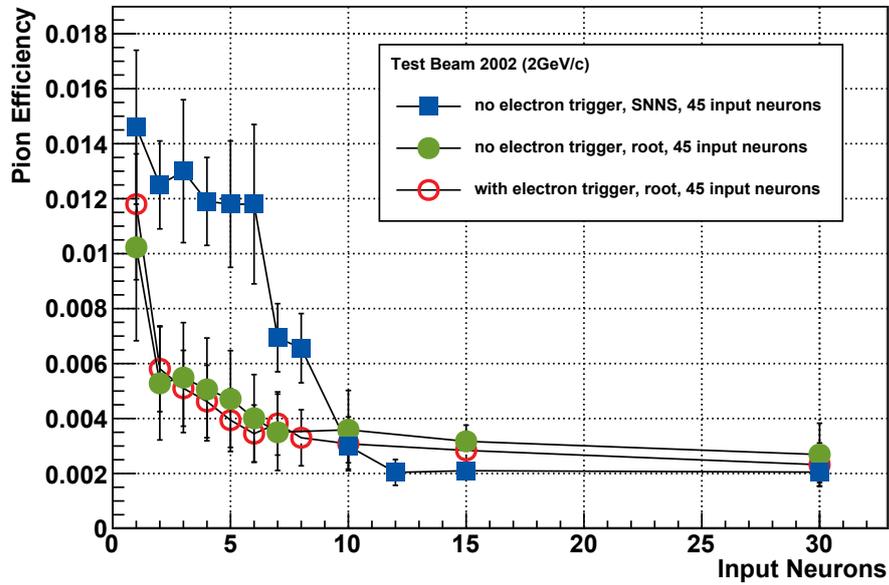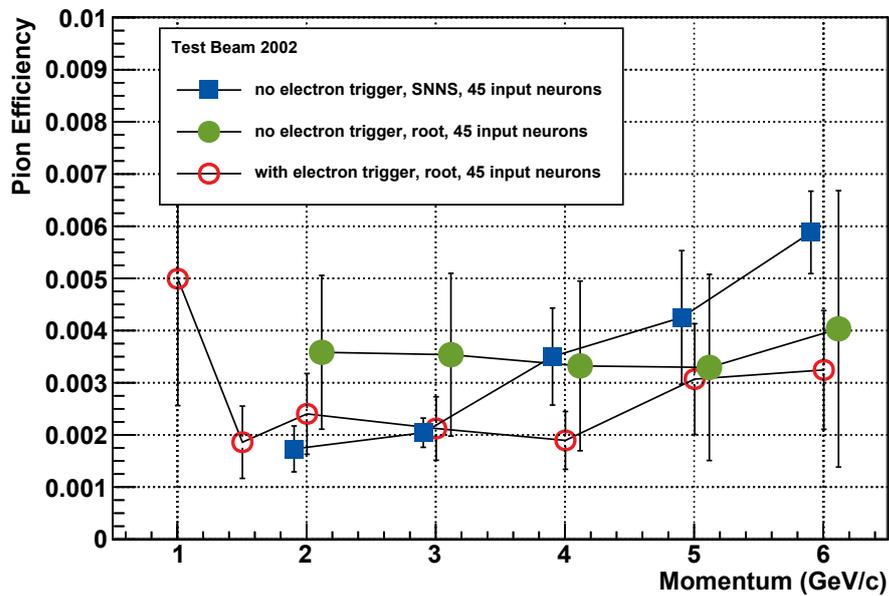
Figure 7.9: Comparison of different results. The results achieved with a different neural network software (SNNS, blue squares) and different validation data (green dots) are shown. They are compared to the results presented in Figure 7.6. In **a)** the pion efficiencies versus the number of input neurons are shown, in **b)** the pion efficiencies versus momentum.

the trend that was expected and visible for the old results – an increasing pion efficiency with increasing momentum – could not be confirmed with the new results but was still also consistent within the error bars.

7.3 Test Beam 2004 - Prototype Testing

7.3.1 Setup 2004 - Measurements with Prototypes

The test beam 2004 took place at the SPS T9 beam line. This test beam had two main goals: One was the precise measurement of transition radiation photons produced by the ALICE TRD radiator. This was done using a small prototype chamber [And06b]. The other one was the first test of a stack of six real size TRD modules with the final electronics [Ems10, Bai06, Wil06]. Instead of two, in the test beam time 2004 four silicon strip detectors were available (Si1 - 4). The setups for the different measurements can be found in Figure 7.1 **c)**.

For the measurement of transition radiation the photon has to be separated from the electron. The emission of transition radiation for particles with $\gamma > 1000$ is almost collinear to the particle track (see Section 4.2.2). In the setup scheme it can be seen that a single radiator was positioned in front of a magnet. When an electron traversed the radiator it could produce a transition radiation photon. The magnet deflected charged particles while photons followed their original path. The radiator was directly followed by a pipe filled with helium. The smaller atomic number of helium compared to that of air provided a minimum absorption probability for photons. After traversing the helium pipe the deflected charged particles and the photons were detected in a drift chamber (a small prototype without radiator). The deflection of the charged particles by the magnetic field was large enough such that electrons and photons could be clearly separated in the chamber. While the transition radiation photon was absorbed in the first drift chamber the electrons and pions traversed it completely and crossed the subsequent three small TRD prototype chambers. The TRD prototypes were identical to the ones used in the test beam of 2002. The three chambers with radiator were used for PID performance studies which are analyzed in this section. The momentum range of the analyzed runs reached from $1\,\mathrm{GeV}/c$ to $10\,\mathrm{GeV}/c$. The stack of real size chambers was not part of this setup. It was implemented once the magnet has been removed from the setup.

7.3.2   Quality Cuts

In 2004 only one Cherenkov threshold counter was available. For both PID detectors, Cherenkov counter and Pb-glass calorimeter, a low and a high threshold was implemented in the analysis. Events with signals above both high thresholds were tagged as electrons, particles with signals below both low thresholds were assumed to be pions. All other events were rejected. An overview of the used PID cuts can be found in Table C.2.1. As for the test beam 2002 an event was only recorded when a signal was registered in two of the silicon detectors. In this analysis Si3 and Si4 were used. Again only events that hit all chambers on pads other than an edge readout pad were used.

Two additional cuts were implemented in the analysis of pion efficiencies in 2004. It was observed that sometimes more than one particle traversed the experimental setup at the same time. This leads to the problem that the PID devices could not be used to unambiguously assign the observed signal to the correct track. Thus, the particle identification information could not be used. In the analysis all events were suppressed in which the value of deposited charge in the whole chamber minus the deposited charge on pad_{max} and its neighbors was larger than a threshold value. Sometimes there were events where only very little charge was deposited in one or more of the drift chambers. These events containing noise were eliminated by imposing a cut at the minimum charge that had to be deposited.

The used runs and the number of events before and after cuts can be found in Table C.2.2.

7.3.3   Pion Efficiency

The pion efficiencies were calculated in the same way as for the 2002 test beam data. The number of chambers used for the extrapolation of the pion efficiency was in this analysis only three instead of four. The first chamber in the setup was used to measure transition radiation photons directly and independently of the particle's deposited charge due to ionization. Consequently, chamber one was not used for the pion efficiency analysis.

The pion efficiencies for different numbers of input neurons were calculated in the same way as for the 2002 test beam data. Figure 7.10 **a)** shows the results for the training data set as well as for the validation data set. It can be seen that they were consistent within the error bars, but the validation data set was systematically shifted towards lower pion rejection. The reason for the better pion efficiency was on the one hand that the results for the training data set were systematically shifted to produce better results since this was the data that was known by the network. On the other hand, fluctuations in the
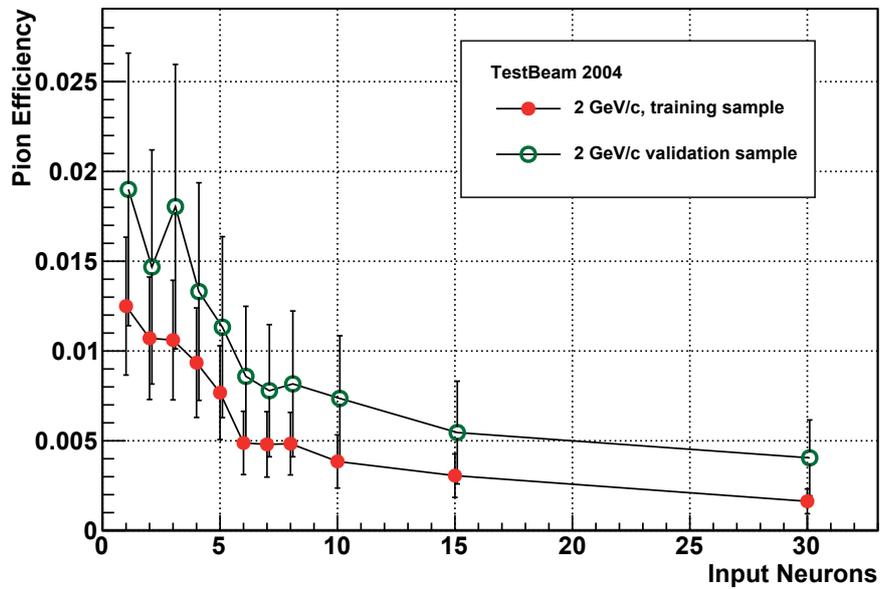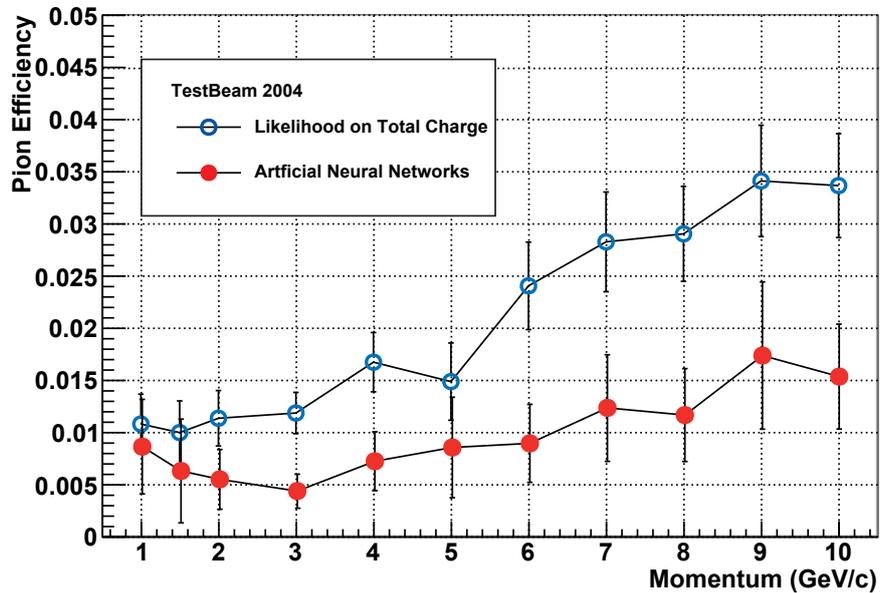
Figure 7.10: Extrapolated pion efficiency for six small prototype chambers. **a**): Pion efficiency versus number of input neurons. **b**): Pion efficiency versus momentum.
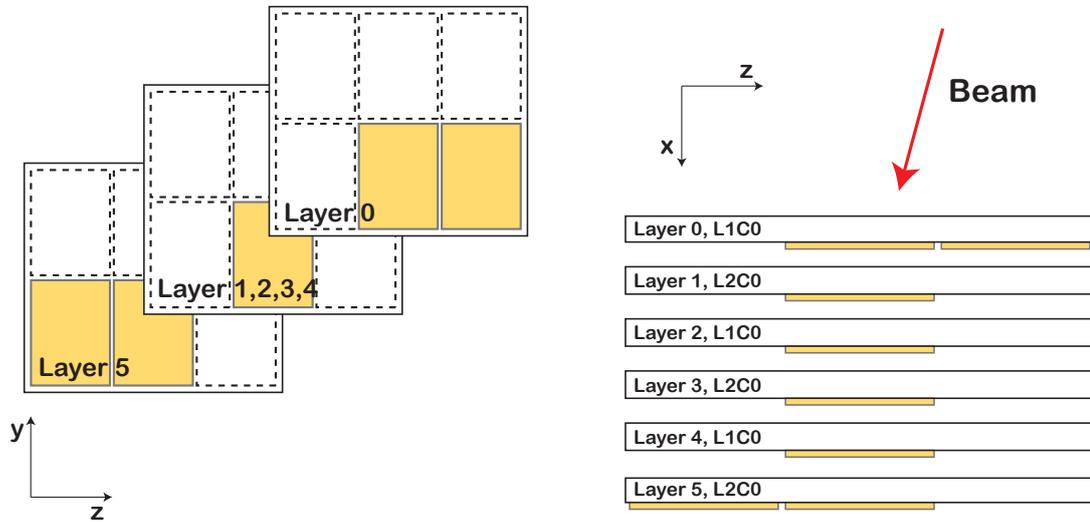
Figure 7.11: Position of the eight readout boards on the different TRD modules. The boards were arranged such that a maximum of possible angles could be measured. The stack consists of two different chambers types (L1C0 and L2C0).

———————

data itself could also cause this variation. Since the data sets for each data points were identical, the fluctuation of pion efficiency tends always towards the same direction. It is also possible that the validation data can show better results than the training data set (see Figure 7.13 **a)**), this is caused by fluctuations of the data sets.

Pion efficiencies were estimated for likelihood on total charge (LQ) and artificial neural networks using ten input neurons. In Figure 7.10 **b)** the results are plotted for a momentum range from 1 - $10\,\mathrm{GeV}/c$. The results show a clear momentum dependence. The larger the momentum, the larger the pion efficiency, and consequently the smaller the pion rejection. As for the 2002 test beam data the pion efficiency is better for neural networks by a factor between two and three.

7.4   Test Beam 2004 - Test of a TRD Stack

Although the test of a stack of TRD chambers was carried out at the same test beam time as the prototype tests of 2004 (Section 7.3), its performance was investigated in a different analysis and is therefore discussed separately in this section.

7.4.1   Setup 2004 - Measurements with the Stack

The measurement with the stack of six Transition Radiation Detector modules was carried out with a similar setup as the test of the small prototypes in 2004. The only difference was that the magnet was removed and replaced by the stack. The stack consisted of six chambers of two different types[1]. The chambers are now part of the ALICE TRD. One aim of the test beam was to test the final readout electronics. Therefore, the chambers were equipped with the TRD readout boards. Since only eight readout boards were ready at that time, the four inner chambers (1 - 4) were equipped with one board while the first and the last chamber (0 and 5) had two boards. The readout boards were positioned such that a large variety of incident angles could be measured. A schematic view of the stack with the readout boards is shown in Figure 7.11. The stack was mounted on a frame which could be moved horizontally and vertically. With that frame it was possible to take data at various angles of θ (in z direction) and ϕ (y direction). The runs that were analyzed here were taken at angles of $\theta = 15°$ and $\phi = 5°$. The runs taken at these angles were the only available data recorded for different momenta. The analyzed momenta were 4, 6, 8, and 10 GeV/c.

7.4.2   Pion Efficiency

Contrary to the procedure for the small prototype chambers the pion efficiencies for the stack of six TRD chambers were not determined with the extrapolation method. The six chambers of the stack allowed to calculate the pion efficiencies directly. In addition, a truncated mean on deposited charge was also tested and compared to the pion efficiency performance of likelihood on total charge and neural networks. For the following analyses the same cuts were used as for the pion efficiency calculations of the small prototypes described in Section 7.3.2. The used runs are listed in Table C.2.3.

Truncated Mean

The truncated mean method is a standard particle identification method for gas detectors using specific energy loss (e.g. time projection chambers). It is presented in Section 6.2.1. For the truncated mean all six Transition Radiation Detector chambers of the stack were treated as one single detector without any internal signal structure. Each of the 180 clusters was treated in the same way, independently of its position in a chamber or the

---

[1]The used chamber types were L1C0 and L2C0. In a supermodule they would be positioned at layer 1 (L1C0) or layer 2 (L2C0) respectively in the central stack.
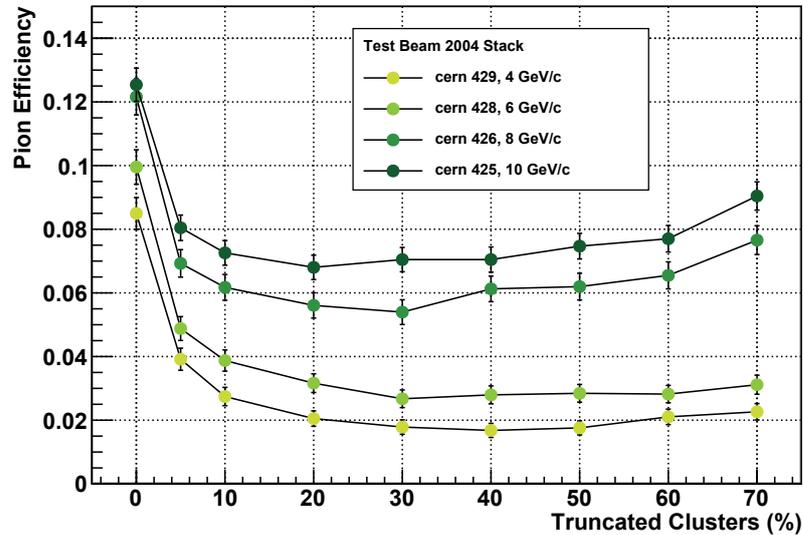
Figure 7.12: Pion efficiency versus rate of truncated clusters for 4, 6, 8, and 10 GeV/*c*. For all measurement the 5% smallest clusters were rejected. A minimum of pion efficiency is reached if about 30-40% of the largest clusters are truncated.

position of the chamber in the stack. The clusters were arranged according to the charge deposit. The clusters with the largest deposited charge were removed.

The first step using the truncation method was the determination of the optimal fraction of truncated clusters. This is illustrated in Figure 7.12. The pion efficiencies for 4 GeV/*c* versus the fraction of truncated clusters are plotted. A fraction of zero truncated clusters corresponds to the integrated charge deposit over all six chambers. The larger the fraction of truncated clusters, the better is the pion efficiency. This is the trend up to a value between 30% and 40%. The improvement of the PID capability is caused by the suppression of large clusters, e.g. from δ electrons. The tail of the pion distribution towards higher charge deposit vanishes (see also Figure 6.3). For larger truncation fractions the pion rejection power decreases again caused by the reduced signal to noise ratio.

Results

The pion efficiency versus the number of input neurons for the stack data is shown in Figure 7.13 **a)**. The results for the training data are plotted in red (open circles) and the validation data in green (dots). As for the small prototypes (2002 and 2004) the pion efficiency decreases quickly and saturates for increasing numbers of input neurons. For
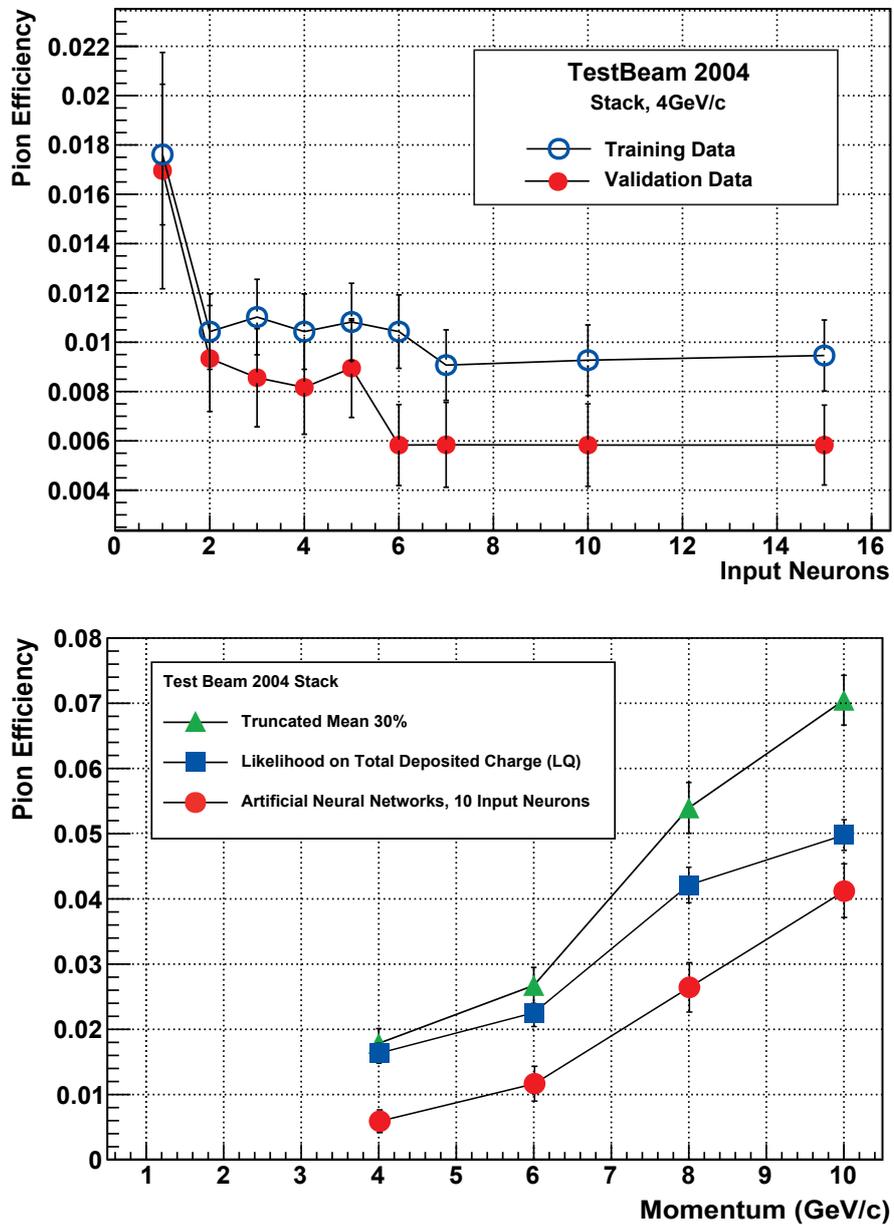
Figure 7.13: Pion efficiency of the stack. **a)**: Pion efficiency versus number of input neurons for $4\,\text{GeV}/c$ data. **b)**: Pion efficiency versus momentum.

the training data no significant improvement is visible for more than two input neurons. The pion efficiency of the training data is significantly larger than that of the validation data set.

The pion efficiencies for different PID methods and momenta are plotted in Figure 7.13 **b)**. The results for a truncated mean method, cutting the 30% largest clusters (green triangles), likelihood on total deposited charge (blue squares), and artificial neural networks with ten input neurons (red dots) are shown. An interesting result is that the truncated mean method is as good as likelihood on total charge at 4 GeV/c and 6 GeV/c. For larger momenta the likelihood method discriminates electrons from pions significantly better than truncated mean. Artificial neural networks show again the best electron/pion separation performance. At a momentum of 4 GeV/c they are about a factor of three better than likelihood and truncated mean. At larger momenta the discrimination is again better for neural networks, too, but not by such a large factor.

7.4.3 Comparison with Small Prototype Chambers

The results on pion efficiency with artificial neural networks for the small prototype chambers and the stack of six TRD modules are summarized in Figure 7.14. The results for artificial neural networks (**a)**) and likelihood on total deposited charge (**b)**) are shown. The results for small prototypes are plotted as red dots, the results for the stack are blue squares. While for 4 and 6 GeV/c the results are consistent with each other, for momenta of 8 and 10 GeV/c a clear deviation can be seen for both PID methods.

Although the real size TRD modules are much larger than the prototypes, the geometrical size should not affect the particle identification performance. The quality cuts which have been used in both analyses were identical. The most obvious difference is that for the prototypes the extrapolation method was applied while for the stack the pion efficiency is calculated directly. Figure 7.14 also shows the pion efficiency for the real-size chambers determined by extrapolation from the first three chambers (open green squares). The pion efficiency is about 20% lower compared to the direct calculation at all momenta and both PID methods. For momenta of 8 and 10 GeV/c the extrapolated results for the stack match better to the small prototype results, especially for the LQ method. The extrapolated results for the neural networks are between the other results but are not consistent with them within the error bars. The results for LQ indicate that not the optimal weights were found for the neural networks used with the stack. Additional training as well as a new training with different starting parameters did not improve the performance. A possible explanation is that in the training procedure only a local minimum was reached, due to problems that may occur using the backpropagation algorithm (see Section 5.4.3).
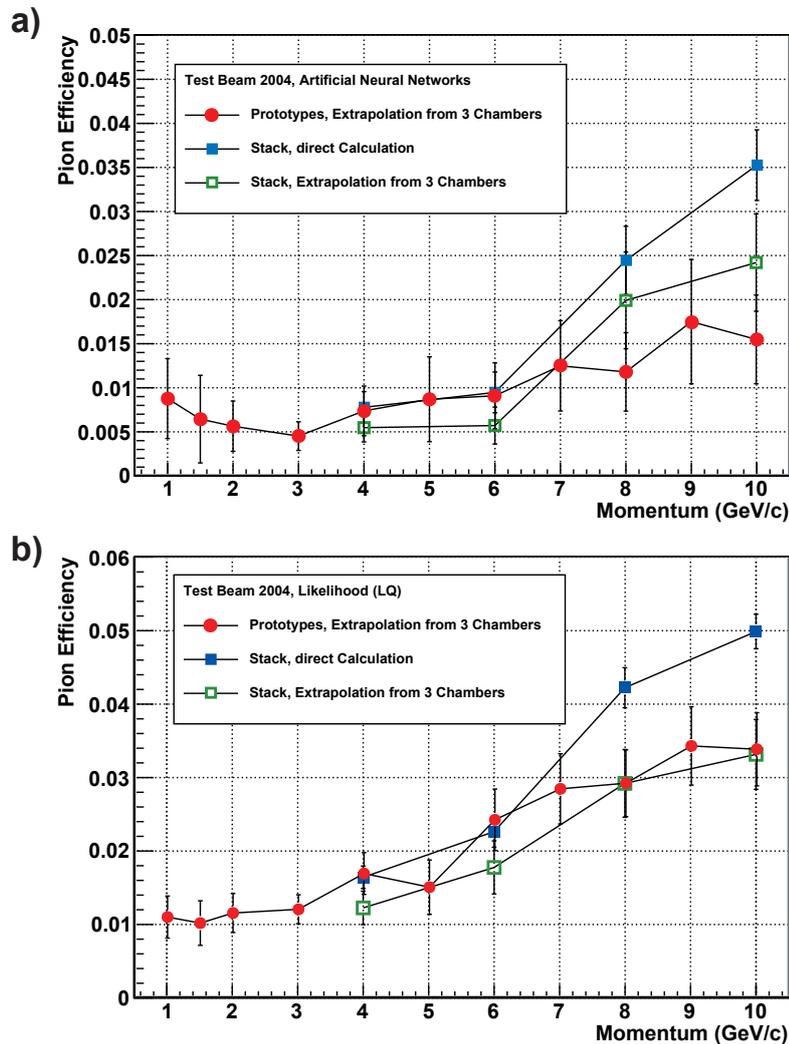
Figure 7.14: Comparison of 2004 prototype results (red dots) on pion efficiency with results achieved with the stack (blue squares) for neural networks **a)** and likelihood **b)**. The results at 4 and 6 GeV/c are consistent with each other. The results for higher momenta differ. In addition, the pion efficiencies for the stack using extrapolation are shown (green open squares).

It is possible that the optimal weights are not accessible with the training procedure used here.

Figure 7.15 illustrates the calculated values of neural network pion efficiency for 10 GeV/c (blue dots) as well as the fit function (black line) and the extrapolated value from three to six chambers (red star). In case the signals in the different chambers are independent measurements Equation 7.1 should be valid and the results should follow
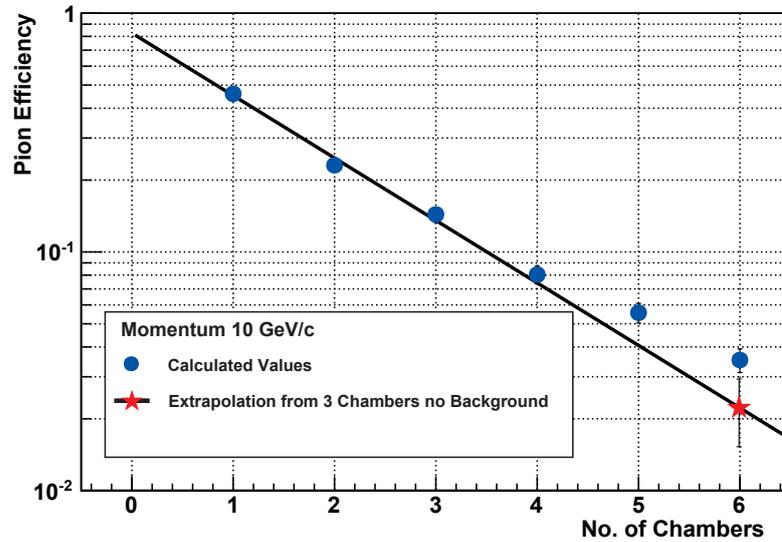
Figure 7.15: Extrapolation method for $10\,\text{GeV}/c$ stack data. Shown is pion efficiency versus numbers of chambers that are taken into account. For the fit only the results of the first three chambers were used. A clear difference can be seen for the extrapolated result (red star) and the directly calculated results (blue dots).

———————

an exponential fit function (shown as black line). The deviation from the exponential behavior is obvious. The reason for the difference will be discussed in the following.

Electron Contamination of the Pion Sample

One possible explanation for the difference between extrapolation and calculation could be a contamination of the pion sample by electrons. Let us assume that a small percentage of the particles tagged as pions would be not pions but electrons. Most of the electrons would be correctly identified as electrons by the TRD, but since they are tagged as pions they contribute to the "misidentified pions". The result of the pion efficiency calculation for n TRD modules would not follow Equation 7.1, instead the equation needs to be modified by adding a shift parameter in order to describe the pion efficiency (ε_π) correctly:

$$\varepsilon_\pi(\varepsilon_e = 0.9, n) = ae^{-bn} + c, \tag{7.3}$$

a and b are fit parameter representing the scale and the slope of the function, and c is the shift corresponding to the fraction of electrons in the pion sample. The electron contribution to the calculated pion efficiency cannot be reduced by the TRD.
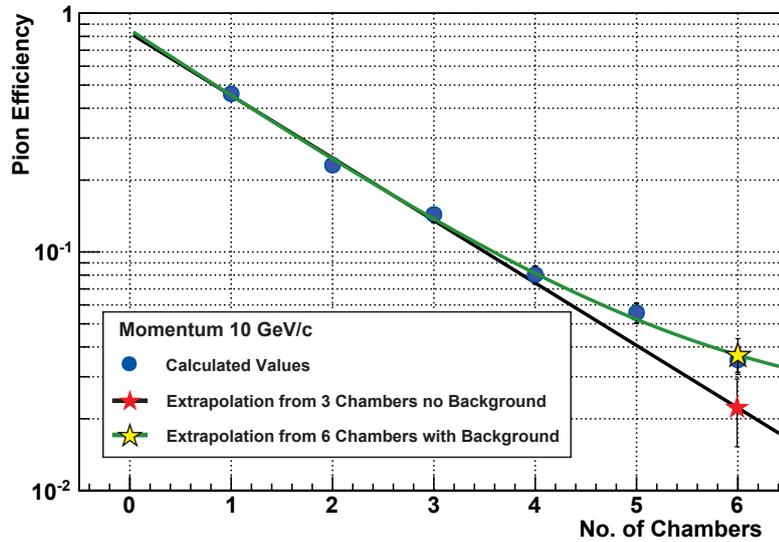
Figure 7.16: Extraction of the shift parameter by fitting the pion efficiencies to an exponential function including a constant shift (green line). The yellow star represents the evaluated pion efficiency using the fit function. The blue dots represent the calculated pion efficiencies versus the number of layers taken into account. The black line is the fit function as used by the extrapolation method, the red star is the corresponding pion efficiency.

The electron contamination of the pion sample does not play a big role as long as the number of misidentified pions (and consequently the statistical error) is large compared to the contamination. With increasing number of chambers taken into account, the pion suppression increases and the electrons in the sample of misidentified pions become dominant. In case of estimating the pion efficiency with the extrapolation method (with the assumption of no contamination) and a reduced number of chambers (e.g. three as for the prototype tests in 2004) a deviation for the pion efficiency compared to a direct calculation is seen as shown in Figure 7.15.

In order to estimate the contamination of electrons to the pion sample Equation 7.3 can be fitted to the calculated pion efficiencies used for the extrapolation method (see Figure fig:Extra10GeVCont) instead of Equation 7.1. Since the goal was to find the shift parameter and not compare the pion efficiencies to the results of the small prototype chambers, all of the six calculated pion efficiencies were taken into account. The extracted shift parameter was about 2% which corresponded to the difference in pion efficiency between the prototype chambers and the stack. The extracted shift parameters can be found in Table 7.1. However, it is not clear whether the shift parameter in fact corresponds to the electron contamination of the pion sample. It is also possible that other effects play

p (GeV/c)	Run	Shift Parameter	Cont. in Cher	Cont. in Pb	Combined Cont.
4.0	429	(0.36±0.23)%	5.61%	1.66%	0.09%
6.0	428	(0.58±0.29)%	7.34%	2.61%	0.19%
8.0	426	(0.91±0.71)%	5.76%	6.70%	0.39%
10.0	425	(2.05±0.69)%	9.91%	3.20%	0.32%

Table 7.1: Estimated contamination of the data samples for stack data in 2004. The shift parameter was estimated with the extrapolation method using all six TRD layers. The electron contaminations of the pion samples are shown for the different detectors. The combined contamination corresponds to the multiplication of the two contaminations in the single detectors. In case the deviation of extrapolation method (assuming no background) and the direct calculation is only caused by the contaminations, the shift parameter should be roughly identical to the combined contamination.

————————

a role. In order to clarify wheter misidentified electrons are the only signifiant source for the shift parameter, an alternative estimation of the contamination was done based on the PID detectors used in the test beam.

In Figure 7.17 the responses of Pb-glass (upper plot) and Cherenkov detector (lower plot) from test beam 2004 for 6 GeV/c are shown. The black line represents all measured values. The red (electrons) and the blue (pions) areas are the particles that pass the PID cuts for both detectors. The red and blue lines show the detector response of the respectively other PID detector, e.g. the red line in the Pb-glass plot corresponds to all particles identified as electrons by the Cherenkov detector. It can be seen that particles identified as pions in the Cherenkov counter have a long tail towards high energy deposition in the Pb-glass. The contamination is at about 7.3%. Vice versa, the particles identified by the Cherenkov counter as electrons have a smaller tail towards low energy deposit (contamination around 2.6%). This methods allows to determine the fraction of particles where both detectors return opposite identities. The total contamination of the data sample with wrongly identified particles can be estimated by multiplying the two contaminations. A combined contamination is then at about 0.2% for 6 GeV/c. The observed value of 0.2% contamination aproximately reproduces the observed deviation between the extrapolation and the direct calculation of pion efficiency at a momentum of 6 GeV/c (see Figure 7.14). The contamination values for the other momenta are of a comparable size (see Table 7.1), but are small compared to the deviation between extrapolation and direct calculation for momenta of 8 and 10 GeV/c.

The extracted shift parameters are much larger than the contamination levels estimated with the particle identification detectors, for all momenta. It seems that the shift
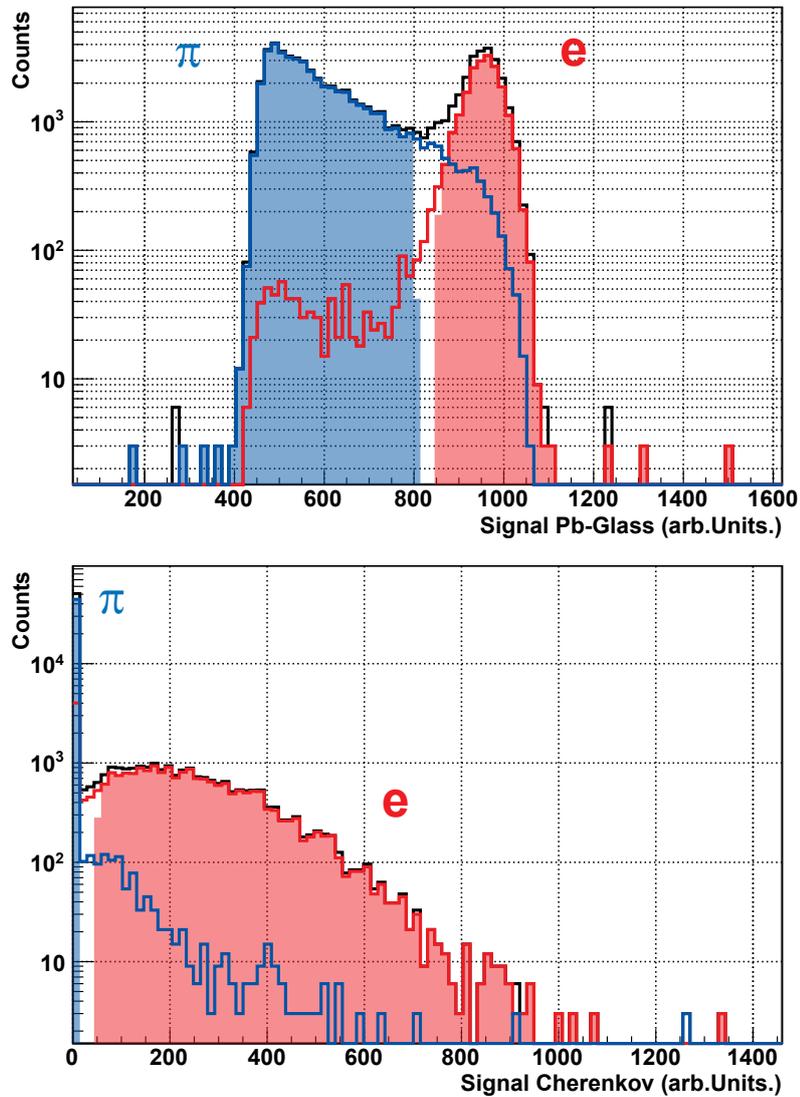
Figure 7.17: Pb-glass (upper plot) and Cherenkov (lower plot) for a run with a nominal momentum of 6 GeV/c. The black line represents all entries, the red and blue areas show the particles tagged as electrons and pions, respectively. The red and blue lines stand for the electrons and pions that are identified by the other PID detector.
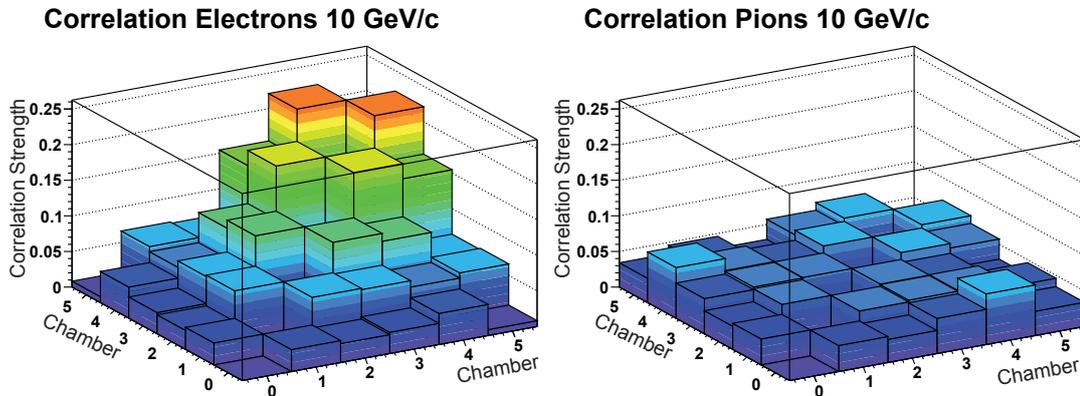
Figure 7.18: Correlation matrix for particles with momenta of $10\,\mathrm{GeV}/c$. The strength of correlation is represented by the color. For electrons correlations between the last chambers are visible, for pions the correlations are smaller. The diagonal representing correlations of the same chambers is suppressed since it is always unity.

———————

parameters are not identical with the contamination. The deviation between extrapolation (assuming no background from electrons in the pion sample) and direct calculation cannot be solely explained by contamination, at least at high momenta. Here, the difference is much larger than contamination estimates would suggest and an alternative explanation is needed.

Correlation Studies

An additional contribution to the observed deviation is the correlation of the signals in different TRD layers. In case the layers are not independent, the probabilities achieved from particle identification procedures cannot simply be multiplied with each other. A multiplication would lead to an overestimation or an underestimation of the real likelihood. As shown by *B. Vulpescu* the 2004 test beam data exhibit indeed a correlation between the chambers for electrons, but not for pions. It was observed that the correlation increases as a function of momentum and probably comes from bremsstrahlung [Vul05].

A measure for correlations between two quantities is the *correlation coefficient*. It is defined for two data sets ($x = x_1, x_2, ..., x_n$ and $y = y_1, y_2, ..., y_n$) by [Köh07]:

$$r_{xy} := \frac{\sum_i (x_i - \bar{x})(y_i - \bar{y})}{\sqrt{\sum_i (x_i - \bar{x})^2 \cdot \sum_i (y_i - \bar{y})^2}}, \qquad (7.4)$$

where $\bar{x}$ and $\bar{y}$ are the mean values. The correlation coefficient can reach values between -1 for full anti-correlation and 1 for full correlation. In order to check

correlations between different TRD layers, the correlation coefficient is applied to the measured charge deposits. In Figure 7.18 the correlation coefficients for all combinations of layers is illustrated for electrons and pions at 10 GeV/c. On the left side the correlation coefficient for electrons, on the right side that for pions is shown. The correlation for identical chambers is not shown, since it is always unity. A correlation for electrons can be seen. With increasing length the correlation gets stronger. It has to be noted that the correlation coefficient is defined to measure linear correlations between quantities which are Gaussian distributed. Non-linear correlations cannot be identified.

The square of the correlation coefficient is called *coefficient of determination*. The coefficient of determination indicates the influence of the variable x on the variance of y. For the correlation of chambers four and five at 10 GeV/c (Figure 7.18) this means that 5% of the variance of the deposited charge for electrons can be explained by linear correlations [Sac78]. An attempt to exploit the correlation with an additional artificial neural network which combines the outputs of the networks for the single chambers was not successful, since the correlations are too small.

It is not obvious how large the influence of the correlations on the deviation between extrapolation method and direct calculation is. However, the combination of electron contamination of the pion sample with the observed correlation could be the reason for the difference between direct calculation and extrapolation.

7.5 Test Beam 2007 - Test of Super Module III

7.5.1 Setup 2007

In 2007 the SPS T10 beam line at CERN was again used for a test beam. This time a fully equipped supermodule was tested. The supermodule is now part of the ALICE TRD as Supermodule III. The goal of the test beam 2007 was to test a TRD supermodule with the full chain of data taking, i.e. taking raw data (including zero suppression and digital filtering), converting it to AliRoot files, and finally reconstructing and analyzing it.

Another important task was to study the possibility of acquiring a first reference data set for particle identification. Several alternatives exist for the extraction of reference data. One possibility is to use simulations, another method makes use of photon conversions. Both methods have advantages and disadvantages, they will be discussed in detail in Section 9.1.1. A problem of simulations is that it cannot be assured that simulated particles behave like real particles in the detector. Unknown detector effects could possibly make the simulated data worthless as references for the real experiment. Photon

conversions provide a clean sample of electrons. However, during the first months of data taking references from conversions will not be available. An alternative are references from test beam data. In this section the performance and problems of the test beam with respect to particle identification will be analyzed. The analyzed beam momenta were 1, 2, 4, and 6 GeV/*c*. The analysis was done on fully reconstructed data. The reconstruction was performed by *A. Bercuci* and *M. Fasel* [Ber08b] using the stand-alone TRD tracking software [Ber08b].

7.5.2 Analysis Procedure and Quality Cuts

The analysis procedure for the test beam 2007 was different in many aspects from the previous test beam analyses. For the analysis of the test beam data 2007 fully reconstructed tracks in AliRoot format were used. In AliRoot it is not foreseen to have additional beam monitoring detectors. Therefore the analysis was first split into two parts. One part was the extraction of TRD chamber data from the AliRoot format, the second part was that of beam monitoring data. Finally, both parts were merged and the merged data file was used for the analysis.

The AliRoot data was reorganized into a `TTree` which had one entry for each found track. To be able to merge the two separated data sets, the event number was added to the output. Other global parameters were the number of found tracks and the number of found clusters in each event. Further data belonging to single tracks was extracted from the `AliTRDtrack` object. Each output entry contained 180 charge measurements for 180 possible `AliTRDclusters` (30 time bins $\times$ 6 chambers) per track and the number of TRD modules that were hit. The number of hit detectors was determined via the different cluster positions that belong to each track. The local geometrical position of the first cluster was saved, in order to be able to match it to position information from the silicon detectors. In addition, the number of clusters belonging to the track and the χ^2 of the linear track fit was observed. The second part of data extraction was made directly on the raw data. The only information that was extracted were the hit positions in the silicon strip detectors and the signals measured by Cherenkov detector and Pb-glass calorimeter.

The final step in data extraction was the merging of the information. At this stage the cuts were applied. For the beam monitoring detectors the same type of cuts were used as for the data of older test beam times. Only events were used that have exactly one reconstructed track which hit all six detector layers. Based on this data the neural networks were trained. The resulting pion efficiency was disappointing. Figure 7.19 illustrates the likelihood distribution for 2 GeV/*c* data obtained with artificial neural networks. It can be seen that there is a large contamination of pions at electron
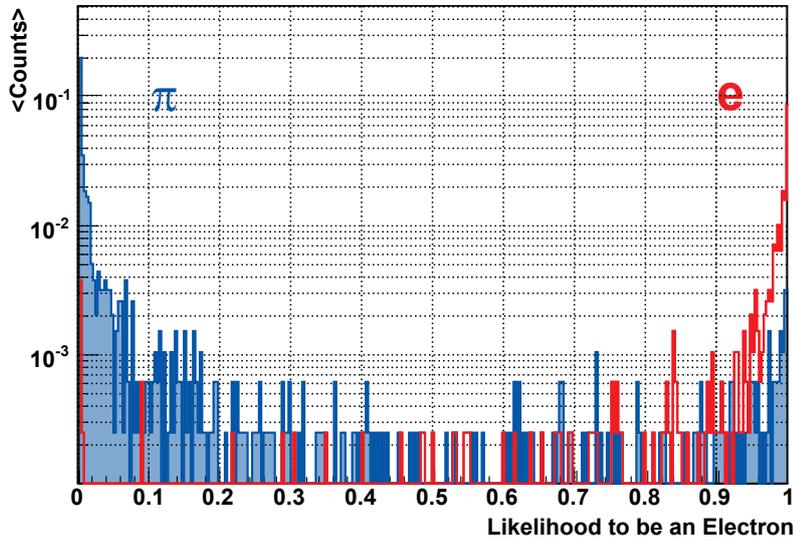
Figure 7.19: Likelihood distribution of electrons (red) and pions (blue) with a nominal momentum of 2 GeV/*c*. A large contamination of pions at large electron likelihoods is clearly visible.

_____

probabilities close to one as well as some electrons at small electron likelihoods. The reason for the huge contamination will be discussed in the following section.

7.5.3   Contamination Studies

The first guess for a reason of having the large amount of misidentified pions was that these particles actually were electrons. That would suggest that the PID detectors did not work correctly or the cuts were not set properly. In Figure 7.20 the correlated signal for Cherenkov counter and Pb-glss calorimeter for 2 GeV/*c* data is shown. It can be directly compared to the correlation plots of 2002 (see Figure 7.3). At first sight an obvious difference is visible. In 2007's data it seems that a fraction of electrons deposited only parts of their energy in the Pb-glass calorimeter. A possible explanation is that they did not hit the Pb-glass centrally and parts of the shower signal were lost [Gra09]. However, these events were excluded by the particle identification cuts and did not contribute to the likelihood plot. An estimation of the pion contamination of the electron sample based on the signal distribution of Cherenkov and Pb-glass detectors (as described in Section 7.4.3) gave a result of about 0.1% of contamination.

An additional check whether the pions with high electron likelihood (in the following called *fake pions*) were electrons can be made with the average pulse height distributions. In case a particle was an electron and was somehow misidentified by the PID detectors,
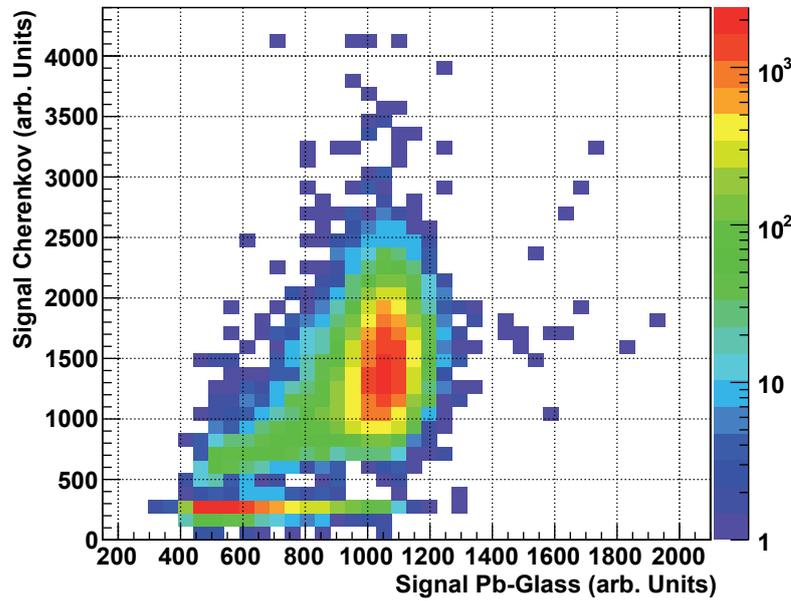
Figure 7.20: Correlation plot for Pb-glass and Cherenkov detector for $2\,\mathrm{GeV}/c$ data. Contrary to the correlation plots of 2002's beam time (Figure 7.3), a fraction of particles with a high Cherenkov signal but small energy deposition in the Pb-glass can be seen.

––––––––––
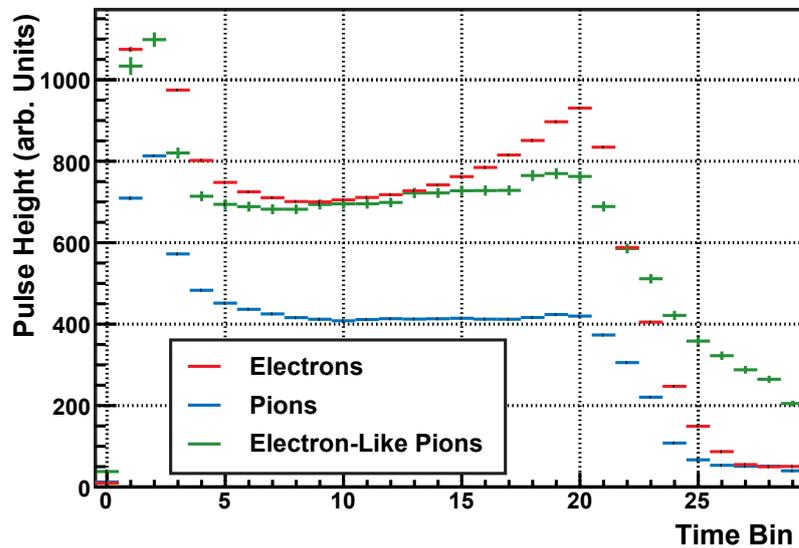
Figure 7.21: Average pulse height distributions for electrons (red), pions (blue), and pions with an electron likelihood larger than 0.99 (green). Pions with large electron likelihood show in contrast to the other particle classes a clear signal at time bins larger than 24.

––––––––––

it should nevertheless produce transition radiation in the TRD. For the analyses below all pions with an electron likelihood larger than 0.99 were treated as fake pions. In order to get enough events to produce an average pulse height plot with small fluctuations for the fake pions, the cut on the silicon strip detectors was removed. The resulting average pulse height is illustrated in Figure 7.21. The electron distribution is red, the pions (including the fake pions) are blue, and the fake pions alone are green. The electron and the pion distribution behave as it is expected. The electrons have the transition radiation peak. For the fake pions the average pulse height is different from both other distributions. The amplitude is about twice as high as for pions (similar to the distribution for electrons), but no transition radiation peak is visible. This means that these were with a very high probability no electrons. Otherwise they would have been electrons which did not produce Cherenkov radiation, no shower in the Pb-glass, and no transition radiation, which is very unlikely.

Besides the absence of a transition radiation peak but electron-like amplitude for the fake pions, another effect is visible. In the last ten time bins, the signal for the fake pions does not decrease as quickly as for electrons and pions. The difference is obvious especially in the last five time bins and quantified in Figure 7.22. The probability for the occurrence of a cluster in three different chamber regions (section 7, section 8, and section 9) for the six TRD layers are shown. A section consists of three time bins and is equivalent to the neural network input for one input node. Starting with section 0 and time bin 0, sections 7 − 9 are the input for the last three input neurons, equivalent to the last nine time bins. In section 7 a clear difference is visible between pions (blue stars) and electrons (red stars) for all chambers. Since no tail cancellation (see Section 4.4.2) was applied to the data, this can be easily explained by the tails of the deposited charge of the electrons which is in average higher than for pions. The probability to find a cluster in the section 7 is about 95% for electrons and only about 80% for pions. The points for the fake pions (open blue stars) are very close to the points of electrons. This changes in sections 8 and 9. The probability for finding a cluster in section 8 is around 40% for electrons, around 20% for pions, but around 65% for pions with high electron likelihood. In section 9 electrons and pions have only 10% probability for a cluster, fake pions around 45%. A possible explanation for that would be that instead of the signal of single particles, the signal of two combined particles is observed. In case there is a time shift between the particles, the second particle would deposit charge in the last time bins which leads to the observed clusters.

In case the above assumption is correct, not only the temporal signal shape should be affected, but also the width of the signal should be different for the double particle tracks. The width of a signal can be quantified using the number of pads that contribute
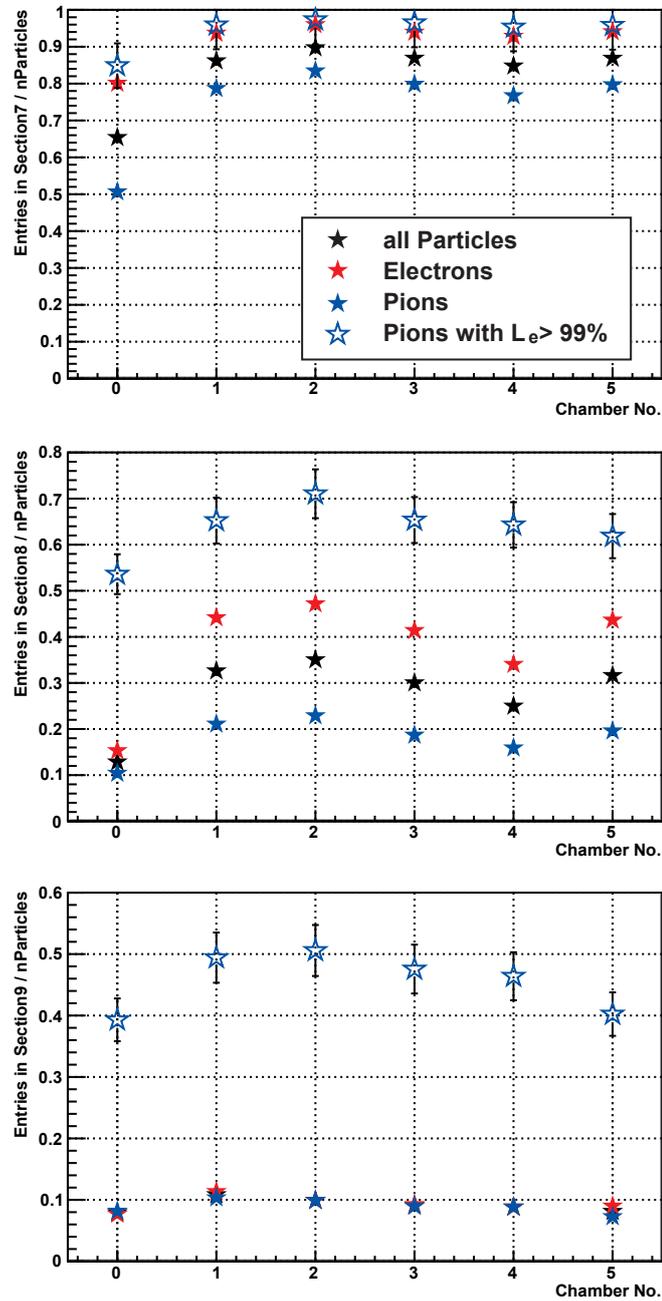
Figure 7.22: Probability for the occurrence of clusters in time bins 22-24 (upper plot), 25-27 (middle plot), and 28-30 (lower plot) versus TRD layer. Shown are the probabilities for electrons, pions, and pions with electron likelihood > 0.99. Electron-like pions show a clearly larger probability for occurrence of clusters at high time bins compared to the other particle classes.
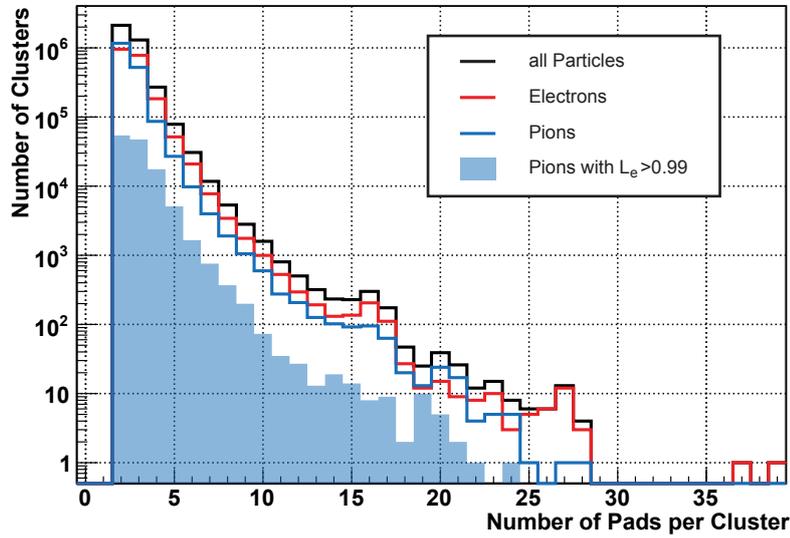
Figure 7.23: Number of Pads used for a cluster. Shown is the total amount of clusters with different size for all particles (black line), electrons (red line), pions (blue line), and fake pions (blue area).
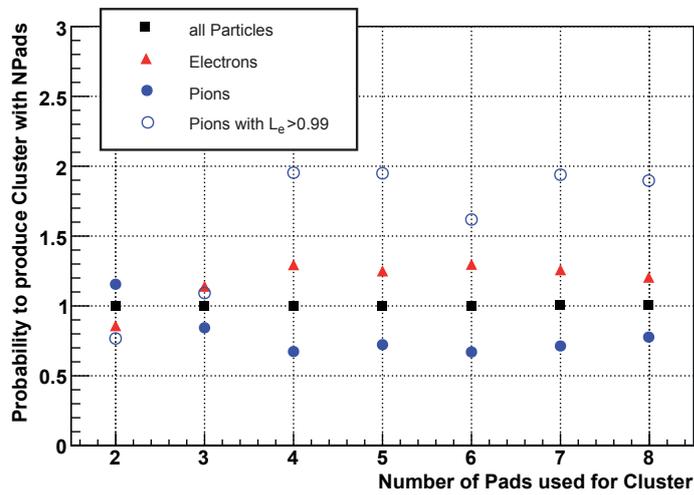
Figure 7.24: Relative probability of occurrence of different cluster sizes for different particle classes. For details please refer to the text.

to a reconstructed cluster. In Figure 7.23 the distribution of pads that contribute to a cluster is shown[2]. The most probable value for used pads per cluster is two, for all particles (black line), electrons (red line), pions (blue line), and fake pions (blue area). Figure 7.24 visualizes the relative probabilities for the occurrence of clusters with a given number of pads using a double ratio R. For each class of particles the number of clusters with a given number of pads is divided by the total number of clusters for the according particles. The double ratio is generated by dividing by the ratio of all particles:

$$R_p^i = \left(\frac{n_p^i}{N_p}\right) \bigg/ \left(\frac{n_{all}^i}{N_{all}}\right) , \qquad (7.5)$$

where n_p^i is the number of clusters made of i pads for particle class p and N_p is the total number of clusters for the regarded particle class. In Figure 7.24 the following can be seen: The probability for pions to produce 2-pad clusters is higher than the average probability of all particles to produce them. This changes for larger clusters. For pions with large electron likelihood a clear enhancement for clusters built of more than three pads can be seen. The probability for such large clusters is about two times higher than the average.

The analysis of the cluster distribution in the last nine time bins and the analysis of the cluster size indicates that the assumption of having double tracks could be an explanation for the poor pion efficiency. The tracks have to be close to each other in space and also in time. The reason for the occurrence of double tracks is not clear. It has been proven that the observation does not come from a bad reconstruction. A contamination and a resulting poor pion efficiency was also observed by another analysis directly based on the raw ADC signals [And08a].

7.6 Comparison and Discussion of the Different Test Beam Times

In this chapter the pion efficiency of three test beam times using different particle identification methods was analyzed. In Figure 7.25 the results of 2002 and 2004 are summarized for artificial neural networks (**a**)) and likelihood on total deposited charge (**b**)). The best performance was reached with 2002 data. All test beam results shown in the plot achieved with artificial neural networks fulfill the design goal of a

---

[2]For the calculation of the cluster size first the pad with maximum charge deposition is determined. Starting from that pad, the pads in both directions of the pad column are counted until the charge deposit of the actual pad is below a threshold or above the value of the previous pad.
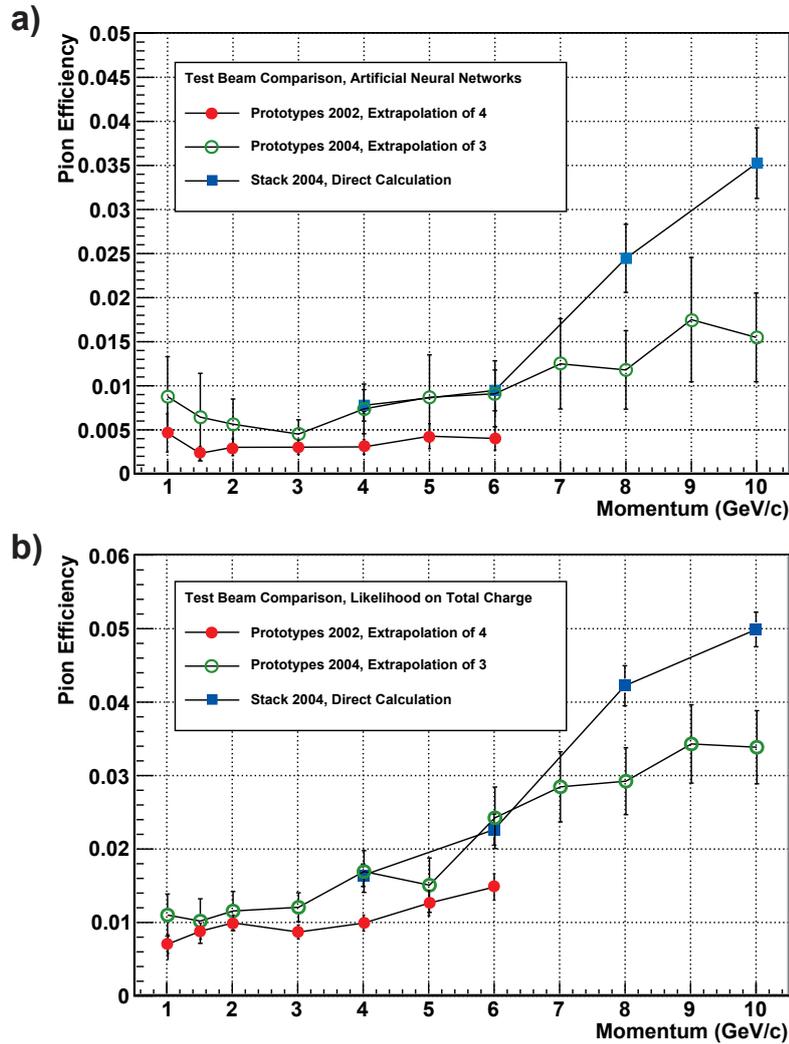
Figure 7.25: Pion efficiencies of the different beam times for neural networks (**a**)) and likelihood on total deposited charge (**b**)).

pion efficiency below 1% for 90% electron efficiency. The test beam results of 2002 and 2004 differ nearly by a factor of two for neural networks, but are consistent within the error bars. This difference is also visible for the likelihood method but is not so large. However, a clear shift towards larger pion efficiency can be observed for 2004 test beam data compared with 2002 data, for both methods. The difference between the pion efficiencies of 2004 prototypes and the stack data of the same year are discussed in Section 7.4.3.
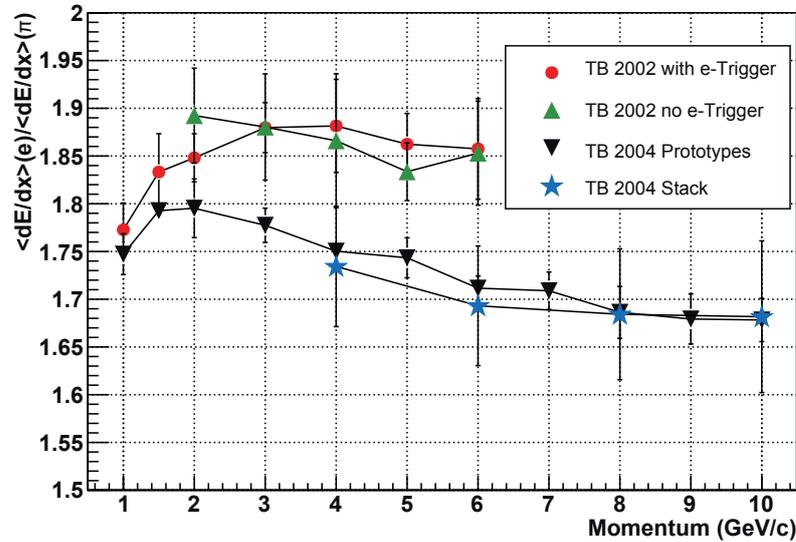
Figure 7.26: Ratio of the mean deposited charge for electrons and pions versus momentum. Ratios for 2002 data (with electron trigger (red dots) and without electron trigger (green triangles)) and 2004 data (prototypes (black triangles) and stack (blue stars)) are shown. The plotted ratios are the average values for all the chambers used in the run.

————————

The Transition Radiation Detector's performance for electron/pion discrimination is strongly connected to the difference between the electron signal and the pion signal. The ratio between the mean value of total deposited charge in a chamber by electrons and that of pions can be found in Figure 7.26. The average ratio for all chambers used in a run is shown for data sets of 2002 (with and without electron trigger) and of 2004 (prototypes and stack). While the electron/pion signal ratios of the same year are consistent to each other, the ratios of different years differ significantly. The ratio increased up to $2\,\text{GeV}/c$ for both cases. For data of 2002 the ratio stayed at a large level, while for 2004 it decreased for higher momenta. An explanation for the different signal ratios is that the electrons in 2002 may have produced bremsstrahlung, but did not in the test beam in 2004. Bremsstrahlung could be produced in one of the detectors (beam detectors or TRD chamber) which were traversed by the beam particles and could subsequently been absorbed in the gas volume of a TRD chamber.

In Figure 7.27 the ratios of deposited charge for electrons and pions are shown for each chamber: in **a)** for the test beam in 2002, in **b)** for the prototype tests in 2004, and in **c)** for the stack measurements in 2004. For the 2002 data it can be seen that the ratio increases significantly with the chamber number. This increase indicates that additional bremsstrahlung is produced at each TRD layer. It can be seen that this is not the case for
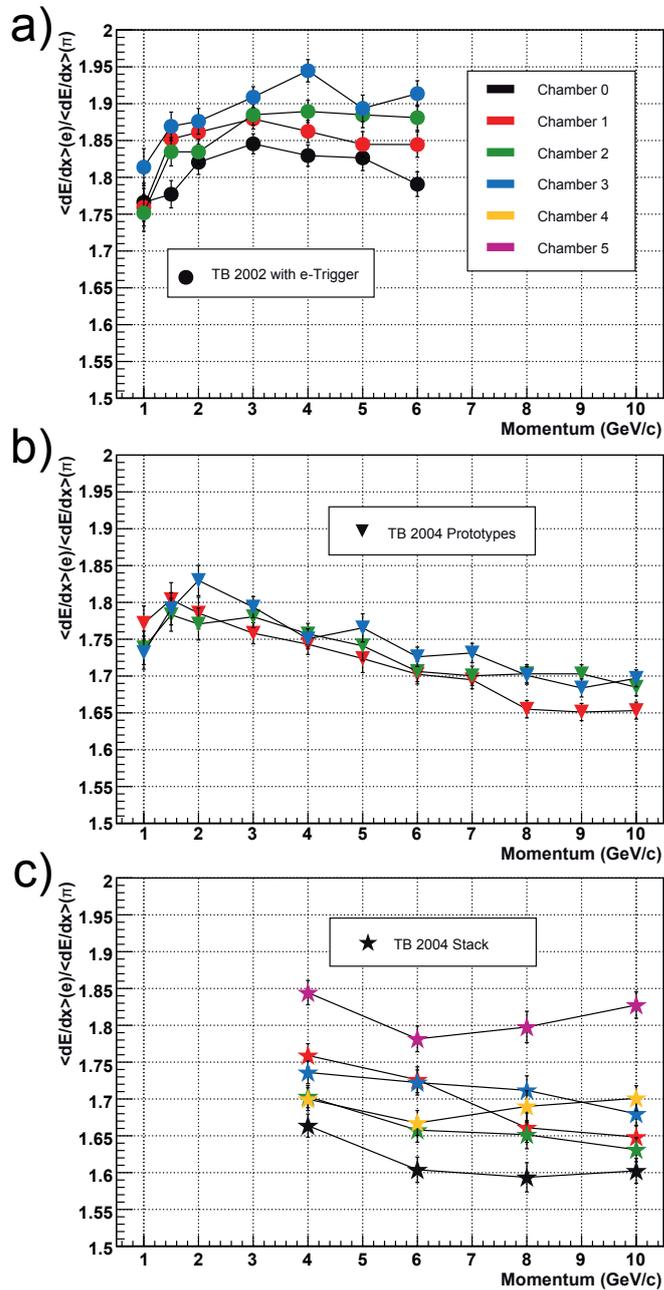
Figure 7.27: Ratio of the mean deposited charge for electrons and pions versus momentum in each TRD chamber. Ratios for **a)** 2002 data (with electron trigger (dots), **b)** 2004 prototypes tests (triangles), and **a)** stack measurements (stars) are shown.

the 2004 prototype data. Here, the ratio for all chambers is approximately identical for all chambers. A possible source for bremsstrahlung was identified in References [Bai05, And09b]: in 2002 the connectors for the chamber read out were hit by the particle beam. However, it seems that bremsstrahlung produced in the connectors cannot be the only explanation. In 2002 chamber 0 also has a significantly larger electron/pion signal ratio than any prototype chamber in 2004. Since the connectors were installed on the backside of the chambers in 2002, the electron/pion signal ratio for chamber 0 should be identical to that of the chambers in 2004.

Bremsstrahlung produced in the beam monitoring detectors could be an additional source contributing to the higher electron signal in 2002. In 2004 the beam was deflected by a magnetic field, and neutral particles (e.g. photons) did not traverse that TRD chambers which were analyzed here and could not contribute to the signal. However, in case this bremsstrahlung would contribute to the charge deposit in data of 2002, it should be visible for the stack data. For the measurements with the stack of TRD chambers the magnet was removed. In Figure 7.27 **c)** it can be seen that the electron/pion signal ratio for most of the chambers is as high as for the prototype measurements in 2004 (see Figure 7.27 **c)**).

Alternative contributions to the difference of the electron/pion signal ratio might be a different transition radiation yield for the two beam times. In 2002 and 2004 slightly different radiators have been used. It cannot be excluded that in 2002 more transition radiation was produced in the radiators. In case the transition radiation spectrum is hard enough, the photons could be detected in subsequent chambers and lead to the observed increase of the electron signal with increasing chamber number.

For the stack data a large fluctuation of the electron/pion signal ratio could be seen. While chambers 1, 2 3 and 4 were approximately consistent with the results of the prototype chambers in 2004, the ratio was significantly smaller for chamber 0 and significantly larger in chamber 5. The behavior of chamber 0 and chamber 5 is not fully understood. It seems that the transition radiation yield was smaller for chamber 0 and larger for chamber 5. For chamber 4 and chamber 5 also a smooth increase of the electron/pion signal ratio is visible. This again indicates again absorption of radiation that is preferably produced at high momenta, probably bremsstrahlung.

Another issue is that the improvement in pion efficiency for neural networks compared to likelihood on total deposited charge is smaller for 2004 data. The additional charge in 2002 due to bremsstrahlung should influence both methods; neural networks should not benefit more from the bremsstrahlung than LQ. The reason for the different improvement is the smaller drift time in 2004 compared to 2002. This is illustrated in Figure 7.28. The average pulse height for pions in chamber 2 is shown. It can be seen that the drift
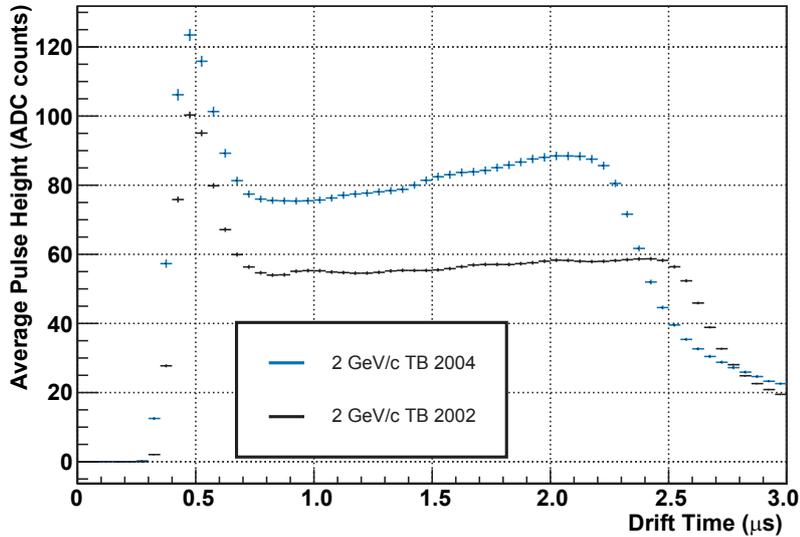
Figure 7.28: Average pulse height of pions at $2\,\mathrm{GeV}/c$ in chamber2 in 2002 (black) and 2004(blue). While the maximum drift time is at the nominal value of $2\,\mu\mathrm{s}$ for 2002 data, the maximum drift time in 2004 is smaller ($\approx 1.6\,\mu\mathrm{s}$).

time for 2002 data (black) was at the nominal value of $2\,\mu\mathrm{s}$ in the drift region, while it is only $1.6\,\mu\mathrm{s}$ for data of 2004 (blue). The smaller drift time led to less information for the neural network, since the information is splitted on less time bins. For likelihood on total deposited charge a smaller drift time has only small effects. Smaller drift time results in a larger signal per time bin. Consequently, the signal to background ratio increases. However, this is not expected to improve the pion efficiency significantly.

In this chapter it was shown that electron/pion discrimination using artificial neural networks improves the pion efficiency in test beams by a factor of 2 - 3 compared to likelihood on total deposited charge. A clear difference in the ratio of charge deposit for electrons to pions was observed, probably due to bremsstrahlung produced in 2002 in the read out connectors of the TRD chambers. Due to the observed differences it was not possible to quantify the final pion efficiency. However it was shown that the neural network method fulfilled the design goal in all test beams and showed the best electron/pion discrimination of all methods.

8. Particle Identification in AliRoot Simulations

The second analysis part of this thesis is the determination of particle identification capabilities of the Transition Radiation Detector in AliRoot simulations. In this chapter first some analysis tools are described as they are implemented in AliRoot. Later on the particle identification performance of a data set with a flat momentum spectrum and in simulated proton collisions is analyzed. Finally, the influence of contaminations of the training data set is discussed and the results of the particle identification in simulations are compared to test beam results. Unless stated otherwise, the data was simulated and reconstructed using AliRoot v4-17-Rev-12.

8.1   Analysis Tools for AliRoot

For the analysis of the particle identification performance with the Transition Radiation Detector using artificial neural networks in AliRoot simulations, three different tasks and one helper class are used. The first task, `AliTRDpidRefMaker`, provides functions for data extraction, and with the `AliTRDpidRefMakerNN` task neural networks can be trained and the training performance can be monitored. `AliTRDcheckPID` checks the particle identification performance of a data sample. The helper class is `AliTRDpidUtil` and provides functions for determining the particle identification performance.

8.1.1   The AliTRDpidUtil Class

The central function of `AliTRDpidUtil` is `CalculatePionEffi(TH1*,TH1*)`. This function performs the calculation of the pion efficiency and its error, the estimation of the threshold for a given nominal electron efficiency, and the resulting electron efficiency after the calculation of the pion efficiency. The desired electron efficiency and the final electron efficiency can differ from each other due to binning effects. The calculations are done as described in Section 6.4. The only input that is needed are two histograms (`TH1`) containing the likelihood distributions for two data sets (usually electrons and pions). The calculated values can be accessed via dedicated getters:

- `GetPionEfficiency()`,

Bin No.	nominal value (GeV/c)	Range (GeV/c)
0	0.6	< 0.7
1	0.8	$0.7 - 0.9$
2	1.0	$0.9 - 1.25$
3	1.5	$1.25 - 1.75$
4	2.0	$1.75 - 2.5$
5	3.0	$2.5 - 3.5$
6	4.0	$3.5 - 4.5$
7	5.0	$4.5 - 5.5$
8	6.0	$5.5 - 7.0$
9	8.0	$7.0 - 9.0$
10	10.0	> 9.0

Table 8.1: Default momentum bins used for the particle identification as implemented in the `AliTRDpidUtil` class.

────────

- `GetError()`,

- `GetThreshold()`,

- and `GetCalcElectronEfficiency()`.

The desired electron efficiency can be set via `SetElectronEfficiency(Float_t)`.

`AliTRDpidUtil` also provides the default momentum bins that are used for the analysis of the pion efficiency. Eleven momentum bins with various bin widths are used. The bin widths are not equal for the different momentum regions. The average charge deposit of the particles, which have momenta below their point of minimum ionization, changes with small momentum variations (see Equation 4.1 and Figure 6.2). In that momentum region the binning has to be finer than in the region beyond this points, where the changes of charge deposit do not vary so strongly. An overview of the binning is given in Table 8.1.

8.1.2   The AliTRDpidRefMaker Task

For the production of reference data the `AliTRDpidRefMaker` task is used. `AliTRDpidRefMaker` is a class which only collects the input from the available data by

looping over all available events. The production of references is performed by the two daughter classes `AliTRDpidRefMakerLQ` and `AliTRDpidRefMakerNN`.

Data Extraction with the AliTRDpidRefMaker

For the `AliTRDpidRefMaker` the identity of the used particles needs to be known. The particle identities can be extracted from the reconstruction, from Monte Carlo information, or using displaced vertices. In this section the focus lies on the production of references using the Monte Carlo particle information. Displaced vertices are discussed in Section 9.1.2. The usage of the reconstructed PID is not discussed in this thesis and is not recommended, since the purity of the particle samples is poor. The expected pion efficiency for the Time Projection Chamber is below 1% at momenta $p < 2\,\mathrm{GeV}/c$, but gets worse ($\approx 30\%$ at $10\,\mathrm{GeV}/c$) with increasing particle momentum [Ale06].

For constructing references the deposited charges have to be extracted for each track in several slices for each traversed Transition Radiation Detector layer. The input that is used for the data extraction can be the `AliESDtrack` or the `AliTRDtrack` object. `AliESDtrack`s contain the deposited charges for each track in eight slices for each traversed Transition Radiation Detector layer. Since `AliTRDtrack` objects contain all the information (charge, position, etc.) of the clusters according to a track, the number of used slices is not fixed here. The deposited charges are the reconstructed charges normalized to the track length and the cluster width in x direction. It is planned to expand the possible input to `AliAODtracks` also. This would allow to run the `AliTRDpidRefMaker` on all available data storage objects (AODs, ESDs, and ESDfriends).

The particle identification capability is momentum dependent. Therefore, it is necessary to produce reference data for different momenta. The default is to use 11 momentum bins from 0.6 - $10\,\mathrm{GeV}/c$ provided by the `AliTRDpidUtil` class. It is necessary to store not the global momentum of a track, but the momenta of the single tracklets for each traversed TRD chamber. The reason for this is that particles, especially electrons, can lose a significant part of their momentum on the way to and through the TRD. Hence, the global momentum of a track can be very different from the local one. In this task, there are two possibilities for the determination of the momentum of a tracklet. The first one is using the Monte Carlo momenta of the simulation, the second one is to use the reconstructed momenta as they are stored during the track reconstruction in the `AliESDtrack` object. It is possible to set a momentum threshold in order to suppress the amount of tracklets with small momenta.

The `AliTRDpidRefMaker` task is part of the Physics Working Group 1 (PWG1) train [Otw09] which is planned to run regularly on the grid. The PWG1 train monitors

the detector and reconstruction performances. For the Transition Radiation Detector this includes for instance monitoring of the alignment, calibration, and tracking as well as the performance of particle identification.

Reference Building with AliTRDpidRefMakerNN

After the extraction and merging of the data the references need to be constructed. For the two-dimensional likelihood method it is done by the `AliTRDpidRefMakerLQ` task. The reference neural networks are trained using the `AliTRDpidRefMakerNN` class.

The first step before training is the generation of `TTrees` that are used for the training of artificial neural networks. A network is trained for each momentum bin. The data that is stored by the `AliTRDpidRefMaker` task contains all momenta. The speed of training using `TMultiLayerPerceptron` depends on the size of the `TTree`. This time, not the speed of the training in epochs is meant, but the actual performance in computing time. It takes a longer time to train the network if a lot of unused patterns are part of the training tree, since the complete `TTree` has to be loaded and kept in the computer memory. Therefore, the tracklets are stored in different `TTrees` according to their momentum. In older versions of the `AliTRDpidRefMakerNN` the layer that was traversed by the tracklet was also taken into account. The number of trained networks was larger by a factor of six. In simulations it was shown that the particle identification performance of the artificial neural networks does not suffer from using only one network for all TRD layers. Another benefit is the smaller number of needed reference tracks. In case the layer dependence is taken into account the required number would be six times larger.

The training and validation samples for each momentum bin are determined by the function `MakeTrainingLists()`. For the neural networks two `TEventLists` have to be built. Training list and validation list are built taking all five particle species (electrons, muons, pion, kaons, and protons) into account. The training sample is twice as large as the validation data set. All particle species have to be equally represented in the two event lists, only that ensures an adequate training for all species. Since no muons and no kaons can be obtained as references by using displaced vertices (see Section 9.1.2) they are excluded from building the `TEventLists` in case their number is zero.

The neural network training is done for each momentum bin separately in the function `MakeRefs()`. The momentum bin that should be trained can be set by a steering macro using `SetTrainMomBin()`[1]. The first thing that is done by `MakeRefs()` is the creation of a directory where the trained networks are stored. A directory is created with a name

---

[1]It is also possible to train all momenta at once, but this is not recommended since it takes very long. A better solution is to train the networks for the different momentum bins separately on different computers.
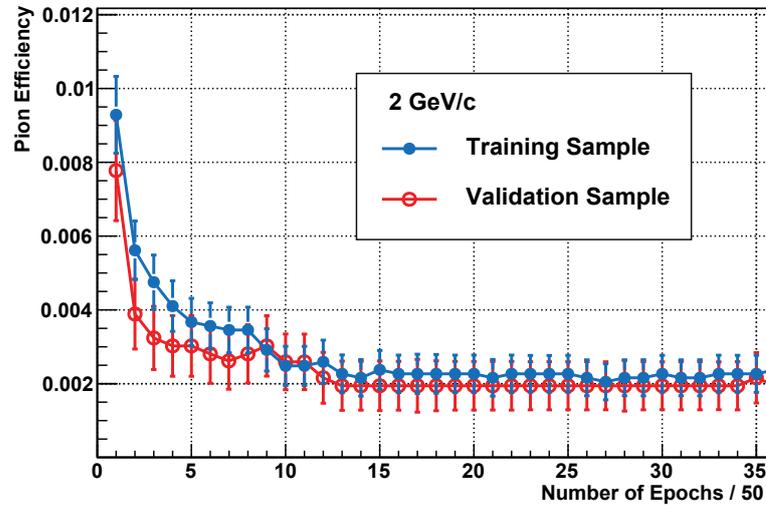
Figure 8.1: Monitoring of the training performance of simualted data with a momentum of 2 GeV/*c*. The pion efficiency for training (blue) and validation data (red) is plotted versus the number of training epochs.

———————

containing the date of the training and a subdirectory with the momentum bin. Such a structure allows to continue the training in case the network needs more training epochs. The number of training epochs can be set by the user with `SetEpochs()`. The training method is online backpropagation with a learning parameter of $\eta = 0.001$. The default number of training epochs is 1,000. The networks are saved after every 20 training epochs. Storing the networks enables the user to monitor the training progress.

The training of the networks has to be supervised in order to find the best network and to avoid overtraining. This is enabled in the `AliTRDpidRefMakerNN` task by the function `MonitorTraining()`. For this function the saved networks are reloaded one by one and the pion efficiencies are determined by applying training data and validation data to them. An example of the monitoring of training for 2 GeV/*c* data is given in Figure 8.1. Shown is the pion efficiency for the training patterns and the validation data set. A comparable structure as in the training progress for test beam data can be seen (Figure 7.8). After a fast drop the pion efficiency reaches a first plateau. With further training a second plateau is reached. The monitoring shows no further improvement. For about 50 k patterns the training is done after a loop of 1 k epochs. In case the monitoring implies that further training would still improve the pion efficiency, the training is continued with another loop of 1000 training epochs. The training usually needs more computing time for simulated data than for test beam data. The reason is that the total number of patterns is smaller for test beam data. In AliRoot simulations (and also in real data) five particle species

are taken into account, compared to only two for test beams. In addition, the number of simulated tracks is larger than the number of tracks after cuts in the discussed test beams.

After validation the neural networks are stored in the Offline Conditions Data Base (OCDB) and can be used for particle identification.

8.1.3   The AliTRDcheckPID Task

The central part of the particle identification performance analysis, the determination of the final pion efficiencies for 2-dim likelihood and artificial neural networks, is done with the `AliTRDcheckPID` task which is part of the official AliRoot framework. `AliTRDcheckPID` is also part of the Physics Working Group 1 (PWG1) train. The `AliTRDcheckPID` task uses as input `AliESDfriends` which contain the complete information of the tracks passing the TRD.

`AliTRDcheckPID`'s main purpose is to monitor the TRD PID information that is stored in the Event Summary Data (ESDs) and to recalculate it for the 2-dim likelihood and the artificial neural networks method. In addition some monitoring plots are produced for each particle species and a set of momentum bins separately. The plots are:

- likelihoods to be an electron (for ESDs, 2-dim LQ, and neural networks),

- deposited charge in each detector module,

- deposited charges in three slices of each chamber,

- average pulse height (versus time bin and versus x position),

- number of tracklets for each track,

- number of clusters for each tracklet,

- momentum for each track,

- and the momentum bin.

The particle species is obtained from the Monte Carlo information of the simulation. For real data, or in case no Monte Carlo information is available, the reconstructed particle identity is used. In case only the reconstructed particle information is available, the determination of pion efficiency does not work but the monitoring plots allow simple performance checks, e.g. if the deposited charges or the average pulse heights are as expected for the different particles. It is planned to expand the particle identity

information to be able to run on PID information also including displaced vertices (see Section 9.1.2). Using displaced vertices will allow to run also the pion efficiency determination on real data.

Usually the monitoring plots are produced for the default momentum binning stored in `AliTRDpidUtil`, but the number of momentum bins as well as the bin range can be adjusted via a setter. In order to limit the number of produced histograms, one-dimensional plots of the same kind (for the different particle species and different momenta) are stored in two-dimensional histograms. The binning in x direction is given by the number of particle types and momentum bins, the y axis binning depends on the plot type.

The likelihoods to be an electron for two-dimensional likelihood on deposited charge and artificial neural networks are calculated based on the `AliTRDtracks` as described in Section 6.5. The likelihoods stored in the ESDs are extracted directly from the `AliESDtrack` objects. These likelihoods are calculated during the reconstruction. Since the default particle identification method in AliRoot is the neural network method, the resulting likelihoods are identical in case the same Offline Conditions Data Base (OCDB) is used. In case the OCDBs are different, the performance of the references used during the reconstruction and the references used for the recalculation can be compared directly. The deposited charges, average pulse heights, and number of clusters are also extracted from the tracklets stored in the `AliTRDtrack`, the number of tracklets directly from the `AliTRDtrack`. The momentum is either extracted from Monte Carlo information if available, otherwise the reconstructed value is taken from the `AliTRDtrack`. The pion efficiency is calculated based on the likelihoods distributions and estimated using the `AliTRDpidUtil` class.

For a quick check of the particle identification performance several plots are produced and saved automatically in the `AliTRDcheckPID::PostProcess()`. There are two general performance plots:

- the pion efficiencies for 90% electron efficiency for each momentum bin

- and the according threshold in electron likelihood.

In addition monitoring plots for each particle type in the momentum bin around $2\,\mathrm{GeV}/c$ are produced. These plots are shown in Figure 8.2:

- **a)**: total deposited charge,

- **b)**: average pulse height versus time bin,
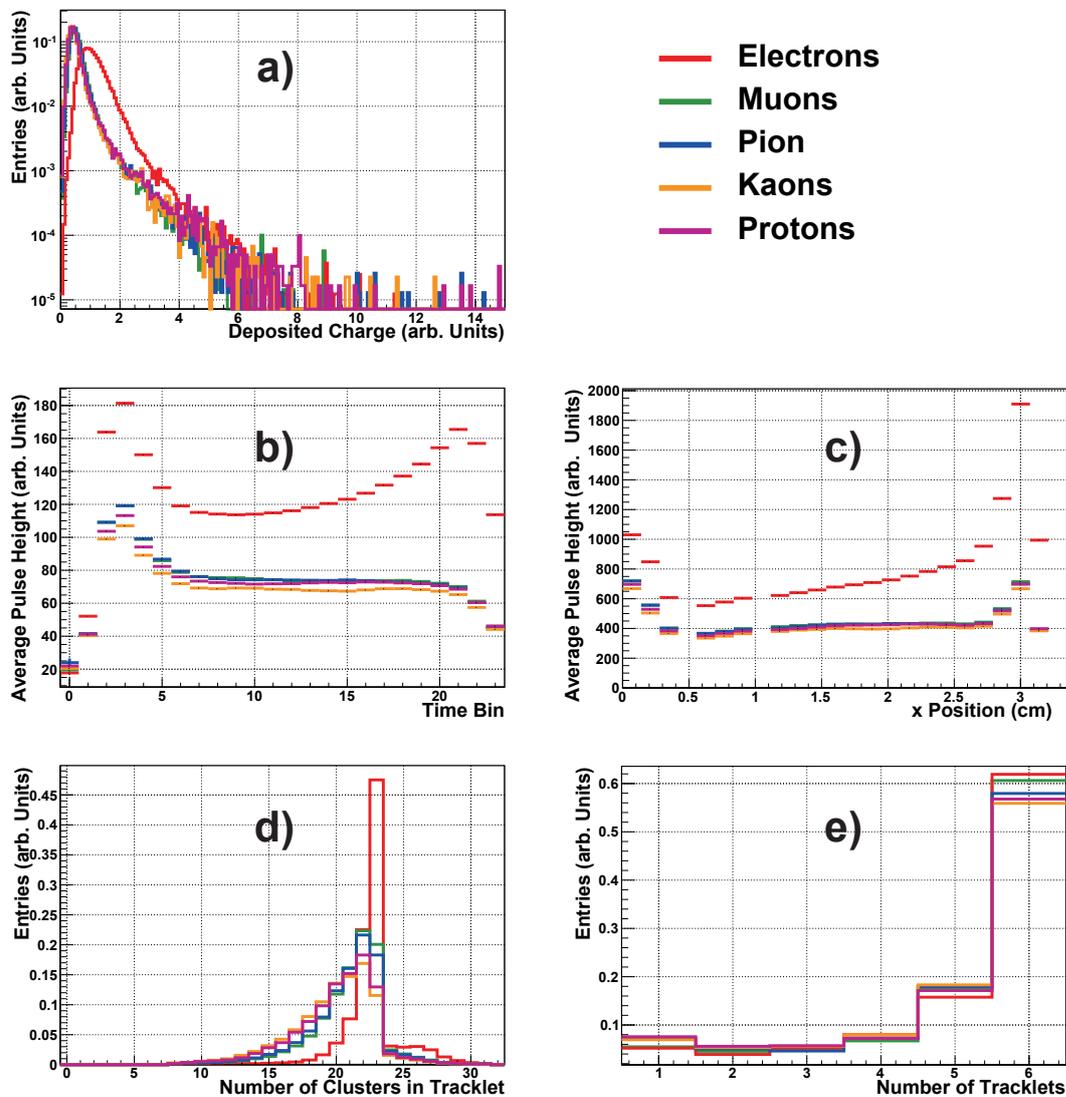
Figure 8.2: Monitoring plots of the `AliTRDcheckPID` task. The plots are shown for electrons (red), muons (green), pions (blue), kaons (orange), and protons (purple) with a momentum of $2\,\text{GeV}/c$. The plots are **a)** the deposited charge per tracklet, **b)** average pulse height versus time bin, **c)** corrected average pulse height versus x position, **d)** number of clusters per tracklet, and **e)** number of tracklets per track.

- **c)**: average pulse height versus cluster's x position in the TRD chamber,

- **d)**: number of clusters per tracklet,

- and **e)**: number of tracklets per track.

It can be seen that the total deposited charge (**a)**) and average pulse height in each time bin (**b)**) are as expected. The temporal structure of the signal in the Transition Radiation Detector is only an approximation of the x position of the clusters. For particle identification instead of the time bin the x-corrected cluster position is used. In addition the charge of the clusters is normalized to its width and with respect to the angle of the according particle track. The average pulse height in x direction (**c)**) monitors the input for the particle identification. The number of clusters per tracklet (**d)**) shows that the probabilities for the particles to produce clusters are not equal. For electrons the most probable cluster number is 23, for the other particles it is 22. The reason for the differences are fluctuations of the deposited charge. The probability for non-electrons to produce small clusters which may not be reconstructed is larger than for electrons. It can be seen that there are also entries for numbers of clusters larger than 24. In case a track crosses two pad rows the clusters on both sides are counted. This is needed for quality checks of the track reconstruction [Ber09a]. Therefore, the number of clusters can exceed the theoretical limit of 24. The number of tracklets per track (**e)**) is also not the same for all particle species, but the differences are not large.

8.2 PID Performance in Simulations with Flat Transverse Momentum Distribution

For the analysis of detector performances it is not useful to simulate physics events, such as *pp* or *PbPb* collisions. Since the transverse momentum spectrum of particles drops very steeply, a lot of events need to be simulated to evaluate the performance at high momenta. Instead of simulating collisions, events with unrealistic momentum and particle distributions are produced.

8.2.1 Data Production

For the determination of the particle identification performance events containing 200 particles are simulated. The mixture consists of 20 electrons, 20 muons, 20 pions, 20 kaons, and 20 protons as well as of an equivalent number of the respective anti

particles. In order to populate also high momenta, the simulated momentum spectrum is flat and reaches from 0.15-15 GeV/c. Since we are only interested in the Transition Radiation Detector, only the ALICE *Inner Barrel* is simulated. This includes the Inner Tracking System (ITS), the Time Projection Chamber (TPC), the Transition Radiation Detector (TRD), and Time Of Flight (TOF). The simulated pseudo-rapidity range for the particles is $-1.5 < \eta < 1.5$ and the magnetic field is set to 0.5 T which is the nominal field strength of the L3 magnet. For this analysis 11,000 events were simulated. This corresponds to 440,000 particles (plus anti particles) for each simulated particle species.

All events are fully reconstructed using the global track reconstruction. For each track also the `AliESDfriends` are saved. In the `AliESDfriends` for the TRD, information about tracklets and the according clusters (e.g deposited charge, time bin) produced in the Transition Radiation Detector are available. This allows to use the maximum information for the analysis and not just the information stored in the ESDs.

The data production was done several times and for different AliRoot versions in order to build reference data for the neural networks using the `AliTRDpidRefMaker`. The training was done as described in Section 8.1.2. The data that will be discussed in this section was simulated and reconstructed with AliRoot v4-17-Rev-12. The determination of the pion efficiency for 2-dim LQ and neural networks was done using the `AliTRDcheckPID` task. The references for the analysis have not been rebuilt. Instead, the default OCDB entries of the AliRoot version were used.

8.2.2   Pion Efficiency

1-dim Likelihood

Contrary to the artificial neural networks and the two-dimensional likelihood method, the one-dimensional likelihood method is not yet implemented in AliRoot. Therefore the extraction of likelihoods for the LQ method was not performed by the `AliTRDcheckPID` task directly. Instead, a modified `AliTRDcheckPID` task was executed twice on the complete data set. For the first loop, the task does not necessarily needed to be modified. The only function of the first loop was the production of reference data for the one-dimensional likelihood method. References for the 1-dim LQ method are the distributions of total deposited charge. These deposited charge distributions are produced by default by the `AliTRDcheckPID` task. The distributions were saved and used in the second data loop as reference histograms. During the second loop the total deposited charges of the tracks were compared to the references and the likelihoods were calculated using Equations 6.2 and 6.4. The resulting one-dimensional likelihood plot is shown in Figure 8.3 **a)**. The
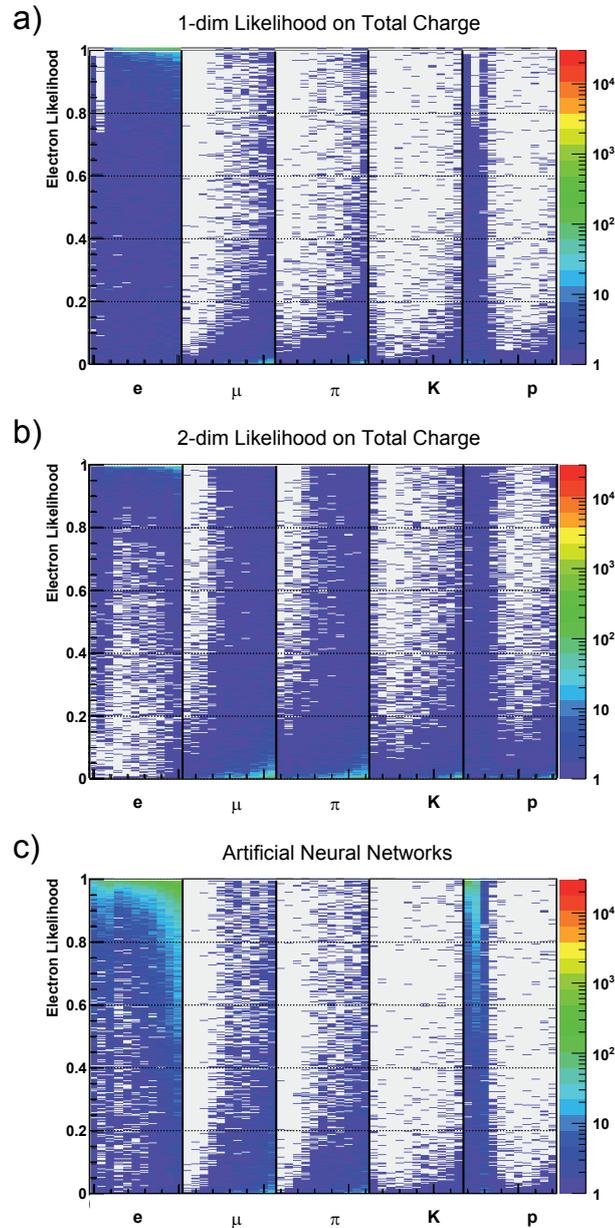
Figure 8.3: Likelihood to be an electron for **a)** one-dimensional likelihood (LQ), **b)** two-dimensional likelihood (2-dim LQ), and **c)** artificial neural networks. The likelihood is plotted versus different particle classes. A particle class is given by one of the eleven default momentum bins and the particle identity. The color represents the frequency of occurrence on a logarithmic scale. The missing entries for 1-dim likelihood for electron and protons at the second momentum bin (0.8 GeV/c) and high electron likelihood is caused by the fact that electrons and protons in this momentum region deposit the same amount of charge and therefore could not be well discriminated.
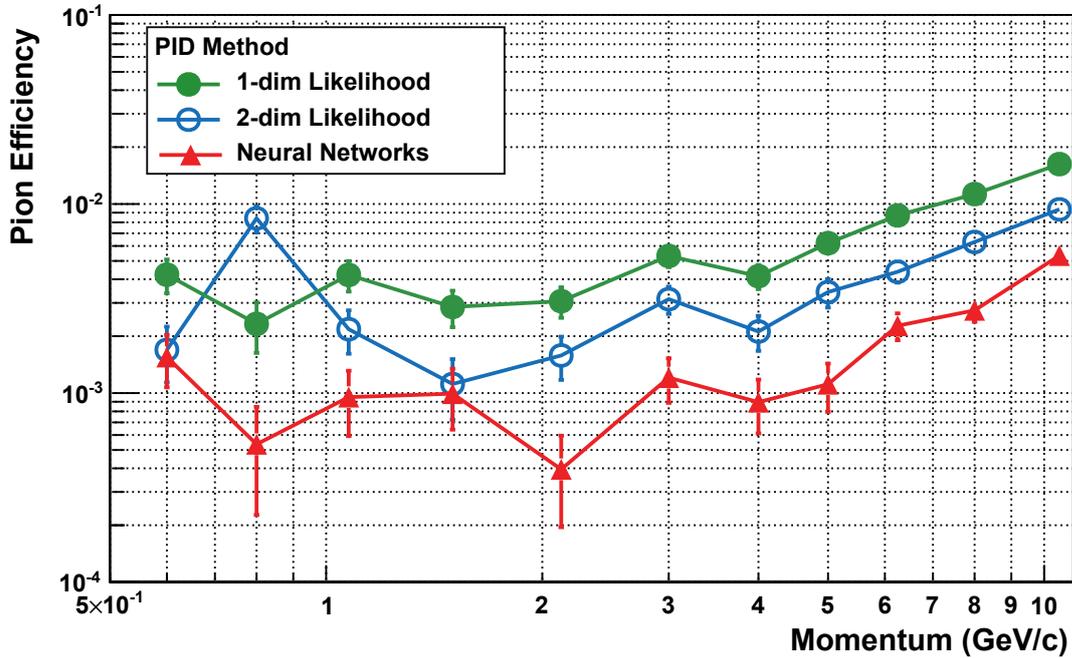
Figure 8.4: Pion efficiency versus momentum for neural networks (red triangles), 1-dim likelihood (green dots) and 2-dim likelihood (blue circles). It can be seen that the pion efficiency depends on the complexity of exploited information. The more information is taken into account the better is the performance.

electron likelihoods for the 11 momentum bins of the five different particle species are shown. The color represents the number of observed particles. The missing entries for 1-dim likelihood for electron and protons at the second momentum bin (0.8 GeV/*c*) and high electron likelihood are caused by the fact that electrons and protons in this momentum region deposit the same amount of charge. Consequently, they cannot be well discriminated.

2-dim Likelihood and Neural Networks

The two-dimensional likelihood method and the artificial neural networks are standard methods for particle identification in AliRoot using the TRD. The likelihoods are monitored directly by the `AliTRDcheckPID` task. They are shown in Figure 8.3 for the 2-dim LQ method **b)** and for the neural networks **c)**.
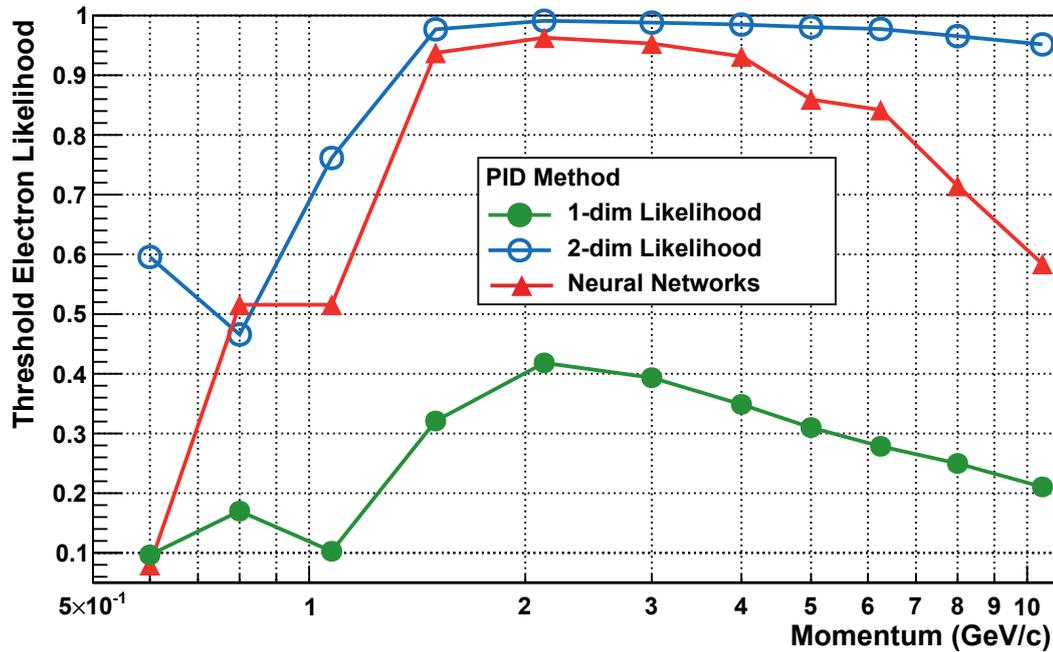
Figure 8.5: Threshold for 90% electron efficiency versus momentum for neural networks (red triangles), 1-dim likelihood (green dots, and 2-dim likelihood (blue circles).

Results

The resulting pion efficiencies are shown in Figure 8.4, the thresholds for 90% electron efficieny in Figure 8.5. The green dots represent results for the 1-dim likelihood method, the blue circles that of the 2-dim likelihood, and the red triangles that of artificial neural networks. A clear trend is visible: the best performance is achieved with neural networks followed by the two-dimensional likelihood method. The one-dimensional likelihood method has the worst electron/pion discrimination capability. The difference between the results of neural networks and 2-dim LQ is about a factor of two, between neural networks and 1-dim LQ about four. It can be seen that for momenta above $2\,\text{GeV}/c$ the trend in pion efficiencies of the different methods is identical, the pion efficiencies vary in the same direction. For momenta below $2\,\text{GeV}/c$ this is only true for 1-dim LQ and neural networks. The pion efficiencies in the low momentum region for 2-dim LQ do not follow the trend of the other two methods.

The average deposited charges for the different particles have crossing points at low momenta for electrons and kaons (at about $0.5\,\text{GeV}/c$) as well as for electrons and protons (at about $0.8\,\text{GeV}/c$, see Figure 6.2). The average deposited charge coming from

a high value decreases fast with rising momentum for kaons and protons until the point of minimum ionization is reached. This means that for kaons and protons the average deposited charge strongly fluctuates in a small momentum range. In addition, at low momenta only few kaons reach the TRD due to their limited life time. The 2-dim likelihood method needs more particle tracks for reference building. The described factors could lead to non-ideal references and could cause the worse pion efficiency of 2-dim LQ compared to the other methods [Ber09a].

8.2.3   Hadron and Muon Efficiencies

The Transition Radiation Detector was designed to suppress pions at momenta above $1\,\text{GeV}/c$. However, the TRD's particle identification capability is not limited to discriminating electrons from pions. The deposited charges of other hadrons as well as of muons behave similar to that of pions. They do not produce transition radiation for the momenta discussed here[2]. The deposited charge depends only on the energy loss due to ionization (Bethe-Bloch, Equation 4.1). Consequently, the TRD should not only be able to suppress pions but also muons, kaons, and protons.

The expected performance (see Section 6.1) of the muon suppression is slightly worse than for the pion suppression. The reason is the smaller mass of the muon which leads to higher values of $\beta\gamma$ at same momenta. The result is a smaller difference to the electron charge deposition than it is for pions. The kaon suppression is expected to be better at higher momenta, for the same reason. For small momenta, the energy deposition of kaons is larger than that of electrons. This leads to a worse performance compared to pions. The same is true for protons, but the effect should be even larger than for kaons. In Figure 8.6 the muon efficiency (**a**)), the kaon efficiency (**b**)), and the proton efficiency (**c**)) are shown. It can be seen that the expectations are fulfilled for all particle types, momenta, and particle identification methods.

8.3   Particle Identification in Proton-Proton Collisions

In the previous section the capability of the ALICE Transition Radiation Detector in discriminating electrons from hadrons and muons was analyzed separately for each particle species. It makes sense to analyze the discriminations separately for each species, since it allows to estimate the total non-electron rejection power of the TRD for any set

---

[2]The threshold for the production of transition radiation is at $\gamma \approx 1000$ (see Section 4.2.2). This means for instance that muons will produce transition radiation for momenta above $100\,\text{GeV}/c$.
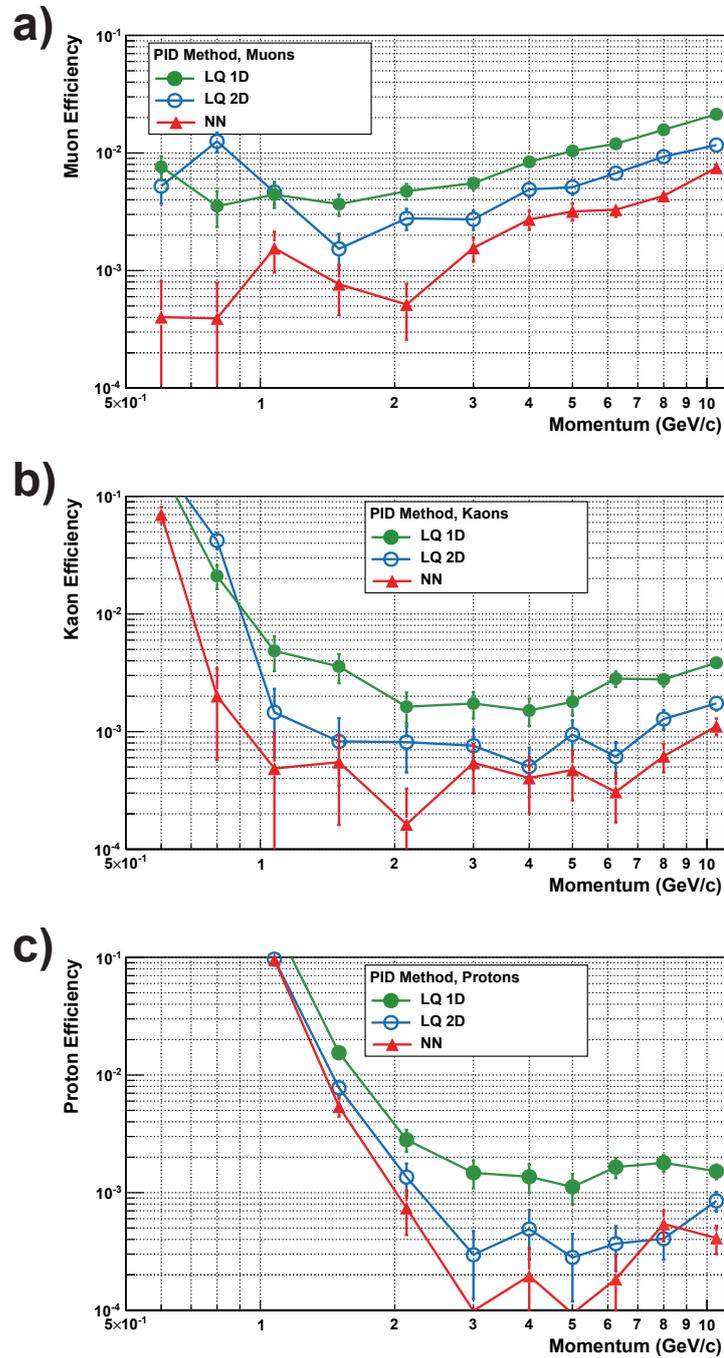
**Figure 8.6: a)** Muon efficiency, **b)** kaon efficiency, and **c)** proton efficiency at 90% electron efficiency versus momentum for neural networks, 1-dim likelihood and 2-dim likelihood.

of particle abundances. Different analyses can have different particle abundances which enter the a-priori probabilities of the Bayesian probability estimation (see Equation 3.4). In this section the TRD particle identification will be analyzed for particle abundances as they are expected in proton collisions. In addition to the electron identification power also the PID capability for the other particle species in *pp* collisions is discussed.

8.3.1   Simulated Proton-Proton Collisions

The electron identification power of the TRD in *pp* collisions was determined on a simulated data set of about 4.5 million proton-proton events with a collision energy of 10 TeV. The data set was part of the regular Monte Carlo data production at *Gesellschaft für Schwerionenforschung* (GSI) [Mas09b].   It was produced with AliRoot v4-16-Rev-05. In the data production the complete ALICE experiment including all 18 TRD supermodules was simulated. The data was analyzed using a task participating in the GSI analysis train [Mas09a].

In Figure 8.7 global parameters of the data set are monitored. The number of found `AliESDtracks` per event is shown in **a)**.   The number of `AliTRDtracks` which are traversing six TRD layers can be found in **b)** and their momentum distribution is plotted in **c)**. In the data set about 3 million `AliTRDtracks` with six tracklets are found. The total particle abundances in the simulated *pp* collisions are shown in Table 8.2, the relative abundances in Table 8.3. Pions are the dominant particle species for all momenta. At low momenta 85% of all particles are pions. The rate of pions decreases with rising momentum to about 65%. The particle abundances stay approximately constant for momenta above 4 GeV/*c*. Kaons reach $\approx 20\%$, protons $\approx 15\%$, electrons $\approx 0.5\%$, and muons 0.25%.

The electron probabilities for all tracks traversing six TRD layers are extracted from the `AliESDtrack` objects. The default particle identification method for the TRD is the neural network method and was not changed in the reconstruction. The pion efficiency determined with artificial neural networks for the default momentum bins and 90% electron efficiency can be found in Figure 8.8. The total amount of electrons with momenta above 3.5 GeV/*c* is so small that the measured pion efficiency might not be representative. The muon, kaon, and proton efficiencies are also shown in Figure 8.8.

8.3.2   Electron Identification in Proton-Proton Collisions

Until now only the pure discrimination power of the TRD compared for electrons and one other particle type was discussed. In the real experiment and in data analyses not just
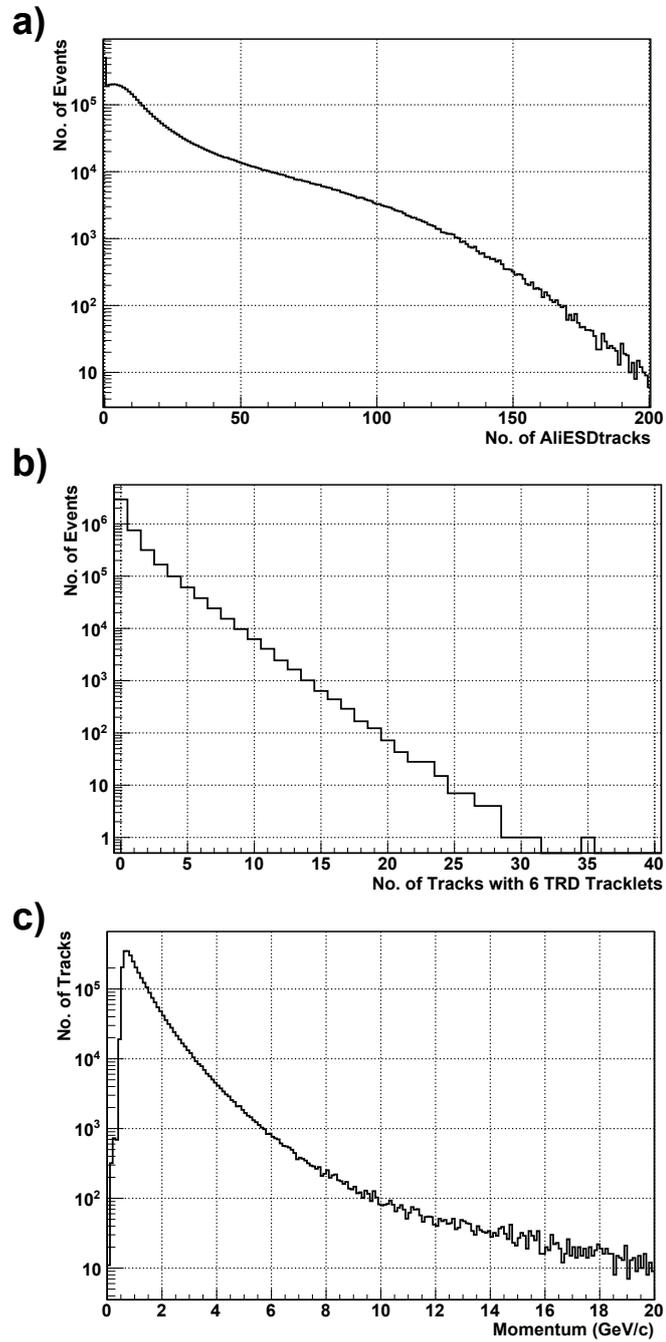
Figure 8.7: Results of simulation of 4.5 million 10 TeV *pp* collisions. **a)** number of ESDtracks per event, **b)** number of TRDtracks traversing six chambers, and **c)** number of TRDtracks traversing six chambers versus momentum.

Momentum (GeV/c)	e	μ	π	K	p	Total
<0.7	9810	14072	489337	27960	35167	576346
0.7-0.9	7029	9453	526839	44831	60841	648993
0.9-1.25	5703	6433	539903	65464	71884	689387
1.25-1.75	3818	2827	365749	61351	56212	489957
1.75-2.5	1903	1034	207251	43694	39707	293589
2.5-3.5	636	318	89505	22685	19841	132985
3.5-4.5	197	115	29736	8434	7016	45498
4.5-5.5	102	40	11671	3405	2977	18195
5.5-7.0	59	41	6789	2076	1608	10573
7.0-9.0	29	10	3119	940	728	4826
>9.0	81	31	4836	1523	1233	7704

Table 8.2: Total particle abundances for `AliTRDtracks` traversing all six layers in 4.5 million 10 TeV *pp* collisions.

————

Momentum (GeV/c)	e	μ	π	K	p	Total
<0.7	0.01702	0.02442	0.84903	0.04851	0.06102	1.00000
0.7-0.9	0.01083	0.01457	0.81178	0.06908	0.09375	1.00000
0.9-1.25	0.00827	0.00933	0.78316	0.09496	0.10427	1.00000
1.25-1.75	0.00779	0.00577	0.74649	0.12522	0.11473	1.00000
1.75-2.5	0.00648	0.00352	0.70592	0.14883	0.13525	1.00000
2.5-3.5	0.00478	0.00239	0.67305	0.17058	0.14920	1.00000
3.5-4.5	0.00433	0.00253	0.65357	0.18537	0.15420	1.00000
4.5 5.5	0.00561	0.00220	0.64144	0.18714	0.16362	1.00000
5.5-7.0	0.00558	0.00388	0.64211	0.19635	0.15209	1.00000
7.0-9.0	0.00601	0.00207	0.64629	0.19478	0.15085	1.00000
>9.0	0.01051	0.00402	0.62773	0.19769	0.16005	1.00000

Table 8.3: Relative particle abundances for `AliTRDtracks` traversing all six layers in 4.5 million 10 TeV *pp* collisions.

————
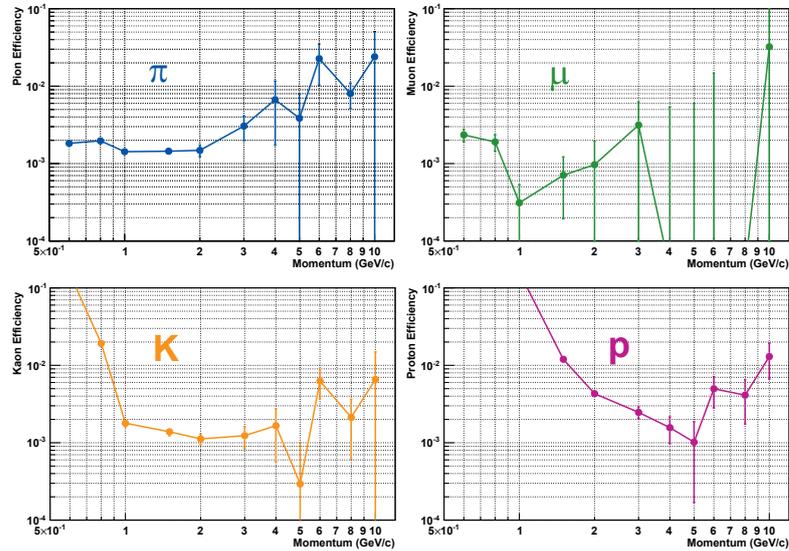
Figure 8.8: a) Pion efficiency, **b)** muon efficiency, **c)** kaon, and **d)** proton efficiency versus momentum for neural networks in *pp* collisions.

————————
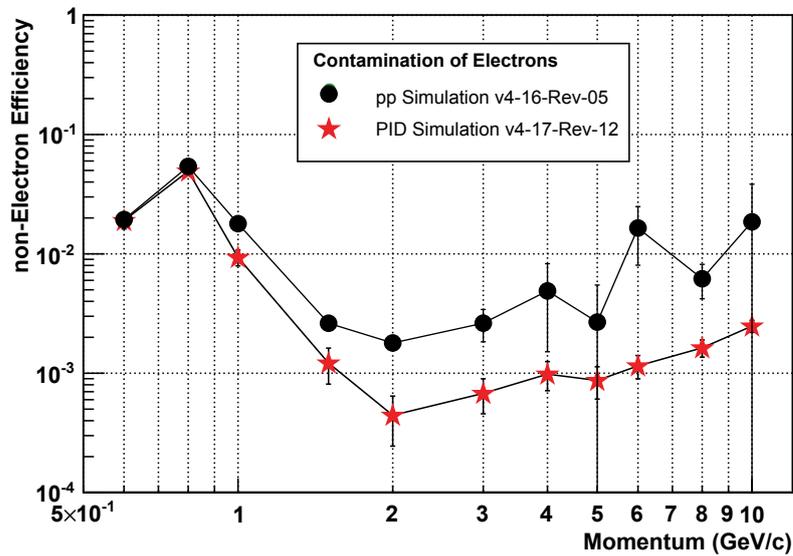
Figure 8.9: Non-electron efficiency versus momentum for artificial neural networks. The results of a direct calculation (black dots) and of an indirect estimation using the momentum dependent multiplicities (red stars) are shown. For details refer to the text.

————————

electrons and e.g. pions are measured. The abundances of the different particle species depend on the type of data analysis and the selection cuts. The discrimination power of the ALICE Transition Radiation Detector between electrons and other particles in minimum bias *pp* collisions is analyzed in this section. The *non-electron efficiency* is the equivalent to the pion efficiency but combined for all particle types and not for one type solely. The non-electron efficiency for a given electron efficiency of 90% using artificial neural networks is shown in Figure 8.9 for the default momentum bins (black dots). The non-electron efficiency is very similar to the pion efficiency (see e.g. Figure 8.8) for momenta above 1.5 GeV/*c*. This is expected since pions, muons, kaons, and protons produce similar signals in the TRD for these momenta. For lower momenta the picture is different. Kaons and especially protons deposit a total charge which is comparable to that of electrons. It is not possible to discriminate them via their deposited charge. The production of transition radiation by electrons does not reach the full yield (due to the low momentum, see Section 4.2.2 or Figure 6.2) and therefore the discrimination due to the distribution of charge in the TRD also fails. The result is a worse non-electron efficiency at low momenta.

As mentioned before the number of tracks with high momenta is very low. Therefore the data sample of 4.5 million *pp* collisions is not well suited to determine the particle identification power at high momenta. Nevertheless, the data set is large enough to estimate the relative particle abundances. Using the relative abundances and the likelihood distributions determined with flat-momentum particle spectra (Figure 8.3 **c)**) it is possible to estimate also the non-electron efficiencies for the higher momentum region.

For the determination of the non-electron efficiency two likelihood histograms have to be created for each momentum bin, one for the electrons and one for the non-electrons. The electron histogram is simply extracted from Figure 8.3 **c)**. The non-electron histogram has to be newly created. Based on a random number the non-electron particle type is determined according to the relative abundances in *pp* collisions. The likelihood distributions can be interpreted as probability distributions for a particle of a given type to have a given likelihood. With a second random number based on the likelihood distribution the likelihood to be an electron is determined and is filled to the non-electron histogram. The procedure is performed until the number of entries for the non-electrons equals the number of electrons. With the electron histogram and the resulting non-electron histogram the pion efficiency is calculated using the `AliTRDpidUtil` class.

The calculated non-electron efficiencies based on the particle abundances of *pp* collisions (extracted using the flat-momentum likelihood distributions) are shown as red stars in Figure 8.9. It can be seen that the non-electron efficiencies determined using

the flat-momentum particle spectra has a significantly better performance than the directly calculated pion efficiencies for most momenta. The reason for this difference could be the different versions of AliRoot that have been used for the simulation and reconstruction of the two data sets. AliRoot v4-16-Rev-05 is from January 2009 and v4-17-Rev-12 is from October of the same year. In the meantime the TRD reconstruction code evolved and a lot of features were implemented which were not available in the older version. Important changes are [Ber09a]:

- Both charges deposited by a particle track on two different pad rows are taken into account for the reconstructed charge deposition (*pad row crossing*).

- The normalization of deposited charges in a cluster was improved by taking into account the bin width in *x* direction.

- The assignment of a cluster's deposited charge to one of the eight slices used for particle identification was changed. In older software versions the time bins were used directly, in newer ones the cluster's *x* position in the chamber is taken.

The changes described above may give rise for the deviation of the non-electron efficiencies for different AliRoot versions. However, it cannot be excluded that the observed deviations of non-electron efficiencies also result to some extent from the different simulation scenarios.

8.3.3 Hadron Identification

The Transition Radiation Detector is not only able to discriminate electrons from other particles. One of the components of the signal used for particle identification in the TRD is the transition radiation, which is only produced (in the regarded momentum range) by electrons. However, the charge deposit due to ionization (Bethe-Bloch equation) is also part of the PID signal and is exploited. The average deposited charge for muons, pions, kaons, and protons differs from each other. The difference can be large at small momenta, but is small at momenta above $1.5\,\mathrm{GeV}/c$.

Analogously to the electrons, the analysis of TRD's identification power can be applied to the other particle species. The results for the other particles using artificial neural networks can be found in Figure 8.10. The non-electron efficiency (red) together with non-muon efficiency (green), non-pion efficiency (blue), non-kaon efficiency (orange), and non-proton efficiency (purple) (labeled as contamination) is shown in a *pp* collision environment for 90% efficiencies. It can be seen that the
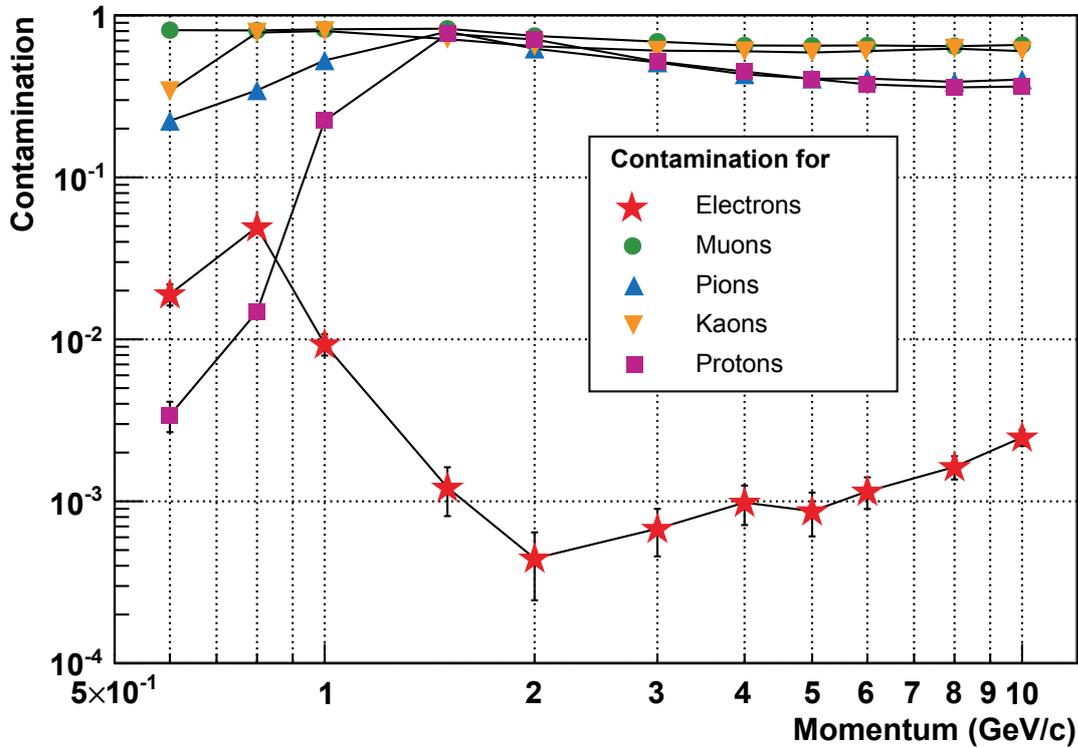
Figure 8.10: Contamination versus momentum for neural networks and different particle species. The results for electron (red stars), muon (green dots), pion (blue triangles), kaon (orange triangles), and proton (purple squares) identification are shown.

identification power for hadrons and muons is not very good, but is also not zero. At low momenta protons can be identified very well. With rising momenta the "contamination" gets worse but improves again for protons and pions. For protons the reason is that they are close to the minimum ionization even at high momenta, while the charge deposition increases again for the other particle classes (see Figure 6.2). Pions are better identified since their average deposited charge is relatively high compared to the other particles. In fact the charge deposition by muons is close to that of pions, but the relative muon abundance is so small that it does not play a role for the identification of pions. Muons cannot be well identified since pions are the dominant particle species in the background. The performance of kaon identification is also very poor. The reason is that its average value for deposited charge is in between that of pions and that of protons. Therefore, pions as well as protons can deposit similar charges as kaons and falsely be identified as kaons.

8.4   Contamination Studies

An important question is how clean a training sample for artificial neural networks has to be in order to train a neural network for particle identification sufficiently well. In simulations it is no problem to generate clean data without any contamination since the Monte Carlo information about the particle's identity is available. In reality this is different. It is possible to extract relatively clean data samples from test beams or from displaced vertices (see Section 9.1.1). However, these data samples are not totally uncontaminated. In this section the level of contamination that could be accepted is analyzed. After that the performance of simulated data applied to the neural networks trained with test beam data from 2007 is determined, which has been found to be contaminated as discussed in Section 7.5.3.

8.4.1   Simulated Contamination in Proton-Proton Collisions

For the study of influences of contaminations on the training performance "contamination" is defined in the following way: A fraction of particles is identified correctly, their true identity is assigned to them for the training. Another fraction of particles is identified incorrectly. This fraction is the so called contamination. The contamination sample is composed such that no particle identification is taken into account and the particle abundances are given by the a-priori probabilities of pp collisions. The contamination sample was obtained using random numbers for its generation. An example of the final particle rates is given in Table 8.4 for $2\,\mathrm{GeV}/c$ data with a contamination of 30%. The pion sample consists of about 90.1% of pions. The 90.1% of pions are composed of 70% of correctly identified pions plus about 20% coming from the contamination sample which consists of about 65% of pions (see Table 8.3)[3].

   For this analysis data was simulated with an AliRoot HEAD version from end of March 2008 (Revision 25008). The used AliRoot version is very similar to AliRoot v4-12-Release. Based on the calculated particle rates for different contamination levels, training samples were created for 2 and $10\,\mathrm{GeV}/c$ data and contaminations of 0%, 1%, 5%, 10%, 15%, 20%, 30%, ..., 100%. The training was done for 1,000 epochs. The validation was carried out with a data set with true particle identities. The results for non-electron efficiency of $2\,\mathrm{GeV}/c$ and $10\,\mathrm{GeV}/c$ data and different levels of contamination is shown in Figure 8.11. It can be seen that artificial neural networks are robust against contamination

---

[3]The numbers deviate from the abundances extracted from the pp collisions. The used abundances were an older estimation of the expected particle rates (e:5.8%, μ:0.5%, π:65.2%, K:7.7%, and p:20.8%). It is not necessary to use the exact particle ratios since only the effect of contamination shall be shown.

Sample of	e	μ	π	K	p	Total
Electrons	0.720	0.002	0.194	0.020	0.064	1.000
Muons	0.019	0.706	0.192	0.020	0.064	1.000
Pions	0.022	0.001	0.901	0.021	0.055	1.000
Kaons	0.018	0.001	0.202	0.71.7	0.062	1.000
Protons	0.018	0.002	0.205	0.025	0.750	1.000

Table 8.4: Relative particle abundances for $2\,\mathrm{GeV}/c$ data and a contamination of 30%. In order to analyse contamination effects the particle samples for the training were changed according to these numbers.

———————
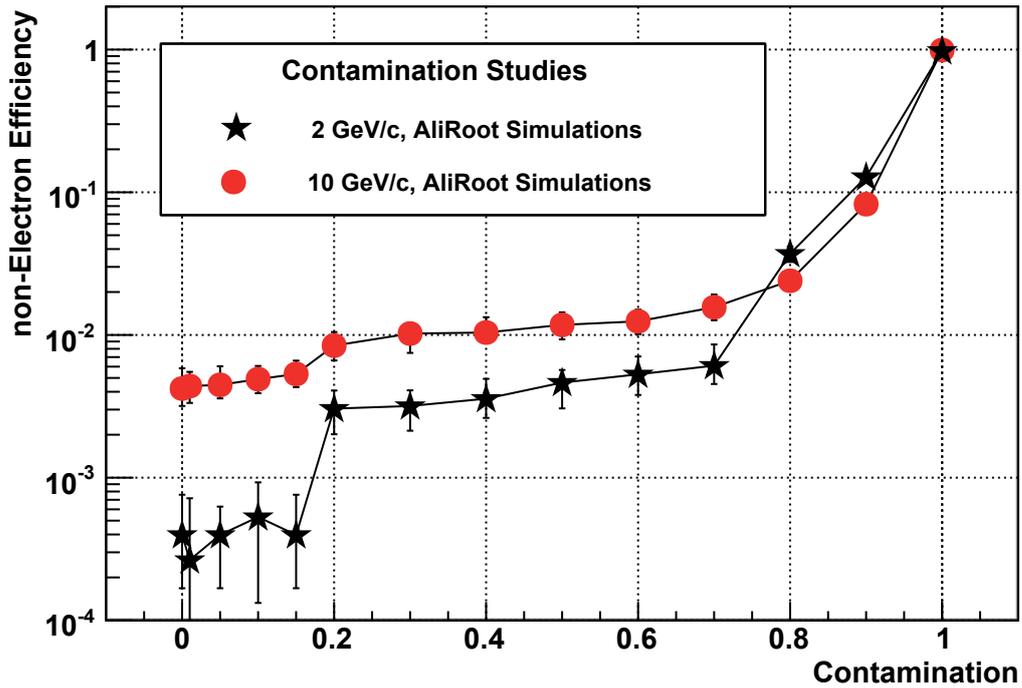
Figure 8.11: Non-electron efficiency versus level of contamination for $2\,\mathrm{GeV}$ (black stars) and $10\,\mathrm{GeV}/c$ (red dots) particles. For details please refer to the text.

———————
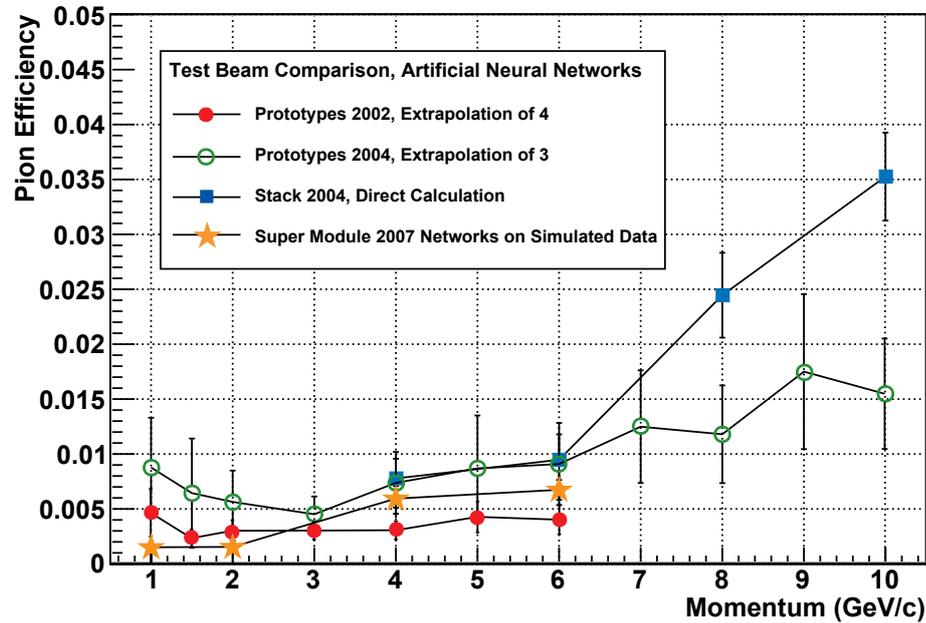
Figure 8.12: Pion efficiency from test beam analyses versus momentum for neural networks. Shown are the results obtained in 2002 (red dots), for prototypes obtained in 2004 (green circles), for a stack of real size chambers in 2004 (blue squares), and simulated data applied to networks trained with data taken in 2007. These results obtained with simulated data fit well with the other test beam pion efficiencies.

of the training sample up to a level of 15%. Even above 15% the pion efficiency remains below a total value 1% (2%) for $2\,\mathrm{GeV}/c$ ($10\,\mathrm{GeV}/c$) data up to contaminations of 70%.

A data set that is extracted in the real experiment may have other a-priori probabilities for the contamination. Nevertheless, it is shown that even with a data set where the particle identities are not totally correct, networks for particle identification can be trained with sufficient quality. Anyway, the contamination should be as small as possible otherwise it is not possible to determine the performance in particle identification correctly in the real experiment.

8.4.2   Performance of Beam Time 2007 Networks on Simulated Data

In the previous section it was shown that networks trained with contaminated training data could, up to a contamination value of 15%, perform equally well as networks trained with non-contaminated data. In Section 7.5.3 it was discussed that the electron and pion samples of the test beam data 2007 are most likely contaminated with double tracks. Due to the contamination no reasonable results of the particle identification performance could

be achieved. One of the main goals of the test beam 2007 was to check if reference data for the real experiment could be extracted. Motivated by the contamination studies an analysis is presented in order to fathom the possibilities of using the networks that were trained with the test beam data of 2007. The used runs can be found in Appendix C.3.2.

For the simulation the same AliRoot version as for the contamination studies was used (Revision 25008). Since the test beam data was not calibrated, a correction factor had to be applied to the deposited charge of the simulated data to match the values of the training data set. This correction value was determined by comparing the deposited charge at the plateau of the average pulse height distributions for pions. For 1 GeV/c particle momentum the correction factor is 0.8, for 2, 4 and 6 GeV/c it is 0.5. The difference comes from changing the voltage of the anode wires of the TRD chambers between the 1 GeV/c run and the other runs. The simulated data has only 24 time bins but test beam data has 30 time bins. This leads to a number of eight input neurons for simulations and ten for test beam data. Therefore, the input vector of the simulated data was modified by adding two components containing zero (neuron eight and neuron nine). These two components represent the slices with largest drift time and contain mostly ion tails. For test beam data after tail cancellation, their contents are approximately zero (see Figures 7.21 and 7.22).

The neural networks were trained with test beam data from 2007. The resulting pion efficiencies obtained with simulated data can be found in Figure 8.12. It can be seen that the pion efficiencies match well to the results from the test beam in 2002. For 4 and 6 GeV/c the pion efficiencies are also consistent with the 2004 test beam results. Even more interesting are the results shown in Figure 8.13. The result of the simulated data applied to networks trained with (contaminated) test beam data (orange stars) yields the same pion efficiencies as data from simulations of pp collisions applied to networks trained with simulated data (open purple squares). In the opposite case, i.e. for neural networks trained with simulated data and pion efficiencies calculated using the contaminated 2007 test beam data, no reasonable results could be obtained. The contamination with double tracks could not be completely reduced and resulted in a large background ($\approx 5\%$) of particles with a high electron likelihood ($L_e > 0.99$) tagged as pions in the validation data set.

8.5   Comparison to Test Beam Results

In Figure 8.13 all pion efficiencies determined with artificial neural networks are summarized. It can be seen that not all the results are consistent with each other. The best performance is achieved with simulations using AliRoot v4-17-Rev-12 with a flat-
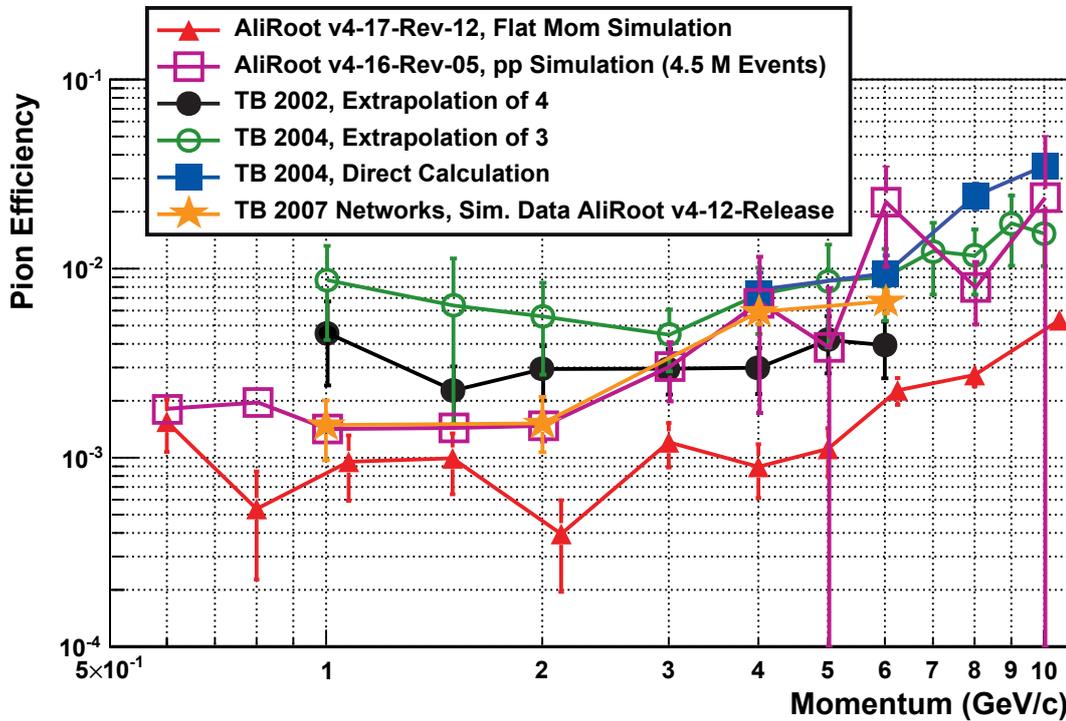
Figure 8.13: Pion efficiency versus momentum for neural networks. The results for simulations using flat-momentum spectra (red triangles) and 10 TeV *pp* collisions (open purple squares), from test beams 2002 (black dots), 2004 (green circles and blue squares), and simulations applied to networks trained with test beam data (orange stars) are shown.

---

momentum spectrum (red triangles). The pion efficiencies of this simulation are better at all momenta and are not consistent with the other results within errors. The result from *pp* collisions (open purple squares) and the result using simulated data on test beam 2007 networks (orange stars) are more consistent with the test beam results. The best performance of real data is achieved with data from test beam in 2002 (black dots). The differences between the pion efficiencies may have several reasons as discussed below.

Simulation One possible reason for the observed inconsistency could be due to deviations between simulations and reality, e.g. a false estimate of the detector material in simulations. A known source for potential discrepancy is the generation of transition radiation. In AliRoot (using GEANT3) it is not simulated directly but parameterized from test beam measurements. These possible differences between simulations and reality are currently under investigation [And09b].

Reconstruction   The test beam data obtained in 2002 and 2004 was not reconstructed using the AliRoot reconstruction code. Instead just charges on the read out pad with largest deposited charge and its two neighbors were used for "cluster building". The deposited charges were assigned according to their time bin. The momentum was assumed to be the nominal momentum of the test beam. In the TRD reconstruction code a momentum correction is applied since especially electrons can lose a significant part of their momentum. As a consequence other references, according to the new momentum, have to be used for these electrons. For test beam data a momentum correction is not possible due to the absence of a magnetic field. Nevertheless, the test beam data are consistent with the results shown for older AliRoot (v4-12-Release and v4-16-Rev-05) simulations and momenta above $3\,\mathrm{GeV}/c$. As discussed before in Section 8.3.2, the differences from the reconstruction point of view are larger for newer AliRoot simulations (v4-17-Rev-12). The cluster position in x direction is corrected and the deposited charge is corrected due to different bin width in x direction. In addition, pad row crossing is taken into account [Ber09a].

Analysis   The analysis procedures are very similar for simulations and test beam data. However, a large difference is of course the estimation of the particle identity. In simulation the Monte Carlo identity is available, but in test beams independent particle identification detectors have to be used. Roughly estimated, the contamination is $< 0.3\%$ (see Section 7.4.3). However, such contaminations should not affect the pion efficiency calculations using the extrapolation method. Another possibility is that the error bars are too small. It was observed that fluctuations in the data sets could cause large differences (see Section 7.3.3). The error bars only take into account the statistical error (see Section 6.4.2), errors coming from the non-ideal references are not considered. Non-ideal references could be caused by problems associated with the neural network training (see Section 5.4.2).

The reasons discussed above may explain all the differences observed. Probably all of them contribute to a certain extent to the observations. However, the data and the procedures outlined above do not provide a handle to clearly identify and quantify the contributions.

9. Applications of the TRD Particle Identification in ALICE

While the topic of the previous two chapters was the electron identification with the Transition Radiation Detector alone, this chapter will shed more light on the TRD PID within ALICE. It includes the generation of reference data for particle identification in ALICE (Section 9.1), electron identification with the Transition Radiation Detector for a trigger on electrons with a high transverse momentum (Section 9.2), and the measurement of dielectrons with the ALICE central barrel (Section 9.3).

9.1 Reference Data for Particle Identification

Particle identification for the Transition Radiation Detector works by comparing an obtained signal to some reference. Based on that the probabilities for the track to originate from different particle species is calculated. For the TRD the references are the two-dimensional histograms, used for the two-dimensional likelihood method, or trained artificial neural networks. In order to get good estimates of the probabilities it is crucial to build the reference histograms and to train the neural networks with high-purity particle samples. A study of the required purity for a successful training of artificial neural networks is presented in Section 8.4.

9.1.1 Sources of Reference Data

There exist several possible sources of reference data. All of them have advantages and disadvantages which will be discussed in the following sections. The considered sources are:

- test beam data with tagged electrons and pions,

- data from AliRoot simulations,

- and references from *pp* collisions using displaced vertices.

Test Beam Data

The goal of the test beam in 2007 was to check the Transition Radiation Detector in its final hardware configuration and to study the possibility of acquiring a first reference data set. The analysis of the test beam data of 2007 is presented in Section 7.5.

One issue of the 2007 test beam data for PID references was the "geometry" of the data taking. Contrary to ALICE, the particles in the test beam hit the Transition Radiation Detector Supermodule always at the same position and with the same angle of incidence. In addition no magnetic field was available, consequently all tracks were straight and no Lorentz angle needed to be taken into account. For the ALICE Transition Radiation Detector, a tracklet's signal is normalized by the calibration procedure (electron gain, drift time, starting time t_0) [Bai08] and the reconstruction (track length, x position) [Ber09b]. This normalization allows to handle the tracklet independently of its geometric attributes, which are e.g. the tracklet position in a TRD module, the position of the TRD module itself, and the tracklet's angle of incidence.

In the analysis of the test beam data it was shown that the data was contaminated. A possible explanation for the contamination are double tracks (see Section 7.5.3). The contamination resulted in a worse pion efficiency compared to the results from previous test beam analyses and results from AliRoot simulations. This impurity due to double tracks may present a larger problem than the mentioned geometric differences. In Section 8.4.1 the influence of contaminations on the particle identification performance for neural networks in proton-proton collisions was analyzed. The results indicated that an impurity up to a level of about 15% showed very small influence on PID capability.

In Section 8.4.2 the neural networks trained with 2007 test beam data were applied to simulated data. The results were comparable to the results from the different test beams and AliRoot simulations. The limited geometric variation of the reconstructed tracks (fixed incidence angle, fixed beam position) did not affect the particle identification performance. The impurity of test beam data had also little influence on the pion efficiency. The successful application of simulated data to networks trained with test beam data indicated that test beam data can be used for training the reference networks. However, a disadvantage of the 2007 test beam data is that it is only available for four momenta (1.0, 2.0, 4.0, and 6.0 GeV/c) and two particle species (electrons and pions).

AliRoot Simulations

Another source for reference data are AliRoot simulations. Simulated data have several advantages compared to test beam data. The exact experimental topology can be taken

into account. Particle abundances and momentum distributions can be simulated as required. In the existing test beam data only electrons and pions are available, in simulations any kind of particle can be generated. Test beam data are only available with fixed momenta, whereas simulations allow to produce particles with a continuous momentum spectrum.

The big disadvantage of simulated data is that it is only a parameterization. In the real experiment effects may occur that are not taken into account in simulations. Possible differences to reality could arise due to geometrical reasons (e.g. wrong estimate of the chamber material) or physical effects which are not correctly taken into account or are ignored in the simulation. An example for a possible error source is the generation of transition radiation in AliRoot simulations. As discussed in Section 4.2.2, the production of transition radiation inside the radiator cannot be simulated by GEANT3 in detail. Instead, a momentum dependent parameterization based on test beam data has been used [And04a, And09a].

9.1.2 Reference Data from Displaced Vertices in Proton-Proton Collisions

In the previous section test beam data and AliRoot simulations were discussed as references for the Transition Radiation Detector. Despite their disadvantages, both methods seem to be usable for generating reference data. Nevertheless, the extraction of references directly from the experiment would be optimal.

A possibility to extract reference data for particle identification for the ALICE Time Projection Chamber (TPC) was presented in Reference [Kal08]. Pairs of charged particle tracks which do not point to the primary vertex originate from decays of neutral particles or photon conversions. The secondary vertex which represents the decay location of an unstable neutral particle is also called V^0, the process itself V^0 *decay*[1]. The daughter particles can be identified with good purity via the reconstruction of the neutral mother particle's invariant mass. The truncated deposited charges of the daughter particles are used to determine the parameters of the Bethe-Bloch curve (see Section 4.2.1) for the Time Projection Chamber. For the Transition Radiation detector the situation is different, since it is not possible to find parameters for a function which represents the detector response. Instead of a response function, single particle tracks with a secure particle identification have to be used to generate two-dimensional histograms or to train artificial

---

[1]The photon conversion to an electron positron pair is not a V^0 decay. Nevertheless, in the following, "V^0" includes also photon conversions since they have a similar topology.
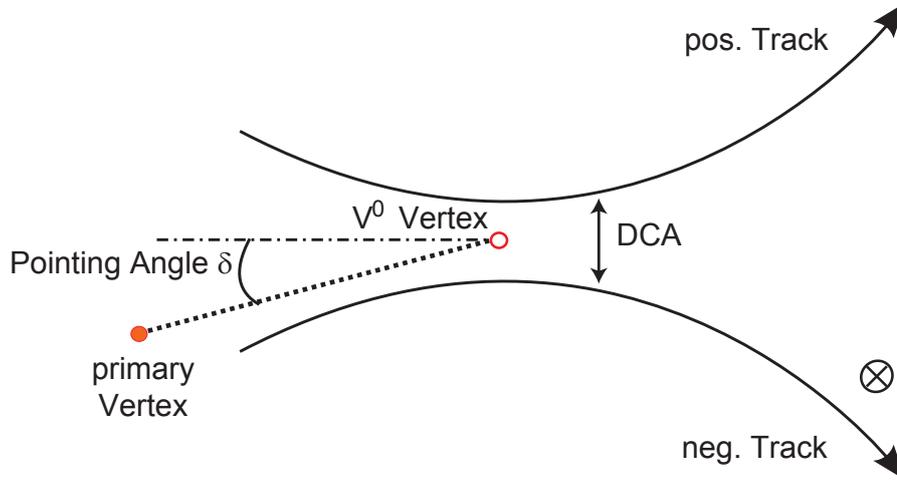
Figure 9.1: Topology of a displaced vertex [Kal08]. A neutral particle does not produce a track in the tracking detectors. In case the uncharged particle decays into a positively and a negatively charged particle, two tracks can be reconstructed. Due to the magnetic field, the tracks are bent in different directions. The reconstructed vertex of the neutral particle decay is the V^0 vertex. Further attributes of a displaced vertex are the Distance of Closest Approach (DCA) between the two reconstructed tracks and the pointing angle δ. The pointing angle is the angle between the reconstructed momentum of the neutral particle and a straight line between the V^0 vertex and the collision point.

neural networks. Nevertheless, displaced vertices can be used to select tracks which then can be used for the generation of reference data.

Possible V^0 decay candidates for reference data extraction are the following processes:

$$
\begin{aligned}
K_S^0 &\rightarrow \pi^+ + \pi^- \ (69.2 \pm 0.05)\%, \quad c\tau = (2.684 \pm 0.001)\,\mathrm{cm}, \\
\Lambda &\rightarrow p + \pi^- \ \ (63.9 \pm 0.5)\ \%, \quad c\tau = (7.88\ \pm 0.06)\ \mathrm{cm}, \\
\bar{\Lambda} &\rightarrow \bar{p} + \pi^+ \ \ (63.9 \pm 0.5)\ \%, \quad c\tau = (7.88\ \pm 0.06)\ \mathrm{cm}, \\
\gamma + Z &\rightarrow e^+ + e^- + Z \ (\approx 6.3\% \text{ in ALICE, from vertex to the first half of TPC}).
\end{aligned}
$$

The branching ratios of the decays are given in the brackets. The data was taken from References [Ams08, Ale06].

V^0 Topology and the Invariant Mass

The topology of a V^0 decay (as well as for a photon conversion) is shown in Figure 9.1. It is characterized by:
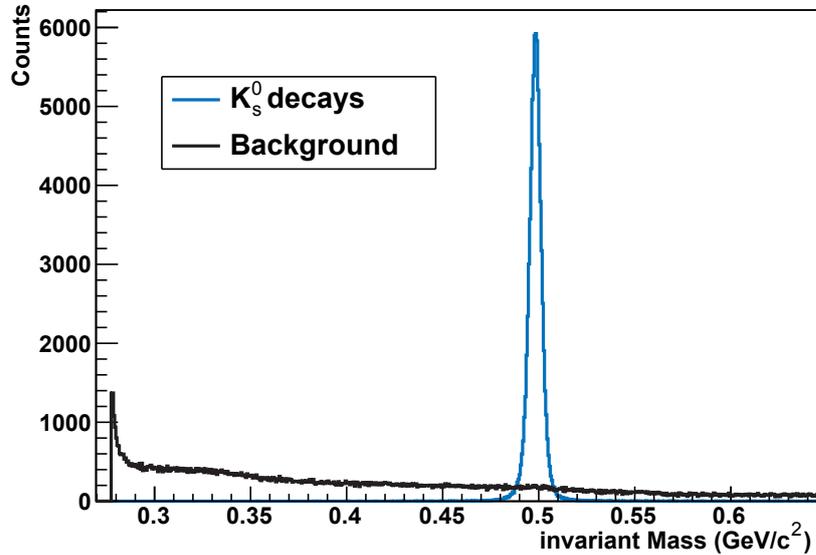
Figure 9.2: Invariant mass of neutral kaons (blue) and background (black) as provided by the ALICE reconstruction V^0 finder [Hei09].

––––––––––

- a V^0 vertex,

- a track of a positively charged particle,

- a track of a negatively charged particle,

- the distance of closest approach (DCA) between the two tracks,

- and the pointing angle δ between the reconstructed neutral particle momentum and the vector from the secondary vertex to the collision vertex.

The V^0 identification happens during the reconstruction with a V^0 reconstructor and is based on the quantities described above [Kal08]. In addition, a causality check is performed. In case the secondary vertex is reconstructed far enough form the collision point, inward detectors (e.g. an ITS layer) will not register any signal from the secondary tracks.

The invariant mass m_{inv} of a decayed particle can be determined by momentum measurements of the daughter tracks and a mass hypotheses for the daughter particles. The invariant mass is given by:

$$
\begin{aligned}
m_{inv}^2 &= (E_1 + E_2)^2 - (\vec{p}_1 + \vec{p}_2)^2 \\
&= E_1^2 + 2E_1E_2 + E_2^2 - p_1^2 - 2\vec{p}_1\vec{p}_2 - p_2^2 \\
&= m_1^2 + m_2^2 + 2E_1E_2 - 2\vec{p}_1\vec{p}_2 \\
&= m_1^2 + m_2^2 + 2\sqrt{\left(m_1^2 + p_1^2\right)\left(m_2^2 + p_2^2\right)} - 2\vec{p}_1\vec{p}_2.
\end{aligned}
\tag{9.1}
$$

E_1 and E_2 are the energies of the two daughter particles, $\vec{p}_1$ and $\vec{p}_2$ their momenta, and m_1 and m_2 their masses. It has to be noted that in case the daughter particles have different masses ($m_1 \neq m_2$) the resulting invariant mass is not the same if the mass assumptions are assigned to the wrong tracks. $m_{inv}(m_1, m_2)$ is not the same as $m_{inv}(m_2, m_1)$ and allows e.g. the discrimination of Λ and $\bar{\Lambda}$ decays.

In Figure 9.2 the invariant masses of simulated K_s^0 decays are shown in blue. The background as it is provided by the ALICE reconstruction V^0 finder is plotted in black. It can be seen that a clear peak is visible at the expected mass of about $m_{K^0} \approx 497\,\mathrm{MeV}/c^2$.

Results and Contamination

The most interesting V^0 process for the TRD is the photon conversion into an electron positron pair. The probability for a photon to convert before the Transition Radiation Detector is reached is at about 6.3%. In Reference [Wil08] a first estimate on the feasibility of using γ conversions for the production of reference data was presented. The following updated preliminary results are based on simulations and were produced by *M. Heide*. Final results with experimental data will be published in Reference [Hei].

For the study about $5 \cdot 10^7$ simulated minimum bias *pp* events were used. The collision energy in the simulation was 10 TeV. A track was only accepted for the study when it produced six tracklets in the TRD, i.e. all six layers of the TRD were hit. In 2010 the Transition Radiation Detector will consist of seven supermodules. The simulation was made under the assumption that eight TRD Supermodules are installed in ALICE. In Figure 9.3 the reconstructed position of true photon conversions are shown, where at least one daughter track was reconstructed in the TRD. "True" means that the particle has the Monte Carlo identity of a photon. The structure of the inner barrel of ALICE is clearly visible.

The simulations differ from the expected situation for ALICE in 2010. Instead of 10 TeV the expected collision energy in the first year will be 7 TeV. Therefore the
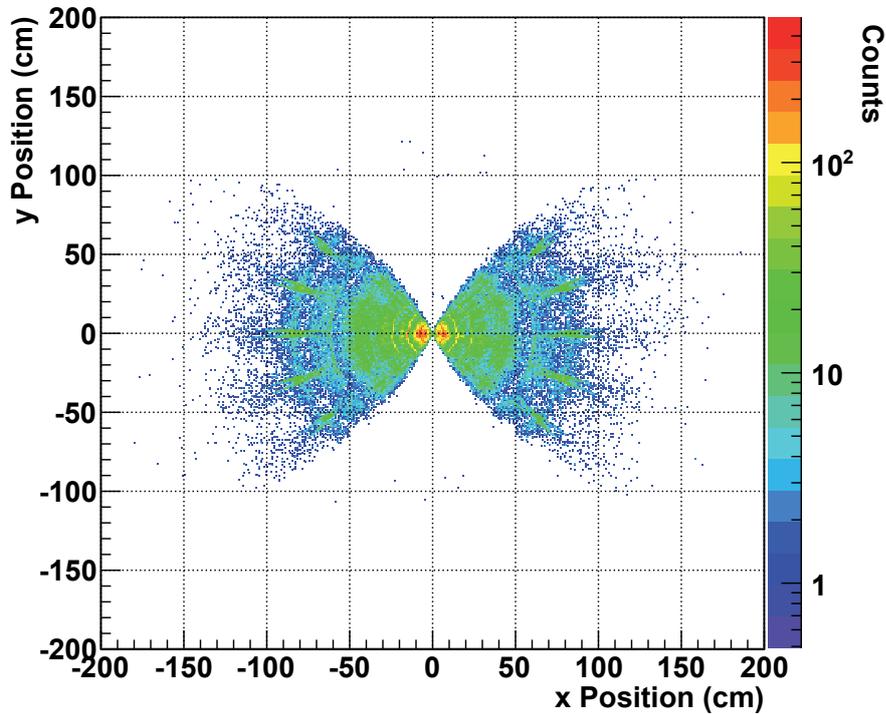
Figure 9.3: Conversions in ALICE for 32 million *pp* collisions at 10 TeV/c [Hei09]. All conversion points are shown where at least one track can be reconstructed in the Transition Radiation Detector. In this simulation eight TRD Supermodules were active. Since photon conversions occur preferably in material with a high nuclear charge *Z*, the layers of the ALICE Inner Tracking System as well as the inner part of the Time Projection Chamber can be seen.

———————

estimated yield of photons, neutral kaons, and lambda baryons will be about half of the simulated one. In addition, only seven TRD Supermodules instead of eight will be installed. The number of accepted particles needs to be multiplied by a factor of 7/8.

The default V^0 reconstructor of AliRoot uses topological information in order to find the displaced vertices. The background of the resulting invariant mass spectrum is quite large [Kal08]. Background components are falsely reconstructed vertices and reconstructed V^0s of the wrong type. The background can be reduced very strongly by the application of some cuts. The cuts for the different processes are presented in Table 9.1.

The most important cut is the one on invariant mass. Only displaced vertices with invariant masses around the requested one are accepted. A cut on the pointing angle can further reduce the number of falsely reconstructed V^0s. The opening angle is used for photon conversions only. It is the angle between the positive and the negative particle track at the reconstructed secondary vertex. Electron and positron are emitted under a

V^0 type	$\gamma \rightarrow e^+ + e^-$	$K_s^0 \rightarrow \pi^+ + \pi^-$	$\Lambda/\bar{\Lambda} \rightarrow p + \pi^-/\bar{p} + \pi^+$
m_{inv}	$< 0.07\,\mathrm{GeV}/c^2$	$m_{K^0} \pm 0.01\,\mathrm{GeV}/c^2$	$m_\Lambda \pm 0.01\,\mathrm{GeV}/c^2$
pointing angle	$< 0.03\,\mathrm{rad}$	$< 0.03\,\mathrm{rad}$	$< 0.03\,\mathrm{rad}$
opening angle	$< 0.1\,\mathrm{rad}$	–	–
opening angle in θ	$< 0.05\,\mathrm{rad}$	–	–
V^0 dist.	$> 6.0\,\mathrm{cm}$	$< 20\,\mathrm{cm}$	–
PID	TPC	TPC + TOF	TPC + TOF
	$(L_e > 0.21)$	$(L_\pi > 0.9)$	$(L_p > 0.5, L_\pi > 0.2)$

Table 9.1: Cuts used for the V^0 reconstruction [Hei09].

small angle since the photon is massless. The magnetic field in ALICE is the only effect that separates the $e^- e^+$ pair. Since the magnetic field has no influence in direction of the polar angle θ (see Apendix B), this angular component should be the same for both tracks. Photon conversions occur preferably in material with high nuclear charge Z (detector material or support structure), particle decays have typical decay times. Thus, a cut on the distance of the reconstructed V^0 to the primary vertex further improves the purity of the selected process. The last cut that is performed is a cut on the PID response of other ALICE detectors. For the identification of photon conversions the likelihood response of the Time Projection Chamber (TPC) is solely used. The PID cut for neutral kaon and lambda identification is made on the combined likelihood of TPC and Time-Of-Flight.

The resulting momentum spectra for electrons from photon conversions, pions from K_S^0 decays, and protons from Λ decays are plotted in Figure 9.4. The black curves represent all particles from the corresponding decays that can be found. All correctly found particles are plotted in a darker color, while particles of the correct type but not originating from the displaced vertex are shown in light colors. This is background which is not relevant, since we are interested in particles of this species in general, independently of their origin. The background that has influence on the purity is plotted in gray. These are all particles which are not of the requested type. About 10000 complete tracks per momentum bin are needed for the training of the neural networks. Assuming about 10^9 pp events in the first year, enough data will be available for the training of neural networks up to a momentum of $4\,\mathrm{GeV}/c$ by the end of 2010 [Hei09].

Using daughter particles of neutral particle decays opens a possibility to access reference data directly from the experiment. Reference data from V^0 decays can be obtained for electrons, pions, and protons. The situation is different for muons and kaons. It is hard to identify muons in the ALICE Inner Barrel. They have a mass that
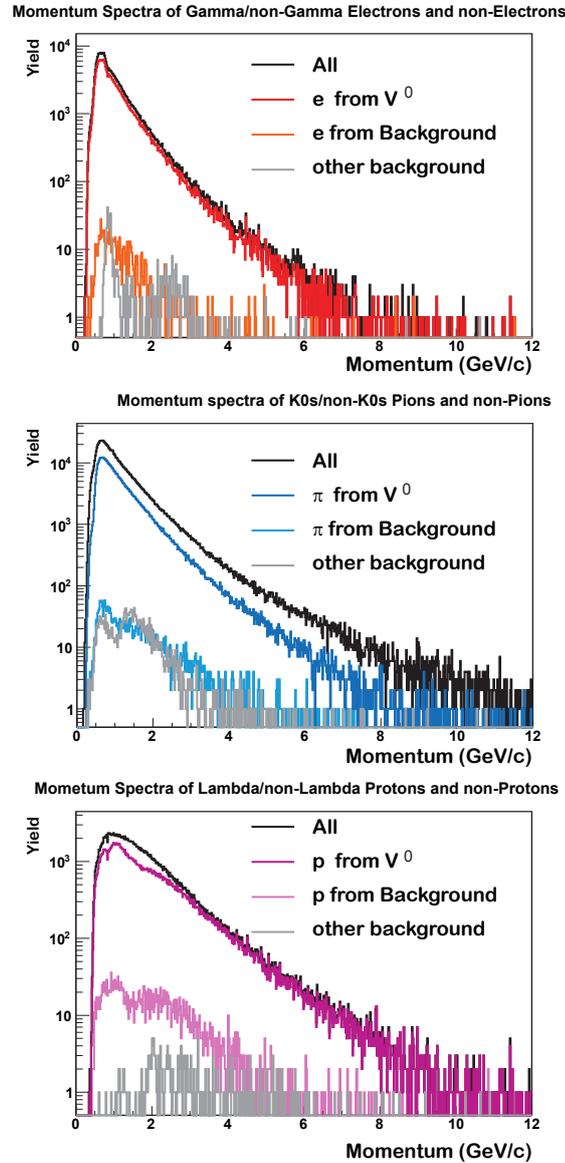
Figure 9.4: Momentum spectra of particles originating from γ conversions and from V^0 decays [Hei09]. The complete spectrum as obtained (black) and the intended extracted particles (dark colors: red for electrons, blue for pions, and purple for protons) are shown. The background is plotted, too. It is split into two components: One component is background that consists of the particles of the regarded species which do not originate from a displaced vertex (light colors), the other component consists of all other particles (gray). Only the gray background component influences the purity of a training sample.

is very close to that of pions ($m_\mu \approx 105.7\,\text{MeV}/c^2$, $m_{\pi^\pm} \approx 139.6\,\text{MeV}/c^2$). Therefore, they cannot be discriminated by the Time Projection Chamber, the Transition Radiation Detector, nor the Time-Of-Flight even if reference data were available. Kaons can be identified with the inner barrel detectors. The kaon mass is above the mass of pions ($m_K \approx 493.7\,\text{MeV}/c^2$). Unfortunately no neutral particle decay with charged kaons as daughter particles has a large branching ratio and small background. However, the combined particle identification using TPC, TOF, and ITS might provide a sample of charged kaons that is pure enough to provide reference data for lower momenta. Using the particle identity from reconstructed tracks for kaon references is currently under investigation [Hei09].

9.2   Feasibility Study for Particle Identification with the TRD Electron Trigger

So far, only particle identification in test beams and on fully reconstructed data has been discussed in this thesis. In this section online particle identification using the TRAP chip will be presented. Online electron identification is needed for the TRD trigger. It was shown with test beam data (Chapter 7) and in simulations (Chapter 8) that artificial neural networks provide good electron identification for the TRD. The improvement compared to a likelihood method on total deposited charge is about a factor of three.

In this section, first a short overview of the ALICE TRD trigger concept is given. After that a feasibility study is presented using artificial neural networks for online particle identification.

9.2.1   The TRD Trigger Concept

In the Transition Radiation Detector's Technical Design Report [TRD01] the TRD trigger was defined. Its tasks are:

- finding and selecting tracks with momenta above $3\,\text{GeV}/c$,

- discriminating electrons from the pion background,

- and determining further information such as invariant mass of two tracks or the multiplicity in a region.

Parameter	Symbol	Granularity	Range	Bits
pad position	$\widetilde{y}$	$160\,\mu m$	[-643.2 mm, 643.2 mm]	13
deflection length	$\widetilde{\theta}$	$140\,\mu m$	[-8 mm, 8 mm]	7
pad row		1	[0,15]	4
electron probability	$P_{electron}$	0.39%	[0,1]	8

Table 9.2: Bit content of a tracklet word [dC03].

The TRD trigger allows to select events in order to enhance physics observables such as J/ψ with large momenta, Υ production [Wes12], dielectrons with invariant masses between 4 and 9 GeV/c^2, and jet production [Bat].

The Transition Radiation trigger consists of two components, the *Local Tracking Unit* (LTU) and the *Global Tracking Unit* (GTU).

Local Tracking Unit

The Local Tracking Unit is composed of Multi Chip Modules (MCMs) located on each of the readout boards. *Online tracklets* are generated in the LTU the (see Section 4.3.3). Online tracklets are track segment candidates represented by a 32 bit word. The word contains information about the *y* position of a track, its deflection length, the pad row, and an associated electron probability [Gut06]. The bit content of a tracklet word is shown in Table 9.2. An online tracklet contains an electron probability with an accuracy of 8 bit. It is calculated locally directly on the TRAP chip (see Section 4.3.3). Compared to offline particle identification, online PID suffers from the following differences:

- no full reconstruction,

- limited input information,

- limited time for the calculation of the electron likelihood,

- and limited output information which is shipped to the GTU.

Reconstruction   Online, only a very limited tracklet reconstruction is performed. Since the trigger is supposed to find stiff tracks with high transverse momentum, tracklets are fit with a straight line [Gut06]. A tracklet is assumed to come from the collision point and to cross a maximum of two pads (in the same pad row) on its path through the chamber. It is not possible to make sophisticated corrections such as normalization to the tracklet length, to the *x* width of the time bin, or to take pad row crossing into account.
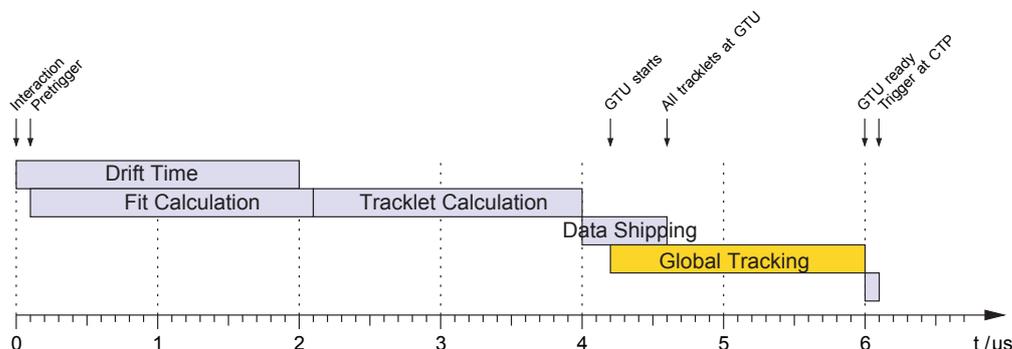
Figure 9.5: Trigger timing for the TRD [dC03].

Available Time on the TRAP Chip   For the calculation of the likelihood to be an electron only limited time is available. In Figure 9.5 the time progress of the trigger is illustrated. The time between an interaction at the collision point and the final decision of the Global Tracking Unit if a trigger signal should be sent is only about $6.5\,\mu$s. The tracklet calculation including the determination of the electron likelihood needs to be finished within $1.8\,\mu$s.

PID Input   For offline particle identification using artificial neural networks, the deposited charges in eight slices (see Section6.3.2) are taken into account. For the online particle identification the deposited charges in only two drift time windows (Q_0, Q_1) can be considered. The sizes as well as the starting points of the two windows can be freely configured. The PID needs references to determine the electron likelihood. In the offline particle identification references are available for eleven momentum bins. For online PID, references can be stored in look-up tables (LUT), which are then saved locally on the Multi Chip Modules (MCM). The maximum number of entries in all look-up tables on an MCM is 2048. This means that one look-up table with a limited resolution has to be used for electron identification for all momenta, which limits the accuracy for input of online PID additionally.

PID Output of the TRAP Chip   As well as the input, the output of the PID on the TRAP chip is limited. The locally determined electron probability is shipped to the Global Tracking Unit via tracklets. The reserved space on the tracklet for electron probability is 8 bit (see Table 9.2).

Global Tracking Unit

The tracklet is shipped to the Global Tracking Unit. In the GTU, Track Matching Units (TMU) combine the tracklets to tracks. Based on the tracklet information the transverse momentum and the electron likelihood are determined. In case certain conditions are fulfilled, a trigger signal is sent to the Central Trigger Processor (CTP) [dC03].

9.2.2 Generation of PID Look-Up Tables

Neural networks perform very well in the discrimination of electrons from pions (see Sections 7.6 and 8.2.2). Thus, the question arises whether artificial neural networks can also be applied to the online particle identification. Actually, the limited time that is available for the estimation of the electron likelihood does not allow to use an artificial neural network in the conventional form. The calculation of the sigmoid function which is needed to determine the output of single neurons (see Section 5.2) is too time consuming [Ang07]. Nevertheless, neural networks can be used to create look-up tables which are used for particle identification on the MCMs. The idea behind this is to train neural networks using two input neurons according to the two drift time windows available for online particle identification. Since the online PID look-up table consists only of 2048 entries, all possible inputs can be presented to the network. The excitations of the output neuron representing the electron likelihood are used as entries for the look-up table.

For the training of the neural networks fully reconstructed particle tracks were used, extracted with the `AliTRDpidRefMaker` task. The particles were simulated using AliRoot v4-17-Rev-02. The momentum distribution and the particle composition were the same as used for the determination of offline particle identification performance (five particle species and a flat momentum distribution, see Section 8.2.1). The charge signals in the eight windows of a tracklet that enter the offline particle identification vary in many aspects from the two charges of tracklets generated online, as discussed previously. Nevertheless, it might be useful to train the networks using the offline information. In case it can be shown that neural networks trained with offline data show a good online electron identification, the networks could be trained with data from the running experiment, using displaced vertices (see Section 9.1.2).

First of all, the width of the two drift time windows for Q_0 and Q_1 had to be determined. Seven data sets were created containing the rearranged deposited charges of the eight offline slices. The eight deposited charges were rearranged into the two
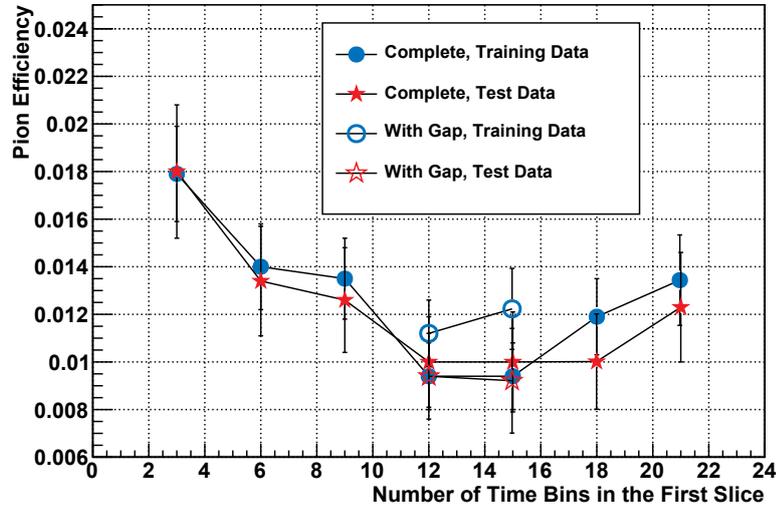
Figure 9.6: Pion efficiency of a neural network with two input neurons versus the number of time bins taken into account for the first slice. The seven different networks were trained for 3,000 epochs. In addition, results are shown for networks with a gap of three time bins. It can be seen that networks with a time bin ratio of 4:4 or 5:3 yield the best pion efficiencies. A gap does not improve the performance of the networks.

values that were used as input for the neural networks. Q_0 and Q_1 were built by adding the deposited charge of different numbers of offline slices. E.g. for the first data set the charge in the new slice 0 was just the charge taken from offline slice 0, that of slice 1 was the sum of the other seven. In order to provide normalized data, Q_0 and Q_1 were divided by the number of used slices. The neural network used for the training had two input nodes (corresponding to Q_0 and Q_1) and two output nodes (one for electron likelihood and the other one for non-electron likelihood). The topology of the hidden layers was identical to the offline neural networks (two hidden layers with fifteen and seven neurons)[2]. The data sets consisted of tracks with a momentum of 3 GeV/c. As usual, they were split into a training data set and a validation data set. The neural networks were trained for the seven data sets and for each layer separately. Training was terminated after 3,000 epochs. Results of the pion efficiency for six TRD layers are shown in Figure 9.6. The pion efficiency is plotted versus the number of time bins taken into account for Q_0 (e.g 12 means that the charges of 12 time bins are used for Q_0 and the 12 remaining ones for Q_1). The results for the training sample as well as for the validation sample are shown. It can be seen that the best performance could be achieved using a time bin ratio with a slightly

---

[2]The topology of the networks might not necessarily need to be so complicated. The performance of networks with a simpler topology (one hidden layer with less neurons) is currently under investigation [Wes12].

smaller window for Q_1. For the further analysis a ratio of 5:3 was used for the drift time windows. In addition networks were tested with a gap of three time bins between Q_0 and Q_1. By using such a gap potential correlations between the two charges could be reduced. The result also shown in Figure 9.6 indicates that no significant improvement can be achieved with this gap.

So far, the pion efficiency performances shown in Figure 9.6 represent only the PID performance using two time slices instead of eight, but apart from that the full offline information. The limitation to 2048 entries in the look-up table of the TRAP chip results in a limited binning for the input charges Q_0 and Q_1. This limitation might further influence the particle identification performance. A reasonable binning for Q_0 is 40 bins and for Q_1 is 50 bins. Q_1 has a slightly finer binning, since transition radiation is expected to preferably contribute to Q_1 (at larger drift time, see Section 6.1). The charge distributions for electrons and pions in the six layers with the respective binning is presented in Figure 9.7. The maximum for Q_0 and Q_1 in arbitrary units is at 1. The trained networks are fed with the bin centers of the 40×50 bins. The resulting output of the neuron representing electron likelihood is shown in Figure 9.8. Red corresponds to a large electron likelihood, blue to a low electron likelihood.

9.2.3 Performance, Summary, and Outlook for Online Particle Identification

For the determination of the pion efficiency the data sets were analyzed again. However, this time, instead of using the neural networks, the likelihood distributions were produced using the look-up tables for the extraction of the electron probability. Data sets for all eleven default momentum bins were produced and applied to the look-up tables. The resulting pion efficiencies are shown in Figure 9.9 for two different data sets per momentum bin. Only one of the $3\,\text{GeV}/c$ data set was used for the training, since only one look-up table is available for all momenta. The $3\,\text{GeV}/c$ data set 1 is used for training and data set 2 for validation. The differences between the results for the other momentum bins are caused by fluctuations of the deposited charge in the single tracks. It can be seen that the pion efficiency is at the level of 1% for momenta of $3\,\text{GeV}/c$ and below, and increases for larger momenta. This behavior is expected, since it agrees with that of test beam data and offline PID using simulations (see Figure 8.13).

The study presented here shows that even though with a smaller accuracy compared to full offline reconstruction a particle identification performance of the order of the TRD design goal can be achieved in simulations. The tracks used here are corrected for track length. This correction cannot be applied online. Instead, the track length can
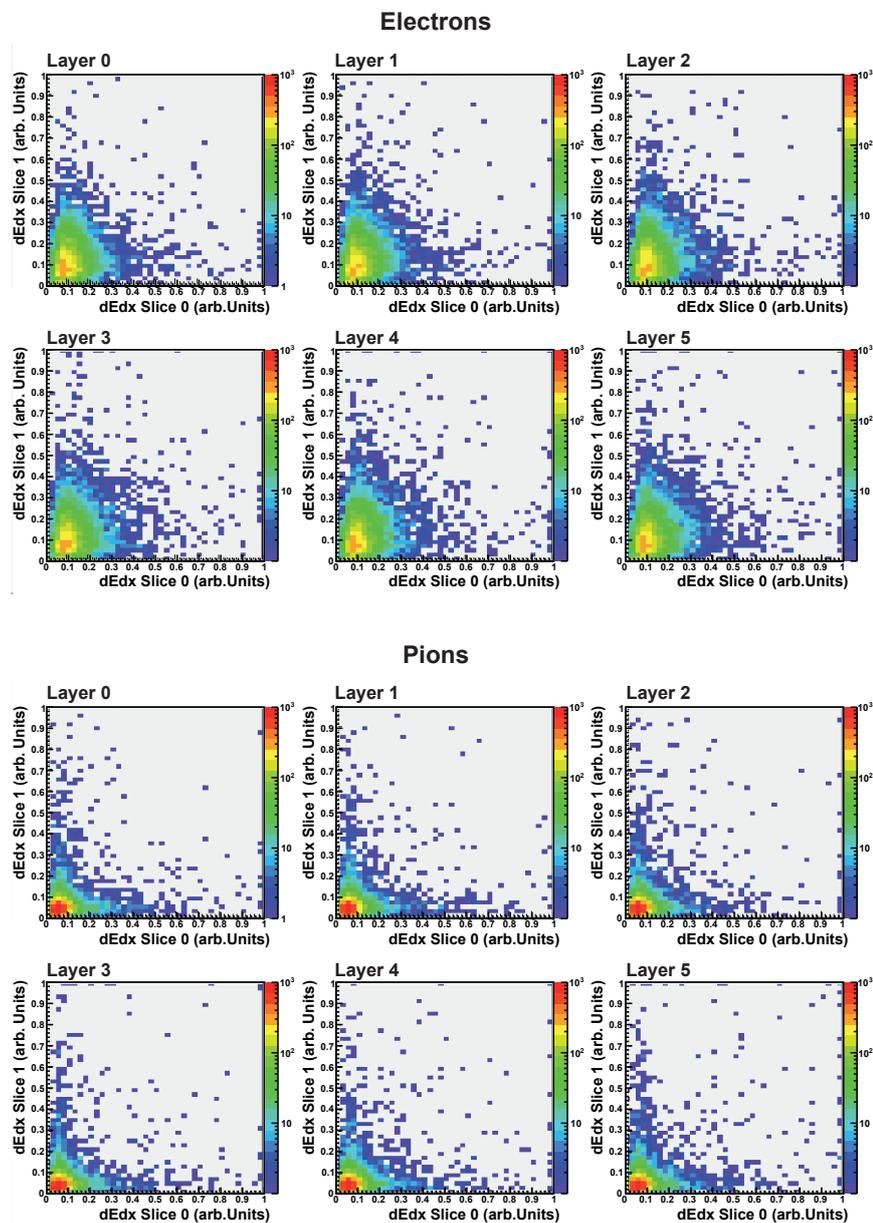
Figure 9.7: Distribution of the deposited charges Q_0 and Q_1 for all six TRD layers. The correlation plots are shown for electrons and pions separately.
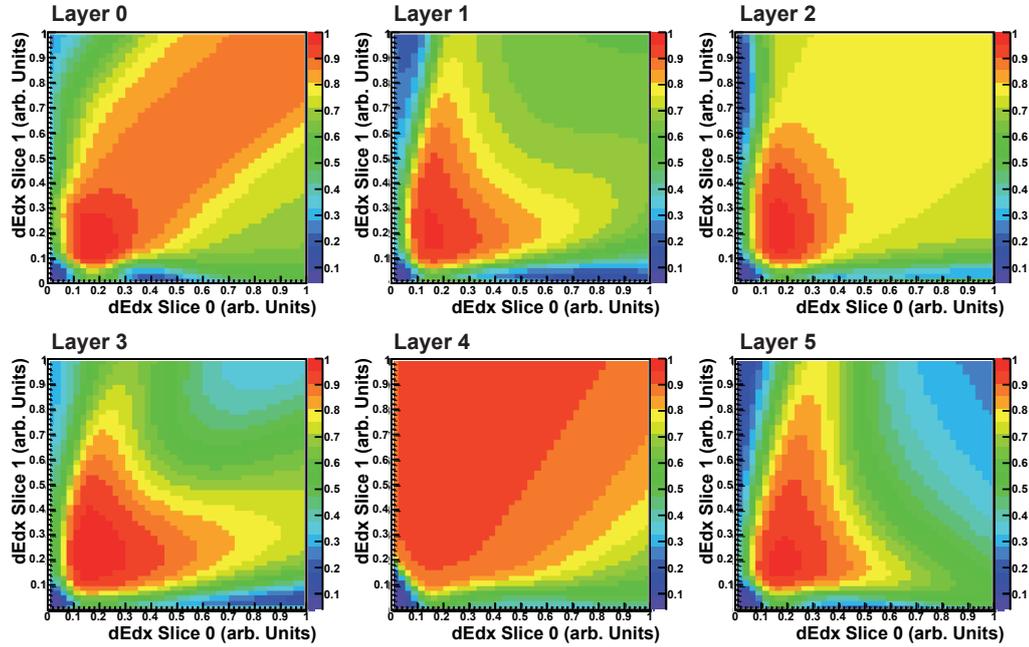
Figure 9.8: Resulting look-up table for the six TRD layers for normalized deposited charges in Slice 0 and Slice 1. The color represents the likelihood to be an electron. The differences in the upper right area are caused by the low statistics in this region. Due to different starting parameters for the training and fluctuations of deposited charge the large differences for the different layers occur. However, due to the limited number of entries in that region (see Figure 9.7) these fluctuations do not have a large influence on the electron identification performance.

————————

be considered in the look-up table, since each MCM can load its own look-up table. The values in the look-up table can be corrected for the geometrical position of the Multi Chip Module in the experiment. The correction is made assuming straight line tracks coming from the collision vertex. A correction for pad row crossing as well as a correction of the time bin width is not applicable online.

It has to be noted that this is not a complete study of the online particle identification. Nevertheless, the look-up table produced here can be used for the PID response simulation of an MCM in AliRoot. For the implementation a scaling factor has to be applied to the look-up table since its range of Q_0 and Q_1 is optimized for neural network training. In addition, until now the digital filters (e.g. tail cancellation, see Section 4.3.3) have not been used in the MCM simulation, but a tail cancellation is applied in the offline reconstruction, which also has to be taken into account. First results of a study
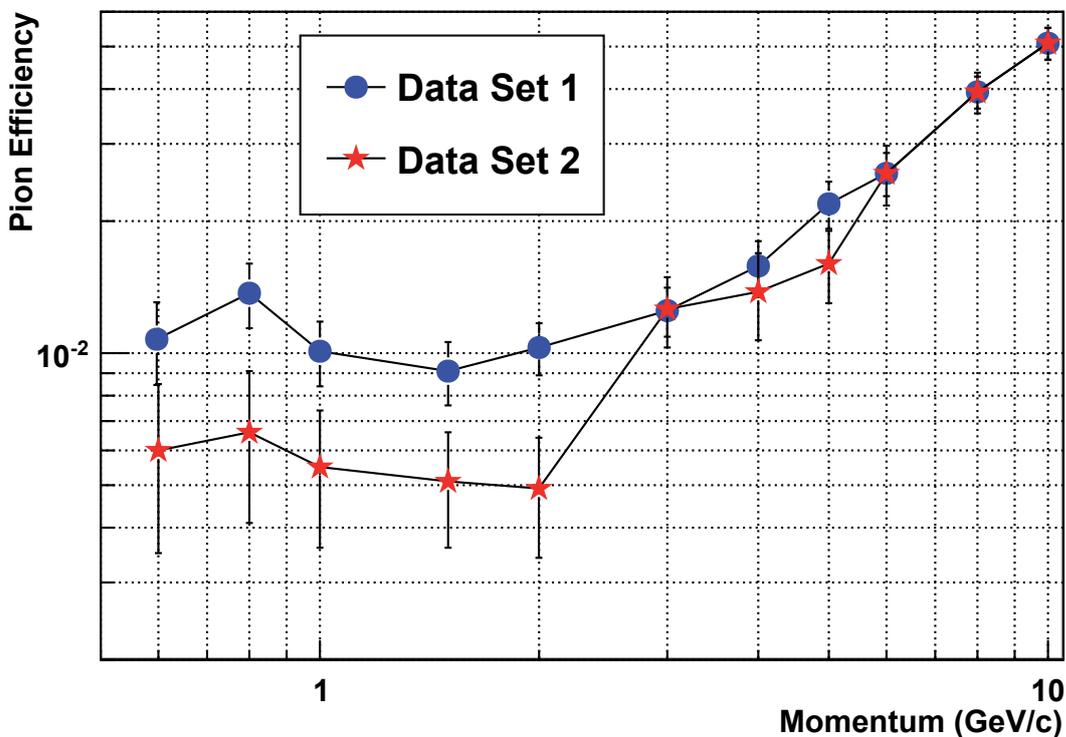
Figure 9.9: Pion efficiency using the look-up tables versus momentum. In each momentum bin results for two data sets are shown. In case of a momentum of 3 GeV/*c*, data set 1 corresponds to the training set and data set 2 to the validation set.

by *U. Westerhoff* [Wes12] indicate that the online particle identification with Multi Chip Modules in AliRoot simulations using the look-up table generated with offline information is about a factor of three worse than the estimate of the present study. The online particle identification using offline information will be good enough to provide a trigger flag for electrons with momenta larger than 3 GeV/*c*.

9.3   Dilepton Measurements at the LHC

An important measurement in ultrarelativistic heavy-ion collisions is the measurement of dileptons. The invariant mass spectrum of dileptons provide information about the quark-gluon plasma (see Section 2.3). ALICE can measure dimuons with the muon spectrometer in a pseudo-rapidity range of $2.5 < \eta < 4.0$ and dielectrons with the central barrel in $|\eta| < 0.9$. Besides ALICE, the other large LHC experiments (ATLAS, CMS, and LHCb) are
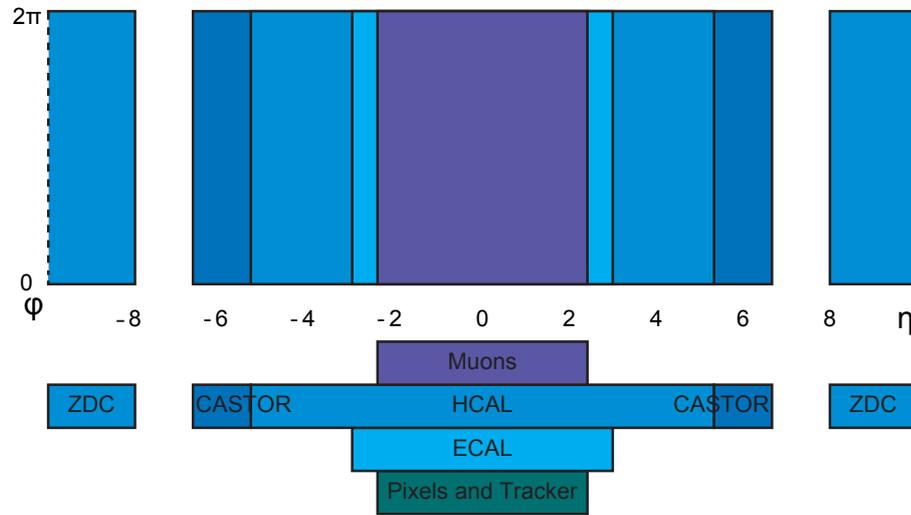
Figure 9.10: The acceptance of the CMS detector systems [d'E08].

also able to measure dileptons. An overview of the plans and their potential for measuring quarkonia is given in Reference [Lan08].

In this section, first a short excursion is made to CMS and its program for quarkonia measurements in the dimuon channel. After that the measurement of dielectrons in ALICE with the central barrel is discussed. The analysis follows the procedure described by *W. Sommer* [Som08] and *F. Kramer* [Kra06]. The influence of artificial neural networks, used for particle identification in the TRD, on the background in the invariant mass region of the J/ψ and the Υ is explored. Finally, the signal to background ratio is compared to that of other PID methods.

9.3.1 Quarkonia Measurement in CMS

CMS has a wide and extensive heavy-ion program which is described in detail in [d'E07]. Because of its design with large-acceptance electromagnetic and hadronic calorimeters as well as muon detectors, CMS has excellent capabilities to measure important observables in heavy-ion collisions. The calorimeters allow full jet reconstruction over a large pseudo-rapidity range, while the trigger system is able to provide high statistics on rare probes [d'E08]. In this section the focus lies on the measurement of dimuons.

As described before, CMS is designed as a barrel detector including end caps. Its inner tracking system covers a pseudo-rapidity range of $|\eta| < 2.4$ and provides a precise reconstruction of secondary vertices [Ado08]. The electromagnetic calorimeter is made of lead tungstate crystals with an acceptance of $|\eta| < 3.0$. The hadronic calorimeter covers
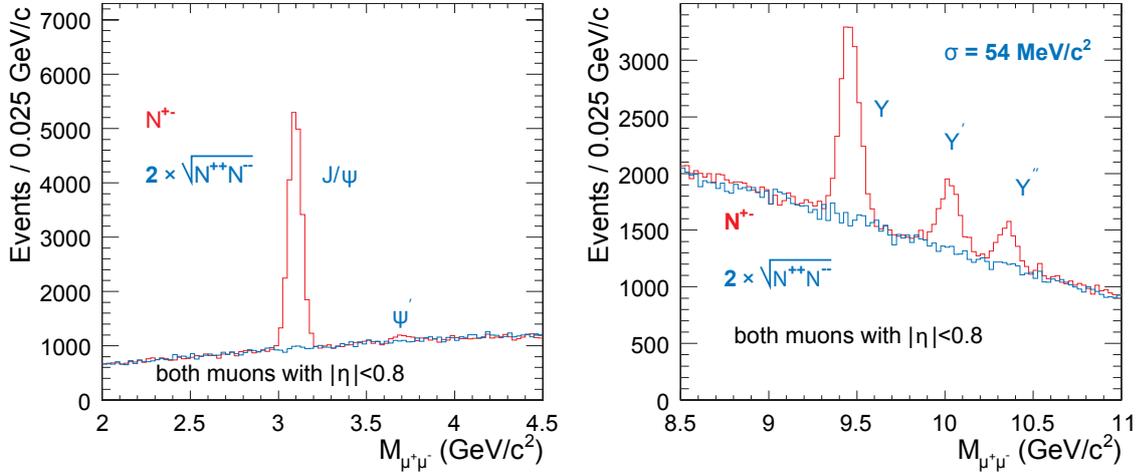
Figure 9.11: Simulated invariant mass spectra of muon pairs in the J/ψ (left) and the Υ region (right) for 5.5 TeV *PbPb* collisions extracted with the central barrel of CMS ($|\eta| < 0.8$). Blue are reconstructed masses with like-sign and red are opposite-sign muon pairs. This distribution is expected after one month of data taking. The simulations were done assuming a multiplicity of 5,000 charged particles per pseudo-rapidity unit and no quarkonia suppression [Bed07].

$|\eta| < 5.0$ and the muon spectrometer $|\eta| < 2.4$. The pseudo-rapidity coverage of the CMS detectors is presented in Figure 9.10. A detailed overview of the CMS detectors is given in [Aco06, Ado08] and of the CMS physics performance in [dR06].

CMS is well suited for quarkonia measurements via the dimuon channel which has a branching ratio of 5.93% for $J/\psi \rightarrow \mu^+\mu^-$ and of 2.48% for $\Upsilon \rightarrow \mu^+\mu^-$ respectively [Ams08]. Although CMS is an experiment built for low multiplicities and high rates, the inner tracker allows even in heavy-ion collisions the suppression of muons originating from charged pion and kaon decays. Since the strong magnetic field and the calorimeters deflect and/or stop particles with low transverse momenta, just muons with momenta larger than 3.0 GeV/*c* reach the muon detectors [d'E07]. As a consequence, a dimuon mass resolution of 1% can be reached at about 100 GeV/*c*^{2} and the charge of muons can be determined for momenta up to 1 TeV/*c* [dR06]. However, this also implies that J/ψs with p_T below 4 GeV/*c* cannot be measured. The trigger increases this threshold further for the CMS barrel part ($|\eta| < 0.8$) to 6–7 GeV/*c* [Bed07]. The acceptance for J/ψ in heavy-ion collisions is about 15% for $p_T > 12$ GeV/*c* for the whole detector and 5% for the central barrel. Bottomium has such a large mass that it can be reconstructed even if it has a negligible transverse momentum. The acceptance (convoluted with the trigger) is about 40% at $p_T = 0$ and decreases to 15% (5% for $|\eta| < 0.8$) for $p_T > 4$ GeV/*c* [d'E07].

System	mass (MeV/c^2)	width (keV/c^2)	Br(e^+e^-) (%)
J/ψ	3096.916±0.011	93.2±2.1	5.94±0.06
ψ'	3686.09±0.04	309±9	0.765±0.017
Υ	9460.30±0.26	54.02±1.25	2.38±0.11
Υ'	10023.26±0.31	31.98±2.63	1.91±0.16
Υ''	10355.2±0.5	20.32±1.85	seen($\approx$ 1.)

Table 9.3: Mass, width, and branching ratio into an electron positron pair of quarkonia [Ams08].

In a CMS research note a simulation study by *M. Bedjidian* and *O. Kodolova* on quarkonia measurements in heavy ion collisions has been presented [Bed07]. Figure 9.11 shows the expected like-sign and opposite-sign dimuon invariant mass spectra at the mass regions of the charmonium and the bottomium. Here, a charged particle multiplicity ($dN_{ch}/d\eta$) of 5,000 is assumed and only events with both muons in the central barrel region are taken into account. The mass resolution for the J/ψ is 35 MeV/c^2 and the signal to background ratio (S/B) lies at approximately 4.5. For the Υ the values are at 56 MeV/c^2 and about 0.97 respectively. This corresponds to $\approx 11,500$ J/ψs and $\approx 6,400$ Υs in a month of heavy-ion running. In addition, two excited states of the bottomium (Υ' and Υ'') can easily be identified. In case the complete muon acceptance is taken into account ($|\eta| < 2.5$), the total number of measured quarkonia increases ($N_{J/\psi} \approx 140,000$ and $N_\Upsilon \approx 20,000$), but the Υ mass resolution (≈ 85 MeV/c^2) and the S/B ($J/\psi \approx 1.2$, $\Upsilon \approx 0.12$) decrease.

9.3.2 Dielectron Measurements with the ALICE Central Barrel in *PbPb* Collisions

ALICE has two possibilities measuring dileptons. One is the measurement of dimuons in forward direction with the Muon Spectrometer, an alternative one uses the detectors of the central barrel for the identification of electron positron pairs. The measurement of dielectrons is discussed in this section. The focus of this analysis is the comparison of identifying electrons using artificial neural networks in the TRD to the electron identification with a likelihood on total charge (LQ).

Particle Composition of Simulated Events

For the simulation of *PbPb* collisions a cocktail of different particles with various momenta has to be created. The event composition should contain the quarkonium signal

as well as background. The signal is composed of five components: J/ψ, ψ', Υ, Υ', and Υ''. Their masses, widths, and the branching ratios into an electron/positron pair are shown in Table 9.3. The background is composed of semi-electronic decays of D and B mesons, and hadrons falsely identified as electrons. In this analysis, a *PbPb* collision is assumed to have a multiplicity of 3,000 charged particles per unit of pseudo-rapidity.

For the simulation of particles composed of heavy quarks, the AliRoot class `AliGenParam` was used. `AliGenParam` allows to load external parameterizations. The parameterization was taken from the AliRoot `AliGenMUONlib` which provides parameters for the transverse momentum, the rapidity distribution, and the particle abundance within a particle family. The momentum and the rapidity distribution were given by the parameterization "Vogt PbPb 2002" provided by `AliGenMUONlib` [Alia]. It is also possible to select the decays that are allowed for the generated particles. For this analysis all decays implemented in PYTHIA were allowed.

J/ψ **Family**   The first signal components are the decays of the charmonium ground state ($J/\psi \rightarrow e^+ + e^-$) and its first excited state ($\psi' \rightarrow e^+ + e^-$) into dielectrons. The expected yield of charmonia is about two orders of magnitude smaller than the total yield of generated charm anticharm quark pairs [BM09a, And07b]. The total yield of $c\bar{c}$ in central *PbPb* collisions is expected to be about 115 produced pairs [Ale06]. In each simulated *PbPb* collision two particles of the J/ψ family were added. The ratio between the two particle production yields is also provided by `AliGenMUONlib` and is:

J/ψ	ψ'
0.98	0.02

This corresponds approximately to theoretical predictions made by the *Color Evaporation Model* (CEM) [Bar80]. However, not all J/ψs which are generated originate from the direct generation of charmonia. A fraction of J/ψs is produced by decays of B mesons. The branching ratio for the J/ψ to decay into an electron and a positron is 5.94% (see Table 9.3). The other decay types are mostly hadronic decays and could contribute to the background due to misidentification of the daughter particles.

Υ **Family**   The other signal components are the dielectronic decays of the Υ family particles ($\Upsilon, \Upsilon', \Upsilon'' \rightarrow e^+ + e^-$). The production cross section for the Υ family is about fifty times smaller than for the J/ψ family [Ale06]. Therefore, in only 4.5% of the

simulated events one Υ was embedded. The ratio between the production yields of the single particles and the total production yield of the Υ family is:

Υ	Υ'	Υ''
0.712	0.184	0.104

Open Charm The electron pairs originating from semielectronic decays of D and B mesons are background components contributing to the invariant mass spectrum of dielectrons. This background component is composed of electrons and consequently cannot be reduced by particle identification. The number of generated charm anticharm quark pairs is about 115 per central *PbPb* collision at a collision energy of $\sqrt{s_{NN}} = 5.5\,\text{TeV}$ [Ale06]. Consequently, in each simulated event 230 charmed particles were embedded. The fractions between the generated charmed particles (plus anti particles) are [Alia]:

D^0	$D^{\pm}$	$D_s^{\pm}$	Λ_c
0.6	0.2	0.12	0.08

Open Beauty The number of expected beauty antibeauty quark pairs is about 4.5 for $\sqrt{s_{NN}} = 5.5\,\text{TeV}$ *PbPb* collisions [Ale06]. Nine beauty particles were embedded into each simulated event. Besides their semielectronic decay mode, B mesons can also decay into a J/ψ with a probability of about 1% [Ams08]. This is taken into account here, since all decays implemented in PYTHIA are allowed. The production yield for beauty particles is:

B^0	$B^{\pm}$	$B_s^{\pm}$	Λ_b
0.4	0.41	0.12	0.07

Charmed and beauty particles can contribute to the background not only via their semielectronic decay, but also due to misidentified pions from their hadronic decays.

J/ψ Family	Υ Family	D mesons	B mesons	HIJING
2	0.045	230	9	21,508

Table 9.4: Input for the simulation of a *PbPb* collision with a charged multiplicity of 3,000 per pseudo-rapidity unit. The numbers stand for the particles simulated per event. In case of the Υ, one was embedded in each 22nd event. All particles were simulated in the rapidity range of -8<*y*<8. The J/ψ, Υ, *D* mesons, and *B* mesons were allowed to decay into all possible states provided by PYTHIA.

Hadronic Background The background of hadrons was simulated with a parameterized Heavy Ion Jet Interaction Generator (HIJING) [Wan91] provided by the class `AliGenHIJINGpara`. The generator produces pions with a probability of about 88% and kaons with about 12%. Pions are generated with an equal amount of π^+, π^-, and π^0, kaons with an equal amount of K^+, K^-, K_S^0, and K_L^0. The transverese momentum distribution follows the measurement of the CDF collaboration [Abe88]. The total amount of simulated particles was such that it matches to a multiplicity of charged particles per pseudo-rapidity unit of $dN_{ch}/d\eta = 3000$. Fluctuations of the particle multiplicity were not taken into account.

Others The simulations for this analysis do not reproduce the particle abundances correctly in all details. Photon conversions have not been simulated. Electron/positron pairs originating from photons are produced outside of the collision vertex in the detector material of ALICE. Secondary vertex measurements can be used to suppress them efficiently [Som08]. Protons are also not simulated here. In the momentum region $p < 3\,\text{GeV}/c$ they can be sufficiently well identified with the Time Projection Chamber and the Time-of-Flight system. For momenta above $3\,\text{GeV}/c$ the suppression of protons using the Transition Radiation Detector exceeds the suppression of pions by a factor of about five (see Section 8.2.2). A complete overview of the simulated particles per *PbPb* collision is given in Table 9.4.

Fast Simulation

In a full simulation of heavy-ion collisions the simulation of the detector responses and the track reconstruction is very time consuming. Depending on the estimated multiplicity more than 30000 tracks have to be taken into account. Therefore, the detector response to particle tracks has been parameterized. A simulation using such parameterization is called *fast simulation*. For the ALICE central barrel a parameterization was made by *J. F. Große-Oetringhaus* [GO05]. The parameterization was made using a full simulation

and reconstruction of HIJING events. Additionally, electrons and positrons with higher transverse momenta were embedded into these HIJING events in order to extract the detector response for high momentum tracks.

The parameterization for the central barrel consists of three components [GO05]:

- efficiency,

- resolution,

- and electron/pion discrimination.

Efficiency The efficiency describes the probability that a particle is detected and reconstructed. The efficiency is not unity due to dead areas in the detector. Two-dimensional efficiency plots are generated for the $p_T - \theta$ and the $p_T - \phi$ plane. An example of the generation of an efficiency response function from the particle generation via track reconstruction to the efficiency response is given in Figure 9.12 **a)-c)** for the $p_T - \theta$ plane. The one-dimensional projections of the p_T, θ, and ϕ efficiency are shown in Figure 9.12 **d)-f)**.

Resolution The resolution describes the accuracy of the reconstruction. It is calculated analogously to the efficiency for the $p_T - \theta$ and the $p_T - \phi$ plane. It is based on the distribution for the difference between generated and reconstructed value of a physical value x:

$$\Delta x = x_{Generated} - x_{Reconstructed}.$$ (9.2)

A Gaussian fit reproduces well the distributions for $\Delta\theta$ and $\Delta\phi$ but fails for Δp_T due to energy loss caused by bremsstrahlung. For Δp_T a Landau distribution convoluted with a Gaussian distribution has to be used. The resolution of all values x is given by the width of the Gaussian distribution fitted to the Δx distribution. In Figure 9.13 **a)-b)** the resolution of p_T, in **c)-d)** that of θ, and in **e)-f)** that of ϕ is presented.

For details on the efficiency and resolution responses as well as the complete extraction of the response functions including applied cuts please refer to Reference [GO05].

PID Response The particle identification response is split into a response for the TPC and one for the TRD. The Time Projection Chamber and the Transition Radiation Detector are the detectors which are expected to contribute most to the particle identification of electrons in the transverse momentum range above $1\,\text{GeV}/c$. For the electron
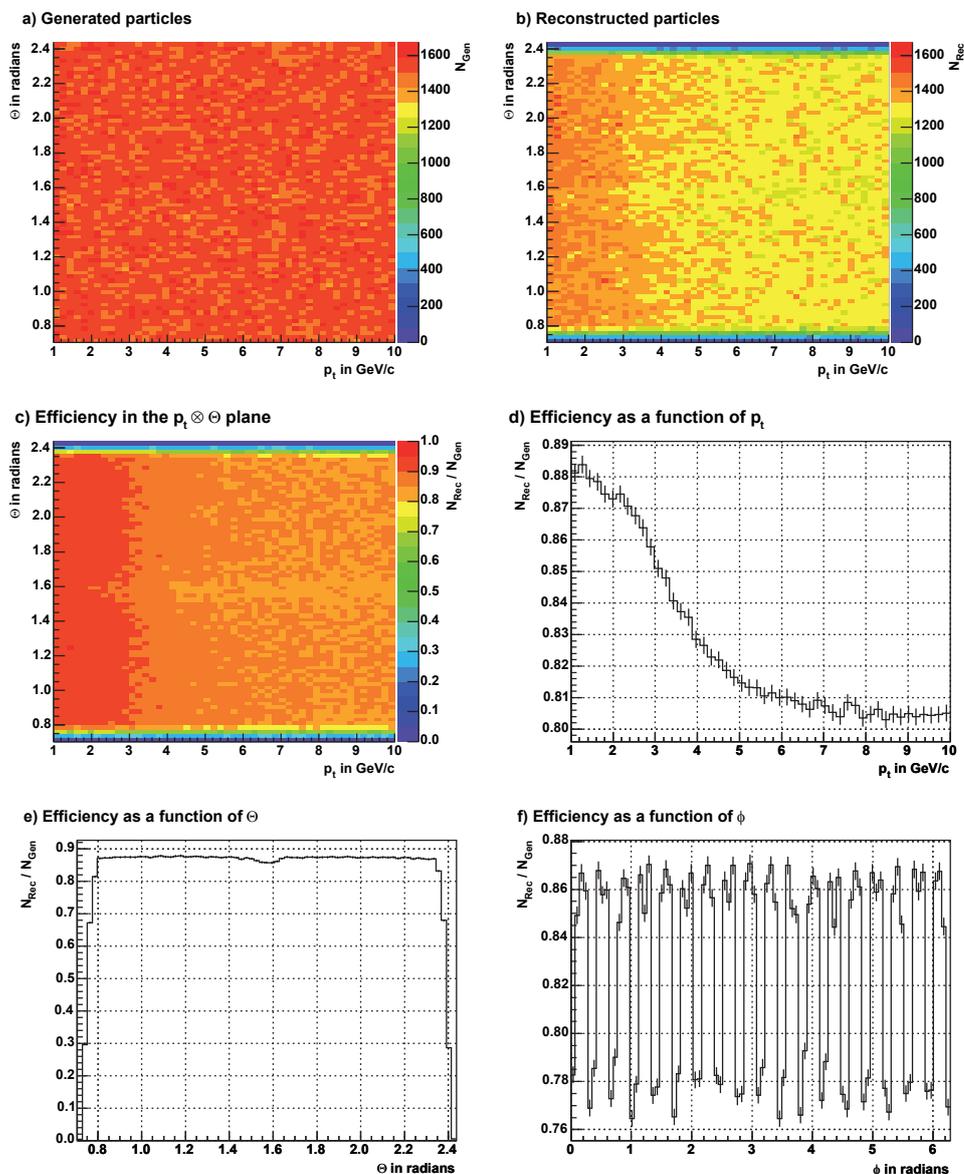
Figure 9.12: Efficiency response functions for the central barrel [GO05]. **a)** shows the number of simulated particles in the $p_T - \theta$ plane. In **b)** the number of reconstructed particles and in **c)** the reconstruction efficiency is presented. In addition the efficiency as a function of **d)** p_T, **e)** θ, and **f)** ϕ is plotted. The small drop around $\theta \approx 1.6$ is caused by absorption or diversion at the central TPC electronde [TPC00]. The 18 drops for the efficiency as a function of ϕ originate from the dead areas of the TPC, the ALICE support structures and the borders between the TRD supermodules.
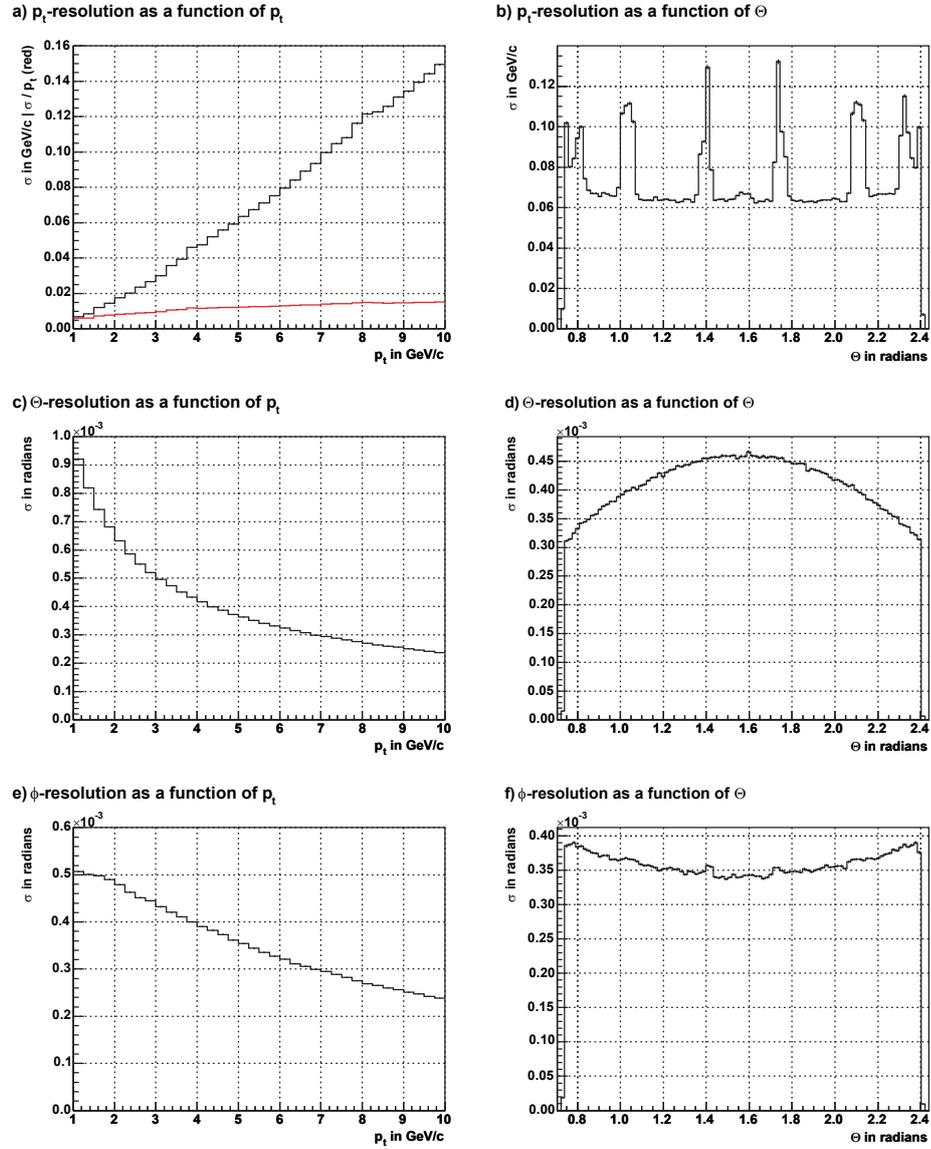
Figure 9.13: Resolution response functions for the central barrel [GO05]. The resolutions in **a-b)** p_T, **c-d)** θ, and **e-f)** ϕ as a function of p_T and θ are shown. The red line in **a)** represents the relative resolution p_T (σ/p_T). It can be seen that for the p_T resolution as a function of θ the resolution is worse in case no TRD information is available.
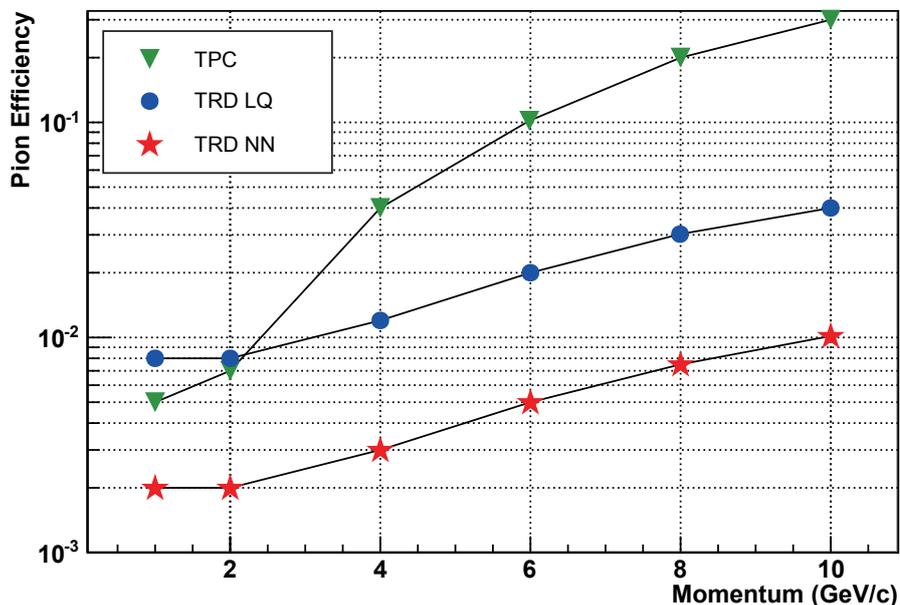
Figure 9.14: Pion efficiency response functions for the TPC (green triangles) and for the TRD are depicted. For the TRD the responses of two PID methods are shown: likelihood on total charge (blue dots) and neural networks (red stars). The pion efficiencies are shown for 90% electron efficiency.

identification only electrons and pions are taken into account. The response functions for the pion efficiency of TPC and TRD at 90% electron efficiency are shown in Figure 9.14. The response function of the TPC was extracted using a likelihood method on total deposited charge [GO05]. For the TRD two response functions are shown. One is the pion efficiency achieved with likelihood on total deposited charge (LQ), the other one is the response of artificial neural networks. The pion efficiencies of the TRD achieved in simulations (see Section 8.2.2) deviate from the pion efficiencies from test beam data (see Section 7.6). In order to be not too optimistic a compromise between the results of test beams and simulations was made. The pion efficiencies used here are estimates based on the available results, which are slightly better than test beam pion efficiencies.

The Invariant Mass Spectrum

For the analysis about 2.2 million *PbPb* events have been simulated. Only electrons and pions with transverse momenta larger than 1 GeV/*c* were taken into account for the analysis. First, it is checked if a particle traverses the central barrel within its acceptance based on the Monte-Carlo information of its transverse momentum p_T as well as of the angles θ and φ. In case the particle traverses the central barrel, its properties are smeared
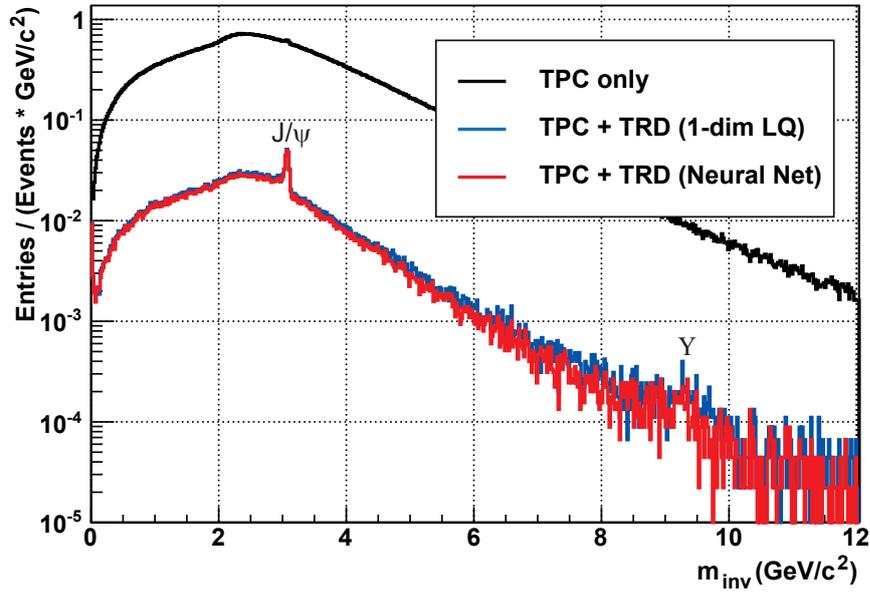
Figure 9.15: Invariant mass spectra of dielectrons in the ALICE central barrel using fast simulations. The spectra are normalized to one event and a bin width of $1\,\text{GeV}/c^2$. The spectrum is shown in case only the TPC is taken into account for electron identification (black line) as well as the spectra for a combined TPC and TRD electron identification. For the TRD PID two different methods were applied, likelihood on total charge (blue line) and neural networks (red line). In case only the TPC is used the electron efficiency is 90%, in case the TRD is taken also into account it is reduced to 81%. A clear peak can be seen at the invariant mass of the J/ψ and an enhancement in the Υ region when the TRD PID information is taken into account.

according to the resolutions provided by the fast simulation. For the smearing of the particles the response functions for a multiplicity of 6,000 particles per unit pseudo-rapidity were used[3]. 81% of all real electrons are further processed. The decision if an electron is used is randomized. In case the particle is a pion the experiment's PID response is estimated based on a random number and the PID response functions for TPC and TRD (Figure 9.14). These random choices are separately done for both TRD PID methods, likelihood on total charge (LQ) and neural networks (NN). Therefore not necessarily the same electrons and pions are taken into account.

---

[3]The multiplicity in this analysis was 3,000 charged particles per pseudo-rapidity unit. Using responses for higher multiplicities decrease the efficiencies and the resolutions of the experiment. However, it was shown that using response functions for $dN_{ch}/d\eta = 6,000$ instead of the nominal one reduces the efficiency only by about 1% [GO05].

The invariant mass of electron/positron pairs is calculated with Equation 9.1. The resulting invariant mass spectrum is shown in Figure 9.15 for different particle identification methods. The black line represents the spectrum in case the TRD is not taken into account and only the PID information of the Time Projection Chamber (TPC) is used. The blue line stands for the combined PID of TPC and the likelihood method on total deposited charge in the Transition Radiation Detector. Red is the combined PID of TPC and artificial neural networks for the TRD. The peak originating from J/ψs is clearly visible for both methods combining the TPC and the TRD. In the invariant mass region of the Υ also an enhancement is visible, but for a clear peak the number of simulated events is too small. It can be seen that the differences in the invariant mass spectrum between the likelihood on total charge method and the neural network method for the TRD are not large.

In order to estimate the difference between the performance of the two methods, the *signal to background* ratio (S/B) and the *significance* (SGN) are calculated. They are defined as [Som08]:

$$S/B = \frac{\sum \left(N_{signal}\right)}{\sum \left(N_{background}\right)}, \tag{9.3}$$

$$SGN = \frac{\sum \left(N_{signal}\right)}{\sqrt{\sum \left(N_{signal}\right) + \sum \left(N_{background}\right)}}. \tag{9.4}$$

The signal to background ratio does not depend on the amount of data, the value for significance increases with increasing number of events. Therefore SGN as well as the signal is extrapolated to the expected number of *PbPb* events in one month of data taking ($\approx 2 \cdot 10^8$ events). The signal is extracted via the Monte-Carlo information within an invariant mass window, which is chosen such that the significance has a maximum value [Som08]. The mass window is defined with a lower mass limit (m_{low}) and an upper mass limit (m_{high}). The background is given by the total spectrum in the invariant mass window minus the signal extracted via Monte-Carlo information. A summary of the S/B, the expected SGN, and the total amount of expected particles for 2×10^8 *PbPb* events is presented in Table 9.5.

Influence of PID Methods on the Dielectron Background in *PbPb* Collisions

It can be seen that the TRD's Particle Identification method has little influence on the measurement of J/ψs. The signal to background ratio is not reduced significantly. For the Υ the improvement is also not significant, but it seems that the PID method could have

	J/ψ		Υ	
PID method	LQ	NN	LQ	NN
S/B	1.03 ± 0.03	1.06 ± 0.03	0.57 ± 0.13	0.79 ± 0.19
SGN	489.7	494.3	45.4	50.0
$Signal$	$(4.75 \pm 0.08) \times 10^5$		$2,960 \pm 487$	
m_{low} (GeV/c^2)	3.0		9.105	
m_{up} (GeV/c^2)	3.116		9.518	

Table 9.5: Signal to background, significance, and total amount of expected particles for J/ψ and *Upsilon* in 2×10^8 *PbPb* events. The values are given for both Transition Radiation Detector PID methods, likelihood on total deposited charge and neural networks. In addition the mass window that was taken into account is presented.

————

a larger influence. The reason for the small influence of the PID method on the S/B is discussed in the following.

The background for quarkonium measurements consists of a reducible background of pions and an irreducible background of electrons. The effect of different electron identification methods on the ratio of signal to background depends strongly on the amount of pions. The different contributions to the background as well as the quarkonia signals are shown in Figure 9.16 for a combined particle identification of TPC and likelihood on total charge for the TRD. An entry is assigned to one of the background contributions if at least one of the two particles originates from a particle containing charm or beauty quarks or is a pion. The pion contribution to the background in the region of the invariant mass of the J/ψ is below 10%. The improvement using different PID methods cannot exceed the limit given by the contribution of pions to the background. In the region of the Υ mass the ratio of pion contribution to the background is larger. The electron/pion discrimination by the TPC gets worse for larger momenta (see Figure 9.14). Consequently a better TRD PID method should have a larger influence in this mass region. A trend that supports this assumption is seen, but the statistical error is so large that a final conclusion on the quantitative improvement cannot be made.

It has to be noted that in Reference [Som08] also a comparison of different PID methods (LQ and 2-dim LQ) was made. The results of this study indicate that the improvement by using advanced PID methods such as two-dimensional likelihood or neural networks might be larger than in the present analysis. Although the analysis made here follows that of Reference [Som08], some differences in the simulation may lead to the observed differences in the signal to background ratio. In Reference [Som08]
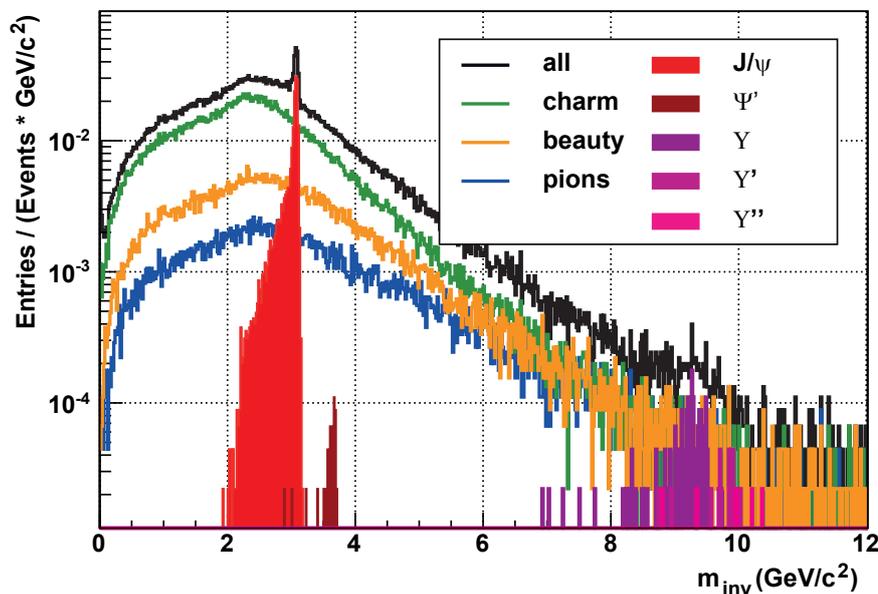
Figure 9.16: Invariant mass spectrum of dielectrons using the likelihood on total deposited charge (black curve). The spectrum is normalized to one event and a bin width of 1 GeV/c^2. The different contributions to the spectrum are also shown. The signals originating from quarkonia are plotted in full color, contributions to the background as lines. Only the contribution of pions can be reduced by particle identification.

quarkonia were simulated with a transverse momentum distribution following a parameterization of the CDF collaboration [Abe88]. The CDF parameterization results in a different p_T spectrum for quarkonia compared to the parametrization used in the present study [Kru08].

It is not clear whether this is the only reason for the observed differences. It seems that in Reference [Som08] the background contains more contributions from misidentified pions and less from heavy flavor electrons than in this study. However, in case of a larger pion background, particle identification using artificial neural networks would further improve the signal to background ratio. The larger the background due to pions (e.g. due to higher charged particle multiplicity), the more important is a sophisticated PID method such as the neural network method presented in this thesis.

Summary

The ALICE Transition Radiation Detector was designed as a tracking detector, as a trigger for electrons, and for the identification of electrons. Electrons are appropriate probes for studying the quark-gluon plasma. The design goal for the Transition Radiation Detector was to reach a pion efficiency below 1% at an electron efficiency of 90% for momenta above 3 GeV/c. The signal that is generated in the TRD has two components. Traversing charged particles deposit energy in the Transition Radiation Detector due to ionization processes described by the Bethe-Bloch formula. In addition, electrons produce transition radiation which is absorbed in the drift region. The resulting clusters are relatively large and contribute significantly to the total amount of deposited charge, too. Using a likelihood method on the total amount of deposited charge (LQ), a pion suppression which is of the order of the design goal of 100 at momenta above 3 GeV/c can be reached. However, the total deposited charge alone does not contain the full signal information for electron identification that is provided by the Transition Radiation Detector. The Transition Radiation Detector signal is time resolved; the time resolution enables a position reconstruction of electron clusters in drift direction. Transition radiation photons are absorbed early in the gaseous volume of the TRD. Thus, the temporal (and therefore spatial) information of large clusters is an additional indicator for particles that produced transition radiation, i.e. electrons. Attempts to exploit this additional information are a combined likelihood on total deposited charge and the time bin with the maximum entry (LQX) and a two-dimensional likelihood method on deposited charge in two parts of the drift region (2-dim LQ). The two-dimensional likelihood method improves the electron/pion discrimination power of the TRD by about a factor of two for simulations. However, even these more sophisticated likelihood methods do not exploit the full information available.

In this thesis the application of artificial neural networks for particle identification (PID) with the Transition Radiation Detector was explored. As input for the neural network, the TRD signal of a particle track in one chamber was split into several slices. A check to determine the optimal width of the time slices with test beam

data resulted in using three time bins for each slice, corresponding to a time window of 300 ns. The deposited charge in the time slices was used as input vector for the neural network. The output of the network provides the Bayesian probabilities for each regarded particle species (e and π for test beam data, e, μ, π, K, and p for simulations). It was shown that artificial neural networks perform better than all other PID methods discussed in this thesis for test beam data as well as for AliRoot simulations. The obtained pion efficiency was below 0.5% at a momentum of 3 GeV/c for all analyzed data sets. Compared to a likelihood method on total deposited charge (LQ) the improvement of pion suppression was about a factor of three, compared to a two-dimensional likelihood method (2-dim LQ) it was about a factor of two.

It was shown that artificial neural networks can be trained with no performance loss using data that is not correctly identified up to a "contamination" of 15%. This important result shows that for the generation of reference data the purity of a data set is not the limiting factor for the particle identification performance of artificial neural networks. Motivated by the results of the contamination study, simulated data were applied to artificial neural networks trained with the contaminated test beam data of 2007. No performance loss compared to networks trained with simulated data was observed.

The results presented in this thesis do not complete the topic of particle identification for the TRD. Two studies that were initiated here, obtaining reference data from displaced vertices and the online particle identification, are part of future PhD theses [Hei, Wes12].

In summary, a framework for particle identification using neural networks has been developed in this thesis. The particle identification was analyzed starting from first results in test beams, its implementation in the simulation framework and reconstruction code of ALICE, and finally, its application within the actual experiment. Particle identification using neural networks showed the best performance of all PID methods. As an outcome of this thesis, it became the standard PID method for the ALICE Transition Radiation Detector. This standard PID method provides an excellent electron identification for the measurement of single electron spectra [Hei], of J/ψ [Kra10, Kru11], and of Υ [Wes12].

Zusammenfassung

Der ALICE Übergangsstrahlungsdetektor (TRD) wurde als Spurrekonstruktionsdetektor, als Triggerdetektor für Elektronen und für die Identifikation von Elektronen konzipiert. Elektronen sind eine geeignete Sonde für die Erforschung des Quark-Gluon-Plasmas. Das Konstruktionsziel für den Übergangsstrahlungsdetektor war eine Pioneneffizienz von unter 1% bei einer gleichzeitigen Elektroneneffizienz von 90% und Impulsen von über $3\,\text{GeV}/c$ zu erreichen. Das Signal das im TRD erzeugt wird besteht aus zwei Komponenten. Geladene Teilchen, die den Übergangsstrahlungsdetektor durchqueren, deponieren Energie durch Stoßionisation gemäß der Bethe-Bloch Formel. Zusätzlich dazu produzieren Elektronen Übergangsstrahlung die im Driftbereich absorbiert wird. Die dadurch enstandenen Ladungswolken sind relativ groß und tragen signifikant zu der gesamten deponierten Ladung bei. Mit einer Likelihood-Methode basierend auf der deponierten Gesamtladung kann eine Pionenunterdrückung in der Größenordnung des Konstruktionsziels von 100 bei über $3\,\text{GeV}/c$ erreicht werden. Die deponierte Gesamtladung alleine umfasst nicht die komplette Information, die vom Übergangsstrahlungsdetektor zur Identifiaktion von Elektronen zur Verfügung gestellt wird. Das Signal des Übergangsstrahlungsdetektors ist zeitaufgelöst; die Zeitauflösung erlaubt eine Positionsrekonstruktion der Elektronenwolken im Driftbereich. Übergangsstrahlungs-Photonen werden früh im Gasvolumen des TRDs absorbiert. Deswegen ist die Zeitinformation (and damit die Ortsinformation) von großen Ladungswolken ein zusätzlicher Hinweis auf Teilchen die Übergangsstrahlung, d.h. Elektronen, erzeugen. Versuche diese zusätzliche Information auszunutzen sind die kombinierte Likelihood-Methode basierend auf der deponierten Gesamtladung und dem Zeit-Bin mit der höchsten deponierten Ladung (LQX), sowie eine zweidimensionale Likelihood-Methode basierend auf der deponierten Ladung in zwei Zeitfenstern der Driftregion (2-dim LQ). Die zweidimensionale Likelihood Methode verbessert Elektronen/Pionen Trennung um einen Faktor von zwei in Simulationen, aber auch diese verfeinerten Methoden nutzen nicht die ganze verfügbare Information aus.

In dieser Arbeit wurde die Anwendung von künstlichen neuronalen Netzwerken für die Teilchenidentifikation (PID) mit dem Übergangsstrahlungsdetektor untersucht. Als

Eingangsgröße für das neuronale Netzwerk wurde das TRD-Signal in mehrere Abschnitte unterteilt. Ein Test um die optimale Breite eines Abschnittes zu bestimmen ergab eine Breite von drei Zeit-Bins pro Abschnitt, was einem Zeitfenster von 300 ns entspricht. Die deponierte Ladung in den Zeitfenstern wurde als Eingabe-Vektor für das neuronale Netzwerk benutzt. Die Ausgabe des Netzwerkes lieferte die Bayes-Wahrscheinlichkeiten für jede berücksichtigte Teilchensorte (e und π in Teststrahldaten, e, μ, π, K und p in Simulationen). Es wurde gezeigt, dass die neuronalen Netzwerke besser arbeiten, sowohl mit Teststrahl-Daten als auch in Simulationen, als alle anderen Teilchenidentifikationsmethoden die in dieser Arbeit untersucht wurden. Die erreichte Pioneneffizienz bei einem Impuls von 3 GeV/c lag unter 0.5% in allen untersuchten Datensätzen. Im Vergleich mit der Likelihood-Methode basierend auf der deponierten Gesamtladung (LQ) wurde die Pionenunterdrückung um den Faktor drei, verglichen mit der zweidimensionalen Likelihood-Methode um einen Faktor zwei verbessert.

Es wurde gezeigt, dass neuronale Netzwerke ohne Effizienzverlust mit Daten trainiert werden können, die eine "Kontamination"von bis zu 15% an nicht korrekt identifizierten Teilchen aufweisen. Dieses wichtige Ergebnis zeigt, dass für die Erzeugung von Refernzdaten die Reinheit eines Datensatzes nicht der limitierende Faktor für die Güte der Teilchenidentifikation mit neuronalen Netzwerken ist. Von den Ergebnissen der Konatminationsstudie motiviert, wurden simulierte Daten auf Netzwerke angewendet, die mit den kontaminierten Teststrahldaten aus dem Jahr 2007 trainiert worden sind. Verglichen mit Netzwerken, die mit simulierten Daten trainiert worden sind, wurde keine Verschlechterung der Effizienz beobachtet.

Die Ergebnisse, die in dieser Arbeit präsentiert wurden, schließen das Thema der Teilchenidentifikation mit dem TRD nicht ab. Zwei Studien, die Extraktion von Referenzdaten aus verschobenen Vertizes und die Online-Teilchenidentifikation, wurden in dieser Arbeit angeregt, die Teile von zukünftigen Doktorarbeiten sind [Hei, Wes12].

Zusammenfassend wurde in dieser Arbeit ein Framework für die Teilchenidentifikation mit neuronalen Netzwerken entwickelt. Die Teichenidentifikation wurde analysiert, angefangen mit ersten Ergebnissen aus Teststrahldaten, über die Implementierung in das Simulations- und Rekonstruktions-Framework von ALICE, und schließlich der Anwendung im tatsächlichen Experiment. Teilchenidentifikation mit neuronalen Netzwerken zeigte die beste Leistung von allen PID-Methoden. Als ein Ergebnis dieser Arbeit, wurde die Teilchenidentifikation mit neuronalen Netzwerken die Standardmethode für Teilchenidentifikation mit dem ALICE Übergangsstrahlungsdetektor. Diese Standard-PID-Methode stellt eine exzellente Elektronenidentifikation für die Messung von Spektren einzelner Elektronen [Hei], von J/ψ- [Kra10, Kru11] und von Υ-Mesonen [Wes12] zur Verfügung.

A. Kinematic Variables in High Energy Physics

In high energy physics it is useful to characterize a particle according to the rules of special relativity by its *four-momentum P*:

$$P = (E, \vec{p}) = (E, p_x, p_y, p_z), \tag{A.1}$$

E is the particle's energy and $\vec{p}$ its *three-momentum* in Cartesian coordinates. In this and all following equations it is:

$$\hbar \equiv c \equiv 1. \tag{A.2}$$

For free particles with the rest mass m_0 the energy-momentum relation is valid:

$$E^2 = m_0^2 + \vec{p}^2. \tag{A.3}$$

The absolute value of the four-momentum is called *invariant mass m_{inv}*. It is invariant under *Lorentz transformations* and given by:

$$m_{inv} = P^2 = -\vec{p}\vec{p} + E^2. \tag{A.4}$$

The invariant mass of a single particle is identical to its rest mass m_0.

Using the four-momenta the Mandelstam variables s, t, and u can be defined. They are used to describe scatterings for two on two particles. With P_1 and P_2 as the four-momenta of the incoming particles and P_3 and P_4 as outgoing ones they are:

$$s = (P_1 + P_2)^2 = (P_3 + P_4)^2, \tag{A.5}$$
$$t = (P_1 - P_3)^2 = (P_2 - P_4)^2, \tag{A.6}$$
$$u = (P_1 - P_4)^2 = (P_2 - P_3)^2. \tag{A.7}$$

$\sqrt{s}$ represents the total energy of a reaction in the center-of-mass system. For ion collisions it is usually given per nucleon pair: $\sqrt{s_{NN}}$.

A particle's momentum $\vec{p}$ can be split into a *longitudinal* component p_L parallel to the beam axis and a *transversal* component p_T perpendicular to the beam axis. For the ALICE coordinate system (see Appendix B) they are given by:

$$p_L = p\cos(\theta) = p_z, \tag{A.8}$$
$$p_T = p\sin(\theta) = \sqrt{p_x^2 + p_y^2}, \tag{A.9}$$

where p is the absolute value of the momentum. While the transverse momentum is invariant under Lorentz transformations in z directions, the longitudinal momentum is not. Instead the *rapidity y* is used:

$$y = \frac{1}{2} \ln \left(\frac{E + p_L}{E - p_L} \right). \tag{A.10}$$

The rapidity is additive under Lorentz transformations. Using the *transverse mass* $m_T = \sqrt{p_T^2 + m_0^2}$, energy and longitudinal momentum can be written as:

$$E = m_T \cosh(y), \tag{A.11}$$

$$p_L = m_T \sinh(y). \tag{A.12}$$

For $E \gg m_0$ the rapidity is approximated by the *pseudo-rapidity* η. For the emeasurement of the rapidity, the energy of a particle has to be determined. This requires particle identification. The pseudo-rapidity can be determined by measuring only the emission angle θ. Therefore it is often used instead of the rapidity. η is given by:

$$\eta = \frac{1}{2} \ln \left(\frac{p + p_L}{p - p_L} \right) \tag{A.13}$$

$$= -\ln \left[\tan \left(\frac{\theta}{2} \right) \right]. \tag{A.14}$$

B. The ALICE Coordinate System

The ALICE coordinate system was defined as a right-handed orthogonal Cartesian coordinate system in Reference [ALI03]. The point of origin $x, y, z = 0$ is at the nominal beam interaction point. The axes, azimuthal angle ϕ, and the polar angle θ are defined as follows:

- *x axis* - horizonztal axis perpendicular to the beam direction and pointing towards the accelerator center.

- *y axis* - perpendicular to the beam direction and the *x axis* pointing upward.

- *z axis* - perpendicular to the *x* and *y axis*, parallel to the beam direction. Positive *z* is from the point of origin towards *Side A*, negative *z* from the point of origin to *Side C*. The muon arm is located at negative *z*.
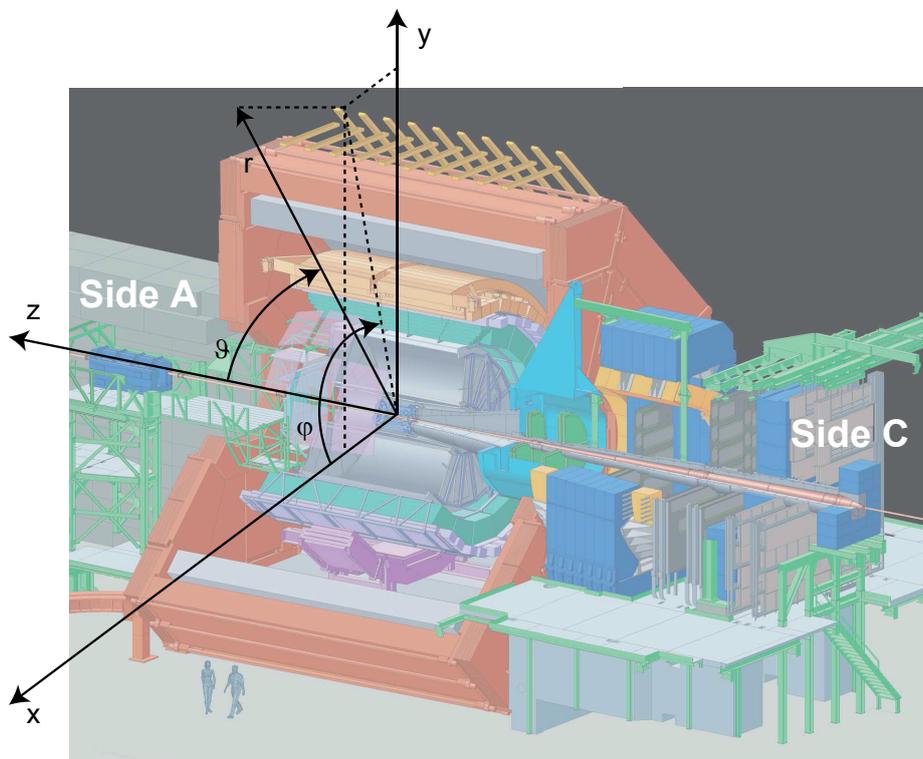

Figure B.1: The ALICE coordinate system. Plot adapted from Reference [GO09].

- *azimuthal angle* ϕ - increases clockwise from x $(\phi = 0)$ to y $(\phi = \pi/2)$ for an observer standing at negative z and looking towards *Side A*.

- *polar angle* θ - increases from z $(\theta = 0)$ passing the *xy plane* $(\theta = \pi/2)$ to $-z$ $(\theta = \pi)$.

C. Data Tables Test Beam

C.1 Test Beam 2002

C.1.1 PID Cuts 2002

Momentum (GeV/c)	Cherenkov1 (ADC counts)	Cherenkov2 (ADC counts)	Pb-glass (π) (ADC counts)	Pb-glass (e^-) (ADC counts)
1.0	20	20	90	160
1.5	20	20	105	250
2.0	20	20	130	350
3.0	20	20	185	550
4.0	20	20	200	750
5.0	21	24	210	1000
6.0	23	28	250	1200

C.1.2   Used Runs 2002

Run	Momentum (GeV/c)	# of Events	# of Events for PID	e^- Trigger
558	1.0	56,480	7,508	yes
559	1.5	58,413	17,162	yes
560	2.0	70,940	18,902	yes
561	3.0	70,300	26,798	yes
562	4.0	59,165	24,758	yes
563	5.0	54,775	16,824	yes
564	6.0	69,391	15,444	yes
565	2.0	14,226	3,392	no
566	3.0	21,759	3,294	no
567	4.0	31,646	2,742	no
568	5.0	38,334	1,848	no
569	6.0	43,839	1,484	no

C.2   Test Beam 2004

C.2.1   PID Cuts 2004

Momentum (GeV/c)	Cherenkov (π) (ADC counts)	Cherenkov (e^-) (ADC counts)	Pb-glass (π) (ADC counts)	Pb-glass (e^-) (ADC counts)
1.0	4	50	120	160
1.5	4	50	180	220
2.0	4	50	200	280
3.0	4	50	450	450
4.0	4	50	500	500
5.0	4	50	700	700
6.0	4	50	800	800
7.0	4	50	900	900
8.0	4	50	1200	1200
9.0	4	50	1400	1450
10.0	4	50	1600	1700

C.2.2   Used Runs for Small Prototypes Analysis 2004

Run	Momentum (GeV/c)	# of Events	# of Events for PID
120	10.0	63,201	15,162
121	9.0	62,056	10,700
122	8.0	59,079	12,450
123	7.0	58,572	12,348
124	6.0	53,677	13,032
125	5.0	57,734	7,278
126	4.0	59,641	16,796
127	3.0	60,398	17,714
128	2.0	37,229	9,828
129	1.5	31,845	4,628
130	1.0	36,010	7,404

C.2.3   Used Runs for the Stack Analysis 2004

Run	Momentum (GeV/c)	# of Events	# of Events for PID
425	10.0	27,718	10,424
426	8.0	23,543	8,070
428	6.0	23,329	11,402
429	4.0	22,366	15,426

C.3 Test Beam 2007

C.3.1 PID Cuts 2007

Momentum (GeV/c) (GeV/c)	Cherenkov (π) (ADC counts)	Cherenkov (e^-) (ADC counts)	Pb-glass (π) (ADC counts)	Pb-glass (e^-) (ADC counts)
1.0	350	900	575	575
2.0	350	900	900	900
4.0	350	900	1700	1750
6.0	350	900	2500	2700

C.3.2 Used Runs 2007

Run	Momentum (GeV/c)	# of Events	# of Events for Training
374	1.0	116,625	3,588
385	2.0	117,634	3,994
387	4.0	140,061	4,926
408	6.0	154,796	4,738

Bibliography

[Aad08] G. Aad *et al.* *JINST* **3** (2008) S08003.

[Aam08] K. Aamodt *et al.* *JINST* **3** (2008) S08002.

[Aam10] K. Aamodt *et al.* *Eur. Phys. J.* **C65** (2010) 111.

[AB91]   M. Aguilar-Benitez *et al.* *Z. Phys.* **C50** (1991) 405.

[Aba97] S. Abachi *et al.* *Phys. Rev. Lett.* **79** (1997) 1197.

[Abb97] B. Abbott *et al.* *Phys. Rev. Lett.* **79** (1997) 4321.

[Abe88] F. Abe *et al.* *Phys. Rev. Lett.* **61** (1988) 1819.

[Abe06] B. I. Abelev *et al.* *Phys. Rev. Lett.* **97** (2006) 152301.

[Aco06] D. Acosta *et al.* *CMS physics: Technical Design Report, Volume I.* CERN,
         Geneva, 2006.

[Ada03] J. Adams *et al.* *Phys. Rev. Lett.* **91** (2003) 072304.

[Ada04] J. Adams *et al.* *Phys. Rev.* **C70** (2004) 044902.

[Ada07a] A. Adare *et al.* *Phys. Rev. Lett.* **98** (2007) 172301.

[Ada07b] A. Adare *et al.* *Phys. Rev. Lett.* **98** (2007) 232002.

[Ada08] A. Adare *et al.* *Phys. Rev. Lett.* **101** (2008) 232301.

[Ada09a] A. Adare *et al.* *Detailed Measurement of the e+e- Pair Continuum in p+p
         and Au+Au Collisions at $\sqrt{s_{NN}} = 200 GeV$ and Implications for Direct Photon
         Production.* nucl-ex/0912.0244v1, 2009.

[Ada09b] A. Adare *et al.* *Phys. Lett.* **B670** (2009) 313.

[Adl03] S. S. Adler *et al.* *Phys. Rev. Lett.* **91** (2003) 072303.

[Adl05a] C. Adler *et al.* *Nucl. Instrum. Meth.* **A552** (2005) 364.

[Adl05b] C. Adler *et al.* *Nucl. Instrum. Meth.* **A540** (2005) 140.

[Adl05c] S. S. Adler *et al.* *Phys. Rev. Lett.* **94** (2005) 232301.

[Adl06] S. S. Adler *et al.* *Phys. Rev. Lett.* **96** (2006) 202301.

[Adl07a] S. S. Adler *et al.* *Phys. Rev.* **C76** (2007) 034904.

[Adl07b] S. S. Adler *et al.* *Phys. Rev.* **C75** (2007) 024909.

[Ado08] R. Adolphi *et al.* *JINST* **3** (2008) S08004.

[Adr08] O. Adriani *et al.* *JINST* **3** (2008) S08006.

[Afa07] S. Afanasiev *et al.* *Enhancement of the dielectron continuum in $\sqrt{s_{NN}} = 200 GeV$ Au+Au collisions.* nucl-ex/0706.3034, 2007.

[Aga05] G. Agakichiev *et al.* *Eur. Phys. J.* **C41** (2005) 475.

[Agg00] M. M. Aggarwal *et al.* *Phys. Rev. Lett.* **85** (2000) 3595.

[Ago03] S. Agostinelli *et al.* *Nucl. Instrum. Meth.* **A506** (2003) 250.

[Ake98] T. Akesson *et al.* *Nucl. Instrum. Meth.* **A412** (1998) 200.

[Ake01] T. Akesson *et al.* *Nucl. Instrum. Meth.* **A474** (2001) 172.

[Aki07] E. Akishina *et al.* *JINR Communications* **E10-2007-17** (2007) 1.

[Ale05] B. Alessandro *et al.* *Eur. Phys. J.* **C39** (2005) 335.

[Ale06] B. Alessandro *et al.* *J. Phys.* **G32** (2006) 1295.

[Alia] *The ALICE Experiment Offline Project.* http://www.cern.ch/ALICE/ Projects/offline/aliroot/Welcome.html.

[Alib] *The ALICE Offline Bible.* http://aliceinfo.cern.ch/Offline/AliRoot/ Manual.html.

[ALI95] *ALICE Technical Proposal.* CERN/LHCC-95-71, 1995.

[ALI96] *ALICE Technical Proposal Addendum 1*. CERN/LHCC 96-32, 1996.

[ALI99] *ALICE Technical Proposal Addendum 2*. CERN/LHCC 99-13, 1999.

[ALI03] *Definition of the ALICE Coordinate System and Basic Rules for Sub-detector Components Numbering*. ALICE-INT-2003-038, 2003.

[ALI06] *ALICE Technical Proposal Addendum 3*. CERN/LHCC 2006-14, 2006.

[Alv08] A. A. Alves *et al. JINST* **3** (2008) S08005.

[Ams08] C. Amsler *et al. Phys. Lett.* **B667** (2008) 1.

[And] A. Andronic. *ALICE TRD prototype tests.* `http://www-linux.gsi.de/~andronic/trd/tests/`.

[And01] A. Andronic *et al. IEEE Trans. Nucl. Sci.* **48** (2001) 1259.

[And03] A. Andronic *et al. Nucl. Instrum. Meth.* **A498** (2003) 143.

[And04a] A. Andronic. *Nucl. Instrum. Meth.* **A522** (2004) 40.

[And04b] A. Andronic *et al. Nucl. Instrum. Meth.* **A519** (2004) 508.

[And04c] A. Andronic *et al. Nucl. Instrum. Meth.* **A525** (2004) 447.

[And06a] A. Andronic. *Nucl. Instrum. Meth.* **A563** (2006) 349.

[And06b] A. Andronic *et al. Nucl. Instrum. Meth.* **A558** (2006) 516.

[And07a] A. Andronic *et al. Phys. Lett.* **B652** (2007) 259.

[And07b] A. Andronic *et al. Nucl. Phys.* **A789** (2007) 334.

[And08a] A. Andronic. Private communications, June 2008.

[And08b] A. Andronic *et al. Phys. Lett.* **B659** (2008) 149.

[And09a] A. Andronic. Private communications, March 2009.

[And09b] A. Andronic. Private communications, November 2009.

[Ane08] G. Anelli *et al. JINST* **3** (2008) S08007.

[Ang05] V. Angelov *et al. ALICE TRAP User Manual*, 2005.

[Ang06] V. Angelov. *Nucl. Instrum. Meth.* **A563** (2006) 317.

[Ang07] V. Angelov. Private communications, 2007.

[Aok06] Y. Aoki *et al. Phys. Lett.* **B643** (2006) 46.

[App88] R. D. Appuhn *et al. Nucl. Instr. Meth.* **A263** (1988) 309.

[Arn06] R. Arnaldi *et al. Phys. Rev. Lett.* **96** (2006) 162302.

[Art75]   X. Artru, G. B. Yodh, and G. Mennessier. *Phys. Rev.* **D12** (1975) 1289.

[ATL97] *ATLAS Inner Detector Technical Design Report, Volume II*. CERN/LHCC 97-17, 1997.

[ATL99] *ATLAS Detector and Physics Performance Technical Design Report, Volume II*. CERN/LHCC 99-15, 1999.

[ATL04] *ATLAS Heavy Ion Physics Letter of Intent*. CERN/LHCC 04-009, 2004.

[Aub01] B. Aubert *et al. Phys. Rev. Lett.* **86** (2001) 2515.

[Awe08] T. C. Awes. *J. Phys.* **G35** (2008) 104007.

[Bai95]   R. Baier *et al. Phys. Lett.* **B345** (1995) 277.

[Bai05]   R. Bailhache. *Energieverlust und e/π-Identifikation im ALICE Transition Radiation Detector*. Diplomarbeit, Gesellschaft für Schwerionenforschung, Darmstadt, 2005.

[Bai06]   R. Bailhache and C. Lippmann. *Nucl. Instrum. Meth.* **A563** (2006) 310.

[Bai08]   R. Bailhache. *Calibration of the ALICE Transition Radiation Detector and a study of Z^0 and heavy quark production in pp collisions at the LHC*. Ph.D. thesis, Technische Universität, Darmstadt, 2008.

[Bal03]   M. Ballintijn *et al. The PROOF Distributed Parallel Analysis Framework based on ROOT*. physics/0306110, 2003.

[Bar80] V. Barger, W. Y. Keung, and R. J. N. Phillips. *Phys. Lett.* **B91** (1980) 253.

[Bar92] E. Barbarito *et al. Nucl. Instrum. Meth.* **A313** (1992) 295.

[Bas98] G. Bassompierre *et al. Nucl. Instrum. Meth.* **A411** (1998) 63.

[Bat]   B. Bathen. *Thesis in preparation*. Ph.D. thesis, Institut für Kernphysik, Münster.

[Baz09]   A. Bazavov *et al.* *Phys. Rev.* **D80** (2009) 014504.

[Bea04]   I. G. Bearden *et al.* *Phys. Rev. Lett.* **93** (2004) 102301.

[Bed07]   M. Bedjidian and O. Kodolova. *J. Phys.* **G34** (2007) N143.

[Bel93]   R. Bellotti *et al.* *Comp. Phys. Comm.* **78** (1993) 17 .

[Ben87]   H.-U. Bengtsson and T. Sjostrand. *Comput. Phys. Commun.* **46** (1987) 43.

[Ber07]   A. Bercuci. Private communications, March 2007.

[Ber08a]   A. Bercuci, A. Andronic, and M. Ivanov. *GSI Scientific Report 2007* (2008) 243.

[Ber08b]   A. Bercuci and M. Fasel. Private communications, January 2008.

[Ber08c]   A. Bercuci, M. Fasel, and M. Ivanov. *GSI Scientific Report 2007* (2008) 242.

[Ber08d]   A. Bercuci and M. Ivanov. *GSI Scientific Report 2007* (2008) 244.

[Ber08e]   A. Bercuci and D. Miskowiec. Private communications, May 2008.

[Ber09a]   A. Bercuci. Private communications, December 2009.

[Ber09b]   M. J. Berger *et al.* *XCOM: Photon Cross Sections Database.*
           http://physics.nist.gov/PhysRefData/Xcom/Text/XCOM.html,
           February 2009.

[Bil84]   P. Billoir. *Nucl. Instrum. Meth.* **A225** (1984) 352.

[Bjo83]   J. D. Bjorken. *Phys. Rev. D* **27** (1983) 140.

[Blo69]   E. D. Bloom *et al.* *Phys. Rev. Lett.* **23** (1969) 930.

[Blu08]   W. Blum, W. Riegler, and L. Rolandi. *Particle Detection with Drift Chambers*.
           Springer-Verlag, Berlin, 2nd edition, 2008.

[BM07]   P. Braun-Munzinger and J. Stachel. *Nature* **448** (2007) 302.

[BM09a]   P. Braun-Munzinger and J. Stachel. *Charmonium from Statistical
           Hadronization of Heavy Quarks – a Probe for Deconfinement in the Quark-
           Gluon Plasma*. nucl-th/0901.2500, 2009.

[BM09b] P. Braun-Munzinger and J. Wambach. *Rev. Mod. Phys.* **81** (2009) 1031.

[Brü04] O. S. Brüning *et al. LHC Design Report*. CERN, Geneva, 2004.

[Bra08] E. L. Bratkovskaya, W. Cassing, and O. Linnyk. *Low mass dilepton production at ultrarelativistic energies*. nucl-th/0805.3177, 2008.

[Bre69] M. Breidenbach *et al. Phys. Rev. Lett.* **23** (1969) 935.

[Bri90] J. S. Bridle. In D. S. Touretzky (Editor) *Advances in Neural Information Processing Systems, Volume 2*. Morgan Kaufmann Publishers, 1990 .

[Bru93] R. Brun and F. Carminati. *GEANT, Detector Description and Simulation Tool*. CERN Program Library Long Writeup W5013, 1993.

[Buc99] D. Bucher. *Produktion direkter Photonen in ultrarelativistischen Schwerionenstößen*. Ph.D. thesis, Institut für Kernphysik, Münster, 1999.

[Bus04] O. Busch. *Nucl. Instrum. Meth.* **A522** (2004) 45.

[Cab75] N. Cabibbo and G. Parisi. *Phys. Lett.* **B59** (1975) 67.

[Car04] F. Carminati, (Ed.) *et al. J. Phys.* **G30** (2004) 1517.

[Cas03] G. L. Case and M. L. Cherry. *Proceedings of the 28th International Cosmic Ray Conference* (2003) 2241.

[CER00] *CERN Press Release: New State of Matter created at CERN*. `http://press.web.cern.ch/press/PressReleases/Releases2000/` `-PR01.00EQuarkGluonMatter.html`, 2000.

[Che74a] M. L. Cherry, D. Mueller, and T. A. Prince. *Nucl. Instrum. Meth.* **115** (1974) 141.

[Che74b] M. L. Cherry *et al. Phys. Rev.* **D10** (1974) 3594.

[Che03] M. L. Cherry and G. L. Case. *Astroparticle Physics* **18** (2003) 629.

[Che06] M. Cheng *et al. Phys. Rev.* **D74** (2006) 054507.

[Col05] J. Colas *et al. Nucl. Instrum. Meth.* **A550** (2005) 96.

[COM05] *ALICE Technical Design Report of the Computing*, 2005. CERN-LHCC-2005-018.

[Cor02]   P. Cortese *et al. Addendum to the Technical Design Report of the Time-of-Flight System*. CERN/LHCC 2002-016, 2002.

[Dah08]   T. Dahms. *Dilepton spectra in p+p and Au+Au collisions at RHIC*. Ph.D. thesis, Stony Brook University, 2008.

[dC03]   J. de Cuveland. *Entwicklung der globalen Spurrekonstruktionseinheit für den ALICE-Übergangsstrahlungsdetektor am LHC (CERN)*. Diplomarbeit, Physikalisches Institut, Heidelberg, 2003.

[d'E07]   D. G. d'Enterria, (Ed.) *et al. J. Phys.* **G34** (2007) 2307.

[d'E08]   D. G. d'Enterria. *J. Phys.* **G35** (2008) 104039.

[Dem00]   W. Demtröder. *Experimentalphysik 3, Atome, Moleküle und Festkörper*. Springer-Verlag, Heidelberg, 2000.

[Dem05]   W. Demtröder. *Experimentalphysik 4, Kern-, Teilchen- und Atomphysik*. Springer-Verlag, Heidelberg, 2005.

[Den84]   A. Denisov *et al.* Presented at Annual Mtg. of Div. of Particles and Fields of the APS, Santa Fe, N. Mex., Oct 31 - Nov 3, 1984.

[Den99]   B. Denby. *Comp. Phys. Comm.* **119** (1999) 219 .

[dF07]   P. de Forcrand and O. Philipsen. *JHEP* **01** (2007) 077.

[Doe06]   P. Doetinchem *et al. Nucl. Instrum. Meth.* **A558** (2006) 526 .

[Dok01]   Y. L. Dokshitzer and D. E. Kharzeev. *Phys. Lett.* **B519** (2001) 199.

[Dol93]   B. Dolgoshein. *Nucl. Instrum. Meth.* **A326** (1993) 434.

[dR06]   A. de Roeck *et al. CMS physics: Technical Design Report, Volume II*. CERN, Geneva, 2006.

[Dur97]   L. Durieu *et al. Proc. Physics Acc. Conf.* (1997) 228.

[Ego00]   V. Egorychev, V. Savelev, and S. J. Aplin. *Nucl. Instrum. Meth.* **A453** (2000) 346.

[Ems10]   D. Emschermann. *Construction and Performance of the ALICE Transition Radiation Detector*. Ph.D. thesis, Physikalisches Insitut, Heidelberg, 2010.

[Eva08]   L. Evans, (Ed.) and P. Bryant, (Ed.). *JINST* **3** (2008) S08001.

[Fas03]   A. Fasso *et al. The physics models of FLUKA: Status and recent development*. hep-ph/0306267, 2003.

[Fas08]   M. Fasel. *Hadronenproduktion in Proton-Proton Kollisionen*. Master thesis, Institut für Kernphysik, TU Darmstadt, 2008.

[Fos99]   I. Foster and C. Kesselmann (Editors) *The Grid: Blueprint for a New Computing Infrastructure*. Kaufmann, San Francisco, CA, 1999.

[FWD04]   *Technical Design Report of the ALICE Forward Detectors: FMD, T0 and V0*. CERN/LHCC 2004-025, 2004.

[Gar57]   G. M. Garibian. *Zh. Eksp. Teor. Fiz.* **33** (1957) 1043.

[Gar75]   G. M. Garibian, L. A. Gevorgian, and C. Yang. *Nucl. Instrum. Meth.* **125** (1975) 133.

[Gar04]   C. Garabatos. *Nucl. Instrum. Meth.* **A535** (2004) 197.

[Gat79]   E. Gatti *et al. Nucl. Instrum. Meth.* **163** (1979) 83.

[Ger86]   V. Gerthsen, Kneser. *Physik*. Springer-Verlag, Heidelberg, 1986.

[Gin45]   V. L. Ginzburg and I. M. Frank. *J. Phys. (USSR)* **9** (1945) 353.

[Gla70]   R. J. Glauber and G. Matthiae. *Nucl. Phys.* **B21** (1970) 135.

[GM64]   M. Gell-Mann. *Phys. Lett.* **8** (1964) 214.

[GO05]   J. F. Große-Oetringhaus. *Determination of the Physics Performance of the ALICE Central Barrel using a Distributed GRID Computing Environment*. Diplomarbeit, Institut für Kernphysik, Münster, 2005.

[GO09]   J. F. Große-Oetringhaus. *Measurement of the Charged Particle Multiplicity in Proton-Proton Collisions with the ALICE Detector*. Ph.D. thesis, Institut für Kernphysik, Münster, 2009.

[Gra09]   R. Grajcarek. *Feasibility Study on Determining the Average Radiation Thickness of the ALICE Transition Radiation Detector from CERN Test Beam Data*. Diplomarbeit, Physikalisches Institut, Heidelberg, 2009.

[Gri02a] V. M. Grichine. *Phys. Lett. B* **525** (2002) 225 .

[Gri02b] V. M. Grichine. *Nucl. Instrum. Meth.* **A484** (2002) 573.

[Gru93] C. Grupen. *Teilchendetektoren*. BI-Wiss.-Verl., Mannheim, 1993.

[Gun03] T. Gunji. *Study of Electron Identification Capability of the ALICE Transition Radiation Detector*. Master thesis, Department of Physics, Graduate School of Science, University of Tokyo, 2003.

[Gut02] M. Gutfleisch. *Digitales Frontend und Preprozessor im TRAP1-Chip des TRD-Triggers für das ALICE-Experiment am LHC (CERN)*. Diplomarbeit, Kirchhoff Institut für Physik, Heidelberg, 2002.

[Gut06] M. Gutfleisch. *Local Signal Processing of the ALICE Transition Radiation Detector at LHC (CERN)*. Ph.D. thesis, Kirchhoff Institut für Physik, Heidelberg, 2006.

[Gyu05] M. Gyulassy and L. McLerran. *Nucl. Phys.* **A750** (2005) 30.

[Han75] G. Hanson *et al. Phys. Rev. Lett.* **35** (1975) 1609.

[Heb49] D. Hebb. *The Organization of Behavior*. Wiley, New York, 1949.

[Hei]

[Hei09] M. Heide. Private communications, November 2009.

[Hil05] C. E. Hill *et al. AIP Conf. Proc.* **749** (2005) 127.

[HMP98] *Technical Design Report of the ALICE High-Momentum Particle Idenfication Detector*. CERN/LHCC 98-019, 1998.

[HN90] R. Hecht-Nielsen. *Neurocomputing*. Addison-Wesley, Reading MA, 1990.

[Hoe08] C. Hoehne *et al. Nucl. Instrum. Meth.* **A595** (2008) 187.

[Hop82] J. J. Hopfield. *Proc. Natl. Acad. Sci.* **79** (1982) 2554.

[ITS99] *Technical Design Report of the ALICE Inner Tracking System*. CERN/LHCC 99-012, 1999.

[Jac98] J. D. Jackson. *Classical Electrodynamics*. Wiley & Sons, New York, 1998.

[Joh03] I. J. Johnson. *Nucl. Phys.* **A715** (2003) 691.

[Kal08] A. Kalweit. *Energy Loss Calibration of the ALICE Time Projection Chamber*. Master thesis, Institut für Kernphysik, TU Darmstadt, 2008.

[KB04a] C. Klein-Bösing. *J. Phys.* **G30** (2004) S975.

[KB04b] C. Klein-Bösing. *Production of Neutral Pions and Direct Photons in Ultra-Relativistic* Au + Au *Collisions*. Ph.D. thesis, Institut für Kernphysik, Münster, 2004.

[KB09] M. Klein-Bösing. *Transition Radiation Detector and Reconstruction of Photon Conversions in the CBM Experiment*. Ph.D. thesis, Institut für Kernphysik, Münster, 2009.

[Köh07] W. Köhler, G. Schachtel, and P. Voleske. *Biostatistik*. Springer-Verlag, Berlin, 4th edition, 2007.

[Kim08] B. Kim *et al.* *Electron/Hadron Separation: Neural Networks as a Tool*. Presentation at the ALICE Physics Week in Prague, March 2008.

[Kir07] T. Kirn. *Nucl. Instrum. Meth.* **A581** (2007) 156.

[Kli09] M. Kliemant. *Analysis of ALICE - TRD Test Beam Data*. Presentation at the DPG Spring Meeting in Bochum, 2009.

[Koc97] V. Koch. *Int. J. Mod. Phys.* **E6** (1997) 203.

[Kra06] F. Kramer. *Studie zur Messung von Quarkonia mit dem ALICE-TRD und Aufbau eines Teststandes für seine Auslesekammern*. Diplomarbeit, Institut für Kernphysik, Frankfurt, 2006.

[Kra10] F. Kramer. *Thesis in preparation*. Ph.D. thesis, Institut für Kernphysik, Frankfurt, 2010.

[Kru08] D. Krumbhorn. *Study of J/ψ Production in pp Collisions at $\sqrt{s} = 10\,TeV$ with the Transition Radiation Detector of ALICE*. Diplomarbeit, Physikalisches Institut, Heidelberg, 2008.

[Kru11] D. Krumbhorn. *Thesis in preparation*. Ph.D. thesis, Physikalisches Institut, Heidelberg, 2011.

[Kwo08] Y. Kwon. *Physics-Motivated Neural Networks Approach to Electron/Hadron Separation*. Presentation at the ALICE Analysis Meeting at GSI, February 2008.

[Lan08] J. P. Lansberg *et al. AIP Conf. Proc.* **1038** (2008) 15.

[Leb09] S. A. Lebedev and G. A. Ososkov. *Phys. Part. Nucl. Lett.* **6** (2009) 161.

[LeC98] Y. LeCun *et al.* In G. Orr and M. K. (Editors) *Neural Networks: Tricks of the trade*. Springer, 1998 .

[LHC08] *CERN FAQ - LHC the guide*. CERN-Brochure-2008-001-Eng, 2008.

[Lip06] W.-M. Lippe. *Soft-Computing*. Springer, Berlin, 2006.

[Lit03] L. Litov. *Nucl. Instrum. Meth.* **A502** (2003) 495.

[Lud81] T. Ludlam *et al. Nucl. Instrum. Meth.* **180** (1981) 413.

[Mar07] A. Marin and T. Dietel. *Physics with Conversion Photons in ALICE*. Presentation at the ALICE Physics Week in Münster, 2007.

[Mar08] A. Marin. *Exploring the LHC medium with electromagnetic probes*. Presentation at the 3rd International Conference on Hard and Electromagnetic Probes in High Energy Nuclear Collisions, 2008.

[Mas09a] S. Masciocchi. *Analysis Framework and Analysis Train.* `http://alice-wiki.gsi.de/cgi-bin/view/Analysis/AnalysisFrameworkAndAnalysisTrain`, January 2009.

[Mas09b] S. Masciocchi. *Simulation Production at GSI*. `http://alice-wiki.gsi.de/cgi-bin/view/Data/SilviasMCProduction`, March 2009.

[Mat84] E. Mathieson and J. S. Gordon. *Nucl. Instrum. Meth.* **227** (1984) 277.

[Mat86] T. Matsui and H. Satz. *Phys. Lett. B* **178** (1986) 416.

[McC43] W. S. McCulloch and W. Pitts. *Bulletin of Math. Bio.* **5** (1943) 115.

[McL07] L. McLerran and R. D. Pisarski. *Nucl. Phys.* **A796** (2007) 83.

[Mes06] D. Meschede (Editor) *Gerthsen Physik*. Springer-Verlag, Heidelberg, 2006.

[Mil07] M. L. Miller *et al. Ann. Rev. Nucl. Part. Sci.* **57** (2007) 205.

[Mit03]   V. A. Mitsou. *The ATLAS transition radiation tracker*. hep-ex/0311058, 2003.

[MP08]   J. Mercado Peréz. *Development of the Control System of the ALICE Transition Radiation Detector and of a Test Environment for Quality-Assurance of its Front-End Electronics*. Ph.D. thesis, Physikalisches Insitut, Heidelberg, 2008.

[Muo99]   *Technical Design Report of the Dimuon Forward Spectrometer*. CERN/LHCC 99-022, 1999.

[Muo00]   *Addendum to the Technical Design Report of the Dimuon Forward Spectrometer*. CERN/LHCC 2000-046, 2000.

[O'B93]   E. O'Brien *et al. IEEE Trans. Nucl. Sci.* **40** (1993) 153.

[Ott96]   R. Ottenhues. *Teilchenklassifizierung im Bleiglaskalorimeter mit künstlichen neuronalen Netzen*. Diplomarbeit, Institut für Kernphysik, Münster, 1996.

[Otw09]   J. Otwinowski. *PWG1 - The Performance Train*. Presentation at the ALICE Offline Week, October, 2009.

[Pei97]   T. Peitzmann. *Kernmaterie unter extremen Bedingungen – Die experimentelle Suche nach dem Quark-Gluon-Plasma*. Habilitation, Institut für Kernphysik, Münster, 1997.

[Pei02]   T. Peitzmann and M. H. Thoma. *Phys. Rept.* **364** (2002) 175.

[Per00]   D. H. Perkins. *Introduction to High Energy Physics*. Cambridge University Press, Cambridge, 2000.

[PHO99]   *Technical Design Report of the ALICE Photon Spectrometer*. CERN/LHCC 99-004, 1999.

[PMD99]   *Technical Design Report of the Photon Multiplicity Detector*. CERN/LHCC 99-032, 1999.

[PMD03]   *Addendum to the Technical Design Report of the Photon Multiplicity Detector*. CERN/LHCC 2003-038, 2003.

[Rap00]   R. Rapp and J. Wambach. *Adv. Nucl. Phys.* **25** (2000) 1.

[Roo]   *An Object-Oriented Data Analysis Framework*. http://root.cern.ch.

[Ros58]   F. Rosenblatt. *Psychol. Rev.* **65** (1958) 386.

[Ruc90] D. W. Ruck *et al. IEEE Trans. Neur. Netw.* **1** (1990) 296.

[Rum86] D. E. Rumelhart, G. E. Hinton, and R. J. Williams. In D. E. Rumelhart and J. L. McClelland (Editors) *Parallel Distributed Processing: Explorations in the Microstructure of Cognition, Volume 1.* MIT Press, 1986 .

[Sac78] L. Sachs. *Angewandte Statistik - Statistische Mthoden und ihre Anwendungen.* Springer, Berlin, 1978.

[Sah04] B. Sahlmüller. *Production of η Mesons in $\sqrt{s_{NN}} = 200$ GeV d+Au and p+p Collisions Measured by the PHENIX Experiment.* Diplomarbeit, Institut für Kernphysik, Münster, 2004.

[Sai03] P. Saiz *et al. Nucl. Instrum. Meth.* **A502** (2003) 437.

[Sch] J. Schwindling. *MLPfit: A Tool for Multilayer Perceptrons.* http://schwind.web.cern.ch/schwind/MLPfit.html.

[Sch97] A. Scherer. *Neuronale Netze: Grundlagen und Anwendungen.* Vieweg, Braunschweig, 1997.

[Sch04] Y. Schutz. *Heavy-Ion Physics at LHC.* Presentation at Quark Matter in Oakland, January 2004.

[Sch09] K. Schweda. *The ALICE Experiment at the LHC.* Presentation at the DPG Spring Meeting in Bochum, March 2009.

[Sel82] S. M. Seltzer and M. J. Berger. *Int. J. of Applied Rad.* **33** (1982) 1189 .

[Shu05] P. Shukla. Private Communications, 2005.

[Sic09] E. Sicking. *Alignment of ALICE TRD Modules Using Cosmic Ray Data.* Diplomarbeit, Institut für Kernphysik, Münster, 2009.

[SNN98] *Stuttgart Neural Network Simulator, UsersManual, Version 4.2.* http://www-ra.informatik.uni-tuebingen.de/downloads/SNNS/ SNNSv4.2.Manual.pdf, 1998.

[Som08] W. Sommer. *Measurement of Quarkonia within the central detectors of ALICE.* Ph.D. thesis, Institut für Kernphysik, Frankfurt am Main, 2008.

[Ste84] R. Sternheimer, M. Berger, and S. Seltzer. *Atomic Data and Nuclear Data Tables* **30** (1984) 261 .

[TOF00] *Technical Design Report of the Time-Of-Flight System.* CERN/LHCC 2000-012, 2000.

[TPC00] *Technical Design Report of the ALICE Time Projection Chamber.* CERN/LHCC 2000-01, 2000.

[TRD01] *Technical Design Report of the ALICE Transition Radiation Detector.* CERN/LHCC 2001-021, 2001.

[vH06] H. van Hees and R. Rapp. *Phys. Rev. Lett.* **97** (2006) 102301.

[Vol08] M. B. Voloshin. *Prog. Part. Nucl. Phys.* **61** (2008) 455.

[Vul05] B. Vulpescu. Private Communications, 2005.

[Wan91] X.-N. Wang and M. Gyulassy. *Phys. Rev.* **D44** (1991) 3501.

[Wan92] X.-N. Wang and M. Gyulassy. *Phys. Rev. Lett.* **68** (1992) 1480.

[Wat86] Y. Watase *et al.* *Nucl. Instrum. Meth.* **A248** (1986) 379.

[Wer74] P. J. Werbos. *Beyond Regression: New Tools for Prediction and Analysis in the Behavioural Sciences.* Ph.D. thesis, Harvard University, Cambridge, MA, 1974.

[Wes12] U. Westerhoff. *Thesis in preparation.* Ph.D. thesis, Institut für Kernphysik, Münster, 2012.

[Wet06] A. A. Wetzler. π^0 *Mesons and Photons measured in AuAu Collisions at an Energy of* $\sqrt{s_{NN}} = 62\,GeV.$ Ph.D. thesis, Institut für Kernphysik, Frankfurt am Main, 2006.

[Wik10] http://en.wikipedia.org, February 2010.

[Wil88] R. W. Williams and K. Herrup. *Annu. Rev. Neurosci.* **11** (1988) 423.

[Wil04] A. Wilk. *Elektronen-Pionen-Separation im ALICE TRD.* Diplomarbeit, Institut für Kernphysik, Münster, 2004.

[Wil06] A. Wilk. *Nucl. Instrum. Meth.* **A563** (2006) 314.

[Wil08] A. Wilk. *Reference Data for PID using Artificial Neural Networks in the ALICE TRD.* Presentation at the ALICE Physics Week in Prague, March 2008.

[Won94] C.-Y. Wong. *Introduction to High-Energy Heavy-Ion Collisions*. World Scientific, Singapore, 1994.

[Wul09] E. S. Wulff. *Position Resolution and Zero Suppression of the ALICE TRD*. Diplomarbeit, Institut für Kernphysik, Münster, 2009.

[Yag05] K. Yagi, T. Hatsuda, and Y. Miake. *Quark-Gluon Plasma*. Cambridge University Press, Cambridge, 2005.

[Zau03] O. Zaudtke. *Simulation einer TRD-Driftkammer des ALICE-Experiments mit GARFIELD*. Diplomarbeit, Institut für Kernphysik, Münster, 2003.

[ZDC99] *Technical Design Report of the Zero-Degree Calorimeter*. CERN/LHCC 99-05, 1999.

[Zwe64] G. Zweig. *An SU(3) Model for Strong Interaction Symmetry and its Breaking. 2*, 1964. CERN-TH-412.

Danksagung

An erster Stelle danke ich Herrn Prof. Dr. Johannes P. Wessels dafür, dass ich meine Doktorarbeit zu einem überaus interessanten Thema im Rahmen einer großen internationalen Kollaboration anfertigen durfte. Ich möchte mich für seine Betreuung sowie für sein offenes Ohr, nicht nur was physikalische Fragestellungen angeht, bedanken. Des Weiteren danke ich ihm für die sehr guten Arbeitsbedingungen am Institut für Kernphysik, sowie für die Möglichkeit während meiner Promotion an zahlreichen Konferenzen sowie Forschungsaufenthalten im In- und Ausland teilnehmen zu können.

Neben Herrn Prof. Dr. Johannes P. Wessels danke ich auch Herrn Prof. Dr. Alfons Khoukaz ganz herzlich für die Begutachtung dieser Arbeit.

Ganz besonders bedanke ich mich bei Dr. Alexandru Bercuci für die sehr intensive Zusammenarbeit bei der Implementierung der neuronalen Netze als Teilchenidentifikationsmethode in AliRoot, sowie für all seine Arbeit für den TRD Tracker. Seine Diskussionsbereitschaft und seine Geduld bei der Beantwortung vieler Fragen haben mir bei der Verwirklichung dieser Arbeit sehr geholfen. Dr. Anton Andronic danke ich nicht nur für die Organisation und die Durchführung der Strahlzeiten. Seine fundierten Antworten auf meine Fragen haben sehr zu meinem Verständnis des Übergangsstrahlungs-Detektors beigetragen.

Dr. Melanie Klein-Bösing danke ich für die zahlreichen kurzweiligen Diskussionen und Ratschläge, ihre Begleitung zu diversen Strahlzeiten sowie für die schöne gemeinsame Studienzeit und für Tine.

Bei Dr. Christian Klein-Bösing, Dr. Thomas Dietel, Markus Heide, Dr. Matus Kalisky und Uwe Westerhoff möchte ich mich für die hervorragende Zusammenarbeit am Institut für Kernphysik bedanken.

Ein dickes Dankeschön geht an die ALICE TRD Kollaboration für all die Unterstützung und das Interesse für meine Arbeit. Namentlich erwähnen möchte ich hier Dr. Venelin Angelov, Dr. Raphaëlle Bailhache, Prof. Dr. Christoph Blume, Markus Fasel, Dr. Chilo Garabatos, Dr. Jan Fiete Große-Oetringhaus, Alexander Kalweit, Jochen Klein, Kathrin

252

bedanke ich mich für jede Menge Ablenkung und jede Menge Aufmunterung, bei Tine für die lange Zeit die sie mich begleitet hat.